DESIGNING SOFT CONTINUUM ROBOTS FOR SENSOR-ENABLED CONTROL

A Dissertation

Submitted to the Faculty

of

Purdue University

by

Jennifer C. Case

In Partial Fulfillment of the

Requirements for the Degree

of

Doctor of Philosophy

August 2019

Purdue University

West Lafayette, Indiana

THE PURDUE UNIVERSITY GRADUATE SCHOOL
STATEMENT OF DISSERTATION APPROVAL

Dr. Rebecca Kramer, Co-Chair

School of Mechanical Engineering

Dr. James Gibert, Co-Chair

School of Mechanical Engineering

Dr. Neera Jain

School of Mechanical Engineering

Dr. Jeffrey Youngblood

School of Materials Engineering

Approved by:

Dr. Jay Gore

Head of the School Graduate Program

To the family and friends I found along this journey.

ACKNOWLEDGMENTS

I would like to thank my advisor, Professor Rebecca Kramer, with whom I have grown as a person and a researcher. It has been a wonderful experience to be part of the Faboratory from the beginning and see the growth that has been made during my time as part of the lab. Professor Kramer has helped me determine the direction of the research and has been instrumental in making sure that I present the work to the best of my ability. Being a member of this lab has given me many opportunities to expand my understanding of what robotics is and what it could be. I would also like to thank my co-advisor, Professor James Gibert, who has been helped me deepen my understanding of the theory behind materials and soft material mechanics. Professor Gibert has helped me remain focused and organized on my thesis when I otherwise would have chased side projects and has provided guidance into the organization of the thesis. Additionally, I would like to thank committee members, Professor Neera Jain and Professor Jeffrey Youngblood, who have taken their time to help in the compilation of the thesis. Thanks to Professor Kartik Ariyur, who helped deepen my understanding of controls and designing systems with controls in mind, and Professor Marcial Gonzalez, who helped me understand continuum mechanics and taught me to always dig deeper into source materials when researching.

I would like to thank the labmates that I have been able to work beside. Thanks to Dr. Edward White, who collaborated with me on several projects and still provides guidance and insight to me. Thanks to Dr. Michelle Yuen and Professor Joran Booth, who have been helpful when discussing manufacturing and design of components for the robotic skin work. Thanks to Ellen Yang, Evelyn Huang, Jane Jacobs, and Gabrielle Branin for assisting in fabrication and characterization of materials, soft structures, and robotic skins.

I would like to thank the NASA collaborators that I have had the good fortune to work with. Thanks to Vytas SunSpiral, who has been very influential with how I look at the world and encouraged me to explore ideas and concepts from other fields. Thanks to Arno Rogg, who has helped broaden my understanding of compliant mechanisms and provided feedback on my research. Thanks to Dr. Brian Coltin and Dr. Michael Furlong, who also helped remind me to keep exploring other fields.

I would like to thank Professor Nicholas Pohlman and Professor Brianno Coller from my alma mater, Northern Illinois University, who encouraged me to pursue a graduate degree and helped send me on the crazy ride that is graduate school.

I would like to thank my wonderful husband, John Heritage, who has been incredible support, especially the past few years, and moved halfway across the country with me. I would also like to thank my family, who have been supportive through the years.

Finally, I would like to acknowledge the NASA Space Technology Research Fellowship program, which has funded both me and my research. A special thanks to Claudia Meyer, who took time to go over the program with me when I had to choose between a fellowship. The conclusions presented in this thesis do not necessarily reflect the views and opinions of NASA.

TABLE OF CONTENTS

LIST OF TABLES

LIST OF FIGURES

ABSTRACT

Case, Jennifer C. Ph.D., Purdue University, August 2019. Designing Soft Continuum Robots forSensor-Enabled Control. Major Professors: Rebecca Kramer, James Gibert, School of Mechanical Engineering.

Soft robots, which leverage flexible, stretchable, and smart materials, are relevant to numerous applications that traditional robots struggle with, such as search-and-rescue, human-robot interaction, and exploration. Since soft robots are composed of soft materials, they are inherently more robust to impacts and falls than their rigid counterparts. Additionally, soft structures are inherently safer for human-robot interaction. While clever use of soft materials offers many advantages, it complicates the control of soft robotic systems. Many of the control strategies that have been established for traditional robotic systems cannot be readily used for soft systems due to the difficulties in modeling soft systems. These control strategies require sensory feedback that can reliably provide the state of the system. However, obtaining sensory feedback from soft robotic systems is non-trivial. It has only been in the past few years that soft sensor technology has begun integrating with soft structures to try to provide the proprioceptive data needed to implement control strategies. This thesis focuses on the use of sensory feedback to compensate for the complex behavior of a soft system. In order to accomplish sensory feedback, multiple soft sensor types were investigated and integrated into soft robotic systems. Simplified analytical models were developed to help design soft systems and to interpret the state from the collected sensory data for use in feedback controllers. These simplified models also allowed the implementation of feedforward controllers. Additionally, this body of work demonstrates how sensory feedback can be used to inform feedforward controllers of certain model parameters.

1. INTRODUCTION

1.1 Overview of Soft Robotics

Soft robotics is expanding the definition of robotic systems by utilizing soft and responsive materials. Examples of soft robots are shown in Figure 1.1. These highly deformable materials create more dexterous systems that have infinite degrees of freedom compared to traditional materials, which create discrete joints. This has the potential to influence the development of several robot applications, such as search-and-rescue robots, exploration robots, human-robot interaction, medical robots, and manufacturing.

In search-and-rescue and exploration applications, robots are required to move through unknown environments, such as rubble or natural disaster ridden areas, to

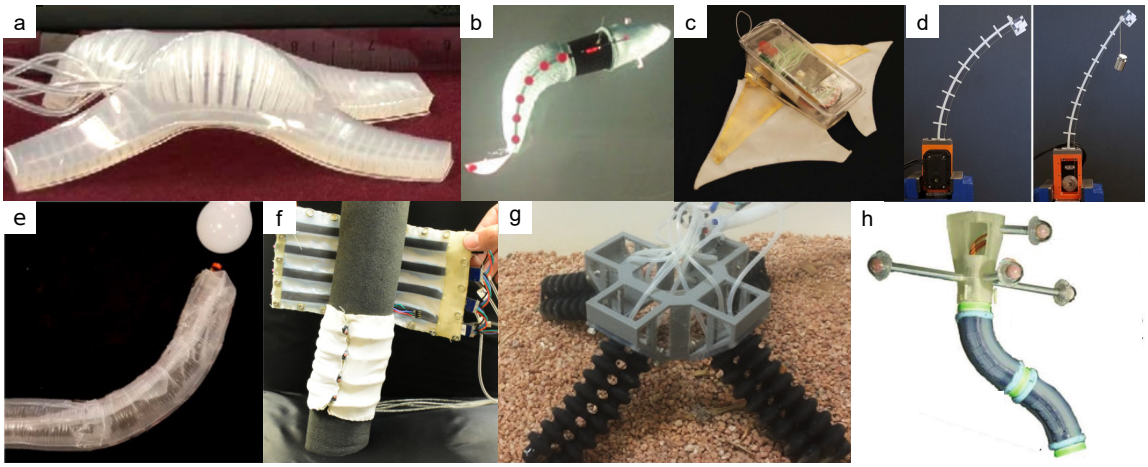

Figure 1.1. Examples of soft robots: (a) multigait soft robot [1], (b) soft robotic fish [2], (c) soft robotic manta ray [3], (d) cable-driven continuum robot [4], (e) growing continuum robot [5], (f) robotic skins [6], (g) quadraped robot with soft pneumatic legs [7], and (h) pneumatically-driven continuum robot [8].

look for potential survivors or safety hazards. Because of the challenging terrain, rigid robots can be difficult to maneuver safely. In contrast, highly deformable soft robots are better equipped to squeeze through small openings in rubble [5] or survive a fall [9]. In human-robot interactions, it is desirable to have robots that are not capable of harming humans to prevent any accidents that could result in injury or death. Some researchers are tackling this by developing complicated joints that will "soften" if an unexpected force is encountered. In contrast, the materials used in soft robotics integrates the safety desired for human-robot interaction at the material level. This material-level safety is also why soft robots are desirable for medical applications. Internal organs are all soft and can be damaged by large pressures that could be applied by traditional materials, which makes maneuvering around with rigid implements undesirable. This inability to move around too much may result in multiple incisions or larger incisions to reach a place of interest in a surgery. In contrast, soft materials will not apply large pressures since they will readily deform due to external forces caused by surrounding objects or the environment. In manufacturing applications, using soft materials can help in numerous ways. A soft gripper at the end of a rigid robotic arm will be able to delicately grasp objects that are difficult for rigid graspers without the need of sensors and controllers, such as food (e.g., eggs and tomatoes) and IV bags. A soft robot arm could benefit small manufacturing plants by being able to work alongside human workers safely. However, in order to perform these applications, the robotic system needs to be controllable.

1.2 Motivation

Control of traditional robotic systems has been established for several decades. Traditional robots can be described in terms of rotational and prismatic joints that generally have predictable behavior. The motors and systems that drive these joints also tend to be well understood and modeled and there are existing sensors, such as encoders, designed to detect the movement of these robotic systems.

In contrast, control of soft robots is complicated by the large deformations (>3%), non-linear material properties, and potentially unknown material properties. In order to address these issues, there are two potential solutions: developing very robust plant models that can be integrated into feedforward control and integrating sensors to achieve feedback control. This thesis considers both approaches, but favors the latter because using only the former would require fully modeling both the system and environment to be of practical use. By having appropriate sensory feedback, it is possible to control a system with minimal information about the system; it only requires knowing how each actuator deforms the system.

In order to address non-linear material properties, the system can be limited to low strains (<40%) which behaves linearly and thus, a nominal elastic modulus can be found. This simplifies modeling significantly such that simplified analytical models are achievable. With a fully characterized system, understanding of system behavior, and appropriate sensory feedback (i.e., knowing the state of the system), unknown material properties can be identified and used with analytical models to provide feedforward control.

When working with soft robotic systems, it is important that control of the system be taken into account during the design phase rather than trying to add controls to a pre-designed system. The design of the system should consider: (1) the structural material(s), (2) the actuators, (3) the sensors, (4) structural geometry, and (5) desired motion and/or task. Knowing these will help establish how sensors and actuators should be placed to achieve a desired motion.

Due to the complexity of this problem across all of soft robotics, this thesis limits the study of soft robotic design and sensor-enabled control to 2D and 3D elastomer-based continuum segments. Continuum segments can serve as a base upon which other systems are designed, such as the body of a snake robot and the legs of a quadraped. An example of a robot made from continuum segments is shown in Figure 1.1h. Additionally, this thesis considers control using robotic skins (see Figure 1.1f), which are 2D planar substrates with embedded sensors and actuators that can be wrapped

around passive objects to "roboticize" those objects using surface manipulation [6]. The robotic skins can be applied and re-applied to various systems to achieve different functions, such as locomotion, grasping, manipulation, etc. While these skins can be wrapped around any object, this thesis focuses on the specific case of wrapping the skins around cylindrical segments, which essentially become continuum segments and can be combined to create multi-segment continuum robots.

1.3 Literature Review

The work in this thesis draws upon previous work in three areas: soft robotic components, control of soft robots, and robotic skins. Many of the actuating soft robots were developed in parallel to many soft sensors. It has not been until recently that the sensors have begun to be integrated into soft robots. Most control of soft robots has either been open-loop or reliant on external sensors, such as cameras. Robotic skins have been shown to be widely applicable to a number of applications, but have only been rigorously demonstrated in open-loop control.

1.3.1 Components

In traditional robotic systems, components, such as actuators, sensors, and the structure, are typically bought or manufactured separately and then combined to create a robot. In soft robotics, separate components can also be combined to create robots, but soft robots can also be fully integrated with the actuators and sensors fabricated directly into the structure of the robot [10, 11]. While this is an exciting prospect for soft robotics, all the manufacturing issues have not been addressed in completely integrated systems, which means that failure of one component requires the entire system to be rebuilt. To narrow focus onto design and control, this thesis utilizes modular systems so that singular components can be replaced quickly and efficiently. The components for soft robots are broken into three parts: materials, actuators, and sensors.

Materials. The majority of soft robots are made using polymer, specifically elastomers [13], as the structural component. The behaviors of these materials are unusual compared to traditional materials and the behaviors can be affected by curing conditions, which makes it impossible to have a singular model of a material. It is important for researchers to understand the behaviors of soft materials as well as the conditions that can influence those behaviors. These materials experience non-linear stress-strain curves and viscoelastic effects, which means that stress and strain in the materials can change over time [14–17]. Many models have been proposed to capture the non-linear stress-strain curves seen in these materials, such as the Neo-Hookean [14], Mooney-Rivlin [18, 19], Ogden [14], Yeoh [20], and Gent [21] models. Similarly, the viscoelastic behavior has had several proposed models, such as the Kelvin, Maxwell, Burgers [15], Zener [16], and extended Maxwell model [17]. Additionally, as the elastomers are stretched, they experience a weakening known as the Mullin's effect (shown in Figure 1.2) [12,22], which is caused by bonds in the polymer matrix breaking. This essentially results in the behavior of the material changing as the polymer matrix breaks. The material behavior is further complicated by curing

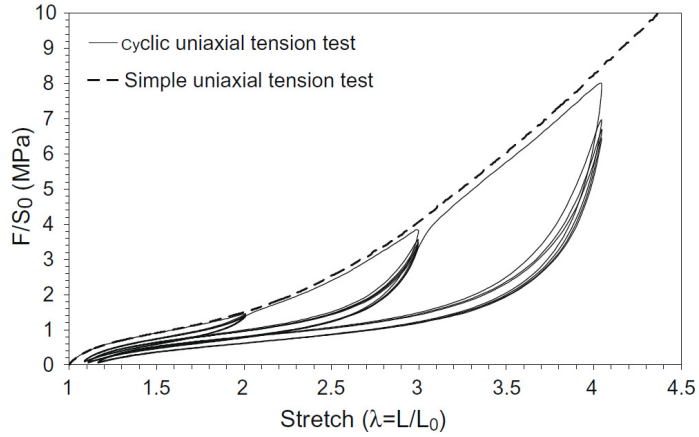

Figure 1.2. Example of the Mullin's effect, which shows softening of the material after the first pull, for a carbon-black filled styrene-butadiene rubber [12].

temperature and the ratio between the elastomer and curing agent [23,24], which can lead to large differences in reported values for elastomers.

Actuators. To actuate soft systems, there are numerous actuators that have been adapted: including fluidic (pneumatic, hydraulic, and combustion) actuators [28,31], shape memory alloys (SMAs) [31,32], cables [33,34], electro-active polymers [31,35], ionic metal-polymer composites [36], and muscle tissue [37]. Examples of some of these actuators are shown in Figure 1.3. This thesis focuses on systems that are driven by fluidic actuators, SMA, and cables, which are the most well understood and easiest to begin integrating into controlled systems. While these are all viable actuators, each one has advantages and drawbacks. Fluidic actuators can produce large deformations and reasonable forces; however, they require pumps, valves, etc., which can be difficult to untether, but not impossible [38,39]. Additionally, these pumps and valves are usually not soft. Shape memory alloys (SMAs) usually only undergo a 2-3% change in length, but if SMA wire is programmed to remember a

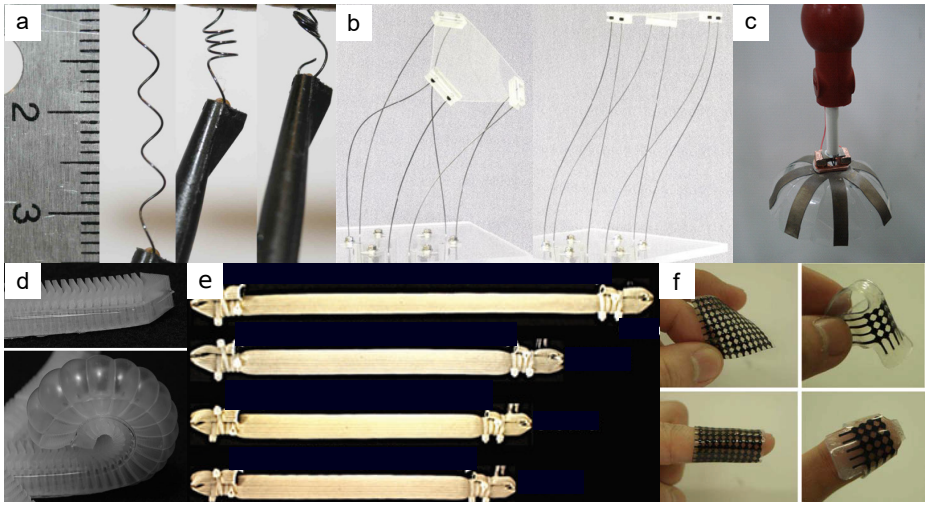

Figure 1.3. Examples of actuators used in soft robotic applications: (a) shape memory alloy [25], (b) cables [26], (c) ionic metal-polymer composites [27], (d) pneunet pneumatic actuators [28], (e) McKibben pneumatic actuators [29], and (f) electro-active polymers [30].

coiled shape, this actuator can undergo significant changes in length, albeit at the cost of force output [25]. SMA actuators require heat to change shape and since the material itself is conductive, they can be Joule heated, which means the system only requires a voltage supply, such as a battery, to power the SMA actuator [40, 41]. Cable-driven systems can withstand large forces, but typically require motors to wind and unwind the cables [9, 42].

Sensors. While a thorough literature review of soft sensing technology is given in Chapter 2, soft sensors used in subsequent chapters will briefly be described here. This thesis utilizes two soft sensor technologies: liquid-metal-embedded sensors and conductive composite sensors. While the work started with liquid-metal-embedded sensors, these sensors were difficult to fabricate and would fail frequently during testing. An attempt to address the issues at the interface between the liquid-metal-embedded channels and copper wires is addressed in Appendix E. However, it became evident that the interface was not the only issue and the connectivity of the liquid metal in the microchannels was unrealiable either due to the scale of the microchannels or the thickness of the sensors. To address the shortcomings of these sensors, robust exfoliated graphite composite sensors were developed [43]. These sensors have been used for numerous research projects [44, 45], including some of the work presented in this thesis.

Researchers have embedded soft sensors into various systems to use the sensors to determine the state of the system. Despite the large quantity of potential soft, stretchable sensors presented in the research, many researchers elect to use flexible sensors [46, 47]. This is likely due to various issues that soft sensors may have. For example, silver nanowire-based sensors often experience hysteresis, which makes them challenging to work with [48]. Liquid-metal-based sensors have been proposed for state estimation of several systems [49–51], but due to the challenges of working with these sensors, they are not used in many controlled systems. In recent years, stretchable optical sensors have been proposed for control systems [52]. One of the

goals of this thesis is to bridge the gap between showing that sensors can be used for state estimation and control to actually demonstrating that control is possible and exploring how sensors should be placed to provide appropriate state estimation.

1.3.2 Control of Soft Robots

Control of soft robots can be broken down into three categories: model-based control, model-free control (i.e., machine learning), and sensor-enabled control [53–55]. Model-based and machine learning approaches allow the system to be run with open-loop feedforward control. While these control strategies can show promising results [56–59], the lack of sensory feedback makes it impossible to determine if an object has blocked the robot's path or trajectory. Sensory feedback is necessary to inform the system of its true state. Additionally, sensors can provide information about the environment around the robot. Sensory feedback will be necessary to bring soft robots from controlled, laboratory environments to real-world applications. Most of the controls in soft robotics, like in this thesis, focuses on continuum robots. This is due to available research on modeling and control of continuum robots, which originally stemmed from traditional robotic systems [33].

Modeling of Continuum Robots. Continuum arms were born from the research of hyperredundant robots, which were long trunk-like and snake-like robots. Hyperredundant robots display continuum-like behavior, but are made from rigid components. In contrast, continuum robots exhibit true continuous deformations due to the materials used, which were originally thin metal rods and have transitioned over to softer materials in recent years, and are actuated by cables, fluidic actuators, or SMA [60]. Hyperredundant robots, by their nature, required piece-wise deformations that would be fit to desired space curves. This same idea was ported over to continuum robots. The researchers began approximating the deformation of these systems using Bessel functions with sines and cosines, wavelets, and eventually landed on piecewise constant curvatures (PCC) [33]. When a moment is applied to a soft or

flexible system, the system tends to take a deformation that approximates a constant curvature. When segments are stacked together, this constant curvature approximation holds and became the foundation for modeling continuum robots and applied to numerous systems [33, 61–64]. Models have been made to explain the static and dynamic properties of PCC robots [33]. However, PCC cannot be used if the robot comes into contact with external forces. For this case, variable curvature models have been developed [60, 65]. To start with the simplest case, this thesis focuses on static models using the PCC assumption. This model is adapted to perform state estimation using measurements from strain sensors. Additionally, the model is adapted to allow twisting of segments as well. This concept has been shown in the literature with the assumption that the system can be modeled with Cosserat rods [66], but this assumption does not hold for the systems considered in this thesis.

Sensor-Enabled Control of Continuum Robots. Sensory feedback for cable-driven continuum robots can be as simple as using motor encoders. This allows the researchers to track the length of the cables, which can inform the deformation of the robot [33, 55]. However, this does not account for external forces and should not be relied upon in situations were the environment is unknown. To track the actual deformation of the system, many researchers have utilized cameras and electromagnetic sensors [55, 63, 67]. Utilizing external cameras for feedback limits the use cases of the continuum robot since system must be visible to the cameras. Similarly, electromagnetic sensors require that nothing interferes with the signal. Additional systems have proposed using IMUs to track the position [68–70] or internal cameras [71], but this requires either embedding or attaching a large rigid component to a soft system. Rather than using rigid components to provide feedback for soft systems, it would be better to utilize soft sensors, which will better integrate with the structure. One of the goals of this thesis is to demonstrate that control is achievable with soft sensors.

1.3.3 Robotic Skins

Robotic skins were designed to create robots on-the-fly by wrapping them around various soft materials. They have embedded sensors to detect changes to the system. Initially, a robotic skin that utilized muslin, embedded-liquid-metal sensors, and SMA demonstrated how the sensor response changed depending on how the skin was oriented on the body [72]. While this work showed proof-of-concept for robotic skins, the demonstrations were limited to bending in a single direction and compression on bodies of foam. Recently, robotic skins made from elastomer films, spandex, capacitive exfoliated graphite sensors, SMA, and McKibben actuators were demonstrated [6]. These skins demonstrated different layouts of components: a rectangular skin with four parallel sensor and actuator pairs and a triangular skin with sensor actuator pairs along the edges. The rectangular skins were wrapped around cylindrical objects to create locomoting robots and a continuum manipulator. The triangular skins were used to wrap more complex geometries to demonstrate a rolling tensegrity icosahedron and a wearable shirt. However, the robotic demonstrations were all run open-loop with the sensors only being used for the wearable demonstration. Closed-loop control was demonstrated such that the length of a single sensor was controlled with a single actuator. While this work does an excellent job of introducing the concepts of robotic skins, the skins are capable of much more. The thesis utilizes the models developed for continuum robots along with the robotic skins to show how robotic skins can be used to identify properties about the structure it is wrapped around. This ability to "learn" information about the system it is wrapped around allows the skins to develop feedforward models for controls. Additionally, this thesis demonstrates feedback control of the state of the continuum structure.

1.4 Thesis Outline

This thesis is outlined as follows:

Chapter 2 provides a literature review of soft sensor technology that has the potential to be used in sensory skins. This chapter breaks down soft sensors by substrate, conductor, and structure.

Chapter 3 focuses on material properties in elastomers and how those properties may affect sensor responses for sensors made from elastomers. This research considers both the nonlinear stress-strain response and viscoelastic properties.

Chapter 4 moves onto demonstrating simple sensory feedback control of a elastomeric beams. Additionally, this work considers how geometric and material changes can influence the behavior and control of the beams. This was one of the first demonstrations of control of a soft robotic system using only soft sensors.

Chapter 5 presents work on a planar cable-driven continuum arm with six segments. This work explores the idea of having highly coupled cabling patterns rather than having individual cables controlling each segment. While having decoupled cabling for each segment simplifies the controls, having highly coupled cabling can reduce the requirements on the actuators.

Chapters 6, 7, and 8 present research on robotic skins that builds towards control of continuum segments and a more generalized design for robotic skins intended for continuum segments. Chapter 6 demonstrates how four parallel and equally spaced sensors can be used to estimate the state of continuum segments. Additionally, this chapter demonstrates that with properly characterized actuators, the robotic skins can estimate the bending stiffness of the underlying structure. Chapter 7 demonstrates how this ability to "learn" about underlying structures can be used to inform feedforward control models. Both feedforward and feedback control is applied to single segments and a two-segment continuum robot. Chapter 8 extends this research by relaxing the skin design to allow actuators and sensors to be placed on angles, which allows the continuum segments to twist as well as bend. A generalized analytical model is provided to explain the behavior of the system.

Finally, Chapter 9 summarizes and provides future directions for this research.

1.5 Thesis Contributions

Contribution 1: A verification that sensors made from soft materials can be designed in such a way that their response is decoupled from complex material behaviors, such as nonlinear stress-strain curves and viscoelasticity. Decoupling of sensor response from material behavior facilitates control with soft sensors by enabling reliable measurements. In this thesis, this decoupling is realized through the use of liquid metal-based resistive sensors and conductive composite-based capacitive sensors.

Contribution 2: A soft robot design study that considers both material choice and geometry for controllability of soft systems. The results of this study enable the design of soft robotic structures for controllability using simple control strategies.

Contribution 3: A 2D cable-driven multi-segment continuum soft robot model with cables that cross sides of the robot between soft segments. This approach enables a highly coupled cable design, which reduces the number or actuators needed and size of actuators required to move the robot without impacting the workspace of the robot compared to traditional cabling methods.

Contribution 4: A new continuum segment model that estimates state based on measured lengths of the segment at locations parallel to the neutral axis. This model was also inverted to determine the required actuator commands as a function of desired state. These contributions enable both feedback and feedforward control of soft, cylindrical structures.

Contribution 5: A model to estimate the material properties of soft cylindrical segments based on the observed deformation and under known actuator commands. This model has the potential to facilitate the development of adaptive feedforward controllers in the future.

Contribution 6: A generalized continuum segment model that relaxes the requirements for sensor and actuator placement from previously derived models. In the new model, sensors and actuators can be placed on angles, rather than only parallel to the neutral axis. This contribution enables twisting and bending motions, rather than pure bending, and broadens the utility of soft continuum segments.

2. SENSOR SKINS: AN OVERVIEW

When systems are made from soft materials, it is important to also develop soft sensing technology to incorporate into the soft structures. Traditional sensors and electrical components are often rigid and are best suited to well-defined systems that have discrete motions and confined trajectories. In contrast to traditional robotic systems, soft structures generally have more degrees of freedom than rigid systems. These degrees of freedom come from the deformability of the soft structures themselves. State information of these soft systems may be obtained by populating the surface of the structure with sensor skins, which are stretchable planar structures with embedded sensing components. The design of these highly deformable sensory skins has been guided by the flexible and stretchable characteristics of elastomers and human skin.

There are a number of different ways that the definition of a sensor skin can be limited including stipulations like stretchability, placement on a flexible host, proprioceptive feedback, etc.; however, this chapter will focus on sensor skins that are mechanically compatible with human skin, meaning that they can undergo at least 20% strain. Other reviews on flexible sensors that do not match this criteria are available for further reading [73–75].

Figure 2.1 shows examples of sensor skins used in different applications. Figure 2.1a is a sensor skin module containing three resistance-based strain gauges capable of measuring deformation. Multiple modules can be combined into an array

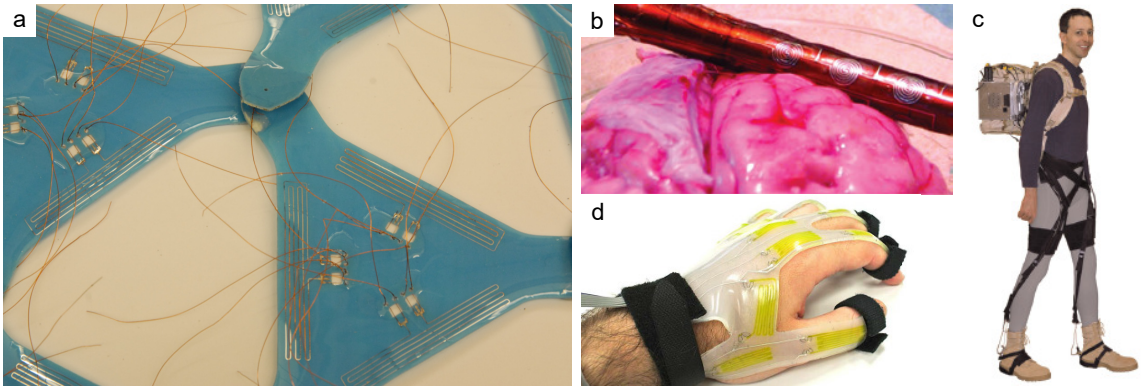

Figure 2.1. Examples of sensors skins. (a) Sensor skin modules composed of silicone elastomer with three embedded liquid metal sensing strain gauges each. (b) Sensor skin composed of liquid metal pressure sensors for detecting tissue damage [76]. (c) Wearable system with liquid metal strain sensors for detecting pose [77]; and (d) wearable system with ionic liquid strain sensors for detecting hand pose [78].

to measure the state of deformation of a host. Figure 2.1b shows an example of a tactile sensor skin used in a surgical environment. This device is composed of an array of pressure sensors to probe the environment without damaging tissues during neuroendoscopy and gives the surgeon another tool to help operate safely on a patient [76]. Two examples of wearable sensor skins can be seen in Figure 2.1c, d. These sensors can detect pose of the lower limbs (Figure 2.1c) [77] and of the hand (Figure 2.1d) [78].

In the following sections, the materials and processing approaches of substrates and conductors, the structures and designs of elements, and the systems used in sensor skins are discussed and this chapter concludes with potential future directions of sensor skins.

2.1 Materials and Processing

Sensor skins are generally composed of at least two types of materials: substrates and conductors. These materials give the skins stretchability as well as the ability

to interact in some capacity with itself or a host. This section overviews common substrates and conductors that have been used in sensor skin fabrication and their processing techniques.

2.1.1 Substrate

A sensor skin is, in essence, a substrate onto which or into which sensors are integrated. Substrates can be defined in terms of attributes such as stretchability, breathability, toughness, tear resistance, weight, and compatibility with the host or existing manufacturing techniques. Due to the wide range of substrates available and the complex interactions between the substrate and the host, the substrate should be carefully chosen so that it matches the target properties of the sensor and the fabrication process. Furthermore, in some wearable applications there is a need to use two substrates: the sensor substrate and the garment that is meant to be worn. The integration of two substrates into a single device adds another layer of complexity, since the compatibility between substrate materials must be considered in addition to the substrate-host compatibility.

In the following subsections, two common types of substrate materials are discussed: elastomers and woven fabrics.

Elastomers. Elastomers are the most common substrates in soft sensor applications. They are capable of supporting structures and encasing functional elements. In addition, elastomers are compatible with other types of substrates, such as woven fabrics [79–81]. There are many commercially available low-cost elastomers with a wide range of stretchability (from 40% [82] up to 700% [83]). Because elastomers are highly stretchable, they are conformable to human skin, which can strain up to 30%, and thus are less likely to limit natural motion than nonstretchable substrates. However, this high flexibility and stretchability comes at a cost; elastomers are subject to viscoelastic behaviors, such as the Mullins effect [22], creep, and stress relaxation [15, 16].

Commercial elastomers usually are sold as two parts (free chains and crosslinker). Polymerization starts by mixing both parts at a specific ratio, and can be triggered by heating [82] or exposure to UV light [84]. Uncured elastomer can be easily cast in a pre-made mold, which is convenient for creating specific geometries for different part functions and material properties. Researchers use different techniques to fabricate molds such as lithography [85] and 3D printing [1].

It is possible to use methods to shape the elastomer other than replica molding, such as spin coating or other coating methods to make thin films. For example, elastomer films cast onto polyethylene terephthalate (PET) sheets can be integrated into roll-to-roll machines. Elastomers can be both physically and chemically altered through processes such as laser ablation [86] and plasma treatment [87].

Elastomers were originally used to coat and support the structure of conductive solid substrates [88–91]. However, the concept of building microchannels into elastomers [92] allowed researchers to build sensor components by filling elastomeric microchannels with functional materials, such as liquid metals [76, 85, 86, 93–105] or ionic liquids [78, 106, 107].

Woven Fabrics. Woven fabric is most recognizable as the material of which garments are comprised. More generally, woven fabrics are composed of two sets of fibers interlaced together. This construction gives rise to the tensile strength and tear resistance of fabrics. Properties of the fabric such as the elasticity, stiffness, chemical resistance, and thermal properties can be tuned based on the choice of the constituent fibers and the pattern with which they are woven.

The first attempts to integrate sensors and fabrics were by means of simple attachment, such as sewing. This concept was improved upon by the invention of conductive fibers that can be woven the same way as conventional fibers and act as sensory elements without additional components [108]. Woven fabrics using conductive threads and fibers have been employed as strain, pressure, respiratory, heart rate, and electrochemical sensors, as well as gesture-input devices [109–111]. Conductive threads

woven with a known spacing can act as capacitive pressure sensors by measuring the change in capacitance between fibers due to thread shifting from applied pressure. Conductive fibers can act as resistive sensors when they are woven as single or multiple threads that gain contact with each other and reduce resistance when strain or pressure is applied to them [111, 112].

Woven skin sensors can achieve higher strains by sewing the components onto pre-wrinkled fabrics. This technique allows the devices to be stretched beyond the stretch limit of the fabric itself [113]. Alternately, conductive coatings can be applied to the same pre-wrinkled construct to form stretchable electronics-compatible fabrics [114, 115].

2.1.2 Conductor

A conductor is a material that allows the flow of electrons or ions through it. In sensor skins, conductors have two major functions: conveying information (i.e. a trace on a circuit board) and collecting information (i.e. a sensor). In many cases, conductors can be used for both purposes. The stability of the conductor and its conformal contact with the interface are essential to ensure efficient sensor performance. In wearable applications, it is also important to consider the biocompatibility (i.e. toxicity) of a sensor.

The conductors that are highlighted in this section are thin metal films, liquid metals, ionic liquids, conductive polymers, and conductive inks.

Thin Metal Films. Conductive materials are, in most cases, rigid. They show flexible behavior when they are shaped as thin films. The first attempt to use thin metal films in flexible electronics was in 1967 to produce the first flexible solar cell [116, 117]. Advanced electronics typically consist of insulators, conductors, and semiconductors, and it is possible to use processes like roll-to-roll to produce electronics at larger scales [118]. Metallic thin films have been fabricated to accommodate moderate strains using clever geometries (waves and nets) made from both

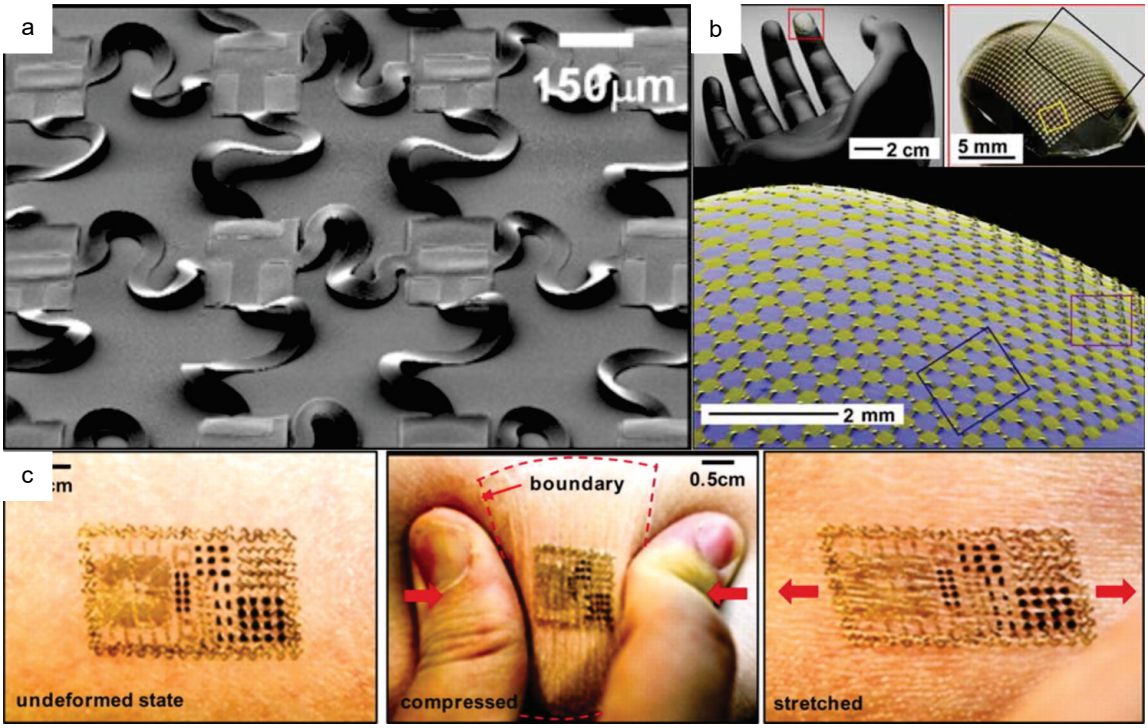

Figure 2.2. (a) Extremely stretchable metal films with serpentine-design bridges [119]. (b) Stretchable circuit with noncoplanar metal films on a model finger tip [128]. (c) A multifunctional epidermal electronic circuit mounted on human skin in undeformed, compressed, and stretched states [129].

highly conductive metals (such as gold, silver, copper, and aluminum) and semiconductors (such as silicon) [119]. Thin-film electronics enable other applications such as displays [81, 120, 121], electrodes [122, 123], LEDs [124] and wearable electronics [125–127].

The devices fabricated using thin metal films are flexible. However, they lack stretchability due to the very low fracture strain of most metals. Researchers have used geometry to cause this nonstretchable material to behave elastically. For instance, curved and wavy metal films can undergo strains that are impossible to achieve using flat films [89–91, 128, 130–133]. Figure 2.2a, b shows two examples of thin film structures. This approach enables stretchable interconnects [134, 135], integrated circuits [136], batteries [137] and epidermal electronics (Figure 2.2c) [129, 138]. With

proper engineering design, the devices fabricated using this technique can be strained up to 200% [139].

Devices fabricated using metal films or wires deform plastically with prolonged use leading to permanent deformation that reduces the device efficiency or totally disconnects the circuit [140–143]. Other conductors, such as liquid metals and ionic liquids, have been recently used as alternatives that do not suffer from this limitation.

Liquid Metal. There is a growing interest in using liquid metals in flexible electronics as alternatives to conventional metals. The most famous liquid metals are eutectic alloys such as eutectic gallium-indium (eGaIn) and eutectic gallium-indium-tin (Galinstan). They have high metallic conductivity ($\approx 3.4 \times 10^6 \Omega^{-1} m^{-1}$ for EGaIn and $\approx 3.1 \times 10^6 \Omega^{-1} m^{-1}$ for Galinstan [144]) and form a thin gallium-oxide skin that allows them to form stable nonspherical structures despite their high surface tension [145,146]. In contrast to mercury, gallium-indium alloys are non-toxic and therefore have potential applications in biocompatible sensors. Gallium-indium alloys can be injected into microchannels due to their low viscosity [85,93,94,100,105,147], and their liquid nature allows them to take the shape of the microchannel even at very high strains (up to 700%) without failure [83].

Researchers have developed fabrication techniques that are more automated than manual injection [148]. For instance, a microtip wet with the liquid metal can transfer patterns on a substrate by direct contact [149]. The tip can be replaced by a syringe needle that continuously extrudes the liquid metal and directly writes onto a surface [96, 146]. Liquid metal can selectively wet parts of a substrate using a predesigned mask [150, 151], or by treating the substrate surfaces such that liquid metal self-assembles into the desired areas [101, 152–154]. Liquid metals are not suitable for inkjet printing due to the high surface tension, its corrosive nature to most other metals and the presence of surface oxide. However, a dispersion of liquid metal nanoparticles in a volatile solvent can be inkjet printed since the dispersion properties

are dictated by the carrier solvent rather than the liquid metal [155]. Finally, liquid metal films maybe subtractively patterned by selective laser ablation [156].

The various patterning techniques have enabled the fabrication of different types of liquid metal-based sensors, such as capacitive pressure sensors [103–105], resistive strain sensors [86, 96, 101, 155], resistive pressure sensors [76, 94, 95, 99, 100, 147, 157], curvature sensors [85, 93] and shear sensors [157]. Examples of other liquid metal-based devices are antennas [158–160], soft wires [78, 107], self-healing wires [161], diodes [162], and capacitors [149].

Ionic Liquids and Solutions. Ionic liquids and salt solutions can also be used in sensor skins. Ionic liquids are molten salts while salt solutions are salts dissolved in a solvent, typically water. These solutions are capable of reflowing and are typically used within an elastomer substrate, where preformed microchannels are filled with the conductive solutions by injection [78, 97, 107] or vacuum [163].

The most familiar form of a salt solution is a sodium chloride (NaCl) solution, which has been used to make sensors [163] and sensor arrays [164]. Researchers have also demonstrated the use of potassium chloride solution (KCl), sodium hydroxide (NaOH), and hydrogen chloride (HCl) in their sensors, but found that both NaOH and HCl were corrosive to the sensor interface and that NaCl had a better range than KCl [163]. An example of an ionic liquid is 1-ethyl-3-methylimidazolium ethyl sulfate [78, 97, 106]. Ionic liquids and salt solutions have been used in fabricating tactile sensors [97, 163, 164], strain sensors [107], curvature sensors [106], diodes [162] and wearable devices [78].

The major drawback of using salt solutions is that popular substrates, like elastomers, are gas permeable, which means that water will slowly evaporate and leave a salt residue in the substrate. Water evaporation can be slowed down by adding glycerol to the solution [107, 165].

Conductive Inks. A conductive ink is a solvent that contains a suspension of conductive particles, such as metallic nanoparticles, organometallic compounds, carbon

nanotubes and graphene [166–168]. Volatile organic solvents (ethanol, toluene, etc.) are commonly used and leave behind the conductive particles on the substrate as they evaporate. Additives are often used to keep particles suspended, increase adhesion onto the surface, or reduce surface tension. In some cases, a means of coalescing or sintering is necessary to bridge gaps between nanoparticles and ensure conductivity [155, 169, 170].

The flow properties of the ink are dictated by the properties of the carrier solvent, therefore conductive inks have a lower viscosity relative to many of the previously described liquid conductors. Hence, conductive inks are compatible with inkjet printing [155, 171–173], screen-printing (polymer thick film) [167, 174] and direct-writing [169,175,176]. Researchers invented conductive silver inks that can be directly written on different surfaces using rollerball pens [177,178]. As previously mentioned, liquid metal dispersion inks have also been developed, which bridge the gap between liquid metal conductors and conductive inks using liquid metal nanoparticles suspended in a carried solvent [155].

Conductive Polymer Composites. Conductive polymer composites generally consist of a polymer mixed with a conductive material that is packed tightly enough in the polymer to maintain conductivity. Example conductive materials include silver nanoparticles [179–181], graphite [180, 182], graphene [183, 184], carbon black [182, 185], carbon nanotubes [182, 184, 186, 187] and liquid metals [188]. Different polymers can be used, such as polydimethylsiloxane [182, 184, 187, 188], polyisoprene [185], polyvinylidene fluoride [180], rubber fibers [181], and a number of other polymers [183]. Conductive polymers have been used to create tactile sensors [182, 185–187] and strain sensors [115, 185, 186, 188].

It is possible to pattern the conductive polymer using different techniques such as extrusion [187], screen printing [179], spray deposition [186] and hot-rolling [180]. The flow properties of the polymer composite affect the patterning process; therefore, it is common to add thinners to the composite in order to reduce its viscosity. Exam-

ples of thinners are reverse micelle solution, which also controls the hardness of the final conductive polymer [187], and cyclohexane [182]. Researchers have developed a novel composite material by embedding liquid metal nanoparticles in elastomer. Initially, the composite is not conductive due to the absence of a conductive path between the nanoparticles; however, applying local pressure on the composite breaks the boundaries between the nanoparticles and creates a conductive path within the composite [188, 189].

2.2 Structures and Designs

It is important to choose the proper materials to fabricate the sensor to ensure stability of the structure and compatibility with the host under representative operating conditions. Therefore, the designer should be aware of different structures and design approaches in order to fabricate a properly functioning device. This section highlights the common features and systems of sensor skins.

2.2.1 Features

There are several features of sensor skins that affect how sensor elements function. These features include microchannels containing liquid conductors (which we discussed in Sect. Conductor) and interfaces within the sensor skins. Examples of the latter include interfaces between two different conductors, between substrates, between the sensor skin and external electronics, and, in the case of wearables, between the sensor skin and the human.

Microchannels. Microchannels are defined as flow passages with dimensions on the order of tens to hundreds of microns [92, 190]. In sensor skins, these microchannels can be used for sensing or as communication pathways. Chossat et al. demonstrated both of these uses in a wearable glove, where microchannels filled with an ionic liquid

serve as the sensing component and microchannels filled with liquid metal serve as a communication pathway [78].

Elastomeric substrates deform under the influence of pressure or strain, therefore changing the dimensions of the embedded microchannels filled with the conductive liquid. This is important for resistive sensors, where the resistance of the channel is guided by $R = \rho L/A$, where R is the resistance, ρ is the resistivity, L is the length and A is the cross-sectional area of the sensor. This is the operational concept behind the variety of liquid-embedded sensors and devices described in Sects. Liquid Metal and Ionic Liquids and Solutions.

Replica molding, subtractive and additive manufacturing are the common techniques used to manufacture microchannels in elastomeric matrices. Molds can be made via 3D printing [94, 95, 157], photolithography [191], patterning films [85] or laser engraving [107]. Microchannels can also be made by subtractively removing material via laser ablation [86] or by adding material via direct printing [96, 187]. The choice of the mold fabrication technique depends on the required resolution of the mold, available time and equipment. For instance, fabricating molds using photolithography produces small features with high resolution, but it is a time-consuming process [192,193]. 3D printing is a fully automated process; however, the feature sizes of the mold are limited by the nozzle size of the printer. Laser ablation is also capable of achieving small feature sizes, but has less control over channel geometry than 3D printing [194].

Interfaces. At physical interfaces within devices, the change in stiffness from a highly deformable substrate to a rigid component or interconnect is a common cause of device failure. As the device is flexed or stretched, rigid parts are unable to follow the change in conformation of more flexible parts. For example, in Figure 2.1a, while the silicone elastomer substrate is capable of withstanding strains up to 150%, the electrical interface between the liquid metal and the copper wire limits the usable strain to 50%. Beyond this limit, the copper wires lose contact with the liquid metal

and fail to deliver strain data out of the sensor. This often also results in permanent failure of the device, as the wires contacting the liquid metal in this device will pull out of the channels, thus breaking the path from the sensing element to the rest of the system.

Researchers have addressed this deficiency in interfacing with liquid metal-based sensors using a variety of methods. For instance, copper wires can be replaced by ionic liquids to detect strain signals, which are transferred to external control circuit using liquid metal wires [78, 97]. Other approaches include using stretchable interconnects [195, 196], stretchable wires [83] and stretchable metal films [197, 198]. Uniaxially conductive polymer composites serve as a signal transmitter between the liquid metal circuit and the skin [199].

In addition to interfaces within the device, the interface between the human and the device greatly affects the device performance efficiency. Though elastomers are biocompatible and useful for wearable electronics, in reality, elastomer devices are difficult to secure onto the skin. Researchers have used skin adhesives to adhere electronic devices to the skin [131, 200]. With regard to garments, sensors have been held in place around joints via straps to create sensory suits [77]. Researchers ensured that the interface between the sensor and the strap was robust during motion by creating a stiffness gradient that transitions from the relatively stiff strap to the much softer sensor.

2.2.2 Systems

Moving beyond the discussion of the individual components and fabrication techniques for soft sensor skins, this section starts looking at examples and applications. This section focuses on sensor skins for robotics and wearables as they fit within the scope of this chapter.

Sensor Skins for Robotics. Most traditional robotic systems have very fine tuned position control and can operate very quickly and efficiently. However, they generally

lack any knowledge of their environment, which poses a potential safety risk for robots working alongside humans. Applying sensor skins to robots would provide environmental information and increase their awareness with their surroundings [35]. Tactile sensors tend to either use capacitive [30, 98, 103–105, 179, 186, 201] or resistive [76, 94, 99, 100, 106, 147, 185, 202] means of measuring pressure or normal force on the surface. Work has also been done to sense shear forces as well as normal forces on a surface [157]. While a lot of these works are on single sensors, these sensors can be arrayed into a sensor skin.

Soft robots need proprioceptive feedback through soft sensors that are mechanically compatible with the bulk of their structure. This proprioceptive feedback can come from strain sensors [78, 86, 94, 96, 102, 107, 115, 155, 165, 185, 188] or curvature sensors [85, 93, 203]. Yuen et al. demonstrated a robotic fabric skin which included a strain sensor that could differentiate between bending and compressing motion [72]. Resistive strain and pressure sensors have also been combined with existing pneumatic actuators to provide data about current state [49, 204]. A modular capacitive sensor skin has been developed to provide tactile information to existing robots [205].

Wearables. Many wearable sensor skin applications are designed for proprioception on conformal interfaces. Proprioceptive devices are used to estimate the state or pose of part of the human body. This can be applied on a smaller scale to measure the state of various joints on the fingers [85, 93] and across the entire hand and wrist [78, 206]. On a larger scale, exosuits have been developed to determine the pose of the lower body [77, 80, 207]. These devices are all composed primarily of elastomers with embedded liquid conductors injected into molded microchannels within the elastomer [208, 209]. Alternate designs rely upon direct adhesion of the strain sensor to the skin [131, 210]. These devices leverage thin film mechanics to measure strain due to skin stretch during joint flexion. The principles used to gather proprioceptive information can also be used to develop user interface devices, such as a wearable keypad [100, 187, 211].

2.3 Frontier and Outlook

The previous sections covered much of the published research in the field of stretchable skin sensors. This section discusses a few examples of the ongoing research and look at future opportunities.

Current research focuses on using new materials and novel fabrication strategies to develop sensors that can do multiple sensing tasks, have higher sensitivity and better mechanical properties, in addition to having a long lifetime. There is a need to develop methods to integrate these devices in a larger soft-bodied system, or to design the sensor as a built-in part of it. Such improvements will have a tremendous influence on the future sensor skins applications. An example of an integrated system is the exosuit that was discussed previously. In the current state, exosuits require large power supplies or power cables, which is a significant drawback that needs to be addressed in order to make these devices practical.

Biocompatible soft sensors have significant potential in surgical robots. Integrating soft sensors in surgical tools will not only allow sensing of the force exerted on the surface but also determine the type of tissue onto which the force is being applied. Furthermore, the developing field of soft robotics holds the promise of creating new soft surgical tools that are mechanically compatible with soft tissue.

2.4 Conclusion

This chapter gives an overview of the current research on sensor skins. Sensor skins are sensor-embedded substrates that have the ability to flex, bend or stretch. Sensor skins are used to estimate large-deformation motions and changes in system states. There is a growing interest in applying sensor skins to human skin and tissues, since most of the materials used are biocompatible.

Sensor skins are generally made of two components: a conductive material which is the sensing and/or signal transmitting element, and a stretchable encasing substrate. The wide variety of materials that have been used in skin sensors provide a

diverse foundation for researchers to develop new devices, fabrication techniques and designs. Within the current state-of-the-art, the shape and dimensions of the devices is controllable and therefore the resulting sensing and mechanical properties are also controllable. However, it is important to ensure both compatibility and stability of the sensor skin with the target host of the device in order to meet performance goals.

3. SOFT MATERIAL CHARACTERIZATION FOR ROBOTIC APPLICATIONS

In order to advance the field of soft robotics, additional knowledge of material behavior is needed. This knowledge will facilitate the design of soft robotic structures and will provide the basis for control of soft-bodied systems. It should be noted that this work does not set out to rigorously characterize and model non-linear and viscoelastic elastomers [14,17,212–216], but rather provides a practical guide to material selection for the soft robotics community. Linear and time-invariant material models do not account for many of the dynamics observed in soft systems. Recent work by Overvelde et al. has started to address this deficiency by investigating soft strain sensors undergoing large deformations [102]. However, the prior work did not include measurements or consideration of the time dependent properties of soft materials.

Furthermore, elastomers of the type commonly used in soft robots typically exhibit variability in material properties between nominally equivalent batches (batch-to-batch variability), which further complicates the modeling of material properties. This effect is particularly acute when developing control algorithms for soft robots, where variability in material properties will drive variability in plant dynamics. Control systems must be robust to this variability in order to achieve effective control.

This chapter presents studies on the mechanical and resistive properties of three elastomers used to create soft robotic devices: Sylgard 184 [85, 217], Smooth-Sil 950, and EcoFlex 00-30 [94,107]. From these materials, two different types of test samples were created. The first type of sample is a homogeneous elastomeric "dog bone" used in stress strain testing. The second type of sample is a liquid-metalembedded

elastomeric strain gauge, used to determine the interaction between the material properties and the output of a soft resistive sensor. The experiments are designed to provide a qualitative assessment on five critical areas: nonlinear behavior, batch-to-batch repeatability, effects of prestraining, cyclic loading, and viscoelastic stress relaxation.

3.1 Previous work on elastomers

Elastomers have been well studied and many of the unique properties of the materials are well known [23, 24]. Although no general theory exists to predict complete viscoelastic elastomeric behavior a priori, progress has been made describing certain aspects of elastomeric behavior. Beginning in the 1940s, Mullins identified an effect in natural rubber whereby straining the rubber resulted in a weakening [22]. Later groups have extended this to other rubber-like materials, suggesting that it is in fact a common effect among all cross-linked elastomers, as summarized in the review by Diani et al [12]. In addition to nonlinear behaviors, elastomers are also susceptible to viscoelastic creep and stress relaxation. Many models have been proposed to capture the effects of viscoelastic materials, including the two-element Maxwell and Kelvin models, and the serial combination of the two called the Burgers model [15]. The Zener model is a modified Kelvin model with an additional spring [16].

Further complicating matters, actual properties differ from nominal properties due to variations in material processing, such as the cure temperature and base elastomer-to-curing agent ratio [24]. As a result of these complexities, there is a wide range of material properties reported in the literature. One reference lists values for the Youngs modulus of polydimethylsiloxane, of which Sylgard 184 is one formulation, spanning a full order of magnitude (360–3000 kPa) [218].

Of the three materials in this study, Sylgard 184 is by far the most represented in the literature. For example, Schneider et al. published a study of the stressstrain relationship of Sylgard 184 under different temperature conditions and with different

compositions [24]. They limited their analysis mostly to the linear region of the stressstrain curve, which is generally below 40% strain. The two other materials considered have not yet been described to this extent in the literature. Additionally, the available soft robotics literature does not address the time-dependent nature of these elastomeric materials.

3.2 Models

This section reviews the analytical models used in this work. The material deformation model subsection presents equations required to obtain the true stress of the material. The material relaxtion models subsection presents equations for various models intended to explain the creep and stress relaxation seen in these soft materials. Finally, the resistive strain gauge model presents the theory for how liquid-metal-embedded sensors will respond to strain.

3.2.1 Material deformation model

Due to the large strains present in the elastomeric samples, the results are presented in terms of true stress, rather than engineering stress. This difference takes into account the reduction in cross-sectional area during the test. The Poisson's ratio is assumed to be $\nu = 0.5$ in all the calculations, as is generally done with rubber-like materials. This assumption is identical to assuming conservation of volume during the test. Assuming that the material is isotropic, and using the differential form of Poissons ratio with no assumptions on linearity, the cross-sectional area is found to be a function of extension,

$$A = WT(1 - 2\delta + \delta^2), \tag{3.1a}$$

$$\delta = 1 - \left(1 + \frac{\Delta L}{L}\right)^{-\nu}, \tag{3.1b}$$

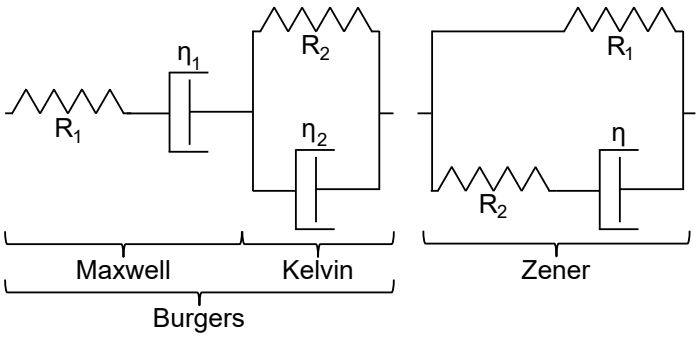

Figure 3.1. Models of viscoelastic creep.

where A is the resulting cross-sectional area, and δ represents the contraction normal to the direction of stretching. Note that ΔL is the corrected length with correction factor applied described later, not the applied extension.

3.2.2 Material relaxation models

The Maxwell, Zener, and Burgers models of viscoelastic relaxation are shown in Figure 3.1. The Maxwell model estimates the time evolution of the stress in a relaxing viscoelastic material. The model is presented below in Equation (3.2) [15],

$$\sigma = \varepsilon R e^{-Rt/\eta}, \tag{3.2}$$

where σ is stress, ε is strain, R is the spring constant, η is the damping coefficient, and t is time.

The Zener model is presented below in Equation (3.3) [16],

$$\sigma = \varepsilon \left(R_1 + R_2 e^{\frac{-R_2(R_1+R_2)t}{R_1 \eta}} \right), \tag{3.3}$$

where R_1 is the parallel spring constant, R_2 is the serial spring constant, and η is the damping coefficient.

The Burgers model is presented below in Equation (3.4) [15],

$$\sigma = \varepsilon \frac{(q_1 - q_2 r_1)e^{-r_1 t} - (q_1 - q_2 r_2)e^{-r_2 t}}{B}, \tag{3.4a}$$

$$p_1 = \frac{\eta_1}{R_1} + \frac{\eta_1}{R_2} + \frac{\eta_2}{R_2},\ p_2 = \frac{\eta_1 \eta_2}{R_1 R_2}, \tag{3.4b}$$

$$q_1 = \eta_1,\ q_2 = \frac{\eta_1 \eta_2}{R_2}, \tag{3.4c}$$

$$r_1, r_2 = \frac{p_1 \mp B}{2p_2}, \tag{3.4d}$$

$$B = \sqrt{p_1^2 - 4p_2}, \tag{3.4e}$$

where η_1 is the serial damping coefficient, η_2 is the parallel damping coefficient, R_1 is the serial spring constant, R_2 is the parallel spring constant, and p_i, q_i, r_i for $i = 1, 2$ and B are intermediate variables. As noted above in the discussion of nonlinear properties, there is no model to predict the coefficients of the models without resorting to experiments. Equations (3.2-3.4) were used to model the time-dependent viscoelastic creep of the elastomers as described below.

3.2.3 Resistive strain gauge model

The strain gauges used in this study utilize liquid metal eGaIn-filled microchannels in an elastomeric substrate [107, 196]. As the gauge strains, the length and cross-sectional area of the microchannels change, resulting in a change in resistance of the liquid metal. The analytical model of the liquid-metal-embedded elastomeric strain gauges is based on several assumptions. First, all of the strain in the gauge is assumed to be parallel to the direction of the microchannels. This assumption is justified since the bulk of the strain gauge is in the center of the dog-bone sample, where stress and strain are nearly uniaxial. Second, the parts of the sensor that are not part of the primary linear pattern are considered negligible. This includes the channels to the bonding ports and the semicircles at the top and bottom of the channels. This assumption is justified since the "negligible" lengths are small compared to the "active" length of the device. Finally, the liquid metal contained in the sensor is assumed to be incompressible. With this assumption, the volume of liquid metal in the strain gauge is,

$$V = 4L_0A_0 = 4LA, \tag{3.5}$$

where V is the volume of the liquid metal, L_0 is the initial length, A_0 is the initial cross-sectional area, L is a deformed length, A is a deformed cross-sectional area, and the coefficient accounts for the presence of four parallel channels in the strain gauge. Thus,

$$A = \frac{4L_0A_0}{4L} = \frac{L_0A_0}{L_0 + \delta} = \frac{A_0}{1 + \epsilon}, \tag{3.6}$$

where δ is the deformation and $\epsilon = \frac{\delta}{L_0}$ is the strain. Further, the resistance of the strain gauge is,

$$R = \frac{\rho L}{A}. \tag{3.7}$$

Combining Equations (3.6) and (3.7) results in the ratio of change in resistance to initial resistance, which is the expression used to compare to experimental results,

$$\frac{\Delta R}{R_0} = \epsilon(2 + \epsilon). \tag{3.8}$$

3.3 Materials and Methods

The three elastomers described in this chapter were all prepared using similar processes. All of these elastomers are delivered as two liquid or paste parts that were mixed together to begin crosslinking. The two liquid parts were massed using a Brecknell MBS-6000 electronic balance with 0.1 g resolution. These parts were mixed using a THINKY ARE-310 centrifugal mixer. The uncured liquid elastomer was spun onto cleaned 3" $\times$2" glass slides using a Specialty Coating Systems Spincoat G3-8 spin coater. All of the samples were spun for 60 s, with 10 s acceleration and deceleration periods. The EcoFlex 00-30 and Sylgard 184 were both spun at 200 RPM, resulting in thickness of 371.4 ± 31.85 μm and 307.6 ± 19.63 μm, respectively. Smooth-Sil 950 was spun at 400 RPM, resulting in a thickness of 643.0 ± 40.57 μm. The thickness measurements were obtained using a Zeta Instruments Zeta-20 True Color 3D Optical Profiler after curing and patterning, described below.

Samples for material testing and blank slides to be patterned into strain gauges were placed into an incubator set to 60°C to cure overnight. Once cured, elastomeric films were patterned using a Universal Laser Systems VLS 230, utilizing a 10.6 μm

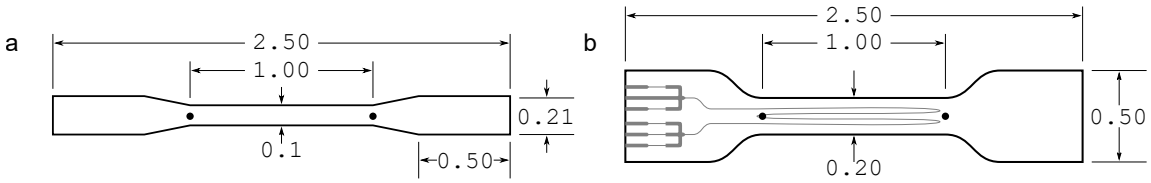

Figure 3.2. Test sample geometry for (a) elastomeric dog bones and (b) strain sensors. Dimensions shown are in inches.

CO_2 laser. All of the material testing experiments (i.e., all experiments without embedded strain gauges) used the same material sample geometry, which is shown in Figure 2a. The geometry is specified in inches to maintain compatibility with the laser drivers. Six patterns of this design can be cut from a single substrate.

In order to fabricate the liquid-metal-embedded strain gauges, two layers of elastomer were utilized. The fabrication sequence consists of patterning a bottom layer of elastomer with microfluidic channels, as seen in Figure 2b, bonding an upper layer of elastomer to close the channels, injecting liquid galliumindium alloy into the channels, inserting wires into the parts for electrical connectivity, and finally sealing the wires in place. In the case of Sylgard 184 and Smooth-Sil 950, the first step in the fabrication of a strain gauge was to pattern a blank slide of elastomer. These are the same slides used to fabricate material test samples described above. To pattern these slides, the same laser system is used, but with lower power to achieve a controlled partial cut into the material. Once patterned and cleaned, another slide with spin-coated elastomer was partially cured until tacky. The patterned elastomeric sheet was then pressed into this tacky layer with the microchannels between the two layers to achieve a bond between the two layers. In the case of EcoFlex 00-30, an SU-8 mold on a glass slide was utilized to pattern the material. Once cured, the patterned EcoFlex 00-30 sheet was bonded to an unpatterned sheet of equal thickness using oxygen plasma in a PlasmaEtch PE-50. Four-terminal measurements were used for these sensors to negate the effect of contact and interface resistances.

Material testing was conducted using an Instron 3345 single-column material tester fitted with a 1 kN load cell using custom-made material grips. A preliminary series of tests was conducted to determine the extension correction factor to convert between applied extension and the actual extension observed within the elastomeric material. In the case of the material test samples, two small black ink dots were applied to the elastomeric sample as shown in Figure 3.2. The samples were placed in the Instron and the distance between the dots was measured using a digital calipers at approximately 0%, 20%, 40%, 60%, and 80% of the extension at failure. In the case of the resistive strain gauge samples, the length from 0 to 35 mm extension was measured in 5 mm increments. The strain in the resistive strain sensor was limited due to electrical failure at higher strains. In both cases, a linear relation was assumed between extension and gauge length. For EcoFlex 00-30, these correction factors (for the material test dog bone and resistive strain sensor) were $L = 25.4 + 0.538E$ and $L = 24.5 + 0.709E$, for Sylgard 184 the factors were $L = 25.4 + 0.515E$ and $L = 25.8 + 0.550E$, and for Smooth-Sil 950 the factors were $L = 25.4 + 0.580E$ and $L = 26.2 + 0.597E$, where L is the gauge length, and E is the extension. These correction factors were used for all subsequent tests. Although this method is not as accurate as measuring gauge factors for each test, it is sufficiently accurate to support our objective of providing qualitative assessment of material properties.

Our tests included five types of tests using three methods, which are pull-to-failure tests, cyclic loading tests, and stress relaxation tests. Within the first method, three types of tests were conducted: variable strain rate tests, batch-to-batch consistency tests, and prestrain tests. Cyclic loading and stress relaxation tests were performed on the strain sensors to determine their resistive response in both of these loading modes. Each test was run three times for each elastomer, with the exception of the cyclic loading tests. The average and 95% confidence interval for the experiment was determined based on the data obtained in each of the three runs.

3.3.1 Pull-to-failure: variable strain rate

The first series of tests involved pulling samples at a constant rate until failure. The cured samples were peeled off of the substrates and placed the samples directly into the sample holders. The stress and strain were measured for all three elastomer types at strain rates of 1, 10, and 100 mm/min. The stressstrain curves for various strain rates for Sylgard 184, Smooth-Sil 950, and EcoFlex 00-30 are shown in Figure 3.3. All three elastomers are shown on a common axis for comparison in Figure 3.4.

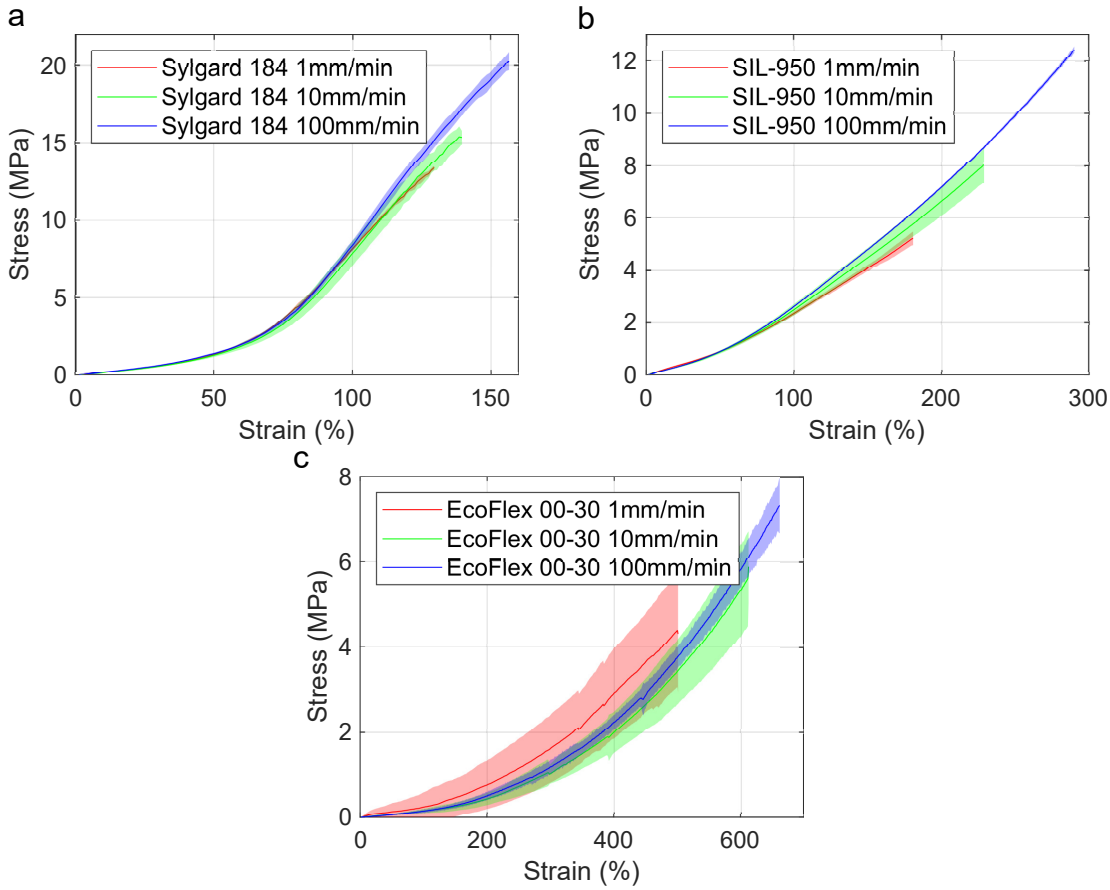

Figure 3.3. Pull-to-failure data for (a) Sylgard 184, (b) Smooth-Sil 950, and (c) EcoFlex 00-30 with 95% confidence interval (shaded region).

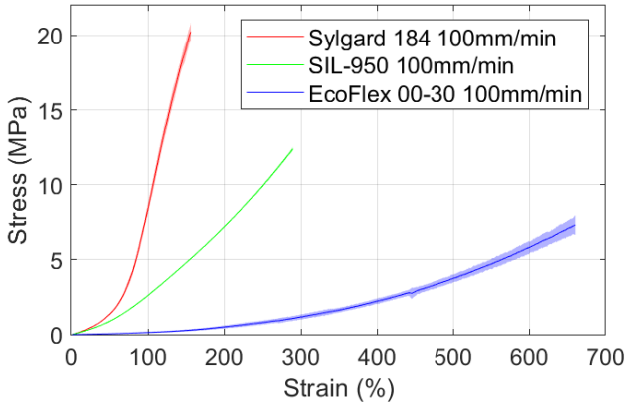

Figure 3.4. Pull-to-failure data for each material at 100 mm/ min. Shaded areas represent 95% confidence intervals.

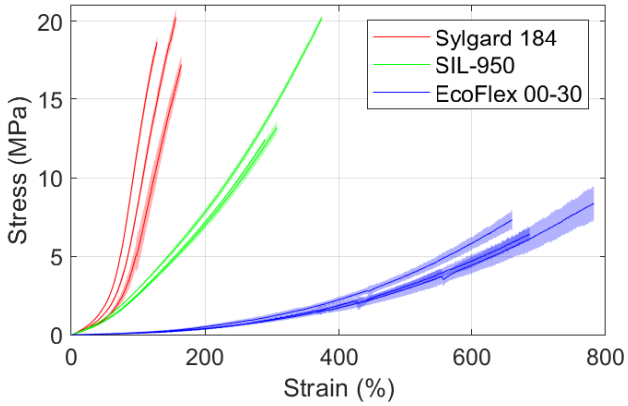

Figure 3.5. Pull-to-failure data for each material at 100 mm/ min of three separate batches. Shaded areas represent 95% confidence intervals.

3.3.2 Pull-to-failure: batch-to-batch consistency

To determine batch-to-batch consistency between the materials, three batches of each elastomer were made over a 20 day period. Samples from all batches were pulled at a strain rate of 100 mm/min. The results of these tests are shown in Figure 3.5. These samples were prepared using common laboratory equipment, and are believed to represent the level of variability that would be expected in practice.

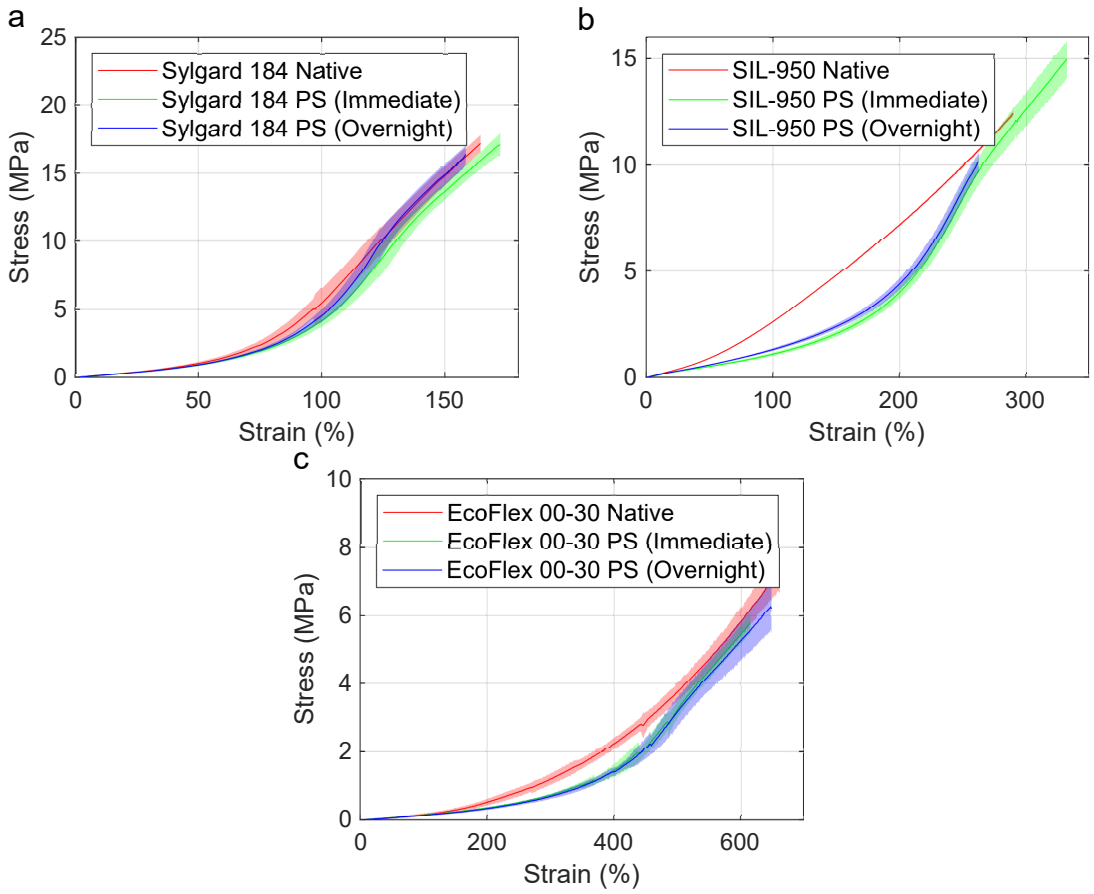

Figure 3.6. Pull-to-failure data for (a) Sylgard 184, (b) Smooth-Sil 950, and (c) EcoFlex 00-30 with prestrained (noted by PS) samples. Shaded areas represent 95% confidence intervals.

3.3.3 Pull-to-failure: effect of prestrain

To determine the effect of prestrain, we removed a sample from the glass substrate on which it was cured, prestrained the sample to approximately 80% of the failure extension, and then relaxed it either briefly or overnight. In both cases, the sample was completely removed from the test fixture. After replacing the sample in the fixture, the sample was pulled to failure at a rate of 100 mm/min. The results for Sylgard 184, Smooth-Sil 950, and EcoFlex 00-30 are shown in Figure 3.6.

3.3.4 Cyclic loading tests

The cyclic loading tests were designed to analyze the response of elastomers in conditions representative of what might be experienced in a robotic application. The samples were extended at fixed rates of 10 and 100 mm/min to approximately 80% of the failure extension, and then returned at the same rate to 0 mm extension, repeating this process for 10 cycles. Cyclic loading tests were performed on strain sensors to capture repeatability. The sensors were cycled between 0 mm to an absolute extension of 32 mm for 10 cycles. The stress-strain curves of tests for the Sylgard 184, Smooth-Sil 950, and EcoFlex 00-30 are shown in Figure 3.7a-c. The resistive sensor results of these tests for Sylgard 184, Smooth-Sil 950, and EcoFlex 00-30 are shown in Figure 3.7d-f.

3.3.5 Stress relaxation tests

The final series of tests were designed to capture the long duration stress relaxation behavior of these elastomers. The bulk elastomer samples were pulled to an extension of approximately 80% of the failure extension at a rate of 1,000 mm/min, and held for 3 h. For strain sensors, an absolute extension of 32 mm was applied at a rate of 1,000 mm/min and held for 3 h. Material stress relaxation curves for each material are shown in Figure 3.8a. The curves for the resistive sensors' stress relaxation tests are shown in Figure 3.8b.

3.4 Results and Discussion

3.4.1 Material properties are dependent on strain rate

Material properties are typically thought of as strain rate invariant. However, these experiments show that this is not a valid assumption in the case of these elastomers. From Figure 3.3, it can be seen that the stress-strain relationship is dependent on strain rate. Sylgard 184 (Figure 3.3a) and Smooth-Sil 950 (Figure 3.3b) shows

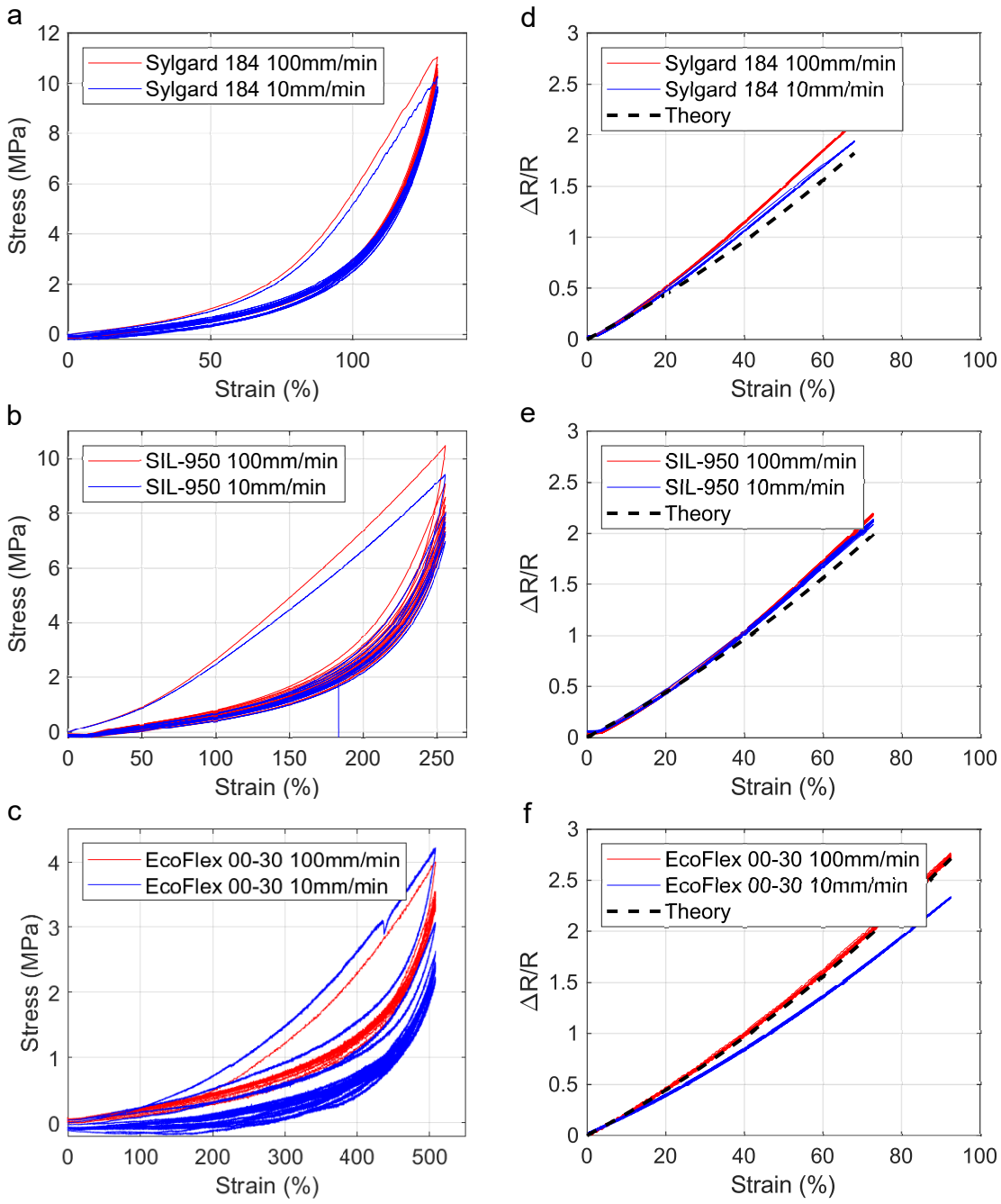

Figure 3.7. Material cyclic loading tests for (a) Sylgard 184, (b) Smooth-Sil 950, and (c) EcoFlex 00-30 and resistive strain cyclic loading tests for (d) Sylgard 184, (e) Smooth-Sil 950, and (f) EcoFlex 00-30. Data are for 10 complete cycles. Jumps in the data are due to slipping of the sample during the course of the test.

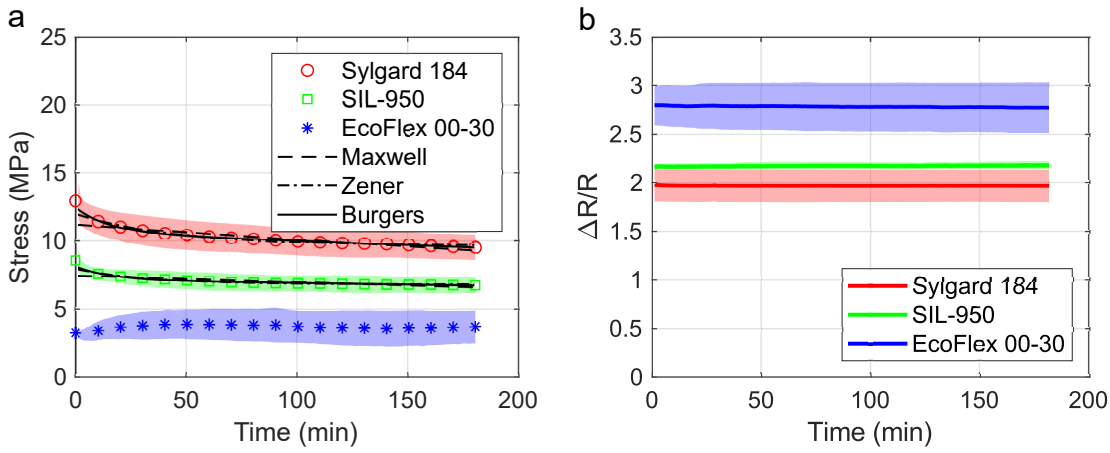

Figure 3.8. (a) Step extension response for Sylgard 184, Smooth-Sil 950, and EcoFlex 00-30. Shaded areas represent 95confidence intervals of the experimental data, the markers represent the averaged experimental data, and the black lines represent the theoretical models: Maxwell, Zener, and Burgers. (b) Step extension response for Sylgard 184, Smooth-Sil 950, and EcoFlex 00-30 strain sensors. Shaded areas represent 95% confidence intervals.

increasing stiffness with increasing strain rate. EcoFlex 00-30 (Figure 3.3c) generally shows softening with increasing strain rates, but the wide confidence intervals prevent any definitive conclusions.The range between 1 and 100 mm/min is believed to be representative of soft robotic applications such as a strain gauge positioned on a manipulator joint for proprioceptive sensing. Without accounting for the effects of strain rate dependence, using a nominal Young's modulus for these elastomers would give erroneous results.

3.4.2 Material properties are sensitive to production variations

From a practical standpoint, the soft robotics researcher should be concerned about the variability of material properties between batches. These experiments have shown that, even with what is considered practical process control over small batches, there was a meaningful difference in material properties between batches. Figure 3.5 shows the stress-strain relationships for three nominally identical batches for each of

our three test materials. Sylgard 184 shows the most variation. For example, at 100% strain, the stress varies from 5.5 to 12.0 MPa. The curves also demonstrate the small confidence intervals within a batch, suggesting that batches are internally consistent, and that samples taken from the same batch exhibit similar material properties. These variations are believed to be a significant contributor to the variation in the published data. For this reason, it is suggested that nominal material values are not sufficient in critical applications. Instead, materials should be measured once fabricated to ensure that accurate material properties are known.

3.4.3 Initial strain results in irreversible material changes

Another significant finding is that material properties change irreversibly after initial strain, a confirmation that the Mullins effect is present in these materials. This is clearly illustrated in Figure 3.6. Of the three materials tested, Smooth-Sil 950 (Figure 3.6b) and EcoFlex 00-30 (Figure 3.6c) exhibited the most pronounced change in stiffness, while Sylgard 184 (Figure 3.6a) exhibited the same effect to a lesser degree. In these materials, straining and relaxing the material had the effect of reducing its stiffness in the middle of the extension regime. As strain increases to yield, the stiffness of the prestrained material quickly increases to match that of the native samples. In the most extreme case, Smooth-Sil 950 shows a 40% reduction in stiffness at 200% strain. There are significant differences in stiffness in Smooth-Sil 950 from nearly 0% strain to 250% strain. In Sylgard 184, the effected region is from 60% to 120%, and in EcoFlex 00-30, it is from 100% to 500% strain. Note that, in the case of Smooth-Sil 950, the material becomes considerably more nonlinear once it has gone through an initial strain cycle. Sylgard 184 and EcoFlex 00-30 are already sufficiently nonlinear that the qualitative changes in behavior are less pronounced. Since most soft robotic applications operate in the middle of the elastic strain regime, where this prestrain effect is most pronounced, it is concluded that this is an important effect

that needs to be considered by soft robotics designers and by those groups measuring material properties for soft robotics applications.

3.4.4 Cyclic loading tests show an absence of work hardening

The cyclic loading tests shown in Figures 3.7a-c show three effects. First, they confirm the results of the prestrain tests discussed above, and show that there is a significant change in material properties after the first loading cycle. Second, they show that no significant changes in material properties take place during the subsequent 10 loading cycles, as all of the subsequent data fall within a narrow band. Third, the figures show that there is little to no mechanical hysteresis observed in the materials at these loading rates, since the loading and unloading traces fall over one another. In the case of EcoFlex 00-30 (Figure 3.7c), the variation in data arises from a low frequency noise source. However, the qualitative results from EcoFlex 00-30 match the other two materials.

3.4.5 Stress relaxation behaviors are well-modeled by the Burgers model

Both the Zener and the Burgers models for viscoelastic stress relaxation show good agreement with Sylgard 184 and Smooth-Sil 950 experimental data. Figure 3.8a shows the 95% confidence intervals for the long-duration creep tests of the three materials, and the Maxwell, Zener, and Burgers models fit for Sylgard 184 and Smooth-Sil 950. A model could not be fitted to the EcoFlex 00-30 data, due to significant low frequency noise. It is hypothesized that this error is thermal in nature, and is either due to time-varying heating of the material, the load cell, or a combination of the two. The Maxwell, Zener, and Burgers models were fit to the observed stress data using a least squares regression. From the data, we can see that a two element model (Maxwell) is not sufficient to capture the transient dynamics of the material. The three-element model (Zener) is better able to capture the "slow" transient dynamics, but still is unable to capture the "fast" transient. The four-element model (Burgers)

captures both the "fast" and "slow" transient effects. That behavior can be seen in Figure 3.8a, which shows a short, fast creep stage ($t < 25$ min), followed by a slower creep stage.

3.4.6 Strain gauge measurements are highly repeatable

Across all of the materials, the resistance response to strain is highly consistent and repeatable with no visible Mullins effect. Further, the resistance response of the strain gauge is well-modeled by the simple analytical model developed in Equation (3.8). Moreover, since the analytical model contains no fitting parameters or arbitrary coefficients, it does not have to be fit to experimental data. Although the material response in terms of stress versus strain exhibits a higher-order nonlinearity, the normalized resistance change versus strain response exhibits only a quadratic effect, as predicted by the model. The results of normalized resistance change versus strain are shown in Figures 3.7d-f. It is concluded from these measurements that embedded liquid-metal-resistive strain gauges are an appropriate sensing modality for proprioception in soft robotic systems.

3.4.7 Strain gauges are not susceptible to material viscoelastic stress relaxation

The long term response of the strain gauge resistance measurements shows little to no effect of stress relaxation. This is predicted by Equation (3.8), which shows that there should be no correlation between stress in the material and the output resistance. Although the stress in the elastomer is changing over time, the strain remains fixed, and hence the resistance is unchanged. The results of these long duration tests are shown in Figure 3.8b. This result supports our conclusion that embedded liquid metal sensors are appropriate for soft robotic proprioception, as they respond to the current strain state without regard for previous strain states.

3.5 Conclusions

These experiments have examined three elastomers that have been used in soft robotic applications. The focus has been on identifying material properties that are of concern to the designer of soft robotic systems. Models for these properties have been developed by Ogden and Simo and Hughes, but require experimental data to determine the coefficients for a particular material. This work begins to fill the void present in the literature with regard to soft material properties. The elastomeric materials discussed in this article are very different from metals, and many of the simplifying assumptions that can be made with small deformations are no longer applicable when discussing finite deformations of viscoelastic materials. Instead, richer dynamics must be evaluated, as demonstrated by the experimental results presented. It is believed that the work presented here will be useful in the design of conformable electronics, soft actuators, active wearable systems, sensory skins, and other highly deformable robotic systems.

These experiments also validated the use of embedded liquid metal strain sensors in soft robotic applications. These devices show good correlation between their output and their current strain state, without significant effect from the material properties of the elastomeric substrate. This is in good agreement with the simple analytical model developed for these devices. In actual soft robotic applications, these experimental results demonstrate that strain gauges can be used to provide proprioception.

4. SENSOR ENABLED CLOSED-LOOP CONTROL OF SOFT BEAMS

Robots manufactured from elastomers possess unique functionalities due to their highly deformable structures. This deformability is the source of both the most compelling advantages and most daunting challenges of these systems. The design process for a soft robot involves developing materials, geometries, and control algorithms simultaneously. This chapter describes the interplay between the mechanical design of a soft structure, the application of soft and responsive material actuators and sensors to that structure, and the integration of control algorithms to the resulting soft assembly. This work is a prototype of the design process that would accompany a full soft robot.

The goal of this chapter is to demonstrate three soft structures undergoing localized deformations. Deformation localization serves two purposes. First, it simplifies the kinematic model of the soft structure. Second, it simplifies the proprioceptive feedback problem, since state only needs to be sensed at the soft "joints," rather than continuously across the entire structure. This chapter focuses on the design fabricated from two dissimilar materials that exhibits motion confined primarily to a soft "joint" between two harder "bones." Multiple joints could be combined with a representative soft body to make a mobile soft robot, as shown conceptually in Figure 4.1a, or a soft gripper; however, in this chapter, the study is confined to single joint systems.

In this chapter, the three structures were fabricated from Smooth-Sil 935 (Shore hardness: 35A), a relatively stiff silicone elastomer, with the exception of one structure that contains a soft joint fabricated from Dragon Skin 10 Slow (Shore hardness: 10A).

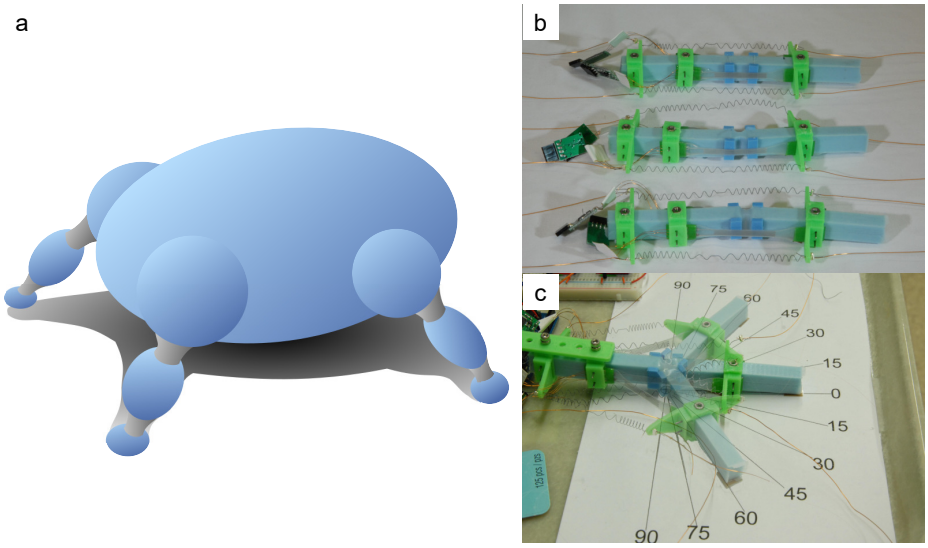

Figure 4.1. This figure shows (a) a conceptual soft robot based on the deformation localization presented in this work; (b) the three elastomer beams with attached sensors and actuators used in this work; and (c) an image showing a beam in neutral and activated configurations.

This design improves the controllability of the structure while successfully localizing the deformation and maintaining the benefits from using soft polymer materials.

To build a complete closed-loop control system, liquid-metal-embedded elastomer strain gauges were integrated to measure joint angle and shape memory alloy (SMA) coils to provide actuation. Using this approach, the strain sensors are able to directly measure the angle of the joint in the structure and use this information as an input to the control system. A proportional-integral-derivative (PID) control algorithm was used to control the angle of the soft robotic joint. The strain gauges were only sensitive to deformations at the soft joint, although the SMA was connected across a much larger portion of the body (see Figure 4.1 for an overview of the system). Confirmation of the accuracy of the measured angle was obtained by visually observing the robotic joint.

4.1 Previous Work

There is growing interest in control of soft systems with many different approaches [53, 219]. Researchers have experimented with several control strategies to date, including open-loop control [1,28,220,221], model-based control [56,63,222], model-free control [57], and closed-loop control enabled by the inclusion of soft sensors to the robotic system [51,223]. In this chapter, the latter approach of employing sensors that provide state feedback and enable correction is used. Given that elastic materials have non-linear responses at high strains and exhibit viscoelastic behaviors [14, 15], this sensor-enabled approach can be used in conjunction with modeling control approaches to allow for simplified models and to correct for modeling errors.

A further measure to simplify the control problem for soft robots is to localize deformations. The objective of localizing deformation has been achieved by various groups using different means, including film-like shape memory hinges between rigid plates [203, 224], particle jamming [225], hinged shape memory polymer films [226, 227], localized heating of hydrogels [228], gradiated elastomers [229], and localized melting of metal alloys [230]. None of these methods are particularly well-suited to the application of freestanding elastomer robots, either due to complexity in manufacturing or actuation. Therefore, deformation has been passively localized by modifying the structure. These modifications, both geometric and material, are easy to apply to any elastomer-based robotic system.

Another design goal is to minimize the mechanical impact of the sensors on the response of the system. Therefore, the stiffness of the sensors has been minimized relative to the host structure, which undergoes strains on the order of 100%. In general, soft sensing is a diverse field with many demonstrated approaches of fabrication [85, 131, 231–233]. This chapter takes the approach of liquid-metal-embedded elastomer strain gauges because they have very low stiffness and minimal impact on the mechanical properties of the system. Additionally, this type of strain sensor exhibits low noise and consistent response to strain [86]. Room temperature liquid

metal alloys made from a combination of gallium and indium are an ideal material to use in this application. Filling microchannels with gallium-indium alloy was first reported by Chiechi, Dickey, and colleagues [145,234]. Since then, the concept of filling microchannels with liquid metal has been applied to create pressure, force, and touch sensors [99,100,147], curvature and joint angle sensors [85,93], and combined strain and pressure sensors [94]. The strain sensors were very similar to those produced previously, except that a different elastomer substrate is used. Previous groups typically used EcoFlex 00-30 (Smooth-On) as a very soft elastomer. However, this material is incompatible with laser-based approach to fabricating sensors, which is describe below. Instead, Dragon Skin 10 Slow (Smooth-On), which was slightly harder, but more compatible with the fabrication process, is used.

SMA was selected as the actuator because it required very little interface hardware compared to pneumatics, which require pumps, valves, pressure sensors, and the like. In SMA systems, the thermally-responsive actuators are activated by Joule heating. This results in a very simple interface. Nickel-titanium SMA such as those used in this work were first described by Jackson, *et al.* [235]. The thermomechanical response behind the shape memory effect is both complex and well studied [236–243]. This class of materials has been used in a wide range of applications, including robotics, endoscopes, vascular stents, morphing structures, and wearable devices. All of these applications could potentially benefit from the integration of position sensing to achieve finer control during actuation. However, note that SMA has several disadvantages as a responsive actuator such as slow deactivation times, thermal sensitivity, and poor energy efficiency, and other soft and responsive actuators, such as shape memory polymers, electroactive polymers, fluidic actuators, and cable driven systems, could be implemented depending on the target application of the system [219].

In this chapter, the natural deformation of SMA is amplified by introducing a coiled geometry. Nickel-titanium alloys are capable of sustaining strains of 1%~2% over many cycles. The use of a coiled shape allows us to achieve the required ~60% deformation required overall, while keeping the local deformation in the material

small [244]. This requirement was dictated by the target range of motion for the soft system of $\pm 60^{\circ}$ and the location of the attachment points of the SMA actuators. The trade-off is that force output from the actuator is reduced proportionally. Since the elastomer structure used in this work was very deformable, it was easy construct actuators capable of providing the required force. The response of the actuator is also a function of the imposed conditions during manufacturing. This work uses the results of Seok, *et al.* to inform the manufacturing approach [41].

As noted previously, SMAs exhibit a complex thermomechanical response. They have a non-linear response to temperature and large hysteresis effects. Despite this, progress has been made in controlling these materials [245–250]. The present work took the approach of Ikuta, *et al.* who used tuned PID controllers to overcome the complexities associated with the thermomechanical response. Given the relatively slow actuation and motions required, a properly tuned PID controller resulted in satisfactory control.

In summary, the individual elements used in this work were either inspired by or directly borrowed from previous work. The focus has been on integrating these elements together in such a way that closed-loop control of a structure comprised entirely of soft materials can be demonstrated.

4.2 Design

4.2.1 Elastomer Beams

The objectives of this system are to localize bending in a specified location along an elastomer beam and to determine if that localized bending facilitates control of the deformation of the elastomer beam. This specified location is referred to as the "soft joint", which will connect "soft bones".

To localize bending, two methods were tested: (1) reducing the width of the joint, and (2) replacing the joint with a softer elastomer. To test the effectiveness of these techniques, this work looked at: (1) a homogeneous elastomer beam with constant

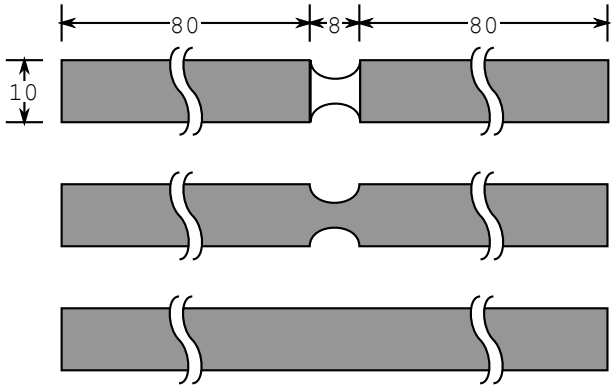

Figure 4.2. Different elastomer structure designs. From top to bottom: a non-homogenous beam, a non-prismatic beam, and a prismatic beam. The bones of the non-prismatic and non-homogeneous beams are 80mm x 10mm x 15mm with an 8mm joint connecting the bones together. The prismatic beam has the same overall length as the other two beams. All dimensions are in mm.

width (prismatic beam), (2) a homogeneous elastomer beam with reduced joint width (non-prismatic beam), and (3) an elastomer beam with a softer elastomer at the joint with reduced width (non-homogeneous beam). These configurations are shown in Figure 4.2.

4.2.2 SMA Coils

The transition temperature of the nickel titanium alloy used in this work was approximately 70°C at no load. However, this transition temperature is a function of the stress of the system. Higher stress causes the transition temperature to increase. Because of this, creating a purely temperature-based control algorithm would not be able to directly control either stress or deformation in the system. Some mechanical feedback is required. Additionally, because an antagonistic configuration of SMA was used, there was an interaction between the two coils that is not present in more traditional actuator systems. As one coil activated, it pulled on and deformed the opposite coil. The force required to complete this was a function of the temperature

of the other coil, which itself was changing over time due to free convection. The approach was to neglect these complexities and treat the system as a black box.

Several different combinations of SMA wire diameter and coil diameters were tested before selecting the coil used in this work. The goal was to balance the force produced by an active coil with the force required to restore an inactive coil. As expected, tighter coils with larger wire resulted in larger blocking force when active, but also required larger force to return to their neutral length. In the case of a 0.5mm wire coiled into a 1.6mm diameter coil, the resulting active force was approximately 7N with a current of 1.5A. These forces were sufficient to buckle the soft structure, and was considerably higher than required to meet the objectives. Note that SMA coils could be designed for larger applications by increasing wire diameter and decreasing coil length, although the latter becomes difficult for larger wires.

4.2.3 Sensor and Actuator Placement

The sensors and actuators were placed over the joint of the elastomer structure. A sensor and actuator pair was placed on either side of the elastomer structure as seen in Figure 4.3. The sensors must be pre-strained along the length of the elastomer joint so that when the soft structure reaches its maximum angles (in this case, $-60°$ to $60°$), neither of the strain sensors buckle. The sensors and actuators are attached to the elastomer structure via mounting brackets, which are pinned in place. The mounting brackets for sensor attachment are pinned 40mm from the ends of the bones. As shown in Figure 4.3, the SMA coil is attached to one of the sensor mounting brackets. The SMA is also attached to a mounting bracket that is pinned 10mm from the end of a bone. The mounting locations were selected as a compromise between maximizing the SMA coil length and allowing multiple soft structures to be joined together in a chain.

During initial testing, instabilities in the system occurred due to both the sensors and actuators. The sensors, being pre-strained, would cause the system to snap

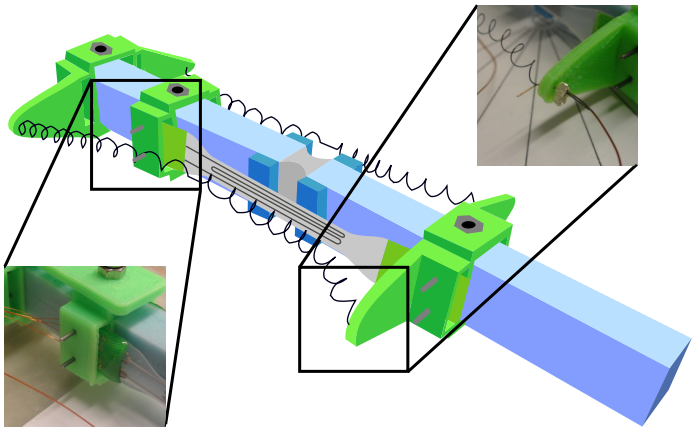

Figure 4.3. An assembled robotic joint with a non-homogenous beam. The mounting brackets are placed over the beam and locked in place with pins. The elastomer struts are visible on either side of the joint. The pins also lock in the sensors on either side of the beam (seen in the lower left inset) and the SMA is crimped through the holes on the mounting brackets (seen in the upper right inset.)

from one side to the other, which prevented system control over the entire range of motion. To fix this snap-through instability,elastomer struts were added (seen in Figure 4.3) to either side of the joint to discourage this snapping behavior by applying a restoring force on the opposing sensor. Snapping also occurred when the actuators were placed directly next to the elastomer beam. By moving the connection point farther away from the elastomer beam, that effect was eliminated. However, note that this instability could be leveraged to achieve rapid motion between two regions. For example, this could be used to deploy a structure and lock it in position.

4.3 Fabrication

A detailed discussion of the fabrication process is provided in the supplementary material provided in Appendix A. A brief summary of the process is provided here. For the elastomer structure fabrication, three different types of elastomeric beams were fabricated as a part of this study using a combination of stiff elastomer, Smooth-Sil 935, and a softer elastomer, Dragon Skin 10, both from Smooth-On.

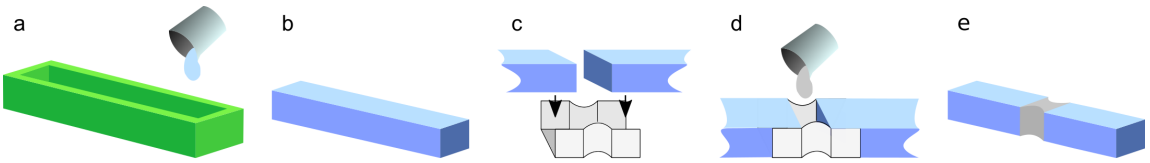

Figure 4.4. Fabrication process for elastomer beams: (a) Smooth-Sil 935 is poured into a mold and leveled with the flat side of a plastic knife and cured at room temperature overnight (length of molds vary for beam type: 168mm for a prismatic beam and 80mm for non-prismatic and non-homogeneous beams); (b) cured beams and bones are removed from the molds (this is the final fabrication step for the prismatic beam); (c) two bones are placed in compression fitted joint mold; (d) either Smooth-Sil 935 or Dragonskin 10 was poured into joint mold and cured overnight in room temperature for the non-prismatic or non-homogeneous beam, respectively; (e) finished joint system removed from the mold (a non-homogeneous beam is shown here).

These elastomers were cast in 3D printed molds, shown in Figure4.4. For the liquid-metal-embedded elastomer sensor fabrication, microchannels in elastomer substrates were created using a laser. These microchannels were then filled with liquid metal and sealed, completing the sensor. The sensors were fabricated from Dragon Skin 10 elastomer, which is the same soft elastomer used the beam structures. This process is illustrated in Figure4.5. Additional information on this class of sensors can be found in previous work [86]. For the actuator fabrication, nickel-titanium wire were programmed into coils at high temperature. The programming procedure was similar to that reported in [251]. In this work, a "counter-coil" design was used for the SMA actuators, which eliminates the torque produced by the coils by combining equal-length clockwise and counterclockwise segments.

4.4 System Integration

Rigid mounting brackets were used to attach sensors and actuators to the outside of the soft structure. These brackets were printed from PLA filament using a

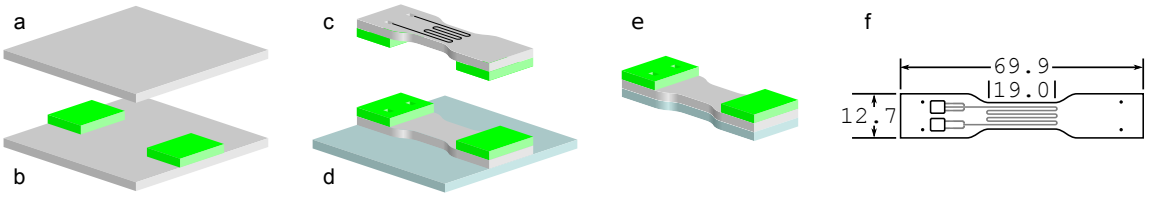

Figure 4.5. The elastomer sensors are fabricated from two films sandwiching a microchannel pattern. The first film (gray) is created by rod coating liquid elastomer on a polymer substrate (a). Elastomer-infused fabric reinforcement pads (green) are bonded to the upper surface of the film (b). This film is removed from the polymer backing (not shown) and inverted. A laser is used to pattern the microchannels into, and cut the sensor from, the film (c). The resulting half-sensors are then cleaned, inverted so that the channels are facing down, and bonded to a second film of elastomer (d). The complete assembly is then cut from the film to final shape with a laser (e). A schematic of the finished sensor is shown in (f). Dimensions are in millimeters.

Printrbot Simple FDM printer. Two different styles of mounting brackets were used, one with and one without horns to attach SMA. The mounting brackets served two functions. First, they provided a rigid attachment point for the SMA to the soft structure. Second, they held the SMA far enough away from the body to limit the snapping instability observed at large deflections. Given the low forces observed in this structure, the strength of the 3D printed parts was not a factor.

These mounting structures were held in place with pins that passed through the mounting bracket and the soft bones of the structure. This resulted in a very mechanically stable attachment scheme. In the case of the brackets holding the sensors, these pins passed through the fabric reinforcement pads on the sensor body as well, holding them securely to the body. SMA was attached to the mounting brackets by passing the wire through holes in the brackets, then joining the SMA with a copper wire using a metal crimp. The crimp not only ensured electrical contact between the copper lead wire and the SMA, it also provides mechanical attachment since the crimp is larger than the hole in the bracket.

4.5 Experimental Setup

The experimental setup consisted of the soft structure with attached sensors and actuators and the interface electronics. The structure is controlled, and data collected, via an Adruino Uno microcontroller connected to a laptop computer. The soft structure was designed to be modular so that the three different structure configurations could easily be secured with the use of two bolts. Each soft structure had twelve electrical connections: two on each SMA (four total) and 4 on each sensor (eight total). Removing and replacing structures in the fixture was possible within a few minutes.

4.5.1 Test Apparatus

The soft structure was clamped on one end and free to rotate on the other end. A printed angular scale attached to the table under the robot was used to facilitate calibration and monitoring of the robot during operation (see Figure4.1(c)). Double-sided tape was used to affix 1cm square pieces of PTFE film to the bottom of the 3D printed attachment brackets to reduce friction and facilitate smoother motion.

The two 3D printed attachment brackets on the non-moving side of the structure are bolted to another 3D printed bracket, which is in turn clamped to a standard laboratory ring stand. This rigidly held the non-moving part of the structure in place.

4.5.2 Electrical Setup

The system uses three power supplies. The Arduino used for communication and control is powered with a 12V laptop-style power supply. This is not required, but it provided more reliable performance than using power from the USB. The SMAs are powered with an independent Korad KA3005D power supply set at 6.00V with a

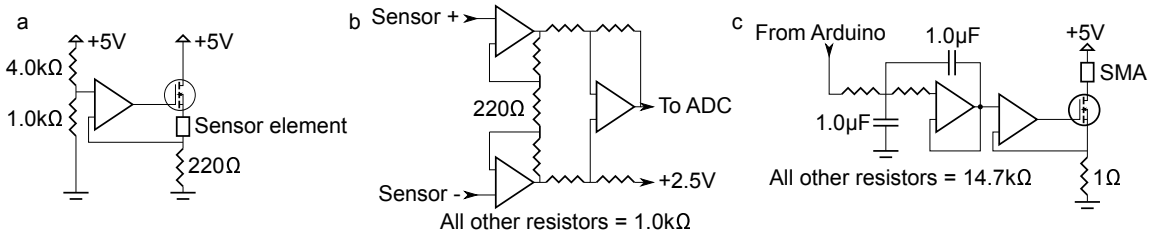

Figure 4.6. The electronics were fabricated from commercially available components. There were three basic modules: a constant current supply for the strain sensors (a), a differencing amplifier to measure the voltage across the resistive strain sensor (b), and a current supply for the shape memory alloy (c). Modules (a) and (b) are integrated on a custom-built PCB (see Fig. 4.1b). Module (c) is fabricated on a breadboard.

maximum output current of 1.00A. A second Korad KA3005D is used to provide a 2.50V reference for the sensor signal conditioning electronics.

The angle of the robotic structure was measured using two liquid metal strain sensors attached at the joint. In order to read these two sensors, a pair of custom-built signal conditioning circuits were used. These circuits provide a constant 100mA current to the sensors while measuring the voltage drop across the resistive sensor element. The resulting voltage difference is then read by a ADS1115 16-bit ADC and communicated to the Arduino Uno. This circuit is shown in Figure 4.6(a-b).

The SMA coils are powered by controlled-current supplies. These were built from IRF 510 N-channel MOSFETs controlled by OPA347 operational amplifiers. The amplifiers sensed the voltage drop across a shunt resistor, and drove the MOSFETs such that a desired shunt voltage was achieved. The components were selected such that the MOSFETs would nominally be able to supply 700mA when $V_{GS} = 5$V. This effectively limited the maximum current that could pass through the SMA actuators. The setpoint voltage was provided via an DAC output from the Arduino Uno. Since the DAC on the Arduino uses a 1kHz signal to produce approximate analog outputs, that signal was passed through a low-pass filter with a cutoff frequency of 30Hz before sending it to the current control amplifier. This reduced electrical noise in the system

since the MOSFET operated as an analog device, instead of in a PWM mode. This circuit is shown in Figure 4.6(c).

4.6 Sensor Calibration

The robotic structure used two Dragon Skin 10 Slow strain sensors to determine the the bend angle of the system. In order to accomplish this, the soft structure was held at angles between -60° and 60° at 15° intervals and the sensors were read. Data were collected at each test angle a total of three times in a randomized sequence to eliminate the effects of hysteresis. Generalized least squares regression was used to determine the coefficients for the following equation:

$$\theta = a_0 + a_1 V_1 + a_2 V_2 \tag{4.1}$$

where θ is the bend angle of the joint, V_1 and V_2 are the voltages across the strain gauges, and a_0, a_1, and a_2 are the coefficients of the fit. Sensor calibration was performed for each elastomer beam. The fit for the non-homogeneous beam is shown in Figure 4.7; it has a 95% confidence interval of 7.53° or 6.28% of the full scale. The fits for the prismatic and non-prismatic beams can be found in the

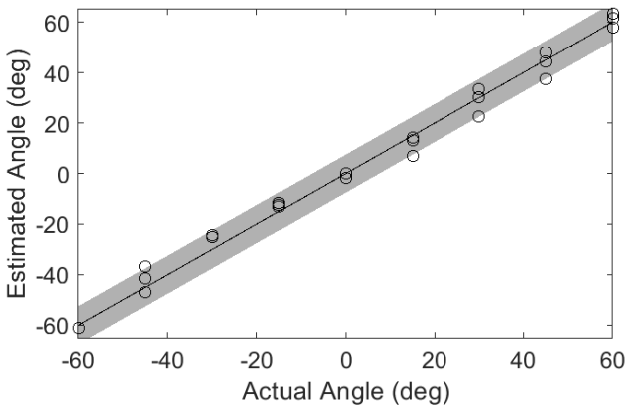

Figure 4.7. Sensor calibration results for the non-homogeneous beam showing how the actual angle compares to the estimated angle. The shaded region represents the 95% confidence interval.

supplementary information in Figures S1-S2 (see supplementary material in Appendix A). The prismatic beam has a 95% confidence interval of 10.6° or 8.83% of the full scale; the non-prismatic beam has a 95% confidence interval of 5.13° or 4.28% of the full scale.

4.7 Actuator Performance

Prior to integration into the soft structure, the open-loop performance of the SMA actuator coils was measured. In this test, identical coils were used to those used in the soft structure tests. The ends of the coils were fixed in an single-column Instron 3345 materials testing machine, then pulled the coils to simulate the deformation in the actual installation. The initial coil length was 26.2mm, and the deformed length was 97.0mm. This latter length matched the nominal length of the coil in a neutral configuration of the soft structure. A constant current of 0.6A was applied to heat the wire and cause actuation. Current was applied for 60s, then allowed the actuator to cool for 120s before repeating the cycle. The resulting blocking force of the actuator

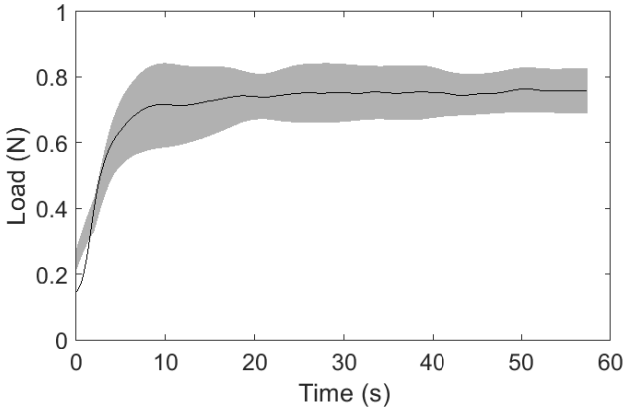

Figure 4.8. Actuator force generation averaged across three coils with four trials each. Shaded region represents 95% confidence interval. The average data has a symmetric moving average filter across 11 points with uniform weight. The shaded region has a symmetric moving average filter across 41 points with a uniform weight.

was recorded as a function of time and is presented in Figure 4.8. Only the current-on data is shown. The current-off response showed roughly a first-order response, which is expected from free convection. This test was performed on three coils, cycling the power on and off five times per coil. The data from the first cycle was discarded due to start-up transient effects. This approach is valid since in operation the coils will never be fully cooled or inactive as they were at the start of these tests. The error clouds in Figure 4.8 show the 95% confidence intervals over those four cycles. The 95% confidence interval of the mean values at the end of the test was 0.0764N, or 10.1% of the average. The non-zero initial value was due to the fact that the actuator does not completely "turn off" once cooled to room temperature and continues to exhibit purely elastic stress.

4.8 Controller Design Optimization

To determine the optimal PID controller design, the system was tested at a number of points in the $\{k_p, k_i, k_d\}$ gain space. A larger space was initially explored on the non-prismatic beam where $k_p \in [2, 20]$, $k_i \in [0, 10]$, and $k_d \in [0, 10]$. From this, an optimal solution was found for all the beams existed in the following subspace: $k_p = \{10, 15, 20\}$, $k_i = \{0.1, 0.4, 0.8\}$, and $k_d = \{0.1, 0.4, 0.8\}$. At each test condition, the system was driven with ten signals, which are a combination of steps and ramps seen in Figure S3 (see supplementary material in Appendix A). These complex signals were used because they are more representative of actual command histories which might be seen in a soft robotic system, rather than simple step and ramp commands. To evaluate the performance of each controller, the sum of the error between the desired and actual angle at 3.3Hz was taken. The total performance of the controller is the sum of the errors across all ten tests. Once the data were collected, the observations

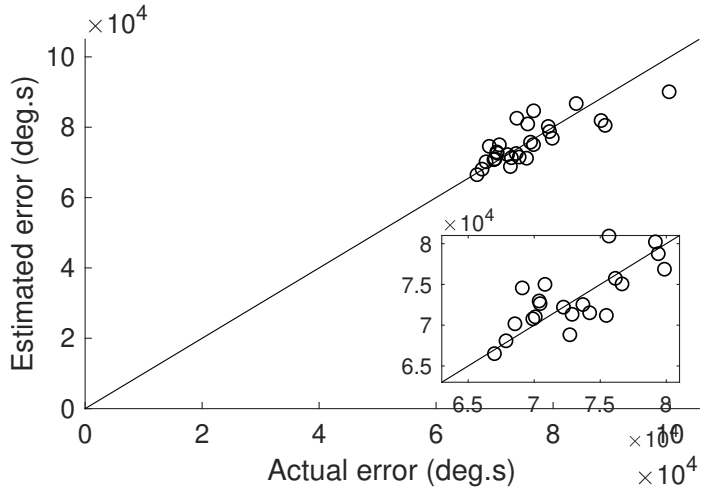

Figure 4.9. Optimization of PID controller for non-homogeneous beam. Blue dots represent represent test controllers. The line represents the one-to-one mapping of actual sum of errors against the theoretical sum of errors.

were fit to get an estimated error value of the form given in Equation (4.2) using least-squares regression.

$$\begin{aligned} E(k_p, k_i, k_d) =& a_0 + a_1 k_p^2 + a_2 k_i^2 + a_3 k_d^2 + a_4 k_p k_i + \\ & a_5 k_p k_d + a_6 k_i k_d + a_7 k_d + a_8 k_i + a_9 k_d \end{aligned} \tag{4.2}$$

Figure 4.9 shows the results matching the actual error to the estimated error for the non-homogeneous beam. The results are all clustered in one area and are relatively close to the 1:1 mapping line shown in black. The inset of Figure 4.9 shows the cluster at the front. It can be seen that a minimum error is reached in the performance of the system. This means that the noise floor of the system has been reached and will not be able to tune it past that floor. Therefore, the best solution is taken as the optimal solution, and, thus, selected the optimal from the discrete set rather than finding the optimal on a continuous space. The error clusters for the prismatic and non-prismatic beams are shown in Appendix A.

The optimal gains were found to be $k_p = 20$, $k_i = 0.4$, $k_d = 0.1$ for the prismatic beam; $k_p = 15$, $k_i = 0.4$, $k_d = 0.1$ for the non-prismatic beam; and $k_p = 20$, $k_i = 0.1$,

$k_d = 0.8$ for the non-homogeneous beam. The optimal controller response for the reference signals can be seen in Appendix A for each of the beams.

Results and Discussion

To test the effectiveness of the controller, the system was tested with both open- and closed-loop controllers and step and ramp inputs. For the open-loop steps, a pulse width modulated (PWM) signal (30 on a scale of 0-255) from the Arduino was sent to one of the actuators at a time for 90s. For the open-loop ramps, a growing PWM signal (0-30 on a scale of 0-255) from the Arduino was sent to one of the actuators at a time that grew linearly over 90s at an update rate of 10Hz. The same tests were then performed with the optimal controllers that were found previously. Each test was performed three times to look at the repeatability of the system. Figure 4.10 shows the results of the tests for each of the elastomer beams. The results in blue were driving the arm to 30° in either a step or ramp and the results in red were -30°.

It can be seen for the open-loop step response, the arm settled to a given angle (the same angle over multiple tests), but the response could be slow and the controller did not know the current state of the system. The open-loop ramps for all the beams were significantly worse than the open-loop steps. This was because the SMA has a threshold temperature where it begins actuating and actuation is not seen prior to reaching this temperature. Once it reaches its actuation temperature, it can change quickly, as seen with the open-loop ramps in Figure 4.10b. These results demonstrated that open-loop control is not sufficient for control of the system.

By closing the loop with the optimal controllers, the response of the system was drastically changed. The settling time for the open-loop steps ranged from 7.5-42.3s, while the settling time for the closed-loop steps ranged from 4.5-7.5s. The closed-loop controllers were able to maintain the desired step and ramp responses considerably better than the open-loop controllers since they did not drift over time like some of

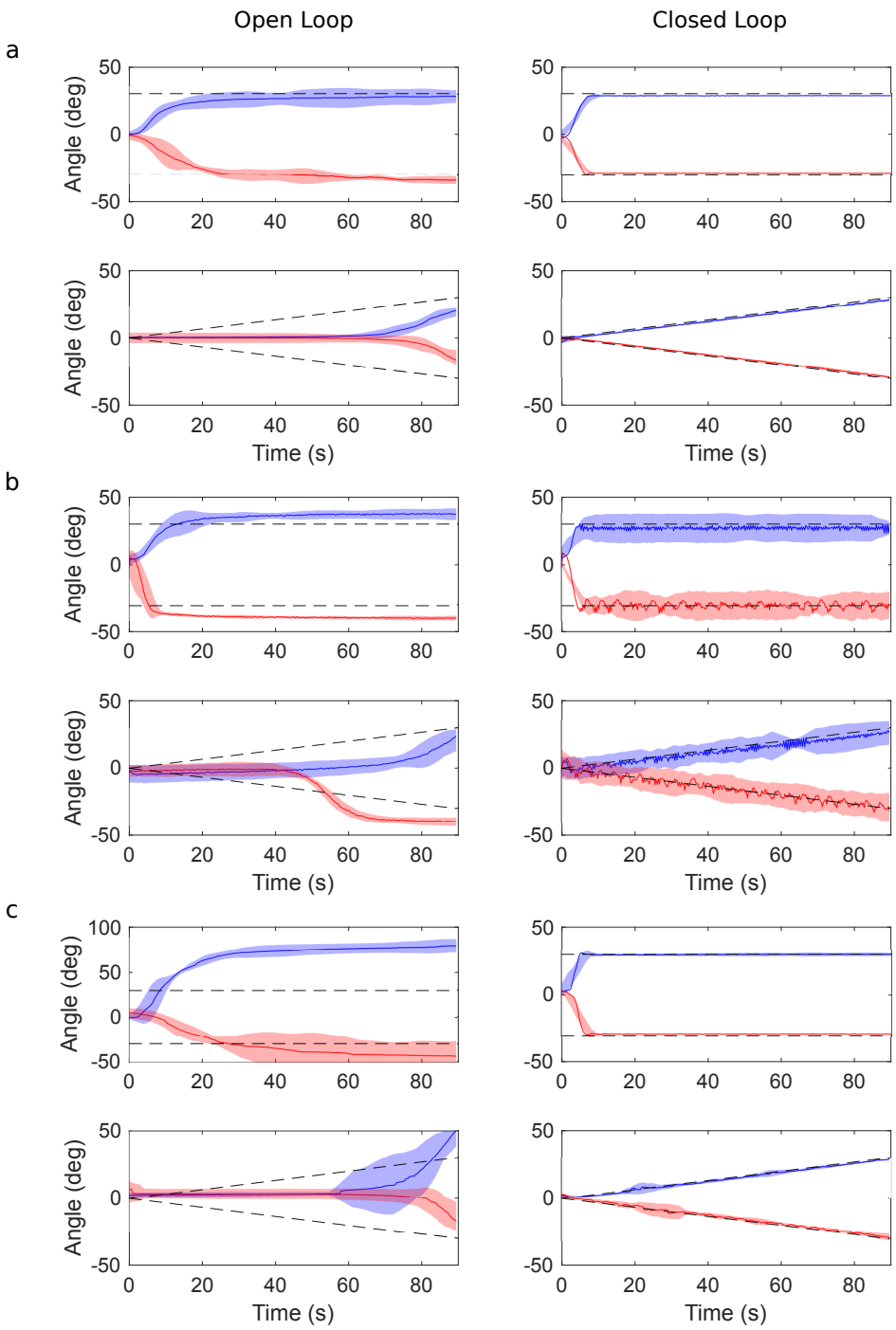

Figure 4.10. Open-loop and closed-loop results of 30° and -30° steps and ramps for (a) prismatic, (b) non-prismatic, and (c) non-homogeneous beam. Three trials are represented in each graph. The shaded region represents the 95% confidence interval with a moving average filter across 11 points with uniform weight.

the open-loop controllers. The closed-loop ramping responses were able to track the desired ramp.

Looking at the closed-loop response of the different beams, the prismatic beam was found to track the steps and ramps very well with little variability in the response. By introducing a joint in the non-prismatic beam, the response of the system was greatly altered and significantly harder to control. This was likely due to instability in the joint caused by the reduced ratio of bending stiffness to compressive stiffness. Snapping was most pronounced in the non-prismatic beam. The system oscillated around the desired angle rather than being able to maintain position as in the case of a prismatic beam. However, when the stiffness of the joint was reduced, the system re-obtained a good response. The results from the non-homogeneous beam (recall that this refers to the beam with two dissimilar materials) closely matched the results of the prismatic beam.

The non-homogeneous beam required less power to control than the prismatic beam because it is less stiff and, thus, took less power to move to or maintain a position. This can be seen in Appendix A where the system did not return to 0° before it started the next test. Another benefit of the non-homogeneous beam was the localization of the deformation. This means jointed soft robotic systems can be created that reduce the degrees of freedom and power consumption in the systems.

4.9 Conclusion

This chapter has demonstrated closed-loop control of three soft robotic systems. These systems used soft sensors to close the control loop and provide sensory feedback. The degrees-of-freedom of two of the systems were limited by introducing a joint. In one case, the system was left materially homogeneous and, the other, the joint was made from a softer elastomer. This effectively localizes deformations to the joint rather than bending over the length of the whole structure. Reducing the width of the joint, while leaving the beam materially homogeneous made the system harder

to control. Furthermore, by making the joint softer, controllability of the system was recovered while reducing power consumption of the system. Soft sensors are beginning to be integrated with soft robots and soft and responsive material actuators, but are not actively being used to control those systems. By integrating control into soft robots, they begin to move towards intelligent, autonomous soft systems.

5. REDUCING ACTUATOR REQUIREMENTS IN CONTINUUM ROBOTS THROUGH OPTIMIZED CABLE ROUTING

The design of soft robots is often inspired by soft biological creatures and components. These creatures and components generally have hydrostatic skeletons (jellyfish [252,253], starfish [254], etc.) or muscular hydrostats (elephant trunks [255,256], tongues [257,258], tentacles [259,260], etc.), which are highly deformable. However, most hydrostatic skeletons and muscular hydrostats exist either on a small scale or in a pressurized environment, such as water or underground. Those that do not exist in such an environment (elephant trunks, tongues, etc.) are generally attached to larger structures that contain a skeletal support system, and, hence are not constantly load-bearing. Purely soft robots can only operate efficiently either at small scales, where gravitational forces are insignificant, or in pressurized environments, where the environment provides support. Accordingly, there is consensus that for soft robots to operate on a large scale, there will need to be structural support [261].

An important structural element to many large-scale species is the spine, which can be thought of as a multi-jointed system. Skeletal spines allow large scale motions to be discretized, which reduces local deformation. In humans, the spine holds them upright and contributes to movement [262]. The musculature of the human spine is comprised of spirals of muscle chains that help move and stabilize the spine [263]. Additionally, recent studies have suggested notable increases in locomotion efficiency due to inclusion of a spine in quadruped robots [264–266]. Continuum manipulators

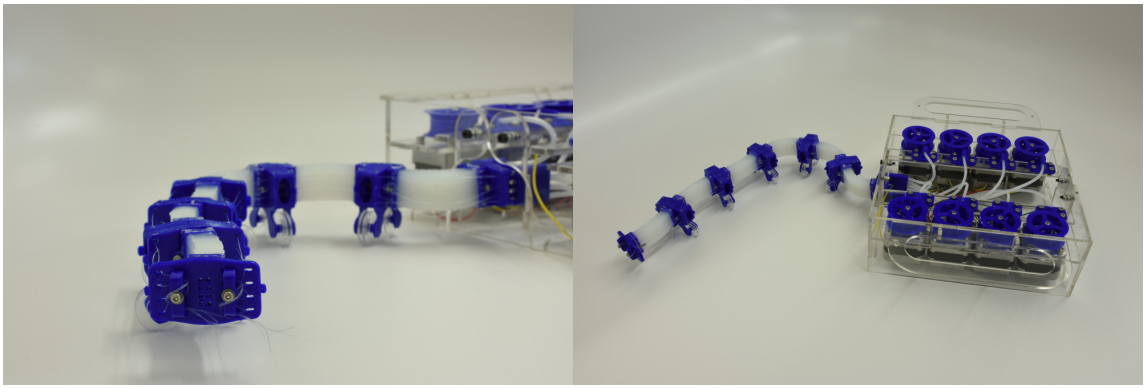

Figure 5.1. Six-segmented multi-jointed spine.

and hyper-redundant manipulators are ideal for approximating spines due to their high flexibility and distributed deformations [267–269]. In particular, cable-driven continuum manipulators have been demonstrated and modeled both statically and dynamically [33, 255, 270–273].

In this chapter, the concept of a planar cable-driven soft spine is explored. The system mimics the disks (soft elastomer segments) and vertebrae (rigid PLA parts) in biological spines and borrows concepts from the highly coupled nature of muscular spirals. Previous planar cable-driven continuum arms typically include a pair of cables controlling each segment [33], such that the total number of system actuators is twice the number of system segments. While this approach is useful for decoupling segments in the system, it misses advantages that come from having a highly coupled and underactuated system. A highly coupled system allows us to reduce the maximum cable tension, which allows us to reduce motor requirements and make more energy efficient systems. An underactuated system allows us to reduce the number of actuators in a system. As an example, a six-segment planar spine is demonstrated (shown in Figure 5.1), in which cables are able to cross through the spine at the rigid segments in patterns, which are referred to as crossing cable configurations. A computational workspace analysis for a number of crossing cable configurations shows the feasibility of this approach and the ability to tune the workspace based

on user requirements. The model is experimentally-verified by showing the behavior of the physical system follows the behavior of the computational model. While this study confined the complexity of the system to 2D in this work, the concept has been extended to 3D systems as well [274].

5.1 Fabrication

The spine system described in this paper consists of two parts: soft elastomer segments and rigid PLA vertebrae. While any elastomer can be used in the elastomer segments, Dragon Skin 10 Slow (Smooth-On, Inc) was chosen due to its low hardness of 10 on the Shore A scale, which reduces tension requirements in the cables, and thus, requires smaller motors. In addition to this, Dragon Skin 10 Slow also exhibits linear material properties below 40% strain, which simplifies the model. Figure 5.2 shows stress-strain data from three samples of Dragon Skin 10 Slow. These samples were tested in an Instron 3345 with a 50N load cell and pulled at a rate of 100mm/min. The stress and strain were calculated using the method described in [86].

The elastomer segments were created using a mold made from acrylic sheets. Both ends of the Dragon Skin 10 Slow segments were inserted into 3D printed end caps made with a Printrbot Metal Plus. The segments were then mechanically locked into

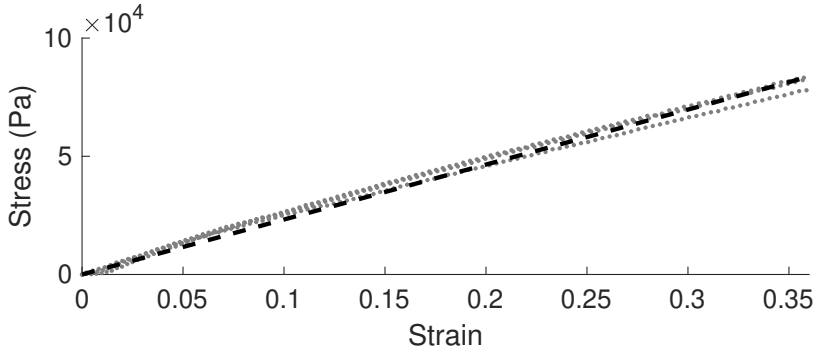

Figure 5.2. Stress-strain data for Dragon Skin 10 Slow. Three trials are shown in gray dotted lines, and a linear approximation is shown by the black dashed line.

the end caps by sealing with more Dragon Skin 10 Slow. The dimensions of the spine segment are shown in Figure 5.3a. In addition to the 40mm segments shown in the figure, 20mm long elastomer segments were also manufactured, which were used for the experimental verification described in a later section.

The rigid vertebrae were 3D printed using a Printrbot Metal Plus. Steel rods were used as cable guides in the rigid vertebrae to reduce friction as the fishing line cables passed through the vertebrae, as seen in Figure 5.3b. The spine was held together with M2 bolts and nuts and fixed to an acrylic box that housed the motors. Eight NEMA-17 stepper motors were used to control the length of the cables. Each motor was fitted to a spool which controlled the length of each cable. The spools were sized such that each step of the motor either lengthened or shortened the cable lengths by 0.5mm. An Arduino Uno with Adafruit motor shields was used to control the motors. The complete spine with motors attached can be seen in Figure 5.1.

5.2 Model

The multi-jointed soft spine was modeled using similar approaches to those proposed by Camarillo, et al [61, 275]. This soft spine system differs from these previous works in two ways. First, external cables were employed rather than internal cables, which means the equations must be recalculated to handle this; external cables are a standard cabling method for continuum manipulators [33]. Second, a crossing cable configuration was introduced rather than a parallel cable configuration, as shown in Figure 5.3b, which complicates the coupling of the segments and requires a redefinition of a multi-segment manipulator.

For this model, several assumptions were made: (1) linear material properties; (2) constant curvature/bending moment of elastomer segments (note that the system is modeled as a beam [276]); (3) friction is negligible (i.e. sliding friction and cable friction); (4) the cables do not contact the body of the spine (this stems from the fact that external cables were used [33]); and (5) external loads are negligible, including

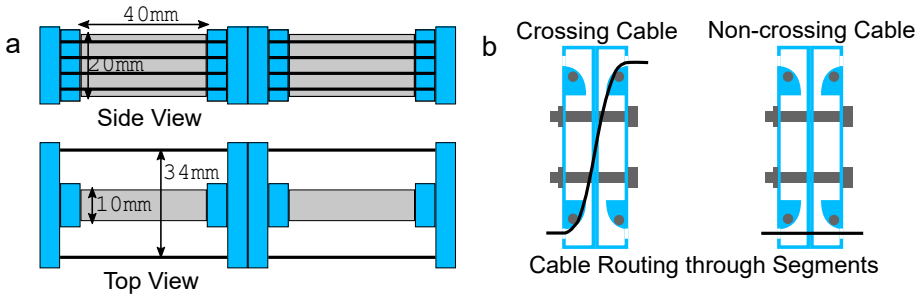

Figure 5.3. (a) Labeled drawing of two segments. The relevant dimensions are shown, as well as how segments are added to each other. The medium gray represents rigid PLA components, the light gray represents elastomer segments, the black represents cables, and the dark gray represents M2 nuts and bolts or steel rods. (b) Demonstration of how cables were patterned through the rigid vertebra with crossing cable and non-crossing cable. Steel pins were pushed through the PLA components to create a reduced-friction contact for the fishing line cables. Note that $I = 1.63\times10^{-9}$ m^4 and $A = 0.2\times10^{-3}$ m^2. A more detailed CAD drawing with dimensions is given in Appendix B.

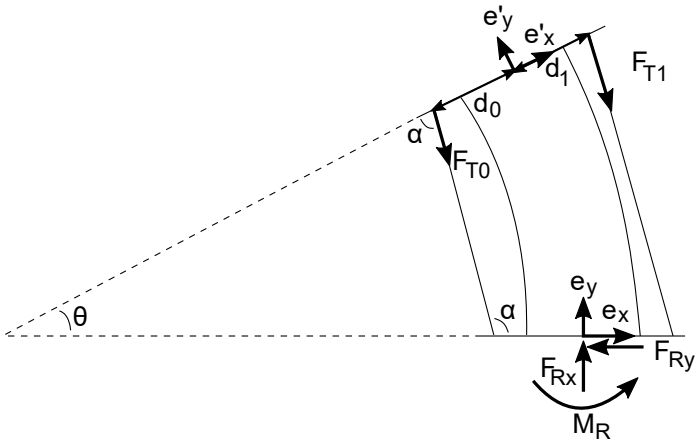

Figure 5.4. Representation of single segment bending.

gravity. The experimental setup is designed to eliminate gravity effects and the spine itself moves orthogonal to gravity.

The analysis begins by considering a single segment that is fixed on one end and free on the other. The segment is defined in two frames, e and e', seen in Figure 5.4. The rigid components that are part of the segment are neglected, which simplifies the

visualization of the segment and does not alter any of the equations that follow, since it is assumed that the rigid components transfer the forces and are not geometrically altered by them. The e frame is on the fixed end of the segment while the e' frame is on the free end of the segment. To transform from the e' frame to the e frame, the following rotation matrix can be used:

$$\mathbf{R}^{e}_{e'} = \begin{bmatrix} \cos\theta & -\sin\theta \\ \sin\theta & \cos\theta \end{bmatrix} \tag{5.1}$$

where $\mathbf{R}^{e}_{e'}$ is the rotation matrix, θ is the angle of the rotation defined by $\theta = \kappa s$, κ is the curvature, and s is the arc length (note that the arc length changes as the segment compresses). Using the e' frame, the force due to a single cable tension can be defined as:

$$\mathbf{F}_{T_i} = -T_i \begin{bmatrix} \cos\alpha \\ \sin\alpha \end{bmatrix} = -T_i \begin{bmatrix} \sin\frac{\theta}{2} \\ \cos\frac{\theta}{2} \end{bmatrix} \tag{5.2}$$

where $\mathbf{F}_{T_i}$ is the force due to the ith cable, T_i is the tension in the ith cable, and α is the angle the cable forms due to the curvature, such that $\alpha = \frac{\pi-\theta}{2}$. Taking a static modeling approach, which is assumed to be valid due to the slow operating speeds, the sum of forces is found to be:

$$\begin{gathered} \sum \mathbf{F} = \mathbf{0} \\ \sum_{i=0}^{n-1} \mathbf{R}^{e}_{e'} \mathbf{F}_{T_i} + \mathbf{F}_R = \mathbf{0} \\ \mathbf{F}_R = \sum_{i=0}^{n-1} T_i \begin{bmatrix} -\sin\frac{\theta}{2} \\ \cos\frac{\theta}{2} \end{bmatrix} \end{gathered} \tag{5.3}$$

where $\mathbf{F}_R$ is the reaction force in both the x- and y-directions at the fixed end of the elastomer segment, and n is the number of cables. In order to look at the moments caused by forces, the moment arm must be considerd. This moment arm can be defined as:

$$\mathbf{r}_{T_i} = \begin{bmatrix} \left(\frac{1}{\kappa} + d_i\right)\cos\theta - \frac{1}{\kappa} \\ \left(\frac{1}{\kappa} + d_i\right)\sin\theta \end{bmatrix} \tag{5.4}$$

where $\mathbf{r}_{T_i}$ is the moment arm to the force, and d_i is the distance from the center to the cable as measured in the e' frame. The sum of moments about the center of the fixed end of the elastomer segment is found to be:

$$\sum M = 0$$
$$M_R = -\sum_{i=0}^{n-1} T_i d_i \cos\frac{\theta}{2} \tag{5.5}$$

Using the assumptions of constant curvature and linear material properties, it follows that:

$$M_R = K_b \kappa \tag{5.6}$$

where K_b is the bending stiffness of the material, such that $K_b = EI$, where E is the nominal Young's modulus of the material, and I is the second moment of inertia of the segment. Combining Equations (5.5) and (5.6), it is found that:

$$\kappa = -\frac{\sum_{i=0}^{n-1} T_i d_i \cos\frac{\kappa s}{2}}{K_b} \tag{5.7}$$

Equation (5.7) shows how the cable tensions relate to the curvature. If the material is allowed to deform due to compressive forces caused by the cable tension, the effects on strain must be considered:

$$\epsilon_b(x) = -\frac{\sum_{i=0}^{n-1} T_i d_i \cos\frac{\theta}{2}}{K_b} x \tag{5.8a}$$
$$\epsilon_a = -\frac{\sum_{i=0}^{n-1} T_i \cos\frac{\theta}{2}}{K_a} \tag{5.8b}$$
$$\epsilon_y(x) = \epsilon_b(x) + \epsilon_a \tag{5.8c}$$

where ϵ_b is strain due to bending moments, ϵ_a is strain due to axial forces, ϵ_y is total strain in the y-direction, x is the distances from the central axis, and K_a is axial stiffness, such that $K_a = EA$, where A is cross-sectional area. A more in-depth discussion on the strain equations can be found in [61], and is not repeated here. From this, it can be seen that the neutral axis is going to shift due to the combined axial compression and bending. The new location was be found to be a distance from the center as:

$$x_{n.a.} = -\frac{K_b \sum_{i=0}^{n-1} T_i}{K_a \sum_{i=0}^{n-1} T_i d_i} = \frac{a_n}{a_d} \tag{5.9}$$

where $x_{n.a.}$ is the distance of the neutral axis from the center, a_n is the numerator of the neutral axis calculation, and a_d is the denominator of the neutral axis calculation. The neutral axis shifts as the spine compresses. These equations can be taken and expressed in shortened form:

$$\mathbf{K}_m\mathbf{q} = \mathbf{D}\boldsymbol{\tau} \tag{5.10a}$$

$$\mathbf{K}_m = \begin{bmatrix} K_b & 0 & 0 & 0 \\ 0 & K_a & 0 & 0 \\ 0 & 0 & K_b^{-1} & 0 \\ 0 & 0 & 0 & K_a^{-1} \end{bmatrix} \tag{5.10b}$$

$$\mathbf{q} = \{\kappa, \epsilon_a, a_n, a_d\}^T \tag{5.10c}$$

$$\boldsymbol{\tau} = \{T_0, T_1, ...T_n\}^T \tag{5.10d}$$

where $\mathbf{K}_m$ is the stiffness matrix, $\mathbf{q}$ is the configuration-space description, $\mathbf{D}$ consists of the multipliers necessary to solve for $\mathbf{K}_m\mathbf{q}$, and $\boldsymbol{\tau}$ is the cable tensions. For a single segment, $\mathbf{D}$ is found to be:

$$\mathbf{D} = \begin{bmatrix} -d_0 \cos\frac{\theta}{2} & -d_1 \cos\frac{\theta}{2} & ... & -d_n \cos\frac{\theta}{2} \\ -\cos\frac{\theta}{2} & -\cos\frac{\theta}{2} & ... & -\cos\frac{\theta}{2} \\ -1 & -1 & ... & -1 \\ d_0 & d_1 & ... & d_n \end{bmatrix} \tag{5.11}$$

This model of a single segment is important, but coupling of the spine segments becomes relevant when there are multiple segments. Camarillo, et al, introduced an analysis for multi-segment continuum arms with parallel cables [275], which serves as the basis for the crossing cable model. A full derivation of the multi-segment continuum arm with crossing cables can be found in Appendix B. To illustrate the difference between the two cabling patterns (traditional and crossing), let us consider a two-segment spine. For this example, there are four cables in both the traditional and crossing cable configurations shown in Figure 5.5. For all cables, $|d_i| = l_c$ for all i. Consider first a simple two segment example for a traditional cable configuration:

$$[\mathbf{K}_m]\{\mathbf{q}\} = [\mathbf{D}]\{\boldsymbol{\tau}\} \tag{5.12a}$$

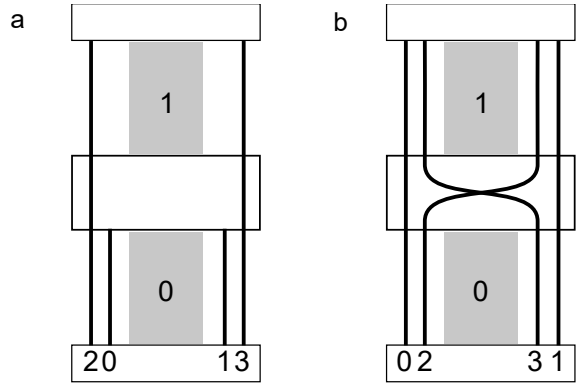

Figure 5.5. Two-segment spine for (a) traditional and (b) crossing cable patterns. The numbers represent the cable number, and the black lines represent the cable pattern.

$$\begin{bmatrix} \mathbf{K}_m & \mathbf{0} \\ \mathbf{0} & \mathbf{K}_m \end{bmatrix} \begin{Bmatrix} \mathbf{q}_0 \\ \mathbf{q}_1 \end{Bmatrix} = \begin{bmatrix} \mathbf{D}_0 & \mathbf{D}_1 \\ 0 & \mathbf{D}_1 \end{bmatrix} \begin{Bmatrix} \boldsymbol{\tau}_0 \\ \boldsymbol{\tau}_1 \end{Bmatrix} \tag{5.12b}$$

where the subscripts in $(\mathbf{q}_j, \mathbf{D}_j, \boldsymbol{\tau}_j)$ refer to these respective vectors and matrices in the jth segment. This can be expanded for any number of segments. Note that the tension is split into $\boldsymbol{\tau}_0$ and $\boldsymbol{\tau}_1$; this highlights the concept of having specific cables for each segment of the manipulator. In a traditional cable pattern, $[\mathbf{D}]$ indicates the decoupling. This can be seen by the upper triangular matrix since the cables from the 0th segment do not influence the outcome of the 1st segment (i.e. the tensions $\boldsymbol{\tau}$ do not affect the 1st segment's configuration $\mathbf{q}_1$), but the cables for the 1st segment do influence the outcome for the 0th segment (i.e. the tensions $\boldsymbol{\tau}_1$ affect the 0th segment's configuration $\mathbf{q}_0$) Here, $\mathbf{D}_0$ corresponds to the cables for the 0th segment and $\mathbf{D}_1$ corresponds to the cables for the 1st segment.

If the cable pattern shown in Figure 5.5a is considered and the complexity of Equation (5.12) is reduced by simplifying such that $\mathbf{q}_j = \{\kappa_j\}$, it is found that:

$$\begin{bmatrix} K_b & 0 \\ 0 & K_b \end{bmatrix} \begin{Bmatrix} \kappa_0 \\ \kappa_1 \end{Bmatrix} = \begin{bmatrix} l_c \cos\frac{\theta}{2} & -l_c \cos\frac{\theta}{2} & l_c \cos\frac{\theta}{2} & -l_c \cos\frac{\theta}{2} \\ 0 & 0 & l_c \cos\frac{\theta}{2} & -l_c \cos\frac{\theta}{2} \end{bmatrix} \begin{Bmatrix} T_0 \\ T_1 \\ T_2 \\ T_3 \end{Bmatrix} \tag{5.13}$$

Note that, in this case, $\boldsymbol{\tau}_0 = \{T_0, T_1\}^T$ and $\boldsymbol{\tau}_1 = \{T_2, T_3\}^T$ since cables 0 and 1 are used to move the 0th segment and cables 2 and 3 are used to move the 1st segment.

In contrast, cables in the crossing cable configurations can cross from one side to the other and are designed to influence every segment rather than decouple. Therefore, segments cannot be broken up and cable tensions cannot be divided per segment. The system must be taken as a whole:

$$\begin{bmatrix} \mathbf{K}_m & \mathbf{0} \\ \mathbf{0} & \mathbf{K}_m \end{bmatrix} \begin{Bmatrix} \mathbf{q}_0 \\ \mathbf{q}_1 \end{Bmatrix} = \begin{bmatrix} \mathbf{D}_0 \\ \mathbf{D}_1 \end{bmatrix} \begin{Bmatrix} \boldsymbol{\tau} \end{Bmatrix} \tag{5.14}$$

where all the cable tensions are described by $\{\boldsymbol{\tau}\}$ and are relevant to all segments. Here, $\mathbf{D}_0$ and $\mathbf{D}_1$ keep track of which side the cable is on for a specific segment. That is, d_0 can be positive in the 0th segment and negative in the 1st segment if it crosses between them.

If the cable pattern shown in Figure 5.5b is considered and the complexity of Equation (5.14) is reduced by simplifying such that $\mathbf{q}_j = \{\kappa_j\}$, it is found that:

$$\begin{bmatrix} K_b & 0 \\ 0 & K_b \end{bmatrix} \begin{Bmatrix} \kappa_0 \\ \kappa_1 \end{Bmatrix} = \begin{bmatrix} l_c \cos\frac{\theta}{2} & -l_c \cos\frac{\theta}{2} & l_c \cos\frac{\theta}{2} & -l_c \cos\frac{\theta}{2} \\ l_c \cos\frac{\theta}{2} & -l_c \cos\frac{\theta}{2} & -l_c \cos\frac{\theta}{2} & l_c \cos\frac{\theta}{2} \end{bmatrix} \begin{Bmatrix} T_0 \\ T_1 \\ T_2 \\ T_3 \end{Bmatrix} \tag{5.15}$$

Note the differences in the simplified $[\mathbf{D}]$ matrix between Equation (5.13) and Equation (5.15), which demonstrate the differences between the two cabling patterns. In particular, the cables can be seen switching between positive and negative signs in the last two columns of the simplified $[\mathbf{D}]$ matrix in Equation (5.15), which is due to the crossing cables and is not present in the representation of the traditional cabling method.

5.3 Simulation Results

To capture the behavior of this analytical model, a computational model was developed using C++. Because Equation (5.10a) is nonlinear, the state $\mathbf{q}$ was solved

for using an iterative solver, employing the root finding secant method. The overview of the simulation and experimentation process is given in a flowchart in Figure 5.6. Note that in this section, only the blocks up to the Simulation Results were used, while the rest of the flow chart is applicable to the experimental validation, which is detailed in the next section.

First, this chapter shows that crossing cable configurations can be designed such that their workspaces closely match the workspace of the traditional cable configuration. In order to do this, different cable patterns need to be define. For the traditional cabling method, cables terminate at each segment, as shown in the green box in Figure 5.7. For a six-segment spine, this implied a total of 12 cables. The goal was to reduce the total number of cables (and subsequently actuators) required to achieve a comparable system workspace using crossing cable configurations. A first intuition for a crossing cable configuration was to use the harmonics of a six-segmented system, which resulted in a spine with 8 total cables, as shown in the blue box in Figure 5.7. Using a reduced number of 8 cables, this chapter compares all the possible crossing cable configurations from the cables shown in Figure 5.7 (31,465 configurations) to the

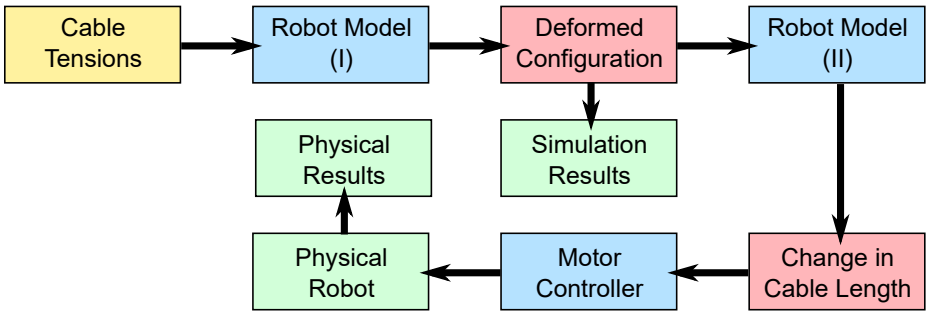

Figure 5.6. Flowchart of simulation and physical spine control. The kinetics portion of the robot model (I) computes the deformed configuration based on cable tensions obtained from the random sample space. The kinematics portion of the robot model (II) takes the deformed configuration and determines the required change in cable length. When working with the physical robot, these changes in cable length are fed to the motor control, which drives the physical robot into the required deformed configuration.

traditional 12-cabled configuration. Note that symmetry was assumed for all these cable configurations (i.e. there are four pairs of cables).

To determine the difference in performance of the cable configurations, the workspace of a six-segment system with 40mm long elastomer segments was explored. This consisted of running samples of randomly generated cable tensions through the model to determine final end position and orientation. The tensions were randomly selected using C++'s rand() command. End position was discretized into a workspace grid, with 1cm resolution. End orientation was discretized into 8 bins divided evenly between 0° and 360°. Two criteria of interest were used: span (the number of position bins the spine reached, regardless of orientation) and intensity (the number of angular bins reached among all locations).

Because of the large number of possible crossing cable configurations, a cursory pass over all the combinations was ran using a total of 10^5 random tension samples ($T_i \in [0,1]N$), which had a low enough resolution to reduce computation time, but high enough resolution to indicate significant trends. The span and intensity was

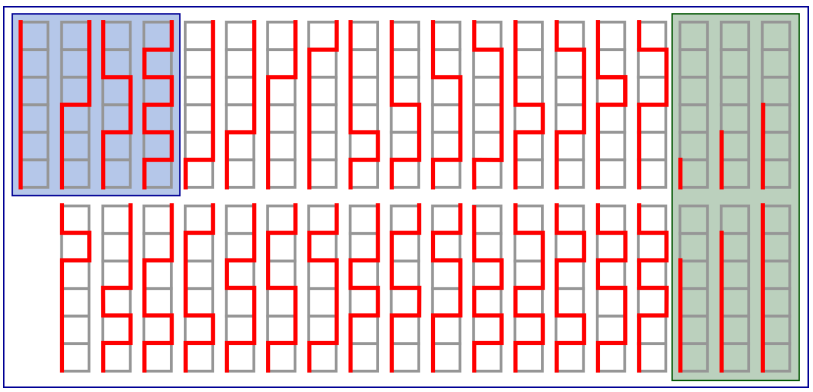

Figure 5.7. Representation of possible cable patterns. Note that cables come in pairs and only half are shown. The cable's pair is opposite and symmetrical to what is shown. The cables shown in the blue box are our initial guess at a harmonic crossing cable pattern. The cables shown in the green box are the cables for the traditional parallel cable pattern. For each spine tested, four configurations are selected from this representation.

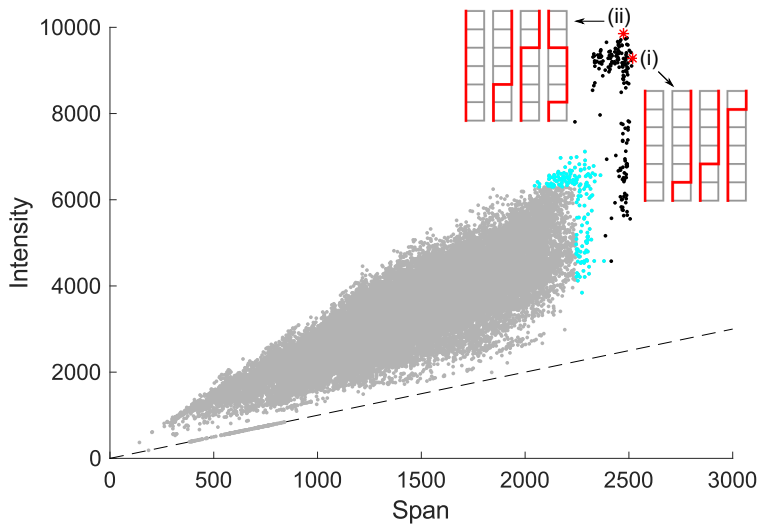

Figure 5.8. Intensity versus span of all 31,465 crossing cable combinations with 10^5 random tension samples shown in gray. The cyan dots represent the 170 selected configurations. The black dots represent those selected configurations run with 106 random tension samples. The red stars indicate the crossing cable configurations with the highest (i) span and (ii) intensity.

tracked for each combination and the results can be seen in Figure 5.8. While there was a wide spread in performance for the crossing cable patterns, focus was placed on the specific configurations that performed well in both span and intensity to match the performance of the traditional cable pattern. Therefore, the top 100 in terms of span and the top 100 in terms of intensity were selected, which resulted in 170 "selected" cable configurations with an overlap of 30 configurations, shown in cyan in Figure 5.8.

These 170 configurations were run at a higher resolution of 106 tension samples ($T_i \in [0, 1]N$). The results from this are shown in black in Figure 5.8. Here, it can be seen that the higher resolution yields even more favorable span and intensity for the selected configurations. The best performing cable configurations can be seen in Figure 5.8, where configuration (i) represents the best performing configuration in terms of span, and configuration (ii) represents the best performing configuration

in terms of intensity. Both of the highest performing crossing cable configurations included a cable pair that goes all the way up the sides without crossing, similar to the traditional parallel cable configuration.

Additionally, this chapter investigated the impact of elastomer segment length on workspace span and intensity. In this experiment, the workspace of the selected crossing cable configurations was compared to the traditional parallel cable configuration with the high resolution of 107 tension samples ($T_i \in [0, 2]N$). As seen in Figure 5.9a, the crossing cable configurations (8-cables) perform comparably to the traditional configuration (12-cables) in terms of both span and intensity. Shortened lengths are more biomimetic, as biological spines have short elastic disks between their rigid vertebrae. The span and intensity values decrease because the spine cannot reach as far with smaller segments. Figure 5.9b-d shows one workspace comparison between the crossing cable configuration with the best performance in intensity (configuration (ii) from Figure 5.8, shown in Figure 5.9b) and the traditional parallel cable configuration (shown in Figure 5.9c), for 40mm elastomer segments. The difference between the workspaces is shown in Figure 5.9d. All of the workspace comparisons shown in Figure 5.9a demonstrate that segment coupling can be used to reduce the total number of actuators in segmented manipulators while maintaining workspace performance.

This chapter also sought to show that crossing cable configurations requires less cable tension than the traditional cable configuration. In the crossing cable configuration, all cables run the full length of the spine and therefore extend to each segment. In the traditional cable configuration, only a subset of cables is available for any given segment. As the crossing cable configuration enables more cables per segment, tension requirements are therefore distributed between a larger number of cables and the tension requirements per cable are relatively reduced. To demonstrate this, the tensions of the crossing cable configuration given by configuration (ii) in Figure 5.8 were compared with the tensions of the traditional cable configuration across a range of spine positions. The spine positions used for comparison are the same positions used in the experimental validation. For this testing, two quantities were considered:

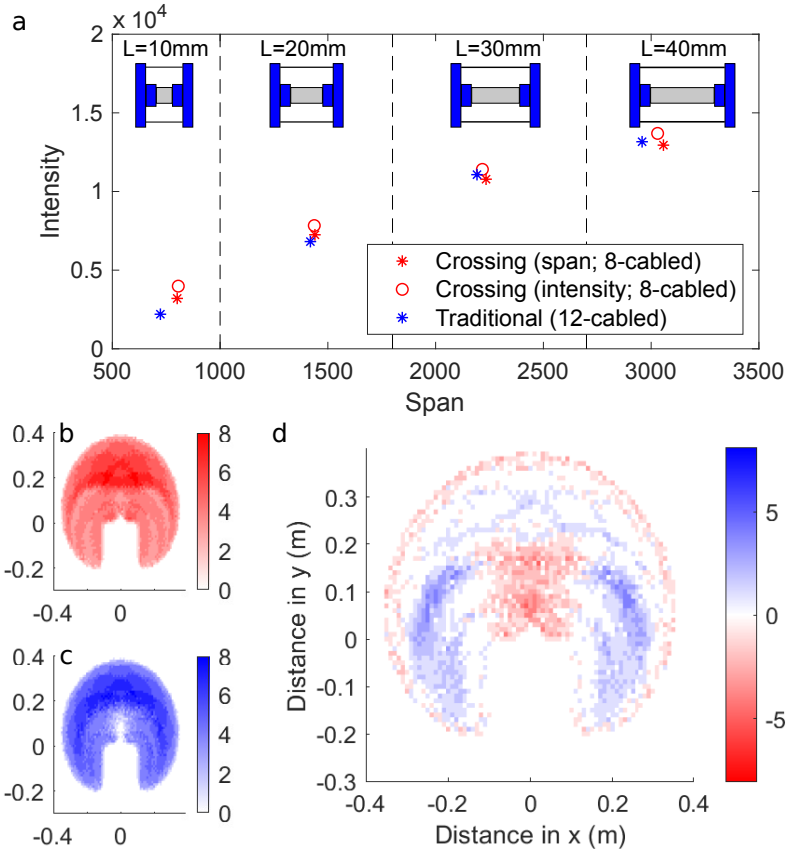

Figure 5.9. (a) Intensity versus span of configurations with changes to elastomer lengths. Note that the cable patterns of crossing span and crossing intensity are represented by those shown in Figure 5.8. (b) Representation of the workspace for the crossing cable configuration with the best performance in intensity [configuration (ii) in Fig. 8]. (c) Representation of the workspace for the traditional parallel cable configuration. (d) Difference between the two cable configurations with 40mm elastomer segments. The base of the spine starts at (0,0). The shaded region is where the spine can reach. The shading scale denotes how many angular position bins the spine is able to reach.Note that the positive numbers indicate that the systemperforms better in the crossing cable configuration, while the negative numbers indicate that the systems performs better in the traditional cable configuration.

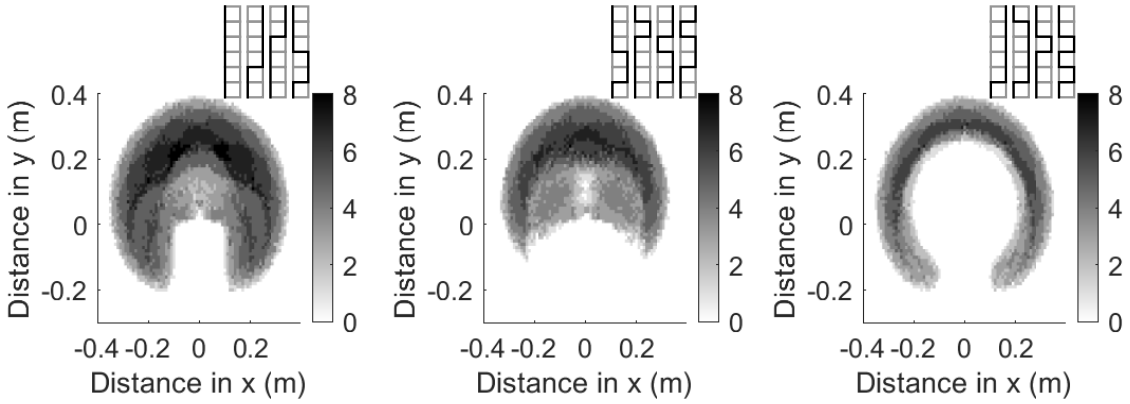

Figure 5.10. Demonstration of different workspaces achievable through different crossing cable configurations. The base of the spine starts at (0,0). The shaded region is where the spine can reach. The shading scale denotes how many angular position bins the spine is able to reach.

(1) the maximum cable tension for each cable configuration for a given spine position ($T_{max,k} = \max\{T_{i,k}\}$ for $i \in [0, n)$, where k denotes a given position) and (2) the peak cable tension of each cable configuration, which is quantified as the maximum value of the cable tensions across all the tested spine positions ($T_{peak} = \max\{T_{max,k}\}$ for all k). The data showing the results can be found in Appendix B. While some isolated spine positions were found for which the traditional cable configuration generated lower maximum cable tensions than the corresponding crossing cable configuration, the crossing cable configuration had a lower peak cable tension over the entirely of the workspace (i.e. all tested spine positions).

Additionally, in contrast to attempting to find crossing cable configurations with workspaces comparable to the traditional cable configuration, this work also sought to identify crossing cable configurations with workspaces that differ drastically from the traditional cable configuration. Such designs are not universally useful, but would be application driven. Some examples of other workspaces are shown in Figure 5.10. Here, the high resolution of 10^7 tension samples ($T_i \in [0, 2]N$) was used. These examples demonstrate that the workspace can be limited by cable configuration,

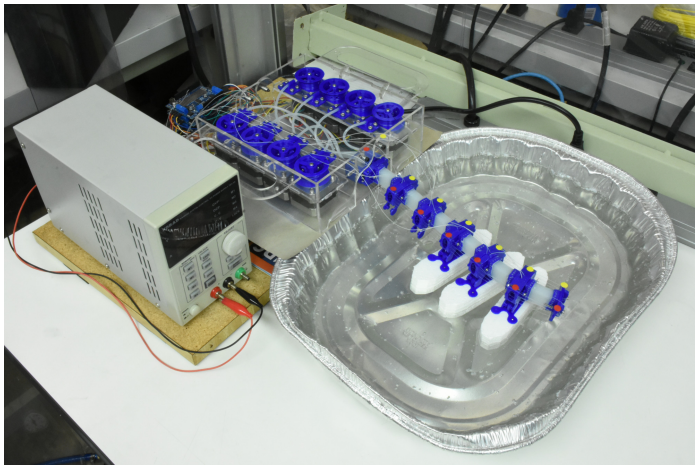

Figure 5.11. Experimental setup with spine floating in water bath.

rather than by software, which could be employed as an additional safety measure in robot manipulator design.

Experimental Validation

In order to determine the accuracy of the model, a physical system was used, shown in Figure 5.11. The system was placed such that it was floating on water with Styrofoam platforms to eliminate friction caused by it sliding on a surface. For the experimental validation, the crossing cable configuration shown in Figure 5.12a was selected, which matches configuration (ii) in Figure 5.8, and used 20mm long elastomer segments. Spine positions yielded from the kinetic model can be translated to cable displacement values using the following kinematic relationship

$$\Delta l_i = l_{neutral} - \sum_{j=0}^{5} l_{i,j} + \Delta l_{tension,i}$$

$$\Delta l_{tension,i} = \frac{T_i l_{total}}{K_t}$$

where Δl_i is the change in length for the ith cable, $l_{neutral}$ is the neutral cable length (this does not account for the cable length that goes through the vertebrae since that is assumed to be a constant length regardless of spine position), $l_{i,j}$ is the length of

the cable for the jth segment, $\Delta l_{tension,i}$ is the change in length (stretch) due to the ith cable tension, l_{total} is the total length of the cable (this accounts for the length going through vertebrae), and K_t is the cable stiffness of the fishing line (96.5N/m).

To control the movement of the spine, a Python program was developed that ran an Arduino with a slave program. The Python program translated the raw cable displacements, given in meters, to motor commands, given as steps in the stepper motors. The motor commands were sent to the Arduino Uno, which used the Adafruit motor shield and AccelStepper libraries to actuate the spine. To determine the actual spine position, a vision tracking system consisting of a Logitech C270 Webcam and OpenCV was used. Red and yellow dots were placed on the spine to facilitate this and can be seen in Figure 5.12. The computer vision (CV) system produced an estimate of the spine position based on the average position of the fiducial dots taken over 50 images. In addition, an outlier rejection filter was applied to remove cases where the CV system misidentified the location of the dots.

Figure 5.12 shows three different comparisons between the predicted and actual spine positions. While the model predictions do not exactly match the physical outcomes, the agreement in the trends of the deformations is convincing that the model is accurate. The error in end position for Figure 5.12b was 30.3 ± 2.3mm; for Figure 5.12c, the error was 46.9 ± 4.4mm; for Figure 5.12d, the error was 36.2 ± 2.7mm. Additional spine configurations can be seen in Appendix B. The main sources of discrepancy between the model and physical system are cable friction and cumulative errors due to positional error in each segments. Since the model does not account for a number of real physical terms, such as friction, the results were expected to be close, but not perfect. As it turned out, the errors were small (on the order of 30mm) and there was good agreement between the models and the shape and behavior of the physical system.

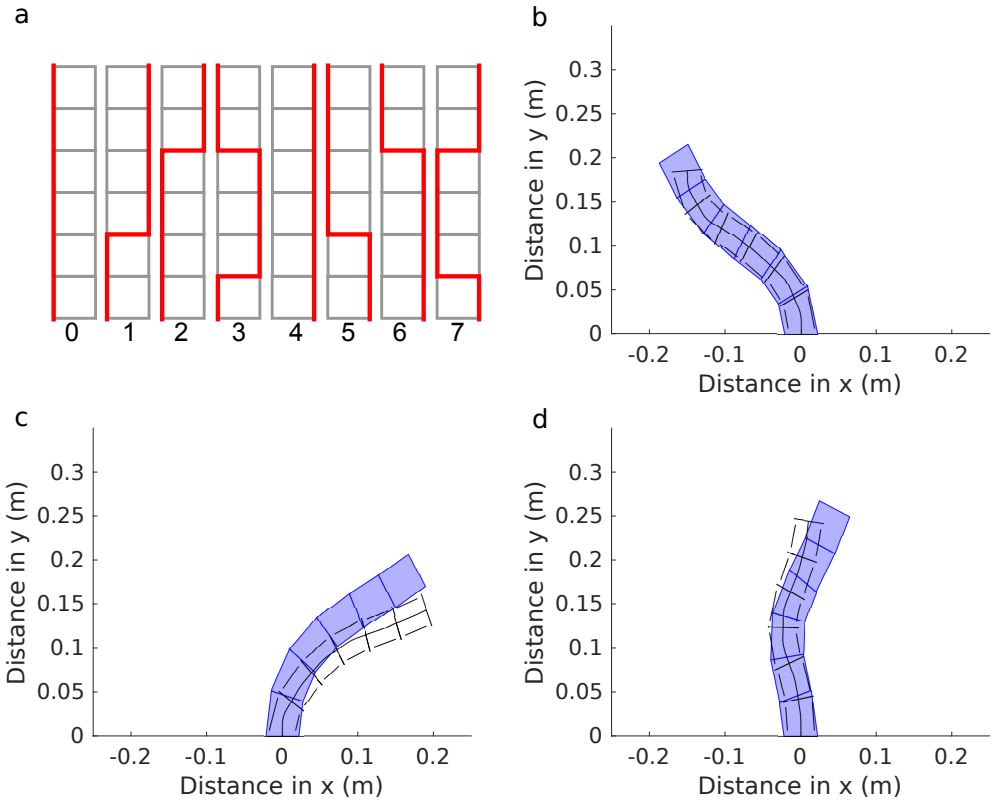

Figure 5.12. Experimental tests for model validation. The recreation of the spine is shaded blue, while the model prediction is shown as a black outline. (a) Shows the cables used and their respective numbers. Changes in lengths for (b) are {11.5, 39.5, 46.5, -10, 8.5, -16.5, -24.5, -31}mm, for (c) are {-9.5, 2.5, -13.5, 11.5, 29.5, 15.5, 31.5, 5.5}mm, and for (d) are {7.5, 24.5, -2.5, 28, 12.5, -5, 22, -10}mm for the respective cables given in (a).

5.4 Conclusion

This chapter demonstrated that actuator count and maximum cable tension can be reduced without loss to workspace performance through the use of crossing cable configurations. Furthermore, it was shown that through the use of crossing cable patterns, it is possible to tune the workspace for a given application, which may be leveraged to increase safety during manipulator operation. This model was expanded to a 3D continuum robot with spiralling cables for use on robots with thick, soft

segments in Appendix F. Use of highly coupled actuation allows for greater flexibility in design and more closely matches the behavior of biological systems.

6. STATE AND STIFFNESS ESTIMATION USING ROBOTIC FABRICS

Soft robots have many applications, but are generally designed with a specific task in mind, such as locomotion [38, 223, 277], grasping [28, 34, 278], or manipulation [63, 279]. In order for soft robots to operate in unstructured environments, they will need to adapt to different environments, tasks, and interactions, and some examples of multifunctional [280–282] and reconfigurable [283, 284] soft robots have been shown. Here, robotic fabrics are proposed. Robotic fabrics integrate both sensing and actuation elements with a fabric substrate, and can be wrapped around soft, passive bodies (*e.g.*, foams, elastomers, tensegrity structures, etc.) to impart motion onto those bodies. By reorienting a robotic fabric on the surface of a deformable body, or placing it on a different body with different properties and/or morphology, different motions and tasks may be achieved [72, 285].

Creating robots out of 2D fabrics has been previously demonstrated. Fabrics have been used to lighten a system while providing a yielding structure [286]. Previous work includes demonstration of a fabric sensory sleeve that provides state estimation of an underlying 3D structure [69], as well as robotic fabrics that include variable stiffness actuating fibers [285] or integrated sensors and actuators [72]. In the latter work, the sensing elements in the robotic fabric were not sufficient to quantitatively estimate system state.

In this chapter, a robotic fabric prototype containing conductive composite-based capacitive sensors and pneumatic McKibben actuators is introduced. This robotic

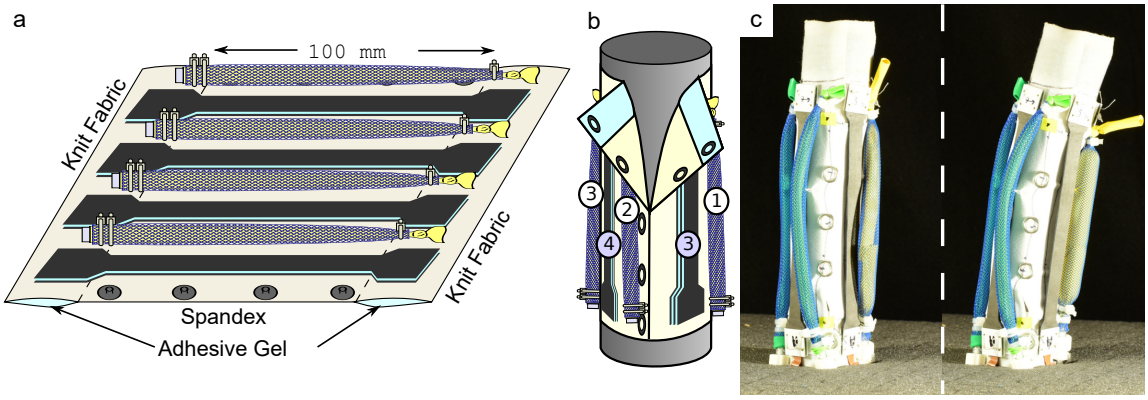

Figure 6.1. (a) Sensors and actuators are placed on fabric in an alternating pattern to create a robotic fabric. Button snaps are placed on the sides and an adhesive gel is applied to the underside of the knit fabric. (b) The robotic fabric is wrapped around a passive body. The actuators are numbered in white while the sensors are numbered in color. (c) An example of a robotic fabric wrapped around and deforming a polyethene foam cylinder.

fabric is wrapped around passive cylindrical bodies to create active continuum joints (*i.e.*, actuators contract along the length of the cylinder). Further, a corresponding analytical model is derived that uses the sensors embedded within the fabric to estimate both state and stiffness of the underlying cylinder.

Robotic fabrics may be applied arbitrarily to passive host bodies, and the material properties of these bodies may not be known beforehand. Therefore, it is valuable to be able to retrieve that data from the robotic fabric itself. Here, the analytical model is applied to a relatively simple configuration to estimate the stiffness properties of the underlying host body by leveraging known actuator forces and system state. In the future, this work can be extended to more complex configurations and systems and could be used to generate system models that benefit feed-forward soft-bodied control approaches.

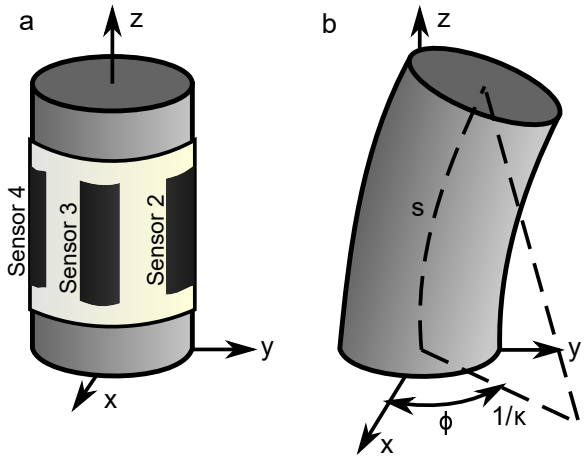

Figure 6.2. (a) Sensor placement. Sensors are placed at even intervals to align with the x- and y-axes. Sensor 1 is on the opposite side of sensor 3 behind the cylinder. (b) Schematic of a constant curvature beam.

6.1 Model

This system consists of a robotic fabric with parallel actuators and sensors wrapped around a cylindrical deformable body (Figure 6.1a-b). When an actuator contracts, it causes the cylinder to curve (Figure 6.1c). To model this system, constant curvature is assumed, which allows us to adapt models developed for continuum robots [33,287]. It is additionally assumed that no compression occurs along the central axis of the cylindrical body and that the system is not subject to external loads. Note that this model is dependent on sensor placement rather than type, and should therefore be extendable to other component choices regardless of the specific components implemented in this paper. Similarly, this model can be used for a variety of actuators as long as the exhibit contracting behavior required for the model.

6.1.1 State Estimation

To estimate system state, it is assumed that the sensors in the robotic fabric follow the curvature of the bending cylinder (*i.e.*, perfect contact between the exterior fabric

and internal body). This robotic fabric prototype includes four evenly spaced sensors, which, when placed around the cylinder, can be used to define a coordinate frame such that the x- and y-axes align with the sensors (Figure 6.2a). A segment with constant curvature is defined in two ways: (1) using the length of the segment (s), curvature (κ), and angular offset of curvature (ϕ); and (2) using the length of the segment (s), curvature along the x-axis (κ_x), and curvature along the y-axis (κ_y). Conversion between these two definitions is possible using $\kappa = \sqrt{\kappa_x^2 + \kappa_y^2}$ and $\phi = \tan^{-1}(\kappa_y/\kappa_x)$. These variables are schematically shown in Figure 6.2b.

With reliable data from all four sensors, the system curvatures are derived as:

$$\kappa_x = \frac{s_4 - s_2}{2sr_b}, \quad \kappa_y = \frac{s_1 - s_3}{2sr_b}, \tag{6.1}$$

where s_i refers to the length of the ith sensor and r_b is the radius of the cylindrical segment. Equation (6.1) assumes that all sensors are giving accurate information. However, unless the cylinder is being simultaneously strained and bent, it is likely that only two or three sensors are giving reliable data while the other sensors are buckled or slack. Using only two or three sensors, the system curvatures can be derived as:

$$\kappa_x = \frac{s_4 - s}{sr_b} = \frac{s - s_2}{sr_b}, \quad \kappa_y = \frac{s_1 - s}{sr_b} = \frac{s - s_3}{sr_b}, \tag{6.2}$$

where the appropriate equations are selected for determining κ_x and κ_y, depending of the axis of curvature. Note that if there are three accurate sensors, a combination of equations can be selected from Equations (6.1) and (6.2) as needed.

6.1.2 Stiffness Estimation

The state estimation model may be extended to also estimate the bending modulus or elastic modulus of the underlying material. Note that in order to estimate the stiffness, the state must first be estimated. For the stiffness estimation, at least one actuator must be placed parallel to the central axis of the body. Contracting this actuator will cause an equilibrium between the actuator force and the passive

cylinder to be reached, which is dependent on the bending stiffness of the cylinder. The bending stiffness (K_b) relates to the actuator force (F) as:

$$K_b = \frac{r_b F}{\kappa}. \tag{6.3}$$

Noting that $K_b = EI$, the elastic modulus (E) of the material can also be determined. Assuming linear material properties, which has been previously validated using similar materials [288], and that the second moment of inertia (I) is known, the elastic modulus can be calculated as:

$$E = \frac{r_b F}{I\kappa}. \tag{6.4}$$

6.2 Materials

The robotic fabric prototype implemented here employs a Spandex fabric substrate, capacitive sensors based on a conductive elastomer composite, and pneumatic McKibben actuators. Note that while this work utilizes some miniaturized pneumatic components [289], the purpose of this work is not to present an untethered system. Additionally, the model should be applicable to other types of actuation that operates on changes in length, such as cables and shape memory alloy coils, which may be easier to untether than pneumatics.

6.2.1 Sensor Fabrication

The capacitive sensors were made from a conductive elastomer composite with expanded intercalated graphite (EIG), as described in [43]. Each sensor consisted of five alternating layers of conductive elastomer composite and inert elastomer, where the two outer layers of conductive elastomer composite were grounded to shield the sensor from environmental noise. The conductive elastomer composite was composed of Dragonskin 10 Slow (Smooth-On, Inc.) mixed with 10wt% EIG, and the inert elastomer was Dragonskin 10 Slow.

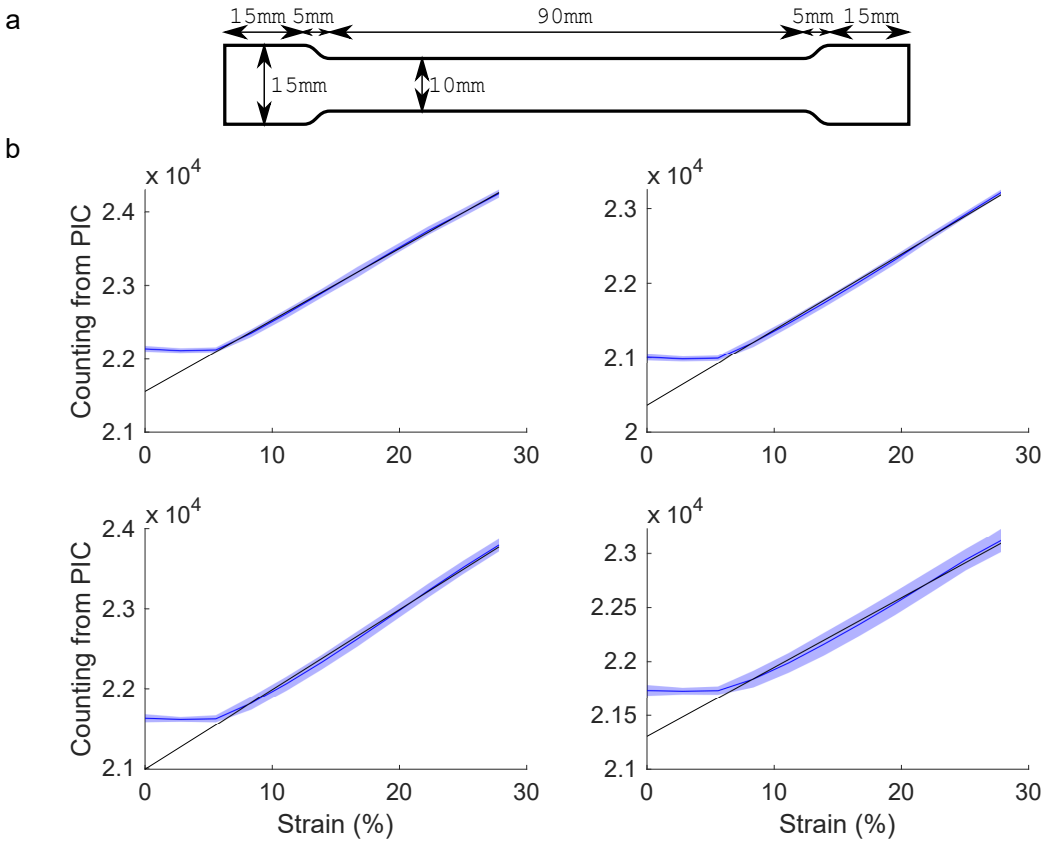

Figure 6.3. (a) Sensor dimensions. (b) Instruction cycle-strain plots for the four sensors used on the robotic fabric. Each plot corresponds to one sensor. The average response is shown as a blue line. The colored clouds around the means represent the 95% confidence intervals for ten cycles. The black line represents a linear approximation of these data.

The sensors were fabricated via rod coating using a 1/2"-10 Acme threaded rod (97014A634, McMaster-Carr). First, a layer of conductive elastomer composite was coated onto a polyethylene terephthalate (PET) film (8567K12, McMaster-Carr) and cured. A subsequent layer of inert elastomer was coated on top, followed by another layer of conductive elastomer composite on just half the surface. A final inert layer was coated and allowed to partially cure until it was "tacky." The multilayer sheet was then folded over for tacky bonding, and a foam roller was used to remove air bubbles. Once cured, the sensors were cut out using a 30 W CO_2 laser patterning system

(VLS 2.30, Universal Laser Systems). The sensors were then removed from the PET film and cleaned of debris with soap and water. A staple was used to electrically connect the two grounded layers of the sensor. The sensors were connected to a signal conditioning board using strips of copper-coated Kapton (Pyralux, Adafruit). Dimensions of the sensors were chosen isolate the deformation to an active region that is 90 mm x 10 mm, as shown in Figure 6.3a.

6.2.2 Actuator Fabrication

To fabricate the McKibben actuators, a figure-8 knot was tied in one end of a latex balloon. The balloon was placed inside a 1/4" mesh (9284K2, McMaster-Carr) and a zip tie was placed just inside the knot to hold the mesh onto the balloon. Tygon tubing (6.4 mm outer diameter, 1.6 mm inner diameter) was inserted in the open end and two zip ties were applied to hold the mesh and balloon tight to the tubing. The McKibben actuators were controlled through a pressure regulator board. The resulting actuators are 120 mm in length fully stretched (Figure 6.4a) and contract to approximately 85 mm when fully actuated.

6.2.3 System Integration

The sensors and actuators were integrated with a fabric substrate. The fabric substrate consisted of a 100 mm x 120 mm spandex fabric section sewn to 20 mm x 120 mm knit fabric on either end. Spandex was chosen for the deformable section of fabric due to its high stretchability. Knit fabric was chosen for the ends because it stretches slightly in only one direction, which allows some uniaxial strain for wrapping around objects, but will not strain where the sensors and actuators are anchored.

The sensors and actuators were sewn in an alternating sensor-actuator pattern onto the knit part of the substrate such that they spanned the Spandex fabric. The sensors were pre-strained to 100 mm (from original length of 90 mm), while the actuators were pre-compressed to 100 mm (from original length 120 mm). This pre-

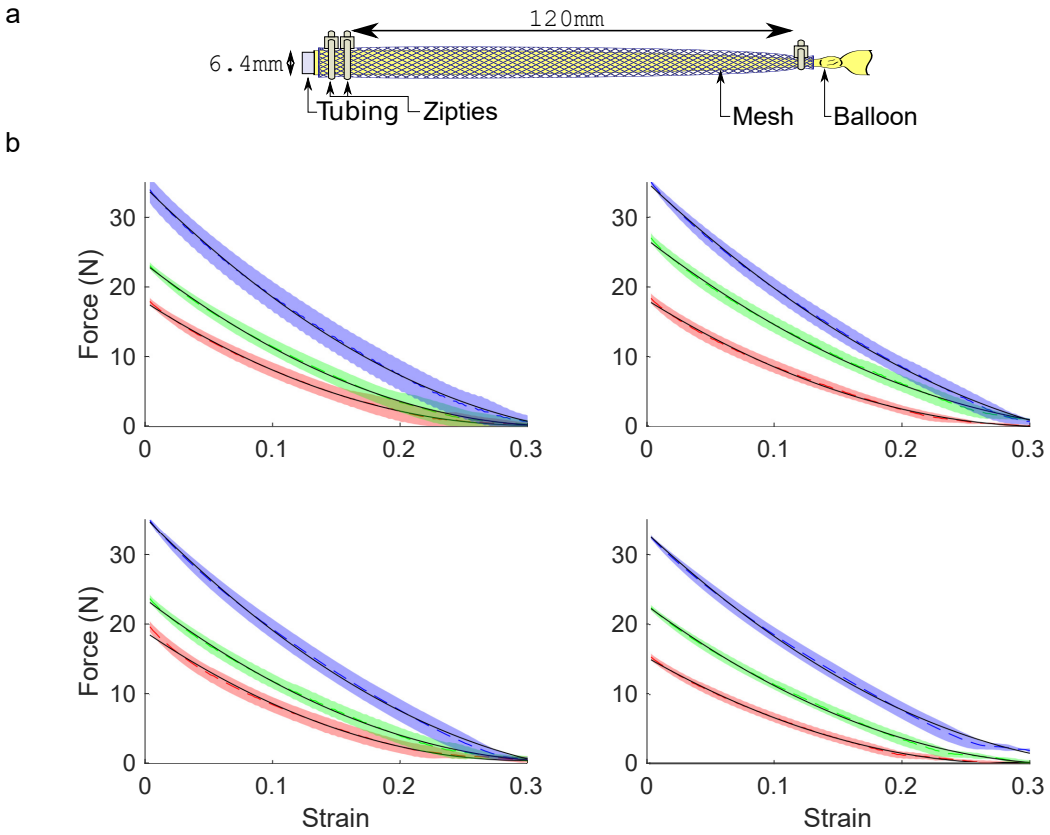

Figure 6.4. (a) Schematic of actuator with dimensions given and parts labeled. Note the drawing is not to scale. (b) Force-strain plots for the four actuators used on the robotic fabric. Each plot corresponds to one actuator. The average response for the experimental data is shown as a dashed line of red for 69 kPa, green for 103 kPa, and blue for 138 kPa. The colored clouds around the means represent 95% confidence intervals for twelve cycles. The black lines represent a 2-degree polynomial fit of the average responses.

compression was done to allow actuators to both stretch and compress while the system bends, since the model assumes both stretch and compression on the outer walls of the cylinder.

Button snaps were applied at the edges of the robotic fabric to allow attachment around a body. Finally, a coating of adhesive gel (Silbione RT gel 4717, Blue Star Silicones) was added to the knit fabric portions to help prevent slipping between the fabric and host body during actuation. The sensors and actuators were controlled

with an Arduino Uno. The Arduino Uno acts as a slave for a Python script run on Lenovo Thinkpad laptop.

6.3 Results & Discussion

6.3.1 Sensor Characterization

Sensors were characterized within the full robotic fabric system. The robotic fabric prototype was sewn to two brass rods on the top and bottom and loaded in a materials testing machine (3345, Instron). The robotic fabric was strain cycled 11 times starting at a length of 90 mm, which was the initial length of the sensors, and pulled to 120 mm, which was the limiting strain due to the actuators. The first strain cycle was not included in the data analysis to remove the Mullin's effect [22]. The results from the ten sequent strain cycles were averaged together for each sensor and are shown in Figure 6.3b. Note that the data from the sensors is reported here in instruction cycles, which is the number of instruction cycles the sensor's microprocessor goes through while the sensor charges and discharges (related to time to charge and discharge and, thus, the capacitance of the sensor). A linear fit ($IC = a_0\varepsilon + a_1$) was implemented for each sensor relating the sensor response to strain, where IC represents instruction cycles from the sensor, ε represents strain, and a_i represent the parameters for the equation, which are given in Table 6.1.

Table 6.1. Parameter values for the linear fit equations that represent the average sensor response. Note that sensor numbering corresponds with Figure 6.1b.

	Sensor 1	Sensor 2	Sensor 3	Sensor 4
a_0	101	100	65	97
a_1	20400	20900	21300	21600

6.3.2 Actuator Characterization

To measure the performance of the actuators, each one was placed in a materials testing machine (3345, Instron) and initially held at 120 mm for a given pressure. True performance of the individual actuator was desired, not performance of the integrated robotic fabric, and therefore the actuators were characterized before they were integrated into the robotic fabric. The actuators were strain cycled between 120 mm to 80 mm at 40 mm/min for 12 cycles. This test was repeated at different pressures: 69, 103, and 138 kPa. The first two cycles were discarded from the analysis since these involved breaking-in of the actuators. The results of this test can be seen in Figure 6.4b. Although theory exists that describes the behavior of McKibben actuators, it does not account for friction or expansion of the balloon and differs from the actual performance significantly [290]. Therefore, a 2-degree polynomial ($F = b_0\varepsilon^2 + b_1\varepsilon + b_2$) was used to represent the responses of the actuators, which matches the responses well. The parameters for this equation are given in Table 6.2.

Table 6.2. Parameter values for the 2-degree polynomial equations that represent the average actuator response. Note that actuator numbering corresponds with Figure 6.1b.

Actuator 1				Actuator 3			
kPa	b_0	b_1	b_2	kPa	b_0	b_1	b_2
69	192.6	-116.5	17.9	69	207.0	-123.5	19.0
103	214.8	-141.1	23.3	103	206.5	-138.8	23.7
138	229.3	-180.3	34.3	138	232.9	-185.1	35.4
Actuator 2				Actuator 4			
kPa	b_0	b_1	b_2	kPa	b_0	b_1	b_2
69	179.5	-114.2	18.2	69	179.4	-104.7	15.4
103	181.2	-140.4	26.9	103	200.1	-135.1	22.8
138	193.8	-171.9	35.1	138	216.1	-170.1	33.2

6.3.3 State Estimation

In order to test the state estimation model, the fabric was wrapped around three different cylindrical body materials: polyethelene foam, Dragonskin 10 Slow elastomer ($E = 265$ kPa), and Smooth-Sil 935 elastomer (Smooth On, Inc; $E = 536$ kPa). Note that despite the fact that elastomers such as Dragonskin 10 Slow and Smooth-Sil 935 have a nonlinear stress-strain response, they have a linear response at low (<40%) strains [288]. The polyethelene foam was hollow with an outer diameter of 35.0 mm and an inner diameter of 18 mm. The two elastomers were solid with an outer diameter of 33.8 mm. The outer diameters correspond to r_b in the model, while s is 100 mm. The length of s is determined by the "active" length of the fabric (*i.e.*, the 100 mm length of spandex).

The cylinder-robotic fabric system was placed vertically, as seen in Figure 6.1, and two markers were placed along the central axis where the curvature occurred. Actuator 1, shown in Figure 6.1b, was activated to a specific pressure after which a single sensor response was collected from all the sensors. Note that this data was

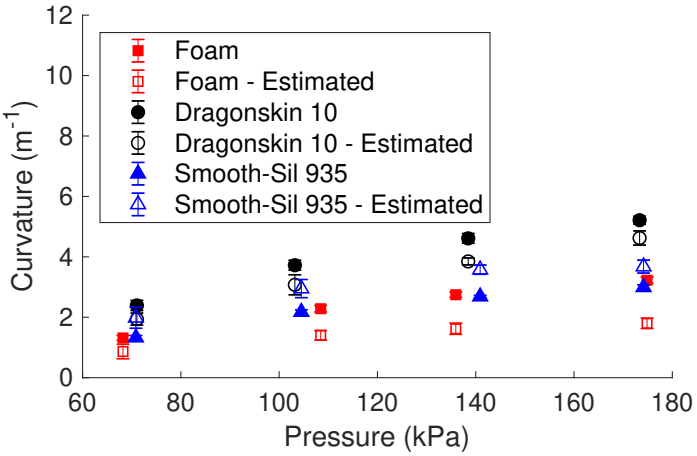

Figure 6.5. Pressure-curvature data for the foam and elastomer cylinders. The curvature from the photos is shown as red filled squares, black filled circles, and blue filled triangles. The model estimation is shown as red hollow squares, black hollow circles, and blue hollow triangles. The error bars represent 95% confidence intervals.

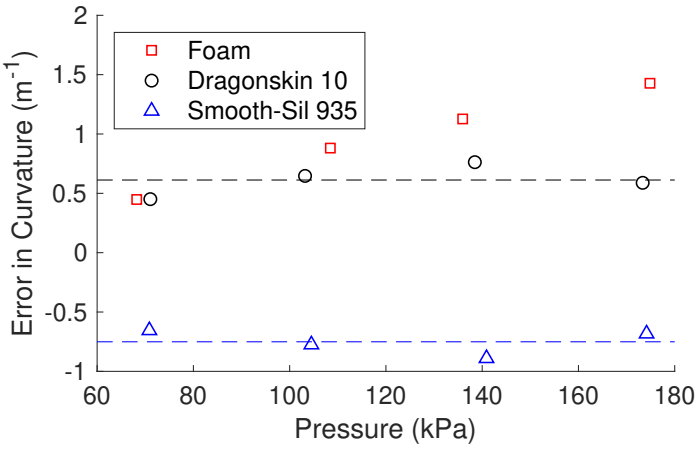

Figure 6.6. Error in estimated and actual curvature. Fits for the data are shown as dashed lines.

collected with an Arduino Uno from each sensor's signal conditioning board. A photo was taken in each deformed configuration, which was used to generate truth state data. Deformation was repeated five times for a number of pressures (approximately 69, 103, 138, 172 kPa, or 10, 15, 20, 25 psi) for each cylinder, thus collecting five sensor responses and pictures at each position. The actual (truth) curvature of the system was determined from the photos using ImageJ, and the estimated curvature was calculated using the sensor data and the corresponding model. Specifically, data from sensors 1 and 4 was used to calculate the curvatures. Note that the sensor data was only used if it fell within the linear region of the sensor response (strain greater than 10%). Figure 6.5 shows the results of these tests.

Using the model to estimate state allows for the analysis of a complex 3D deformation without the need for multiple sensor calibrations at various system positions. Rather, pre-existing models can be adapted around sensor data. However, as with any model, there are limitations, which can be seen in Figure 6.5. The estimated curvature for the Dragonskin 10 Slow and Smooth-Sil 935 elastomer cylinders tracks fairly well, but there is a clear offset between the actual curvature and estimated curvature. In contrast, the estimated curvature for the foam cylinder gets decreasingly accurate with higher pressures, which is due to the material properties of the foam.

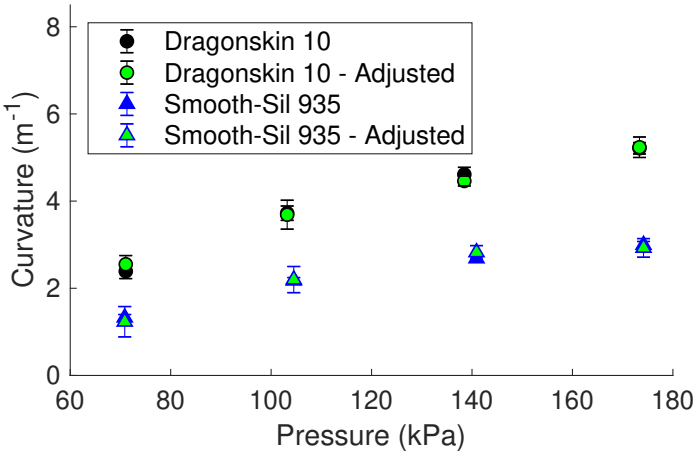

Figure 6.7. Pressure-curvature data for the elastomer cylinders with the estimation data adjusted for the error. The adjusted model estimation is shown as black circles and blue triangles filled in with green for the foam and elastomer, respectively. The error bars represent 95% confidence intervals. This figure shows that in practice the error in the model can be compensated to get more accurate results.

While the sides of the elastomer cylinders are able to stretch and compress as the cylinder bends, the foam cylinder can compress, but does not stretch as well as the elastomer. This means that the foam cylinder does not follow the assumptions of the model and, at most, the model is only useful at low pressures.

The errors between the mean estimated curvatures and mean actual curvatures can be seen in Figure 6.6. Errors in the Dragonskin 10 Slow and Smooth-Sil 935 elastomer responses are nearly constant. Hence, a final adjustment is added to the data to compensate for model error and improve the estimation by adding either the steady state error into model such that:

$$\kappa_{estimated} = \sqrt{\kappa_x^2 + \kappa_y^2} + e, \tag{6.5}$$

where e is the constant error in the curvature for the elastomer cylinders. As an example, Figure 6.7 shows the data adjusted for the observed error, which demonstrates that the model error can be corrected in practice to get more accurate results.

6.3.4 Stiffness Estimation

In order to estimate stiffness, the force from the actuator is required, which can be found using the force-strain equations from Table 6.2. First, the length of the actuator ($s_{actuator}$) is found from the model as:

$$s_{actuator} = s(1 - \kappa r_b). \tag{6.6}$$

This length is then converted to strain and fed into the force-strain equation for Actuator 1 to get the approximate force.

With known forces, the adjusted curvature data from Figure 6.7 can be used along with Equation (6.4) to estimate the elastic modulus for both elastomers at pressures of 69, 103, and 138 kPa, and the results are shown in Table 6.3. Notably, the estimated stiffness is most accurate (less than 10% error) when the results from all the tests are averaged together.

6.4 Conclusion

In this chapter, models have been derived to estimate the state and stiffness of a soft cylindrical body that is deformed from its surface by robotic fabric. The models leverage feedback from sensors embedded within the robotic fabric to estimate curvature state of the cylinder, and further use this state information alongside known

Table 6.3. Estimated elastic modulus at various pressures. The percent error is determined from the mean value.

	Dragonskin 10 Slow		Smooth-Sil 935	
Pressure (kPa)	E_{est} (kPa)	% Error	E_{est} (kPa)	% Error
69	228 ± 14	14%	655 ± 240	22%
103	195 ± 17	26%	459 ± 91	14%
138	296 ± 7	12%	640 ± 51	19%
Avg	**240±91**	**9%**	**585±242**	**9%**

actuator forces to derive the elastic modulus of the cylinder material. The accuracy of the proposed models have been evaluated on representative cylinder body materials and found that the models are highly applicable across a range of curvatures for elastic materials, but only applicable at low curvatures for certain foam materials.

Simplified models that work with sensor data are necessary to track complex 3D movements of soft robotic systems. The state estimation model derived herein may be useful in the development of soft systems that utilize surface strains for information, such as sensory skins, robotic skins, and robotic fabrics. Integrated conformable systems that can manipulate arbitrary deformable bodies from their surface (*e.g.*, robotic fabrics) will further need to infer body material properties, such as stiffness, from the robotic fabric itself to inform system models and predict performance.

7. ROBOTIC SKINS THAT LEARN TO CONTROL PASSIVE STRUCTURES

In this chapter, robotic skins that learn about their underlying host structures to facilitate feedforward control of the system are presented. This approach is demonstrated on cylindrical continuum segments since they are widely applicable in soft robotics and can be easily stacked to create multi-segment arms, as shown in Figure 7.1a. In this work, "learning" is defined as the ability to use sensory information to obtain certain values of the host structure, specifically length, radius, and bending stiffness of the segments, and apply those values to populate control models. Previously, robotic skins were used to estimate both state and stiffness of cylindrical continuum segments [291]. Here, it is demonstrated how this ability to estimate state and stiffness of structures can be extended to learn model parameters of continuum segments made from different materials *in situ*, which enables feedforward control. the necessity of having the skins learn is shown by considering both a generalized feedforward model, which is provided with a bending stiffness, and compare it to the learned bending stiffness estimation. Additionally, the sensors in the robotic skin were used to apply feedback control both on its own and in combination with the learned feedforward model control. Finally, this chapter demonstrates how this ability to learn about the underlying structures is expandable to multi-segment systems and is able to adjust parameters (*i.e.*, the bending stiffness) to account for gravity, which is not included in the model of the cylindrical segment.

While there are many control strategies in soft robotics [55, 292–294], this is the first demonstration of robotic skins learning about structures for control purposes.

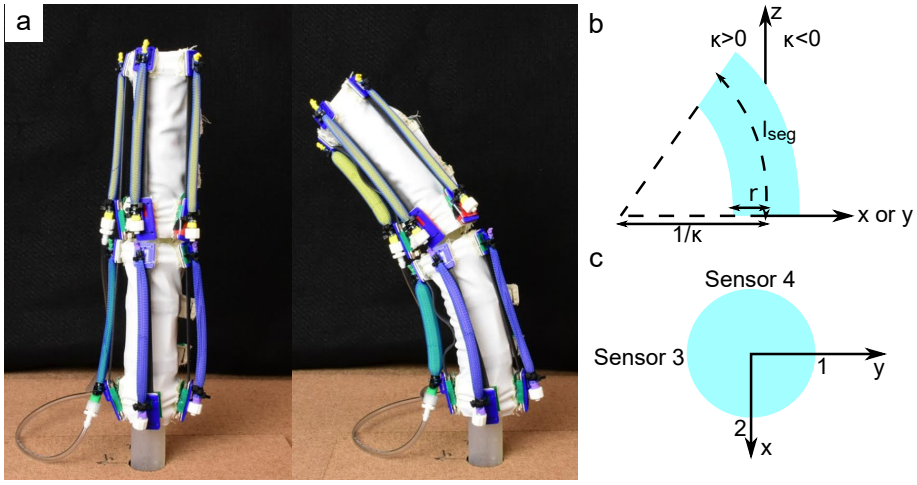

Figure 7.1. (a) A two-segment continuum robot made from two robotic skins wrapped around soft cylindrical segments. The sensors and actuators in the robotic skins are used to derive properties of the underlying segment and to control the system. (b) A visual description of a bending segment. (c) A cross-section of a segment with sensor labels.

By learning about the system, it is possible to change the system on-the-fly without the need to intervene and perform time-intensive system re-calibrations manually.

7.1 Model

The model used in this work was developed from existing models in continuum robotics [33, 60, 287], which describe the deformation of cylindrical segments given loads that run parallel to or spiral around the segment [295]. While dynamic models of these continuum robots exist [66, 296, 297], this work focuses on a static model to demonstrate that simple models can be used with robotic skins to control soft continua.

A full model description is presented in [291], and is summarized briefly here. The state of a cylindrical segment can be described by segment length (l_{seg}) and curvature in the x- and y-axes (respectively, κ_x and κ_y). A visual representation of curvature

is shown in Figure 7.1b. Sensors that are aligned parallel to the neutral axis of the segment can be used to identify the state of the segment:

$$\kappa_x = \frac{l_{s,2} - l_{seg}}{l_{seg} r} = \frac{l_{seg} - l_{s,4}}{l_{seg} r} \tag{7.1a}$$

$$\kappa_y = \frac{l_{s,1} - l_{seg}}{l_{seg} r} = \frac{l_{seg} - l_{s,3}}{l_{seg} r} \tag{7.1b}$$

where $l_{s,i}$ for $i = 1, 2, 3, 4$ is the length of the ith sensor, as shown in Figure 7.1c, and r is the radius of the segment. The bending stiffness of the combined segment and skin (K_b) can be estimated by applying a single actuator force (F) and relating this to the system curvature:

$$K_b = \frac{rF}{\kappa} \tag{7.2}$$

where $\kappa = \sqrt{\kappa_x^2 + \kappa_y^2}$.

7.2 Fabrication

The robotic skins, shown in Figure 7.2a, were designed to fit around cylindrical segments (r = 17.5 mm and l_{seg} = 100 mm). Though the segment dimensions are carried over from prior work [291], the robotic skin design was improved to have it learn all necessary segment properties (r, l_{seg}, and K_b) on its own. Thus, the approach presented here can be readily applied to passive cylindrical segments of arbitrary sizes and materials (within reason). This concept can be expanded to arbitrary shapes in future work. In the following, the fabrication of the actuators, sensors, robotic skins, segments, and the experimental setup is discussed.

7.2.1 Actuators

The model assumes actuators that either contract or elongate and, thus, McKibben pneumatic actuators which contract as they are pressurized were selected for this work. Each actuator was made with a latex balloon bladder surrounded by mesh braid (1/4" dia., McMaster-Carr). The balloon was tied on one end with the braid

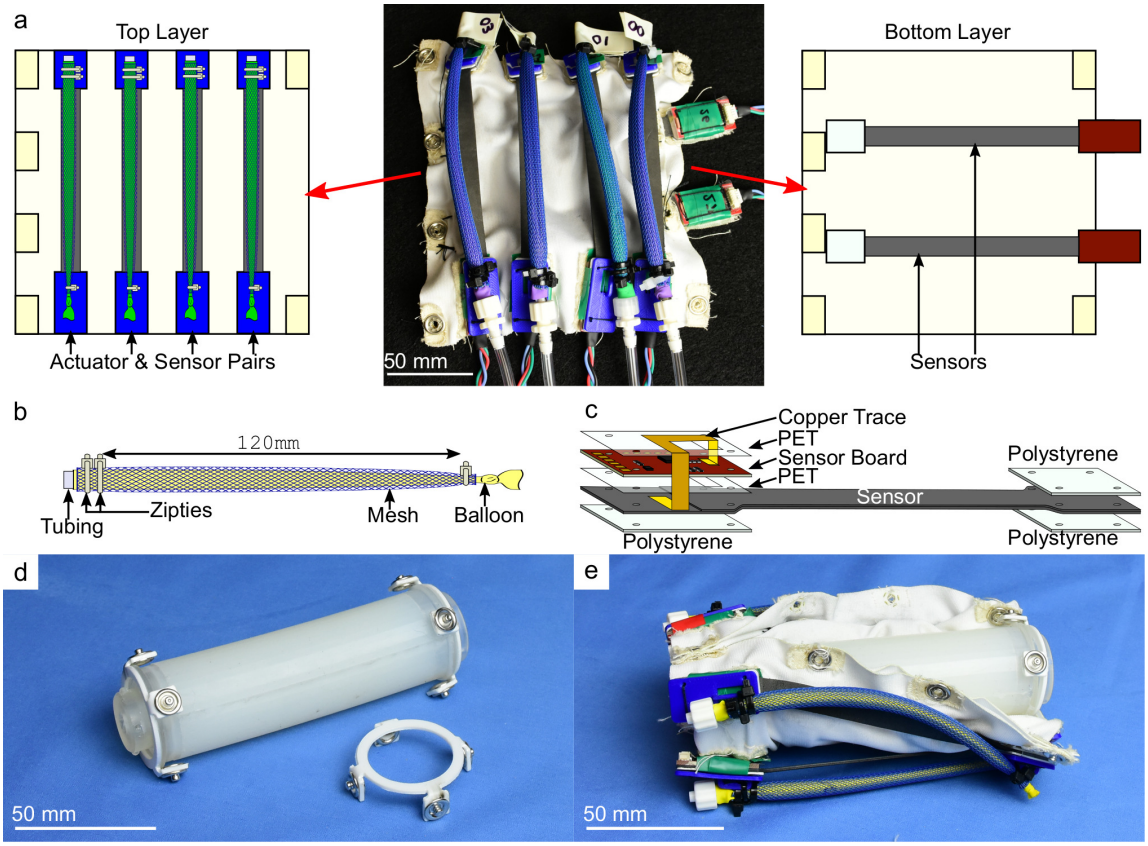

Figure 7.2. (a) The robotic skin is composed of two layers of spandex instrumented with sensors and actuators. Diagrams show the layout of the skin. (b) Diagram and dimensions of the actuators. (c) Components and construction of the sensors. (d-e) A Dragon Skin 10 Slow elastomer segment with polystyrene skin attachments both (d) without and (e) with the robotic skin.

ziptied onto the balloon just inside of the knot, as shown in Figure 7.2b. On the other end, a Tygon tubing (6.4 mm outer diameter, 1.6 mm inner diameter) was inserted into the balloon and secured two zipties over the braiding around the tubing to prevent leaking. The McKibben actuator was designed to be 120 mm long to allow a sufficient range of motion, but still contract enough (to ≈85 mm) to deform the segment when pressurized.

7.2.2 Sensors

Capacitive strain sensors were used to measure the lengths and radii of segments. The sensors were fabricated as a parallel-plate capacitor using an exfoliated graphite and silicone composite for the conductive layers and pure silicone elastomer for the dielectric layers. These sensors have five layers to help isolate the sensors from external disturbances. Descriptions of how to make the exfoliated graphite composite and the five layer sensor material are available in [43] and [6, 291], respectively. The sensors were designed with an active (gauge) length of 80 mm (overall length 132.1 mm). The vertical sensors were pre-strained by 20 mm when installed on the segment; the horizontal sensors were designed with a 16.5 mm pre-strain. The sensors were redesigned from [6, 291] to be more compact and now have the sensor board sitting on top of the sensor material rather than attached externally to the sensor footprint. Figure 7.2c shows how the final sensor components were assembled. The polystyrene (0.65 mm thick) and PET (0.1 mm thick) ends were cut with a laser (Universal Laser Systems VLS 2.30). The ends were sewn through the available holes to hold the sensor together. Finally, the end with the exposed copper was wrapped in electrical tape to prevent spurious signals arising from contact with objects. To reduce noise in the sensor response, an exponential filter was applied to the sensor output, $s_{f,t} = \alpha s_{r,t} + (1-\alpha)s_{f,t-1}$, where $s_{f,t}$ is the filtered response at time t, $s_{r,t}$ is the raw sensor response at time t, and α is the decay rate, which was set $\alpha = 0.8$.

7.2.3 Robotic Skins

The robotic skins, shown in Figure 7.2a, were organized such that they were able to learn the segment dimension. Each robotic skin consisted of two layers of spandex, six capacitive strain sensors and four actuators. Two horizontal sensors in the bottom layer measured the circumference of the underlying cylinder to allow the skin to determine the radius of the system while the other four vertical sensors in the top layer measured the segment length and are aligned as shown in Figure 7.1c.

The sensors were sewn directly onto the spandex fabric. An actuator was ziptied in place over each of the four vertical sensors using a 3D printed actuator attachment (Printrbot Metal Plus).

In order to facilitate testing, snap buttons were incorporated into the skins to allow for quick connection (≈1.5 min) and disconnection (≈0.7 min) from segments (Figure 7.2d-e). The skins themselves were 140.0 mm × 160.1 mm and had muslin reinforcements where the sensor and actuators were attached and where snap buttons were mounted. The button snaps were mounted through both layers of spandex to hold the two layers together and were located underneath all sensor-actuator attachment points and in all four corners of the skin.

7.2.4 Continuum Segments

For the continuum segments, two elastomers with different stiffness properties were used and fabricated such that they could easily connect and disconnect to each other as well as the robotic skins (Figure 7.2d). The segments were molded from Dragon Skin 10 Slow (Smooth On, Inc.) and Smooth-Sil 935 (Smooth-On, Inc.), which have elastic moduli of 265 kPa and 536 kPa, respectively [291]. Male and female end caps were mechanically locked onto either end of the segment by casting the segments with the caps in place so that the elastomer infiltrated the porous body of the caps. The end caps and the molds for the segments were 3D printed with a Form 2 SLA printer (FormLabs). To attach the robotic skin to the elastomer, polystyrene (1.6 mm thick) fabric attachments (Figure 7.2d) were made. These attachments were cut out using a laser cutter (Universal Laser Systems VLS 2.30) and have snap buttons placed on the tabs, which were bent in place by heating the polystyrene and bending the tab over. When assembled with the robotic skin (Figure 7.2e), the tension in the skin holds the fabric attachments securely on the ends of elastomer segment. The ability to rearrange the segments and the skins using the snap buttons made it easy to assemble and disassemble the system for testing.

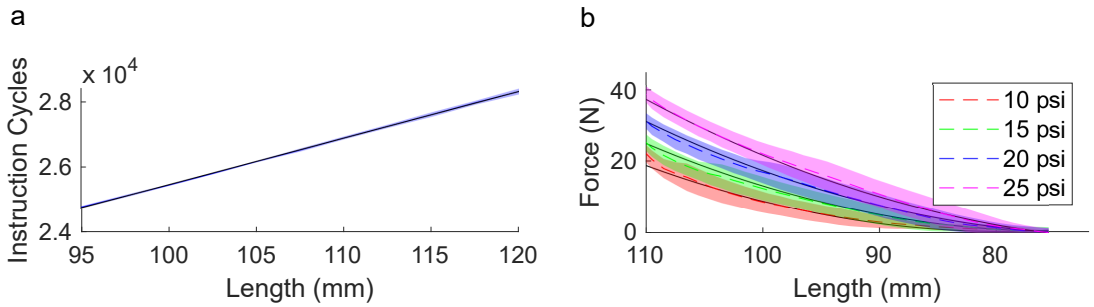

Figure 7.3. Representative plots of (a) sensor and (b) actuator characterization. (a) Sensor characterization relates the sensor length to the sensor response given in instruction cycles. (b) 2D representation of the actuator characterization. The shaded regions represent the 95% confidence interval of the experimental data and the black lines represent the theoretical fits.

7.2.5 Experimental Setup

The robotic skin-elastomer system was attached to a base which held it vertically for experiments (Figure 7.1a). The 3D printed base had a female interlocking mechanism (FormLabs, Form 2) to lock the segment in place. Mortar board was placed over the 3D printed part and clamped in place to stabilize the system. The overall experimental setup was designed to allow the system to be quickly changed for various segments.

A central microcontroller (Arduino Uno) was used to communicate with the skins during operation. This microcontroller used I2C communication to read from and write to the sensor boards and pressure regulators that drive the actuators to a desired pressure [289]. The Arduino Uno relayed all the results to a computer through serial communication to record the system response.

7.3 Characterization

7.3.1 Sensors

The sensors were characterized in a materials testing machine (Instron 3345) after they were integrated into the skin to determine a linear fit for each sensor. The skin was stretched such that the gauge length of the sensor stretched from 95 mm to 120 mm in steps of 2.5 mm; three sensor readings for each sensor were collected at each step. This process was repeated 10 times for a total of 30 data points at each step. The results for each sensor were averaged together and a linear fit, $IC_i = a_{0,i} l_{s,i} + a_{1,i}$, was found for each sensor's response. IC_i refers to the number of instruction cycles corresponding to the discharge time of the ith capacitive sensor within a measurement query and thus, serves as a proxy for the sensor's capacitance. $a_{j,i}$ for $j = 0, 1$ are the parameters of the equation for the ith sensor. A representative plot of the response and fit of a single sensor is provided in Figure 7.3a. Since each sensor is unique, this characterization was performed on each sensor to attain an accurate relationship between length and sensor reading.

7.3.2 Actuators

The actuators were characterized prior to integration to relate the actuator's force response to its length and internal pressure. Each actuator was secured into the materials testing machine at an initial length of 110 mm, inflated to a constant air pressure, and then contracted to 70 mm at a rate of 40 mm/min. This test was performed at several pressures (10, 15, 20, and 25 psi) which were held constant using pressure regulators [289]. The force was then related to both length and pressure to obtain a theoretical surface fit:

$$F_i = b_{0,i} + b_{1,i} p_i + b_{2,i} l_{a,i} + b_{3,i} p_i l_{a,i} + b_{4,i} l_{a,i}^2 \tag{7.3}$$

where F_i is the ith actuator force, p_i is the internal pressure of the ith actuator, $l_{a,i}$ is the ith actuator length (it is assumed that $l_{a,i} \equiv l_{s,i}$ in the model), and $b_{j,i}$ for

Table 7.1. State estimation conditions.

State	p_1 (psi)	p_2 (psi)	p_3 (psi)	p_4 (psi)
1	20	0	0	0
2	0	15	0	0
3	0	15	15	0
4	20	0	0	10
5	0	0	17	0
6	10	0	0	15
7	0	0	0	22

$j = 0, 1, 2, 3, 4$ are parameters for the ith actuator. A representative plot showing the responses and fits of a single actuator is provided in Figure 7.3b. Since each actuator is unique, this characterization was performed on each actuator to attain an accurate relationship between length, pressure, and force.

7.4 Results

7.4.1 State Estimation

State estimation was enabled by the presented model and the actuator characterization. The model was implemented in a MATLAB simulation that predicted the system state (*i.e.*, κ_x and κ_y) given the segment radius, bending stiffness, and actuator pressures. The segment radius was measured from the horizontal sensors using the following equation:

$$r = (l_{s,h} + c + \Delta_{skin})/2\pi \tag{7.4}$$

where $l_{s,h}$ is the average length of the two horizontal sensors, c is the inextensible length of the polystyrene tabs (27.5 mm), and Δ_{skin} is the length the spandex fabric stretched, independent of the sensors. Because the sensors did not wrap all the way around the circumference of the segment, portions of the skin stretched without

being measured by the sensors. For this work, the unobserved stretch was measured manually when needed. Complementing the simulation, the bending stiffness can be found via Equation (7.2) given the actuator characterization results (Equation (7.3)), segment radius, and curvature (*i.e.*, system state). To demonstrate the robustness of this approach, two tests were performed: (1) different segment diameters while holding input pressures constant and (2) different pressure inputs while holding the segment diameter constant.

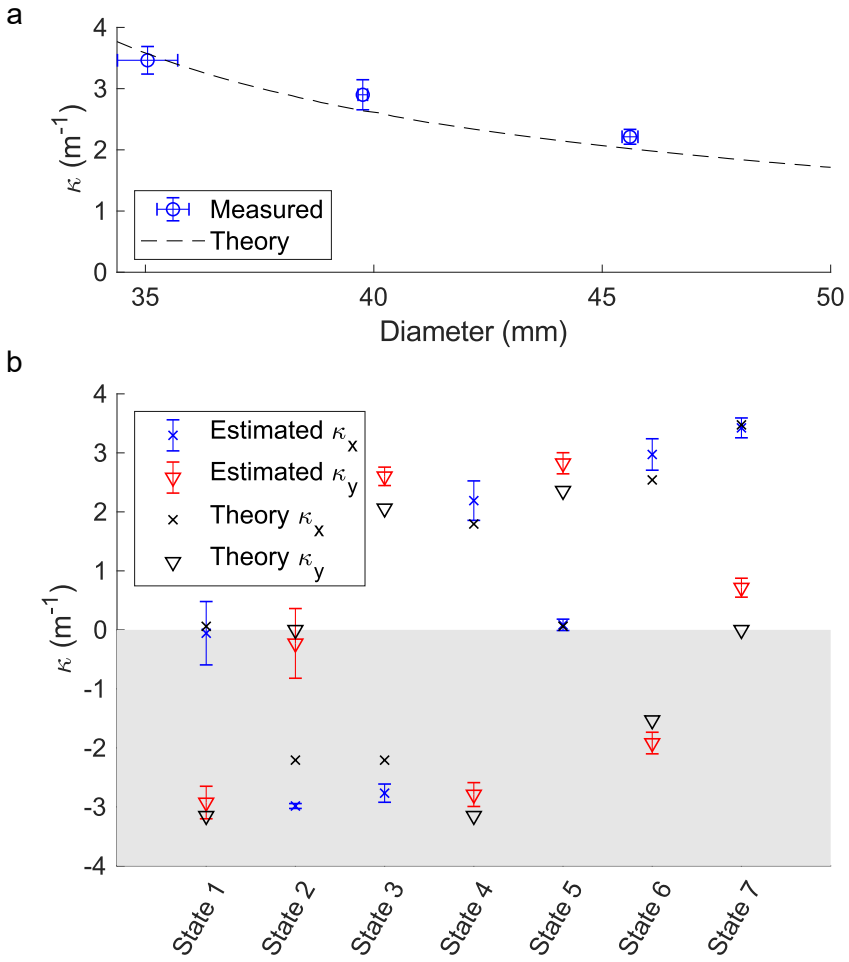

Figure 7.4. (a) Comparison of measured and theoretical segment curvatures across different radii. Additionally, the plot shows the accuracy of the sensor-measured segment diameter. (b) State estimation results for each of the states presented in Table 7.1. The error bars represent the 95% confidence interval.

To demonstrate the skin's adaptability to segments with varying diameters, the skin's theoretical and actual curvature were compared on multiple Dragon Skin 10 Slow segments (35, 40, and 45 mm diameters). A single actuator was set to 22 psi, recorded the horizontal sensor lengths, and captured photos of segment. For the 35, 40, and 45 mm diameter segments, it was found that $\Delta_{skin} = 0, 8, 16$ mm, respectively, which indicates that the stretching skin could be treated as a spring. ImageJ was used to measure the curvature from the images. Figure 7.4a shows how the measured diameters and curvatures compare to the model-predicted curvatures at various diameters. From the measured curvature, the bending stiffness of the different segments was calculated as 56, 82, and 135 kPa for the 35, 40, and 45 mm diameter segments. A linear regression was fit to these values to generate stiffnesses at different segment diameters for the theoretical model. There is good agreement between the measured and theoretical values of curvature.

To verify that the skin's vertical sensors can also be used for state estimation, the state generated by the sensors was compared to the theoretical model. This verification was performed on a Dragon Skin 10 Slow segment across seven actuation states (Table 7.1) each tested 10 times. The segment length was measured with the vertical sensors and the radius with the horizontal sensors ($r = 18.6 \pm 0.6$ mm.). Equation (7.1) requires the segment length to determine the curvatures of the system. Slight variations in the initial segment length can have a large impact on the resulting κ_i calculations, which can result in errors for the state estimation. Thus, unique initial sensor lengths were used ($l_{s,1} = 100.4 \pm 0.3$ mm, $l_{s,2} = 103.3 \pm 0.8$ mm, $l_{s,3} = 101.7 \pm 0.3$ mm, $l_{s,4} = 98.4 \pm 0.4$ mm, with an overall average of $l_{seg} = 100.9 \pm 3.1$ mm) for these curvature calculations depending on which sensors are used for the κ_i calculations. Similar to previous work [291], the state estimation predicted by the sensors required a corrective offset (1.5 m^{-1} for this work) to match the state of the system.

The estimated states, given as κ_x and κ_y, are shown in Figure 7.4b for each state alongside the model-predicted state. The error in curvature did not exceed 0.7 m^{-1},

which is an acceptable level of error for a 2D robotic skin being wrapped around 3D structures. This error can be reduced in the future by improving upon the state estimation model, sensor accuracy, and adaptability of the skin design.

7.4.2 Control

With reasonable state estimation, several control approaches were implemented for the one-segment system to evaluate the efficacy of each. The first approach was feedforward control which uses a model to predict what the inputs (pressures) of the system should be. For this, two feedforward models were considered: a generalized model, which had the bending stiffness supplied, and a learned model, which used a learning sequence in combination with state estimation to determine the bending stiffness of the segment. Additionally, feedback control was explored both on its own and in combination with learned feedforward models. Note that all of these single segment tests were performed with a single robotic skin to demonstrate that a single skin is not characterized for a particular material. The controllers operated at 10 Hz. The performance of each controller is represented by the average error per second (error/s) in Figure 7.5 and the settling times shown in Table 7.2. By analyzing all of these control methods, an appropriate control strategy can be selected for future applications.

Feedforward Control

Because the robotic skins are able to detect material properties from the underlying structures and the constituent components have been thoroughly characterized, an approximate model of the system was developed for feedforward control which predicts what actuator pressures are necessary for a desired state. For a given desired

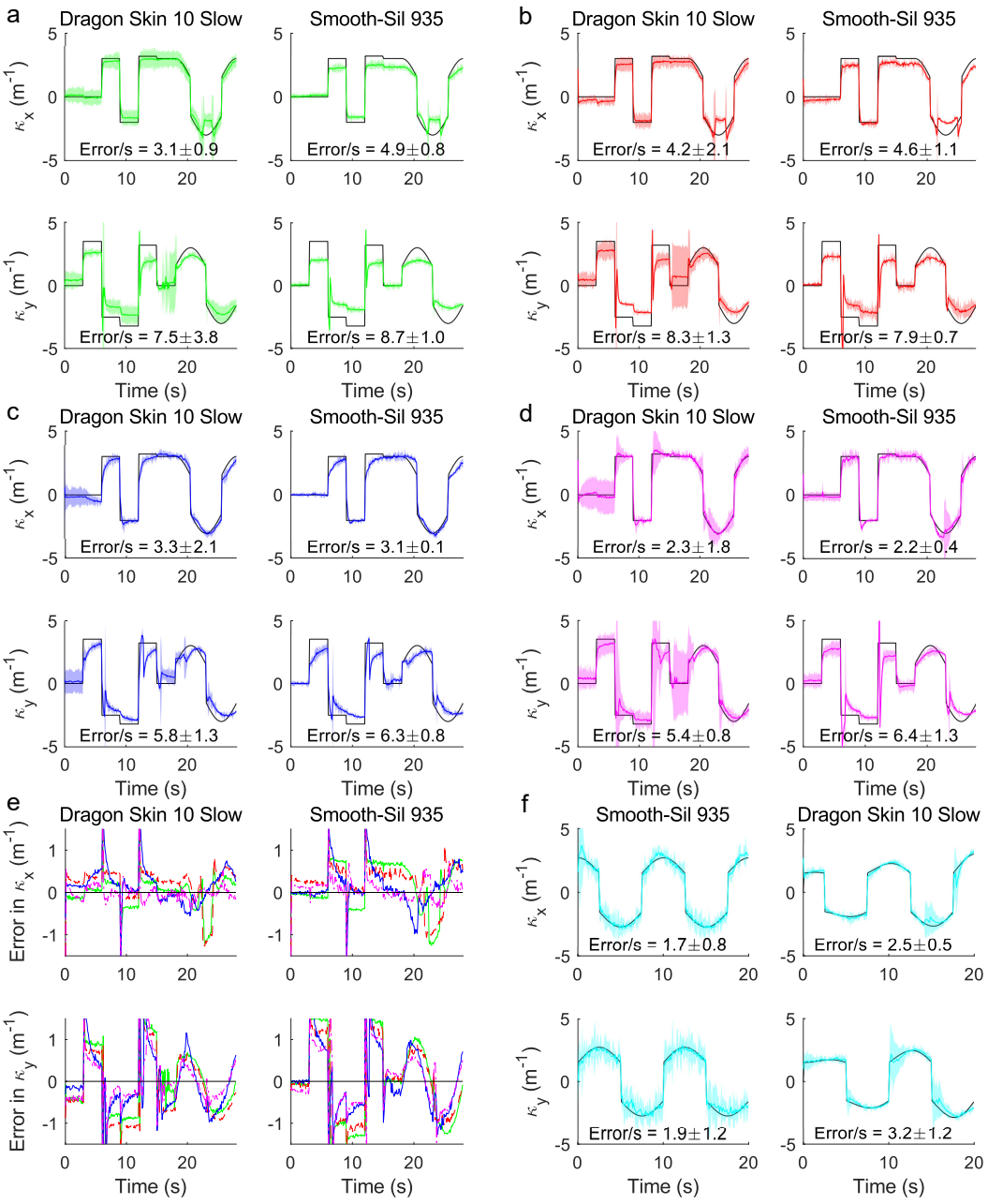

Figure 7.5. Control response using (a) generalized model feedforward control, (b) learned model feedforward control, (c) feedback control, and (d) learned model with feedback control. The average error in control response is shown in (e). The colors in (e) correspond to the controllers in (a)-(d). Control response of two segments is shown in (f). The black line represents $\kappa_{x,des}$ and $\kappa_{y,des}$ while the colored line represents the average system response across three trials. The shaded region represents the 95% confidence interval.

configuration ($\kappa_{x,d}$ and $\kappa_{y,d}$), the actuator pressures should be set as follows from Equation (7.3):

$$p_i = \frac{F_i - b_{0,i} - b_{2,i} l_{a,i} - b_{4,i} l_{a,i}^2}{b_{1,i} + b_{3,i} l_{a,i}} \tag{7.5}$$

where the actuator lengths can be defined as

$$l_{a,1} = l_{seg}(1 + \kappa_{y,d} r) \tag{7.6a}$$

$$l_{a,2} = l_{seg}(1 + \kappa_{x,d} r) \tag{7.6b}$$

$$l_{a,3} = l_{seg}(1 - \kappa_{y,d} r) \tag{7.6c}$$

$$l_{a,4} = l_{seg}(1 - \kappa_{x,d} r) \tag{7.6d}$$

and the forces of the actuators are defined as

$$\text{If } \kappa_{y,d} > 0 : \; F_{a,1} = 0, \; F_{a,3} = \frac{\kappa_{y,d} K_b}{r} \tag{7.7a}$$

$$\text{If } \kappa_{x,d} > 0 : \; F_{a,2} = 0, \; F_{a,4} = \frac{\kappa_{x,d} K_b}{r} \tag{7.7b}$$

$$\text{If } \kappa_{y,d} < 0 : \; F_{a,1} = -\frac{\kappa_{y,d} K_b}{r}, \; F_{a,3} = 0 \tag{7.7c}$$

$$\text{If } \kappa_{x,d} < 0 : \; F_{a,2} = -\frac{\kappa_{x,d} K_b}{r}, \; F_{a,4} = 0 \tag{7.7d}$$

To demonstrate the need for these robotic skins to learn about their underlying material, feedforward control was tested with a generalized model where the bending stiffness was set at $K_b = 60$ kN mm^2 and compared it to a learned model strategy where the stiffness is estimated by the skin ahead of time. Both feedforward models use the learned l_{seg} and r values, which are found immediately when the system is powered, since those are necessary for state estimation. For the learned feedforward model, the stiffness estimation was performed prior to running the controller. Each actuator was sequentially pressurized to 15.0, 18.5, and 22.0 psi. Using the sensors to measure the curvature, a stiffness value was calculated at each condition for a total of 12 stiffness measurements. These measurements were then averaged together to obtain the learned bending stiffness of the system. By allowing the system to learn about the system's behavior *in situ*, the control signal is better tuned to the system, which results in a reduced error.

Table 7.2. Settling time of various control strategies.

	Feedforward	Feedback	Combined
Dragonskin 10 Slow	0.4 ± 0.5 s	1.9 ± 0.6 s	1.0 ± 1.5 s
Smooth-Sil 935	0.4 ± 0.6 s	2.1 ± 1.1 s	1.0 ± 1.8 s

Figure 7.5a shows the results of the generalized model feedforward control for both a Dragon Skin 10 Slow and Smooth-Sil 935 elastomer segment. Here, it can be seen that the feedforward control for the Dragon Skin 10 Slow segment performed well since the generic bending stiffness value was around the bending stiffness for this specific skin-elastomer system. When the feedforward controller with the same generic bending stiffness was applied to a different material (Smooth-Sil 935), the response of the system suffered, as evidenced by the increased error. In contrast, Figure 7.5b shows the system response when the robotic skin learned about its own bending stiffness. The bending stiffnesses were found to be $K_b = 65 \pm 4$ kN mm^2 and $K_b = 105 \pm 7$ kN mm^2 for Dragon Skin 10 Slow and Smooth-Sil 935, respectively. The average error of each response is plotted in Figure 7.5e and this shows the slight improvement in error between the generalized model feedforward (shown in green) and learned model feedforward (shown in red) controllers for the Smooth-Sil 935 segment. For the Dragon Skin 10 Slow segment, the learned feedforward model did not perform as well as the generalized feedforward model due to slight error in the learned stiffness estimation. Overall, the performance of the learned feedforward model is comparable to that of the generalized feedforward model.

Feedback Control

Although the feedforward model showed reasonable accuracy in approximating the system, inaccuracies in the model itself and the input values to the model (*i.e.*, bending stiffness) resulted in non-negligible error between the commanded and achieved

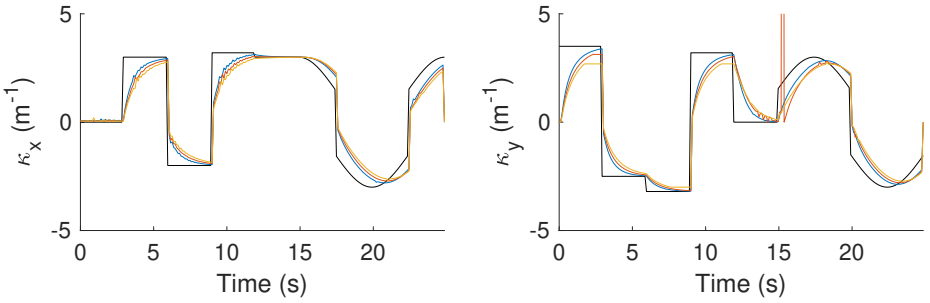

Figure 7.6. Simulation showing how the feedback controller responds to changes in bending stiffness. The black line is the reference while the blue, red, and yellow lines show systems with bending stiffnesses of 60 KN mm^2, 80 kN mm^2, and 100 kN mm^2, respectively.

segment curvatures. Since the robotic skin already has sensors, feedback control was implemented to reduce curvature error by adjusting the actuator pressure. A proportional-derivative (PD) feedback controller was used that applied a change to the pressure based on the error. The controller algorithm is given as

$$\text{If } \kappa_{y,d} > 0: \; p_1 = 0, \; p_3 += k_p(\kappa_{y,d} - \kappa_y) + k_d \frac{\kappa_{y,d} - \kappa_y}{\Delta t} \tag{7.8a}$$

$$\text{If } \kappa_{x,d} > 0: \; p_2 = 0, \; p_4 += k_p(\kappa_{x,d} - \kappa_x) + k_d \frac{\kappa_{x,d} - \kappa_x}{\Delta t} \tag{7.8b}$$

$$\text{If } \kappa_{y,d} < 0: \; p_1 -= k_p(\kappa_{y,d} - \kappa_y) + k_d \frac{\kappa_{y,d} - \kappa_y}{\Delta t}, \; p_3 = 0 \tag{7.8c}$$

$$\text{If } \kappa_{x,d} < 0: \; p_2 -= k_p(\kappa_{x,d} - \kappa_x) + k_d \frac{\kappa_{x,d} - \kappa_x}{\Delta t}, \; p_4 = 0 \tag{7.8d}$$

where k_p and k_d are the proportional and derivative gains and Δt is the change in time.

Here, using only feedback control, shown in Figure 7.5c, was compared to using feedback control alongside the learned feedforward controller, shown in Figure 7.5d. Since the system was entirely modeled, including the actuators, a simulation was built that predicted the system performance given a set of pressure inputs. This simulation was used to tune the feedback controller gains ($k_p = 0.75$ and $k_d = 0.005$), which were kept constant across all the tests regardless of materials, shown in Figure 7.6. For the learned model, the bending stiffnesses were found to be $K_b = 69 \pm 2$ kN mm^2 and $K_b = 100 \pm 5$ kN mm^2 for the Dragon Skin 10 Slow and Smooth-Sil 935 segments,

respectively. The slight variations in the bending stiffness between these and the previous values are due to the fact that the system performs the learning sequence each time the controller is run rather than using a single system learning result across all tests. The average error responses are presented in Figure 7.5e for the feedback (blue) and feedforward and feedback (magenta) controllers. Using only feedback control, the system is controlled well and actually better controlled than the feedforward alone, as seen by the error measurements presented in Figure 7.5. Using a combination of learned model feedforward and feedback, an additional improvement in control of the system can be seen. The settling time of the system is improved due to the feedforward component of the controller, as shown in Table 7.2, while the modeling error is reduced due to the feedback component of the controller.

While there is an advantage in using the combination of feedforward and feedback, this may not be necessary for every application and feedback alone may be sufficient. In scenarios where the system has a slower time response, it would be advantageous to use the combined feedback and feedforward controller, rather than pure feedback, since the feedforward model can be changed to account for the time component of the system.

7.4.3 Multi-segment Control

To demonstrate that this combination of feedback and learned model feedforward control method is expandable to multi-segment continuum robots, a two segment system was assembled with a Dragon Skin 10 Slow segment stacked on top of a Smooth-Sil 935 segment. Each segment was controlled by independent feedforward controllers, and thus, each performed its own characterization to learn about its model consecutively (first the bottom segment, then the top) before beginning the control sequence. The bending stiffnesses were found to be $K_b = 55 \pm 3$ kN mm^2 and $K_b = 140 \pm 10$ kN mm^2 for Dragon Skin 10 Slow and Smooth-Sil 935, respectively. The bottom segment was able to compensate for the additional weight of the top

segment by increasing the bending stiffness estimation for the Smooth-Sil 935 segment. Based on the performance observed in the single-segments tests, the control signal was modified for the two-segment system to keep the desired curvature within the observed limits. The results of this two segment test are shown in Figure 7.5f. From these plots, it is observed that by using this simple learning approach, controller performance is maintained as the system is expanded to multiple segments.

7.5 Conclusion

In this chapter, robotic skins were demonstrated that can be used to learn system parameters to create feedforward models. Additionally, feedforward and feedback controllers were implemented on elastomeric continuum robots. Demonstrations of how different forms of feedforward and feedback control affect system performance were provided. Given highly accurate models, feedforward control can be used alone to control systems. However, in the case of robots created on-the-fly, for example by wrapping robotic skins around arbitrary soft passive bodies, these models may not be available. As such, the efficacy of such on-the-fly robots relies upon the ability to self-characterize or learn system parameters *in situ* for adequate feedforward control. To refine learned feedforward control, robotic skins can simultaneously incorporate feedback to improve overall system performance. The robotic skin-enabled approach presented here allows for greater versatility and deployability of controllable soft robotic systems. Control of these systems can be further improved by applying adaptive control to the feedforward model, and tuning gains of the feedback controller. In conclusion, robotic skins can learn system parameters *in situ* and use the generated feedforward model in tandem with feedback control to effectively transform arbitrary soft passive structures into robots on-the-fly.

8. A GENERALIZED MODEL OF ROBOTIC SKINS FOR DESIGN AND CONTROL OF CONTINUUM ROBOTS

The materials used in soft robotics allow unique deformations that are not easily produced by traditional rigid-bodied robots. By taking advantage of these materials, researchers have been able to produce more life-like deformations and behaviors from soft robots inspired by fish [2] and octopuses [298]. While these demonstrations are impressive, legged soft robots struggle to display the same capability seen in living creatures. Legged biological systems experience continuum deformations throughout the body during locomotion which improves range of motion and efficiency. In contrast, most legged soft robots tend to focus on locomotion driven solely by the legs [277, 299].

Looking to biology, it can be seen that legged vertebrates contain spiralling muscle patterns [263] which enable the spine to assist in locomotion [262]. Spinal-driven locomotion has been studied in rigid-bodied robots inspired by salamanders [300] and snakes [301] as well as in tensegrity robots [302]. When considering spinal-driven locomotion in elastomer-based soft robots, the deformation at the spine tends to be simplified to bi-directional planar bending [56,303], which does not take full advantage of the soft material. A hybrid rigid-soft cheetah-inspired robot demonstrated the use of a cable-driven elastomer-based soft spine capable of bending along two axes [266]. However, this type of spinal bending does not fully capture the complex deformations achievable with spiraling actuation patterns.

By taking advantage of spiraling actuation patterns, spinal-driven locomotion of soft robots should be possible. Utilizing spinal-driven locomotion could increase the functionality of soft robots and reduce the burden of locomotion on the legs, which could lead to more efficient soft robots that require less deformation from any one actuator by taking advantage of a network of actuators throughout the robot.

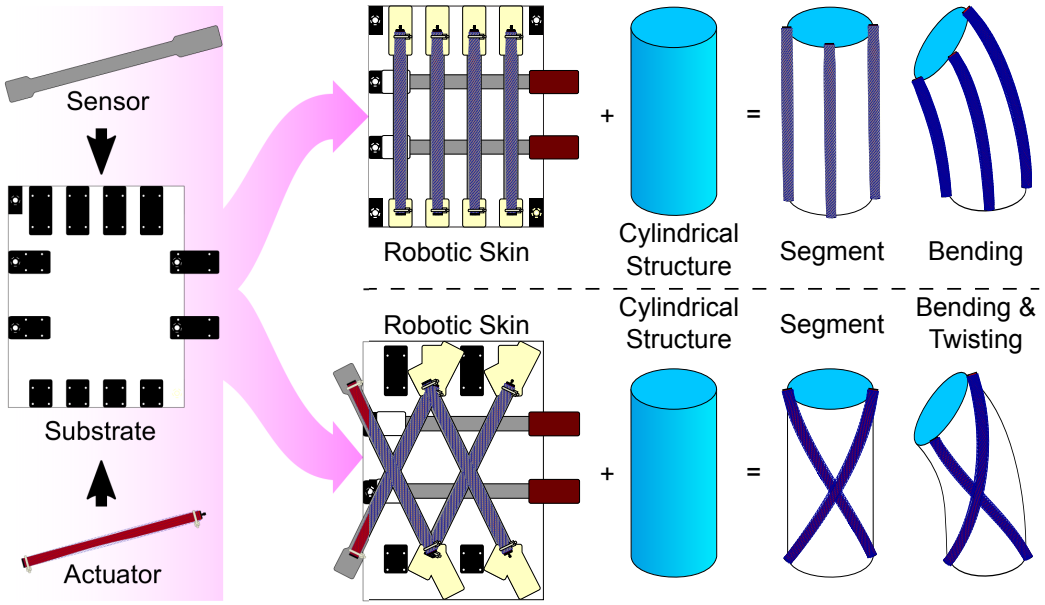

Figure 8.1. Conceptual diagram showing the difference between a skin with sensors and actuators placed parallel to the neutral axis and a skin with sensors and actuators placed on diagonals.

In order to explore this phenomenon of spinal-driven locomotion, a modular and reconfigurable approach was taken through the use of robotic skins [6]. Robotic skins allow assembly of different continuum robots by easily swapping the robotic skin, which contains the actuating and sensing components, from structure-to-structure. This chapter introduces a new model of robotic skins wrapped around cylindrical structures, which relaxes assumptions from previous models [291, 304] presented in Chapters 6-7. This model allows more generalized placement of sensor and actuator elements on the robotic skins, enabling more complex deformations including twisting of cylindrical segments, shown in Figure 8.1. A model-based simulation tool is derived to design the robotic skins and predict behavior of segments made from various robotic skins and cylindrical structures. Further, the model and simulation are validated on a robotic skin with sensors and actuators placed parallel to the neutral axis of the cylindrical structure. Finally, with a model that can handle these complex behaviors, new skins can be designed the enable spinal-driven locomotion. Through

using diagonally-placed actuators which mimic the spiraling muscle patterns found in nature, spinal-driven locomotion of a legged robot is demonstrated.

8.1 Model

For the system of a robotic skin wrapped around a cylindrical structure, Chapters 6-7 focused on relatively simple models that assume a specific actuator placement and a perfect connection between the skin and underlying structure. In this chapter, a holistic approach was taken to analyze how the robotic skins interact with and affect cylindrical underlying structures. For this, the system model was re-defined to allow more generalized sensor and actuator placement, which allowed for the approximation of spiraling actuation patterns, and to allow an imperfect connection between the skin and underlying structure. Additionally, this model acknowledged the forces applied to the cylindrical structure by the sensors and substrate, which was previously unaddressed. It was still assumed that the system exhibits quasi-static behavior and the time component of system behavior was not considered in this chapter.

The complete model consists of two sub-models, a skin model and a segment model, which consists of the cylindrical structure and maps the forces from the skin onto the deformation of the structure. The skin model consists of sub-models for the substrate, actuators, sensors, and the interface between the skin and underlying structure. The segment model consists of the general kinematic deformation and the static mechanics model which uses the forces from the skin model to determine the kinematic deformation. Since more generalized placement of sensors and actuators was allowed, state estimation and controllability of the system are important aspects to consider for new designs and are addressed in this section.

8.1.1 Skin Model

When skins are added to structures, they inherently change the system behavior. In this section, the complete skin model, which includes the substrate, sensors, ac-

tuators, and the interface between the skin and underlying structure, is introduced. While this work focused on how these apply to cylindrical structures, the concepts given here could be expanded to different geometries.

When the skin is applied to a structure, it may require being stretched into place which would apply compressive loading to the structure. However, this stretching onto the structure could improve the contact between the skin and the underlying structure and thus could improve force transduction. To model the compressive loading applied to the structure by the skin, the skin (i.e., the substrate and sensors) was assumed to be thin and plane stress was assumed. The actuators were not considered here since they should be designed such that they do not experience pre-strain. With the plane stress assumption, only forces in the $\mathbf{e}_1$ and $\mathbf{e}_3$ directions were considered. These forces come from strains in the substrate and sensors

$$\mathbf{F}_{skin} = \sum_{j}^{n} \mathbf{F}_{sens.,j,0} + \mathbf{F}_{subs.}, \tag{8.1}$$

where $\mathbf{F}_{skin}$ is the force in the skin due to stretching, $\sum_j^n \mathbf{F}_{sens.,j,0}$ is the summation of sensor forces for n sensors when the sensors are initially strained to fit around a structure, $\mathbf{F}_{subs.}$ is the force of the substrate when it is strained to fit around a structure. The force in the skin can be broken down into directional components, $\mathbf{F}_{skin} \cdot \mathbf{e}_1$ and $\mathbf{F}_{skin} \cdot \mathbf{e}_3$, which are shown in Figure 8.2.

These directional forces seen in the skin as it stretches will apply both axial and radial compression when the skin is wrapped around a cylindrical structure. The axial compression is described as the force $\mathbf{F}_{skin} \cdot \mathbf{e}_3$. The radial compression is better described as a pressure applied to a cylindrical structure, which was found by approximating the skin as a thin-walled pressure vessel and considering hoop stress

$$\sigma_\theta = \frac{P_{skin} r}{t_{skin}} = \frac{\mathbf{F}_{skin} \cdot \mathbf{e}_1}{t_{skin} l_{cyl.}}, \tag{8.2a}$$

$$P_{skin} = \frac{\mathbf{F}_{skin} \cdot \mathbf{e}_1}{r l_{cyl.}}, \tag{8.2b}$$

where σ_θ is the hoop stress, P_{skin} is the pressure applied to the cylindrical structure, r is the radius of the cylindrical structure, t_{skin} is the thickness of the skin, $l_{cyl.}$ is

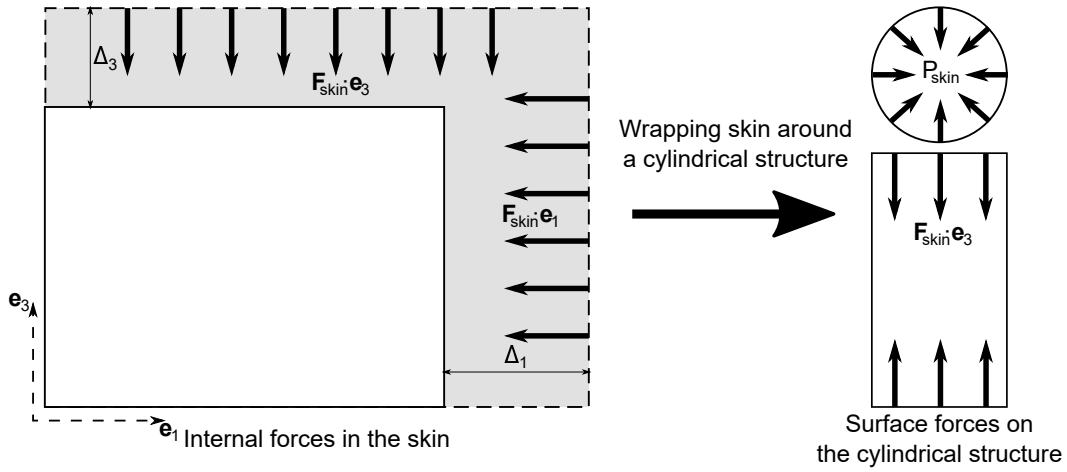

Figure 8.2. Graphical representation of how stretching the skin generates forces and how those forces affect a cylindrical structure it is wrapped around.

the length of the cylindrical segment. For this work, the cylindrical structures were assumed to be incompressible and, thus, this force is negligible, but if the skin was to be applied to a foam structure, this pressure would compress the foam and potentially change the shape of the structure.

Substrate Model. It was assumed that the substrate behaves like an anisotropic, linear material, which means the force generated by the substrate could be simplified as springs. These springs have spring constants that are a function of the directional elastic modulus

$$\boldsymbol{\sigma}_{subs.} = E_{subs.,1}\epsilon_{subs.,1}\mathbf{e}_1 + E_{subs.,3}\epsilon_{subs.,3}\mathbf{e}_3, \tag{8.3a}$$

$$\mathbf{F}_{subs.} \cdot \mathbf{e}_1 = -k_1(E_1, t_{subs.})\Delta_1(l_{subs.}) = -k_1\Delta_1, \tag{8.3b}$$

$$\mathbf{F}_{subs.} \cdot \mathbf{e}_3 = -k_3(E_3, t_{subs.})\Delta_3(w_{subs.}) = -k_3\Delta_3, \tag{8.3c}$$

where $\boldsymbol{\sigma}_{subs.}$ is the planar stress in the substrate, $E_{subs.,i}$ and $\epsilon_{skin,i}$ are the elastic moduli and strains in the $\mathbf{e}_i$ direction, $\mathbf{F}_{subs.}$ is the force in the substrate, k_i and Δ_i is the equivalent spring constant and change in length or width of the substrate in

the $\mathbf{e}_i$ direction, and $t_{subs.}$, $l_{subs.}$, and $w_{subs.}$ are the thickness, length, and width of the substrate.

The stretching that occurs in the substrate changes the stiffness of the skin, which changes the stiffness of the combined substrate-structure segment [304]. Thus, both the substrate and the structure should be considered in the bending stiffness calculation. This stiffness change can be captured empirically

$$K_b = K_{b,struct.} + K_{b,subs.}, \tag{8.4a}$$

$$K_{b,subs.} = a_0\Delta_1 + a_1\Delta_3, \tag{8.4b}$$

where K_b is the bending stiffness of the combined substrate-structure, $K_{b,struct.}$ is the bending stiffness of the structure (e.g., $K_{b,struct.} = EI$ for a homogeneous cylindrical segment where E is the elastic modulus and I is the second moment of inertia), $K_{b,subs.}$ is the contribution to bending stiffness due to the substrate, and a_i for $i = 0, 1$ are empirically-derived constants. The bending stiffness of the substrate is influenced by the substrate choice. It should be noted that the bending stiffness of the substrate only influences the bending stiffness of the system if it has been strained into place. In this work, the skins were designed such that the substates were not strained and this phenomenon was not observed. The force transduction was completed through the use of designed attachments between the skin and the cylindrical structures. However, in design of future skins that eliminate this attachment method for a truer skin-like design that requires stretching to achieve good force transduction, this phenomenon is an important consideration [304].

Actuator Model. Although this work focused on McKibben actuators, the model as a whole is viable for other linearly extending or contracting actuators as long as the actuator model is changed for that specific actuator. There are numerous models that describe McKibben actuators [305–309]. For this work, two different models were used: the Chou and Hannaford McKibben model (during the design phase) [305] and a polynomial fit (during physical experiments) [304]. Both of these models were used since they have different advantages and disadvantages. The Chou and Hannaford

model allows the McKibben actuators to change in simulations for design purposes (such as initial length and braiding parameters), but overestimates force outputs from the actuators. In contrast, the polynomial fit more accurately maps the measured force output of an actuator, but must be done for each actuator, which is not easily integrated into a design simulation. A comparison between these two actuator models is given in Appendix C.

The Chou and Hannaford McKibben actuator model [290, 305] is described as

$$F_{act.,k} = \frac{\pi D_k^2 P_{act.,k}}{4}\left(\frac{3(1-\varepsilon_k)^2}{\tan^2\theta_{k,0}} - \frac{1}{\sin^2\theta_{k,0}}\right), \tag{8.5}$$

where $F_{act.,k}$ is the force of the kth McKibben actuator, $P_{act.,k}$ is the kth actuator internal pressure, D_k is the diameter of the mesh braid, ε_k is the strain ($\varepsilon_k = 1 - l_{act.,k}/l_{act.,k,0}$ where $l_{act.,k}$ is the kth actuator length and $l_{act.,k,0}$ is the unactuated length), and $\theta_{k,0}$ is the unactuated fiber angle.

Our polynomial fit is described as [304]

$$F_{act.,k} = c_0 + c_1 P_{act.,k} + c_2 l_{act.,k} + c_3 P_{act.,k} l_{act.,k} + c_4 l_{act.,k}^2 \tag{8.6}$$

where c_i for $i = 0, 1, ..., 4$ are empirically-derived constants creating a unique description for each actuator.

Sensor Model. As the sensors stretch and deform with the skin and structure, they generate their own forces which affect the behavior of the system. Since the sensors can ungergo large strains, they experience nonlinear stress-strain curves, which can be captured using hyperelastic material models, and plastic deformation. To capture the force-displacement behavior of these sensors, the empirically-derived Ogden material model [214] was used along side an empirically-derived model to capture the plastic deformation seen in our sensors. The force-displacement model is captured by

$$F_{sen,j} = \begin{cases} wt(1-\delta)^2 \sum_{i=1}^{N} \mu_i \left[\lambda^{\alpha_i - 1} - \frac{1}{3}(2\lambda^{-(1+\alpha_i)/2} + \lambda^{1+\alpha_i})\lambda^{-2}\right] & \text{if } l_{sen} \geq l_{sen,0} \\ 0 & \text{if } l_{sen} < l_{sen,0} \end{cases}, \tag{8.7a}$$

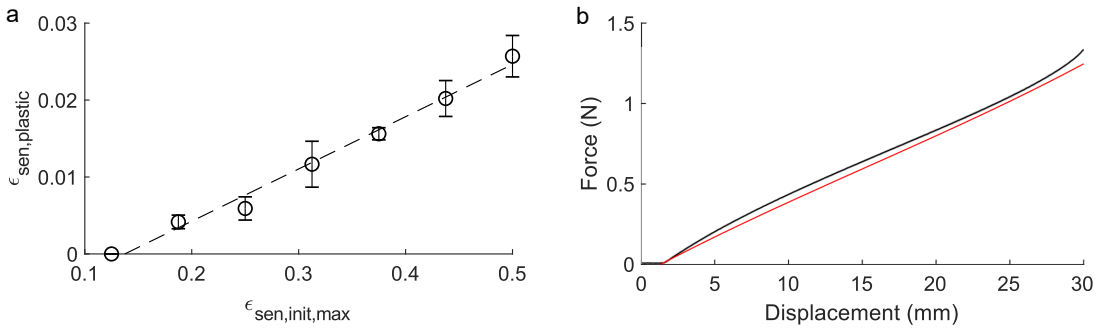

Figure 8.3. (a) The relationship between the strain seen in the initial sensor length and the strain from plastic deformation. (b) Experimental force versus displacement sensor data (shown in black) compared to the theoretical model (shown in red) that accounts for the plastic deformation.

$$\delta = 1 - \lambda^{-\nu}, \tag{8.7b}$$

$$\lambda = 1 + \frac{l_{sen} - l_{sen,0}}{l_{sen,0}}, \tag{8.7c}$$

$$l_{sen,0} = l_{sen,init} + l_{sen,plastic}, \tag{8.7d}$$

where $F_{sen,j}$ is the jth sensor force due to strain, w is the sensor width, t is the sensor thickness, N is the number of terms for the Ogden model, l_{sen} is the strained sensor length, $l_{sen,0}$ is the unstrained sensor length after it has been pre-strained to account for plastic deformation, $l_{sen,init}$ is the initial designed sensor length, and $l_{sen,plastic}$ is the change in length due to plastic deformation. To determine the Ogden model, the model was fit to experimental data from a sensor that was strained 60 mm/min for 12 cycles with a materials testing machine (Instron 3345). A three parameter ($N = 3$) Ogden model was used with a fit of $\mu_1 = 2960$, $\mu_2 = 50200$, $\mu_3 = 75700$, $\alpha_1 = 7.88$, $\alpha_2 = 0.689$, and $\alpha_3 = 0.689$.

To explore the plastic deformation, a sensor with $l_{sen,init} = 80$ mm was cyclically strained in a materials testing machine (Instron 3345) to several deflections (10-40 mm at 5 mm intervals) at a rate of 50 mm/min. The sensor was cycled seven times at each deflection before progressing to the next deflection. The first two cycles of the seven were discarded to eliminate response due to the Mullin's effect [22, 86]. During

these cycles, the sensor's force response plateaued as it approaches the initial designed sensor length (see Appendix C). This plateau was indicative of plastic deformation in the sensor, which buckled as it returned to the original sensor length, and hence experienced no load. By exploring how this plastic deformation changed as the sensor was stretched to higher deflections, an empirical model of the plastic deformation was found. The strain of the initial designed sensor length can be mapped to the strain of plastic deformation, as shown in Figure 8.3a. This mapping is approximately linear,

$$l_{sen,plastic} = \epsilon_{sen,plastic} l_{sen,init}, \tag{8.8a}$$

$$\epsilon_{sen,plastic} = \begin{cases} d_0 \epsilon_{sen,init,max} + d_1 & \epsilon_{sen,init,max} > -d_1/d_0 \\ 0 & \epsilon_{sen,init,max} \leq -d_1/d_0 \end{cases}, \tag{8.8b}$$

where $\epsilon_{sen,init,max}$ is the maximum strain of the sensor taken from the initial sensor length and d_i for $i = 0, 1$ are constants. Using the experimental data, the constants were found to be $d_0 = 0.0679$ and $d_1 = -0.0093$.

The Ogden material model was combined with the plastic deformation model to create a complete sensor force model. This model was compared to experimental data from the sensor that was strained 60 mm/min for 12 cycles with a materials testing machine (Instron 3345). There was good agreement in the force-displacement estimation of the model and the experimental data, shown in Figure 8.3b. Thus, this model was a valid approximation of the force from the sensors.

Additionally, this sensor model could be used to determine what the sensor length should be designed if the desired natural length ($l_{sen,des,0}$) and the maximum sensor length ($l_{sen,max}$), which it will be stretched to before being incorporated into a skin, is known

$$l_{sen,init} = \frac{l_{sen,des,0} - d_0 l_{sen,max}}{1 - d_0 + d_1}. \tag{8.9}$$

Skin-Underlying Structure Interface Model. The connection between the skin and the deformable body is not perfect. The forces from the sensors and actuators

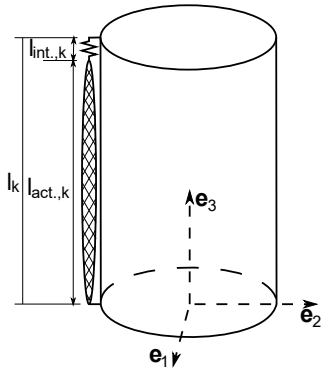

Figure 8.4. Example of the skin-structure interface.

cause internal deformations in the robotic skins at the attachment points. To account for these effects, a virtual interface element was introduced between the ideal representation of the body and the model of the actuator.

This interface was modeled with a linear spring element of the form

$$l_{int} = k_{int}^{-1} F, \tag{8.10}$$

where l_{int} is the length of the interface spring (assumed to be zero when no force is applied), k_{int} is the stiffness of the interface, and F is the force transmitted through the interface.

The interface element creates an unobserved state in the system. The sensors are mechanically coupled to the actuators, and so their observed length is equal to the length of the actuators ($l_{act} = l_{sen}$), which suggests the need for an observer.

From the perspective of the cylindrical structure, the total length along the side of the deformed body is the sum of the actuator and interface length

$$l = l_{act} + l_{int} = l_{act} + k_{int}^{-1} F. \tag{8.11}$$

An example of this skin-structure interface connected to an actuator is shown in Figure 8.4.

8.1.2 Segment Model

Since the segments were made from cylindrical structures, the deformation and mechanics model can be built upon existing literature [33]. This work is similar in nature to continuum robots that have generalized tendon placement. While a model exists to describe generalized tendon placement of continuum robots [295], this model uses Cosserat rods, which assume that the system is made of long slender segments. Since the cylindrical structures used in this system cannot be described as long, slender segments, alternative ways were sought to describe the deformation and mechanics of the system. Although the best derivation of the mechanics come from continuum mechanics principles and utilizes stress fields, a simplified analytical solution was preferred that could model the system well enough without requiring solutions for stress fields. This simplified analytical solution assumes that the principles of superposition apply and that there are point forces.

Kinematic Deformation

Before getting into the kinematics of the deformation, the description of the segment must be discussed. Each segment was composed of an elastomeric cylindrical structure that had two rigid end caps that allowed it to easily connect to other segments, similar to the method described in [304]. Coordinate systems were applied along the length of the cylindrical structure, as shown in Figure 8.5, such that the rigid end caps as well as the elastomeric cylindrical structure of the segment could be easily referenced. To simplify the description of the entire segment, homogeneous transformations were used to describe the deformation of the whole structure. Using homogeneous transformations also simplified describing the deformation of a multi-segment system. Additionally, in this section, the shape the sensors and actuators take when the skin is placed on a cylindrical structure is discussed.

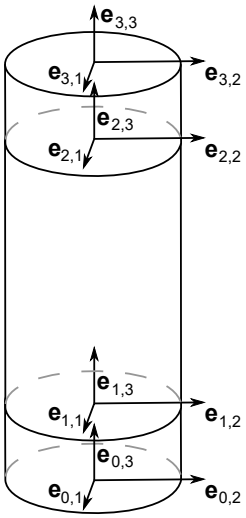

Figure 8.5. Representation of the coordinate frames placed along the cylindrical structure. The coordinate frames can be read as $\mathbf{e}_{i,j}$ where $i = 0, 1, 2, 3$ refers to the ith coordinate frame along the cylindrical structure and $j = 1, 2, 3$ refers to the direction in the given coordinate frame.

End caps. Since the end caps were rigid and were assumed to remain undeformed, the transformation to describe moving from the 0th coordinate frame to the 1st coordinate frame and the 2nd coordinate frame to the 3rd coordinate frame is described simply with

$$ {}^{0}\mathbf{T}_{1} = {}^{2}\mathbf{T}_{3} = \begin{bmatrix} 1 & 0 & 0 & 0 \\ 0 & 1 & 0 & 0 \\ 0 & 0 & 1 & l_{cap} \\ 0 & 0 & 0 & 1 \end{bmatrix}, \tag{8.12} $$

where ${}^{0}\mathbf{T}_{1}$ and ${}^{2}\mathbf{T}_{3}$ are the homogeneous transformations for the end caps on either end of the cylindrical structure and l_{cap} is the length of the end cap.

Cylindrical Structure Deformation. For the deformation of the elastomeric cylindrical structure, piecewise constant curvature is assumed and external forces were neglected. There are a number of models that derive the kinematics of continuum robot under the piecewise constant curvature assumption [33]; however, these

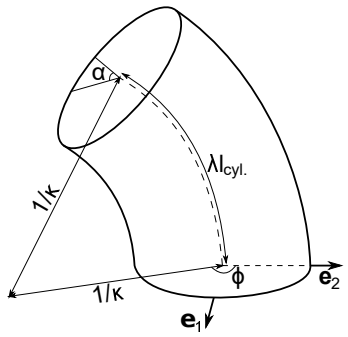

Figure 8.6. General model showing the state of the system.

models assume that the actuators are parallel to the neutral axis of the robot. Since a generalized model was desired for the system with actuators that can curve around the central structure, the existing models were adapted to include a twisting component. Thus, the state of the system can be described as $\mathbf{q} = \{\kappa, \phi, \lambda, \alpha\}^T = \{\kappa_{\mathbf{e}_1}, \kappa_{\mathbf{e}_2}, \lambda, \alpha\}^T$, shown in Figure 8.6, where $\kappa = \sqrt{\kappa_{\mathbf{e}_1}^2 + \kappa_{\mathbf{e}_2}^2}$ and $\phi = \tan^{-1}(\kappa_{\mathbf{e}_2}/\kappa_{\mathbf{e}_1})$. Here, κ is the curvature, ϕ is the angular offset of the curvature, $\kappa_{\mathbf{e}_1}$ is the curvature with respect to the $\mathbf{e}_1$-axis, $\kappa_{\mathbf{e}_2}$ is the curvature with respect to the $\mathbf{e}_2$-axis, λ is the stretch, and α is the angular twist seen by the neutral axis.

The homogeneous transformation from [33] was adapted to accommodate the new state definition. To capture the behavior of generalized actuator placement, the system was assumed to compress and bend according to the model given in [33] and then twist with respect to the original $\mathbf{e}_3$-axis, such that

$$ {}^1\mathbf{T}_2 = \begin{bmatrix} c_\phi v_\theta c_{\alpha+\phi} + c_\alpha & c_\phi v_\theta s_{\alpha+\phi} - s_\alpha c_\theta & s_\theta c_{\alpha+\phi} & -\kappa^{-1} v_\theta c_{\alpha+\phi} \\ c_\phi v_\theta s_{\alpha+\phi} + s_\alpha & -c_\phi v_\theta c_{\alpha+\phi} + c_\alpha c_\theta & s_\theta s_{\alpha+\phi} & -\kappa^{-1} v_\theta s_{\alpha+\phi} \\ -c_\phi s_\theta & -s_\phi s_\theta & c_\theta & \kappa^{-1} s_\theta \\ 0 & 0 & 0 & 1 \end{bmatrix}, \tag{8.13} $$

where ${}^1\mathbf{T}_2$ is the homogeneous transformation describing the system deformation, $c_x = \cos(x)$, $c_{x+y} = \cos(x+y)$, $s_x = \sin(x)$, $s_{x+y} = \sin(x+y)$, $v_x = c_x - 1$, $\theta = \kappa s$ is the angle of curvature, $s = \lambda l_{cyl.}$ is the deformed length of the cylindrical structure, and $l_{cyl.}$ is the initial length of the cylindrical structure.

Single Segment Deformation. In order to get the total deformation of a single segment, the transforms from the end caps and cylindrical structure were combined together,

$$
\begin{aligned}
{}^{0}\mathbf{T}_{3} &= {}^{0}\mathbf{T}_{1}\,{}^{1}\mathbf{T}_{2}\,{}^{2}\mathbf{T}_{3}, \\
&= \begin{bmatrix}
c_{\phi}v_{\theta}c_{\alpha+\phi} + c_{\alpha} & c_{\phi}v_{\theta}s_{\alpha+\phi} - s_{\alpha}c_{\theta} & s_{\theta}c_{\alpha+\phi} & -\kappa^{-1}v_{\theta}c_{\alpha+\phi} + s_{\theta}c_{\alpha+\phi}l_{cap} \\
c_{\phi}v_{\theta}s_{\alpha+\phi} + s_{\alpha} & -c_{\phi}v_{\theta}c_{\alpha+\phi} + c_{\alpha}c_{\theta} & s_{\theta}s_{\alpha+\phi} & -\kappa^{-1}v_{\theta}s_{\alpha+\phi} + s_{\theta}s_{\alpha+\phi}l_{cap} \\
-c_{\phi}s_{\theta} & -s_{\phi}s_{\theta} & c_{\theta} & \kappa^{-1}s_{\theta} + (1+c_{\theta})l_{cap} \\
0 & 0 & 0 & 1
\end{bmatrix}.
\end{aligned}
\tag{8.14}
$$

Multi-segment System. In order to describe the behavior of a multi-segment system, let ${}^{0}\mathbf{T}_{3} = {}^{0}\mathbf{A}_{1}$. The transformation of a two-segment system was determined via

$$
{}^{0}\mathbf{A}_{2} = {}^{0}\mathbf{A}_{1}\,{}^{1}\mathbf{A}_{2}, \tag{8.15}
$$

where ${}^{i-1}\mathbf{A}_{i}$ defines the total transformation of a single cylindrical section and has a $\mathbf{q}_{i-1} = \{\kappa_{\mathbf{e}_1,i-1}, \kappa_{\mathbf{e}_2,i-1}, \lambda_{i-1}, \alpha_{i-1}\}^{T}$ defining the ${}^{1}\mathbf{T}_{2}$ deformation given in Equation (8.13) for each segment.

Actuator and Sensor Mapping onto Cylindrical Structure. With the cylindrical structure well-defined, the definition of how actuators and sensors attach was defined. It was assumed that the actuators and sensors wrap around the cylindrical structure when the skin is applied, and, thus, the actuator and sensor paths were described with space curves. For example, an actuator that wraps around a cylinder with a radius of r and length of $l_{cyl.}$ and starts at 0° and wraps clockwise around the entire length of the cylinder to -90°, shown in Figure 8.7a, will have a space curve defined by

$$
\mathbf{R}_{act.,ex.}(s) = \left\{ r\cos\left(\frac{-\pi}{2l_{cyl.}}s\right), r\sin\left(\frac{-\pi}{2l_{cyl.}}s\right), s \right\}^{T}, \quad s \in [0, l_{cyl.}]. \tag{8.16}
$$

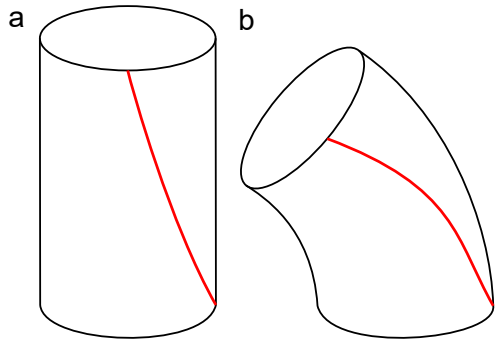

Figure 8.7. Representation of how the sensor and actuator length changes from (a) an initial configuration to (b) a deformed configuration.

A more generalized actuator definition can be made as

$$\mathbf{R}_{act.,gen.}(s) = \left\{r\cos\left(\beta_0 s + \beta_1\right), r\sin\left(\beta_0 s + \beta_1\right), s\right\}^T, \quad s \in [l_{start}, l_{end}], \tag{8.17}$$

where β_i for $i = 0, 1$ are constants defining the placement of the actuator along circumference of the cylindrical structure and l_{start} and l_{end} are define the placement of the actuator along the neutral axis. For this work, $l_{start} = 0$ and $l_{end} = l_{cyl.}$ for all the actuators and sensors. Additionally, the robotic skins used here assumed that sensors are placed alongside the actuators in sensor-actuator pairs. However, sensors could also be defined independently in the same manner of the actuator,

$$\mathbf{R}_{sen.,gen.}(s) = \left\{r\cos\left(\beta_0 s + \beta_1\right), r\sin\left(\beta_0 s + \beta_1\right), s\right\}^T, \quad s \in [l_{start}, l_{end}]. \tag{8.18}$$

While sensors and actuators can technically be placed anywhere, it is important to choose their locations such that the system is observable and controllable. This is discussed later.

Static Mechanics Model

For the static mechanics model, a mapping was needed between the forces from the actuators, sensors, and weight of the system and the kinematic deformation

described previously. For the ith segment in a multi-segment system, which has $\mathbf{q}_i = \{\kappa_{i,\mathbf{e}_1}, \kappa_{i,\mathbf{e}_2}, \lambda_i, \alpha_i\}^T$, this mapping can be described as

$$\kappa_{i,\mathbf{e}_1} = \frac{1}{K_{b,i}}\mathbf{M}_i \cdot \mathbf{e}_2, \tag{8.19a}$$

$$\kappa_{i,\mathbf{e}_2} = -\frac{1}{K_{b,i}}\mathbf{M}_i \cdot \mathbf{e}_1, \tag{8.19b}$$

$$\lambda_i = 1 - \frac{1}{K_{a,i}}\mathbf{F}_i \cdot \mathbf{e}_3, \tag{8.19c}$$

$$\alpha_i = -\frac{l_{cyl.}}{K_{t,i}}\mathbf{M}_i \cdot \mathbf{e}_3, \tag{8.19d}$$

where $K_{b,i}$ is bending stiffness of the ith segment, $K_{a,i}$ is axial stiffness of the ith segment, $K_{t,i}$ is torsional stiffness of the ith segment, $\mathbf{M}_i$ is the moment on the ith segment, and $\mathbf{F}_i$ is the force on the ith segment.

These forces and moments were defined by forces generated by the skins and the weight of the system as a whole. Previously these forces have been described as coming from the substrate, actuators, and sensors. For the substrate, only the force in the $\mathbf{e}_3$-direction, described by Equation (8.3c), is considered since the other force due to the substrate is applied as pressure on the cylindrical segment. When discussing the actuator and sensor forces, described in Equations (8.5)- (8.6) and (8.7), respectively, the magnitude of the forces were discussed, but not direction.

Actuator and Sensor Forces. The directions of the actuators and sensors were found using the previously defined space curves in Equations (8.17) and (8.18). These forces can be defined fully as

$$\mathbf{F}_{act.,k} = -F_{act.,k}\frac{\mathbf{R}'_{act.,k}(l_{end})}{\|\mathbf{R}'_{act.,k}(l_{end})\|}, \tag{8.20a}$$

$$\mathbf{F}_{sen.,j} = -F_{sen.,j}\frac{\mathbf{R}'_{sen.,j}(l_{end})}{\|\mathbf{R}'_{sen.,j}(l_{end})\|}. \tag{8.20b}$$

Segment Weight. The weight of cylindrical structure-skin system was described as

$$\begin{Bmatrix} \mathbf{W}_i \\ 0 \end{Bmatrix} = ({}^0\mathbf{A}_i)^{-1} \begin{Bmatrix} \mathbf{w}_i \\ 0 \end{Bmatrix} m_i g = \boldsymbol{\omega}_i m_i g, \tag{8.21}$$

where m_i is the mass of the ith cylindrical structure-skin system, g is the gravitational constant, and $\mathbf{w}_i$ is a unit vector describing the direction of gravity in the global coordinate frame. The moment arm for the weight, which spans from the origin of the $\mathbf{e}_{i,0}$ coordinate frame for the ith segment to the center of the mass of the cylindrical structure-skin system, is given by $\mathbf{d}_i$.

Single Segment Resultant Force and Moment. For a single segment, one end of the segment is fixed and the other end is free. For a system that has n segments, one end of the 0th segment is fixed and one end of the nth segment is free, while the other ends of the segments are connected to each other. Looking at the last segment, the sum of forces and moments was found to be

$$\mathbf{F}_n = -m_n g \boldsymbol{\omega}_n - \sum_{k=0}^{m-1} \mathbf{F}_{act.,k,n} - \sum_{j=0}^{q-1} \mathbf{F}_{sen.,j,n} + \mathbf{F}_{subs.,n} \cdot \mathbf{e}_3, \tag{8.22a}$$

$$\mathbf{M}_n = -m_n g(\mathbf{d}_n \times \boldsymbol{\omega}_n) - \sum_{k=0}^{m-1} (\mathbf{l}_{act.,k,n} \times \mathbf{F}_{act.,k,n}) - \sum_{j=0}^{q-1} (\mathbf{l}_{sen.,j,n} \times \mathbf{F}_{sen.,j,n}), \tag{8.22b}$$

where $\mathbf{F}_n$ and $\mathbf{M}_n$ are the reaction forces and moments of the nth segment, m is the number of actuators, q is the number of sensors, $\mathbf{l}_{act.,k,n}$ is the moment arm to the kth actuator, and $\mathbf{l}_{sen.,j,n}$ is the moment arm to the jth sensor.

Multi-segment System Resultant Forces and Moments. Adding multiple segments required an expanded form of the model. This was done easily by transferring the reaction forces and moments along the length of system. For an arbitrary ith segment where $i = 0, .., n-1$, the reaction forces and moments were found to be

$$\mathbf{F}_i = - m_i g \boldsymbol{\omega}_i - \sum_{k=0}^{m} \mathbf{F}_{act.,k,i} - \sum_{j=0}^{q-1} \mathbf{F}_{sen.,j,i} + \mathbf{F}_{subs.,i} \cdot \mathbf{e}_3 + \mathbf{F}_{i+1,adj}, \tag{8.23a}$$

$$\begin{aligned} \mathbf{M}_i = &- m_i g(\mathbf{d}_i \times \boldsymbol{\omega}_i) - \sum_{k=0}^{m-1} (\mathbf{l}_{act.,k,i} \times \mathbf{F}_{act.,k,i}) - \sum_{j=0}^{q-1} (\mathbf{l}_{sen.,j,i} \times \mathbf{F}_{sen.,j,i}) ... \\ &+ \mathbf{M}_{i+1,adj} + (\mathbf{l}_i \times \mathbf{F}_{i+1,adj}), \end{aligned} \tag{8.23b}$$

where $\mathbf{l}_i$ is the vector that goes from the center of the $\mathbf{e}_{i,0}$ coordinate frame to the center of the $\mathbf{e}_{i,3}$ coordinate frame for the ith segment. We have adjusted values for some variables that are defined as follows

$$\begin{Bmatrix} \mathbf{F}_{i+1,adj} \\ 0 \end{Bmatrix} = {}^{i}A_{i+1} \begin{Bmatrix} \mathbf{F}_{i+1} \\ 0 \end{Bmatrix}, \tag{8.24a}$$

$$\begin{Bmatrix} \mathbf{M}_{i+1,adj} \\ 0 \end{Bmatrix} = {}^{i}A_{i+1} \begin{Bmatrix} \mathbf{M}_{i+1} \\ 0 \end{Bmatrix}. \tag{8.24b}$$

8.1.3 State Estimation Model

To determine the state estimation of the system, a mapping was needed from the sensor lengths to the state of the system. To do this, an understanding of how the sensor path deforms when the system deforms was required. This was captured for both the actuators and sensors via

$$\mathbf{r}_{act.,gen.}(s) = {}^{1}\mathbf{T}_2 \begin{Bmatrix} \mathbf{R}_{act.,gen.}(s) \\ 0 \end{Bmatrix}, \tag{8.25a}$$

$$\mathbf{r}_{sen.,gen.}(s) = {}^{1}\mathbf{T}_2 \begin{Bmatrix} \mathbf{R}_{sen.,gen.}(s) \\ 0 \end{Bmatrix}, \tag{8.25b}$$

where $\mathbf{r}_{act.,gen.}(s)$ and $\mathbf{r}_{sen.,gen.}(s)$ are the deformed paths of the actuators and sensors. Figure 8.7 shows an illustration of how the deformation changes the path of a sensor or actuator from its undeformed configuration.

The length of these paths were found via

$$l_j = \int_{l_{start}}^{l_{end}} \|\mathbf{r}'_{sen.,j}(s)\| ds. \tag{8.26}$$

This length of the path, however, is not purely due to the sensor length, since the sensor is affected by the skin-underlying structure interface. Thus, the actual sensor length is given by

$$l_{sen.,j} = l_j - l_{int}. \tag{8.27}$$

These lengths, which are functions of the state can then be used to reconstruct the state. However, since the sensors can be placed anywhere, it is important to ensure that the state of the system is observable. To get an observability matrix, a time-dependent model is required. Time-dependent models could be formulated with or without inertial effect. If inertial effects are neglected, there are several ways to model the time-dependent behavior. One approach is to obtain an approximation of the dynamics of the system by taking partials with respect to time of each state. A more realistic and complete approach would be to include inertial effect, flow rates in and out of the actuators, and material loss. One could then simulate the complete model or neglect the inertial terms if they are deemed to have little effect on the response. Taking the initial approach, the change in moments, forces, and pressures could be modeled as ramp functions between time steps, such that their derivatives would result in Heaviside step-functions.

8.1.4 Stiffness Estimation Model

To estimate the stiffness of the segment, the state estimation and proper characterization of the actuators were required. Equation (8.19) is then used to back out the various stiffness values as

$$K_{b,i} = \frac{\mathbf{M}_i \cdot (\mathbf{e}_2 - \mathbf{e}_1)}{\kappa_{i,\mathbf{e}_1} + \kappa_{i,\mathbf{e}_2}}, \tag{8.28a}$$

$$K_{a,i} = \frac{\mathbf{F}_i \cdot \mathbf{e}_3}{1 - \lambda_i}, \tag{8.28b}$$

$$K_{t,i} = \frac{-l_{cyl.}(\mathbf{M}_i \cdot \mathbf{e}_3)}{\alpha_i}. \tag{8.28c}$$

8.1.5 Controls Model

For an approximate feedfoward control model, the model was solved to provide appropriate pressure for the actuators to achieve a desired state. Since there is no time component of the model, this feedforward control model functions more as a look-up table rather than a true time-dependent control model. The pressure could

be found via Equations (8.5) and (8.6) (depending on which model is used for the actuator),

$$P_{act.,k} = \frac{4\pi n_{fiber,k}^2 F_{act.,k}}{3l_{act.,k}^2 - b_k^2}, \tag{8.29a}$$

$$P_{act.,k} = \frac{F_{act.,k} - c_0 - c_2 l_{act.,k} - c_4 l_{act.,k}^2}{c_1 + c_3 l_{act.,k}}. \tag{8.29b}$$

These equations show that the actuator lengths and forces are required in order to predict pressure. Both of these values are dependent on the desired state. The lengths of the actuators can be found similar to the lengths of the sensors,

$$l_{act.,k} = \int_{l_{start}}^{l_{end}} \|\mathbf{r}'_{act.,k}(s)\| ds - l_{int}. \tag{8.30}$$

The actuator forces must be determined from static mechanics model described in Section 8.1.2. Since the actuators can be placed anywhere on the system, it is important to consider which states of the system are controllable. For example, if an actuator is placed on an angle, there will be coupling between all the states. This could result in a limitation of the desired states the system is able to reach. By taking one of the two approaches described previously for developing a time dependent model, the controllability of the system could be determined.

8.2 Design Considerations

While some design considerations have been touched upon, such as the pre-strain in the substrate and sensors which can change system behavior, there are additional design considerations for robotic skins. Ideally, the system can achieve large deformations without buckling. Increasing the achievable deformation can be done by reducing the radius of the cylindrical structure or reducing the elastic modulus of the cylindrical structure. However, "softening" the system in these manners reduces the force required to buckle the system. Because the skin applies a compressive axial force on the cylindrical structure, this can mean that if the system is too soft, the cylindrical structure can buckle under the force of the skin. Additionally, a multi-segment

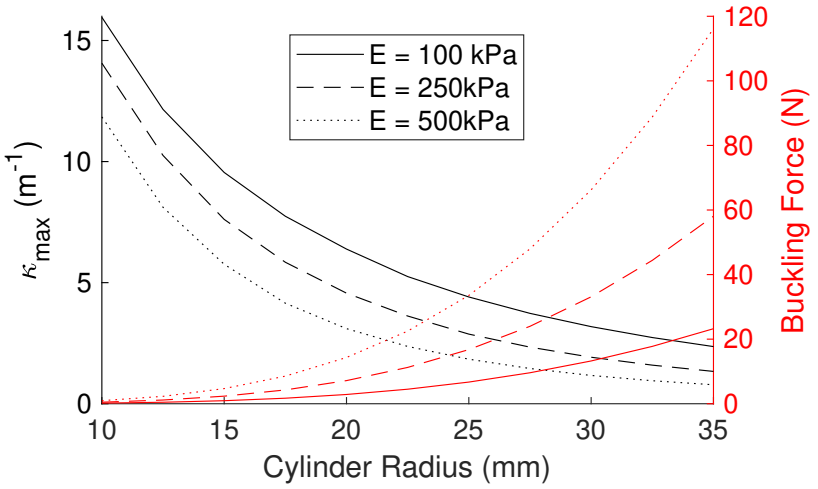

Figure 8.8. Results from a simulation of a cylinder with $l_{cyl.} = 100$ mm, a single parallel actuator on the skin ($l_{act.} = 120$ mm and $P_{act.} = 25$ psi), no gravitation effects, and no stiffness increase due to the skin to highlight the interplay between curvature and buckling force in terms of cylinder radius and elastic modulus.

system can buckle under the weight other segments; this is often why continuum arms, especially those made of elastomers, are suspended upside-down or are put in water, which will minimize the effects of gravity. To test for the buckling of the cylindrical structure, Timoshenko beam theory [310], which is better at modeling the buckling of thicker beams than Euler-Bernoulli beam theory, was used. For a beam with a fixed and free end, the buckling force was found using [311]

$$F_{buckling} = \frac{\frac{\pi^2 EI}{4l_0^2}}{1 + \frac{\pi^2 EI}{4K_s GAl_0^2}} \tag{8.31}$$

where $K_s = 6(1+\nu)/(7+6\nu)$ is the shear correction factor for a circular cross-section [312], ν is Poisson's ratio ($\nu = 0.5$ for rubber-like materials), $G = E/(2+2\nu)$ is the shear modulus, and A is the cross-sectional area. The buckling force is affected by the segment's radius, length, and elastic modulus. From this equation, it can be seen that reducing the segment's radius and elastic modulus or lengthening the segment lowers the buckling force of the segment significantly. A balance needs to be struck in the "softness" of the structure, such that it is soft enough to achieve large

deformations, but not so soft that the system is unstable. This concept is shown in Figure 8.8.

8.3 Simulation

A simulation of this model was written in C++ to facilitate with the design and testing of skins, both for this work and for future skins. With this in mind, the simulation was designed to be modular allowing users high control over the design of skins. The simulation utilizes classes called actuator, sensor, interface, substrate, robotic skin, end cap, cylindrical structure, segment, and whole system. In this section, the structural design of the simulation code, shown in Figure 8.9, is explained as well as what each class does with respect to the whole simulation. During the rest of this chapter, when work is referencing results from the model, this simulation was utilized to obtain those results.

8.3.1 Actuator Class

The actuator class contains the models for the McKibben actuators. It can either run the theoretical model or the empirically-derived model. A user needs to supply the constants for the empirically-derived model if that is being used since the constants are initialized to zero in order to prevent the wrong constants being used. For both models, the user can change the pressure and current length of the actuator. This ability to change the current length of the actuator is removed when this class is embedded in the simulation since the length of the actuator is determined by the physics of the model. For the theoretical model, the user can change the initial angle of the braid and the braid diameter. Changing any of these variables will automatically cause the class to recalculate the force generated by the actuator.

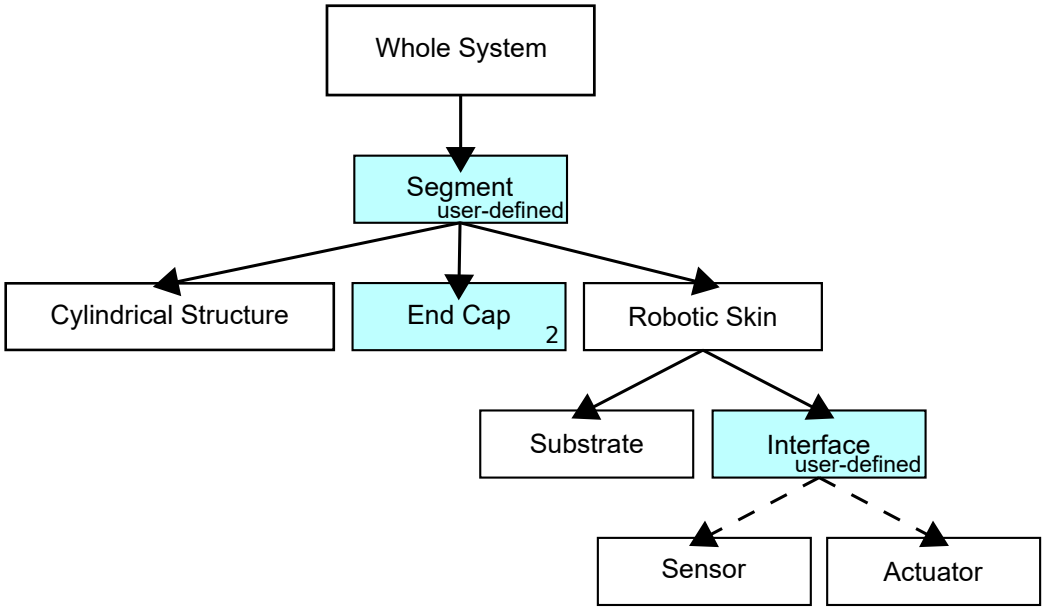

Figure 8.9. Structural design of the simulation code for building a continuum robot made from cylindrical structures and robotic skins. Each block represents a class and the blue blocks indicate a vector of that class. The length of the vector is given in the lower right corner of the block.

8.3.2 Sensor Class

The sensor class contains the full model for the sensors which helps to determine the force generated by straining the sensors. The class contains the plastic constants and Ogden model mentioned previously, but the user could change these if they wanted to use a different sensor material. Additionally, the user can change the sensor width, thickness, initial length, Poisson ratio, maximum length experienced by the sensor, and current length of the sensor. Once again, the ability to change the current length of the sensor is removed when this class is embedded in the simulation since the length of the sensor is determined by the physics of the model. Similar to the actuator class, changing these variables will automatically recalculate the plastic deformation of the sensor and force generated by the sensor.

8.3.3 Interface Class

The interface class acts as an intermediary between the sensor and actuator classes and the robotic skin class. This class contains the model for the skin-underlying structure interface. The interface class can have either an actuator, a sensor, or an actuator-sensor pair. This class also contains the attachment constants from Equations (8.17-8.18) that determine the placement of the actuator/sensor on the skin. This class takes control over changing sensor and actuator lengths and bonds the two together if they are part of an actuator-sensor pair. It can also calculate the magnitude of the force as well as the direction of the force since the constants for the attachment onto the skin are contained in this class. Although, calculating the force vector requires a radius and length is provided to simulate a cylindrical structure; this information is provided automatically in the simulation. The user can change the spring constant and the length of the sensor/actuator. Once again, this ability to change the length of the sensor/actuator is removed when the class is embedded in the simulation. When the length is changed, the force from the sensor/actuator is automatically recalculated.

8.3.4 Substrate Class

The substrate class contains the model of the substrate. To get meaningful force data from this class, the user must supply the appropriate spring constants for the substrate. To get meaningful bending stiffness changes from this class, the user must supply appropriate stiffness constants. The user can change the initial length and width of the substrate as well as the current length and width of the substrate. Changing these values will cause the class to automatically recalculate the force vector and bending stiffness due to the skin. The ability to change the current length and width is removed once the class is embedded in the simulation since the length and width will be determined by the cylindrical structure it is wrapped around.

8.3.5 Robotic Skin Class

The robotic skin class acts as an intermediary between the segment and the substrate and interface class. The robotic skin contains a single substrate and a vector of interfaces whose length is determined by the user when the class is constructed. During the construction of this class, the user also needs to provide the attachment constants for the interfaces as well as if that interface contains an actuator, a sensor, or both. This fully defines the design of the robotic skin. Note that this class does not combine the force vectors from the substrate and interface classes. Rather, the forces from the substrate and interfaces are considered separately in the segment class.

8.3.6 End Cap Class

The end cap class contains the transform for the end caps on either end of the cylindrical structure. The user can change the length of the end cap. Doing so will recalculate the transform of the end cap.

8.3.7 Cylindrical Structure Class

The cylindrical structure class contains the model of the cylindrical element, such as the state of the element and the transform of that state. The user can change both an outer radius and an inner radius of the element if they want a hollow element. In this work, the elements are not hollow, so the inner radius is set to zero, but the option is available if needed. The user can also change the length, elastic modulus, and Poisson ratio of the structure. The class automatically recalculates bending, axial, and torsional stiffnesses of the structure as well as the buckling force. Note that this class does not calculate the state, it simply is where the state is stored for the simulation.

8.3.8 Segment Class

The segment class contains the majority of the physics of the model. It consists of a cylindrical structure class, a robotic skin class, and an array of two end cap classes, for each end cap on either side of the cylindrical structure. While the end caps for this work are designed to be identical on either end, the user technically has independent control of these end caps in case they choose to use two different end caps. When constructing the segment class, the user must define the number of interfaces used on the robotic skin, the attachment constants, and whether an actuator, a sensor, or an actuator-sensor pair is attached for each interface. This information is then used in the construction of the embedded robotic skin class. The segment class also contains the mass, gravitational acceleration, the direction of gravity, and the reactionary force and moment vectors. During initialization, the skin is stretched onto the cylindrical structure using the length and circumference of the cylindrical structure and then the stiffnesses of the system are recalculated taking into account both the cylindrical structure and the substrate.

The segment class contains functions that optimize for the state given pressure inputs for the actuators and that optimize for pressure given a desired state. An example block diagram of a segment that contains a single actuator-sensor pair is shown in Figure 8.10. This block diagram is easily extendable to segments with multiple interfaces. To optimize for state, the pressures must be input into the actuators before running the function that optimizes state since it is easier to select the appropriate actuator and change it rather than providing a vector or array to change all the pressures at once. To optimize for pressure, the desired state is given as an input into the function that optimizes pressure. For the function that optimizes pressure, the system is not immediately moved to the desired state because the state requested may not be achievable by the robotic skin; therefore, it starts at the current pressure and evolves the pressures in the actuators to achieve the desired state or as close to the desired state that is possible for the segment. To determine the state from the

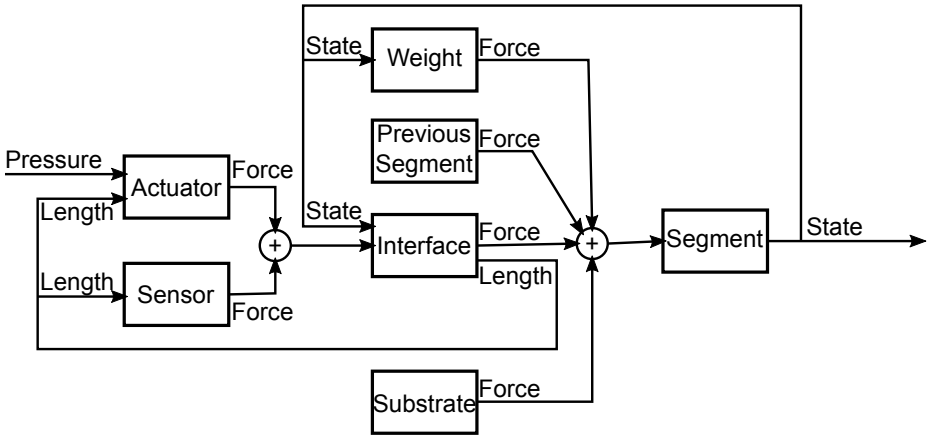

Figure 8.10. Example of a segment block diagram with one sensor and actuator pair.

pressures, the force and moment vectors are calculated from the weight of the segment, the forces from the interfaces (which contain the actuator and sensor forces), the compressive force from the skin, and the force and moment from a previous segment (which needs to be provided by the user). Then Equation (8.19) is used to predict the state of the system given those inputs. This prediction is used to move the current state closer in line to the predicted state. Moving directly to the predicted state causes issues because the predicted state, especially from the neutral state of $\mathbf{q} = \{0, 0, 1, 0\}^T$, is inaccurate due to large force estimations from the actuators and can lead the entire system to oscillate between extreme states, which may become unstable or never settle, or to have the segment twist over on itself and "break." Taking small steps in optimizing both for state and pressure allow both of these functions to settle appropriately.

During these optimization methods, additional work balancing the lengths related to the interface classes occur. This is necessary since both the sensor and actuator change in force as their length changes. As the force increases, the length of the interface increases, which will decrease the length of the actuator and sensor, which decreases their force. Fortunately, this is a relatively easy force balance for the simulation.

The segment class can be used by itself to run tests on individual segments since it contains all the necessary information to fully define a segment.

8.3.9 Whole System Class

The whole system class allows for the creation of multi-segment continuum robots. To initialize this class, the user must provide a vector of segments and the global gravity direction. The vector of segments can be constructed in two methods. In the first method, a single segment can be made and added repeatedly to a vector until the vector contains the desired number of segments. This can then be used to construct the whole system class and the segments can be edited from the whole system class to the desired segment. This however, is impractical if segments are intended to have a different number of interfaces since the number of interfaces need to be defined during the construction of the segment. In the second method, each segment is constructed individually and then added to a vector in sequence. This is then used to constructed a fully defined system without the need of altering it afterwards. Both methods work, but the second method of pre-defining the segments allows for more variety of systems.

Similar to the segment class, the whole system can be optimized for either state given pressure inputs or for pressure given desired state inputs. The whole system class takes care of adjusting weight vectors as segments are deformed and providing the segment class with the force and moment from previous segments. While this is necessary for multi-segment systems, this is very convenient for working with individual segments as well.

8.4 Fabrication and Characterization

To test the generalized actuator and sensor placement model, two skin types were designed: a parallel skin, which is similar to the designs presented in previous works [6,291,304] and allows the system to bend, and a new twisting skin, that places

the actuators and sensors at angles to allow the system to bend and twist. Two of each type of skin were fabricated. Additionally, cylindrical structures were manufactured using three elastomers with varying stiffnesses. To design the cylindrical segments and skins used in this work, a simulation was made from the model and used to determine various system parameters. This analysis can be found in Appendix C. Lastly, robotic skins must be placed on the cylindrical structures and actuated at known pressures to determine the skin-underlying structure interface spring constant.

8.4.1 Robotic Skin Fabrication and Characterization

The skin consists of three separate components that need to be fabricated and characterized separately: the substrate, actuators, and sensors. The details of these individual fabrication and characterizations are provided in Appendix C. This section focuses on the integration of these individual components.

The substrate, actuators, and sensors were integrated into two types of robotic skins: parallel and twisting. Both of these skins utilize a spandex substrate, four actuators, and six sensors (two that measure the circumference of the underlying structure and four that can be used for state estimation running along the length of cylindrical structures). The skins have dovetail-shaped fabric attachments sewn onto their back end to allow them to quickly attach to and detach from the cylindrical structures, which have corresponding dovetail-shaped slots. The skins also have actuator attachments sewn over the sensors in order to attach the actuators via zipties. Both the fabric attachments and the actuator attachments were 3D printed with an SLA printer (FormLabs 2). Additionally, these skins have iron-on fabric reinforcments where the sensors and fabric attachments are sewn onto the substrate.

The parallel skins were designed similar to the previous work presented in Chapter 7. However, the two layer approach significantly increased the stiffness of the skin, so a single layer was used in this work. While there is coupling between sensors if they are read as fast as possible, putting a delay in reading sensors, such as 10 ms,

makes this coupling vanish. The parallel skin design is shown in Figure 8.11a. This skin has four button snaps on the edges to close the skin after it is wrapped around a cylindrical structure.

The twisting skins have a more complex design with the actuators and sensors running in two "X"-shapes around the skin. This design is shown in Figure 8.11b in which the skin has been flattened to be easier to understand. In a fully assembled skin, the sensor and actuator pairs with green and blue dots are wrapped around to the other side of the skin to line up with the green and blue dots found on the actuator attachments. The fabric attachments are located underneath the actuator attachments and the black iron-on reinforcements on either end of the skin. These locations match the parallel skin and allows the twisting skins to be applied to the same cylindrical structures as the parallel skins. There are two button snaps located with each horizontal sensor. The two ends of the skin were sewn together and thus it needs to be stretched over the cylindrical segment rather than being able to be wrapped around like the parallel skin.

8.4.2 Cylindrical Structure Fabrication

The cylindrical structures were designed and fabricated similar to the segments presented in the last chapter. Molds were 3D printed to manufacture cylindrical structures with a radius of 15 mm and a length of 100 mm. The end caps were resized to fit this new diameter and lengthened to allow room for the sensor boards when segments are stacked together. This work utilizes three cylindrical structures: Dragonskin 10 Slow ($E = 265$ kPa, Smooth-On, Inc.), Smooth-Sil 936 ($E = 536$ kPa, Smooth-On, Inc.), and EcoFlex 00-50 (unknown elastic modulus, Smooth-On, Inc.). While the EcoFlex 00-50 elastic modulus has not been measured, it is not necessary for this work since the model can be used to approximate the stiffness. EcoFlex 00-50 is, however, softer than Dragonskin 10 Slow and, thus, should have a lower elastic modulus.

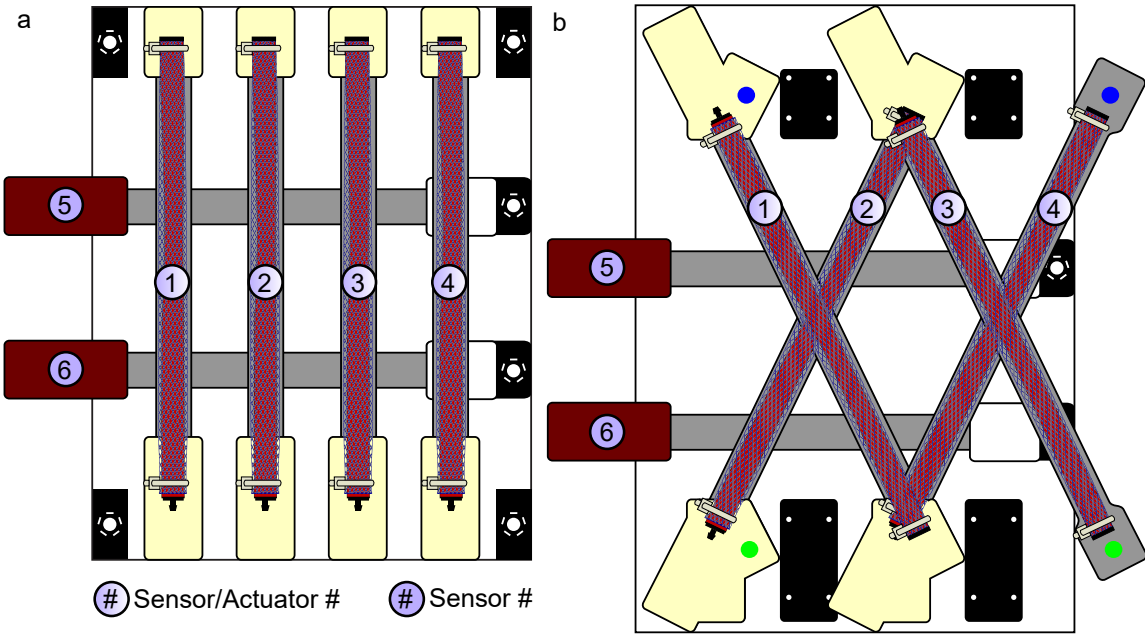

Figure 8.11. Basic layout for the (a) parallel skin and (b) twisting skin. The actuators and sensors are labeled for reference.

For this work, dovetail-shaped slots were made in the end caps to allow the skin to quickly attach and detach from the cylindrical structures rather than using the button snaps and polystyrene attachments or the adhesive gel shown in the previous chapters.

8.4.3 Skin-Underlying Structure Interface Characterization

To characterize the skin-underlying structure, experimental data was collected on the Dragonskin 10 Slow cylindrical structure with the parallel skin 1 to determine how much curvature is achieved under various pressure conditions (10-25 psi applied to actuator 1 in steps of 2.5 psi). The experimental data relating pressure to curvature was measured from three photos of the system at each pressure value in ImageJ. This experimental data was compared to the model response of this simulated system. To get the model response to match the experimental data, the skin-underlying structure interface spring constant was tuned to be 650 N/m. The results of this is shown in

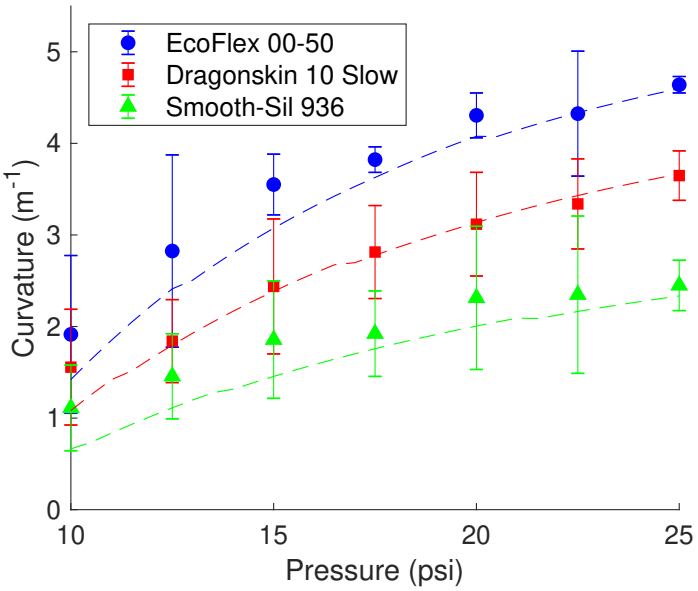

Figure 8.12. Experimental data (shown as markers with error bars) and model response (shown as dashed lines) for curvature response at different pressures. The error bars represent the 95% confidence interval.

red in Figure 8.12. The model is within the error bars at 10 psi, but matches fairly closely for the remaining pressure values.

8.5 Results

The results demonstrated for this work include: testing the model performance on the other two cylindrical structures (using parallel skin 1), simulating feedforward control performance (using parallel skin 1), and demonstrating a multi-segment legged robot that is driven by spine locomotion (using the two twisting skins). This demonstrates the abilities of the model and simulation as well as the usefulness of having off-parallel actuator placement that enables new capabilities for the robotic skins.

8.5.1 Model Response on Different Cylindrical Structures

The skin was calibrated using experimental results from Dragonskin 10 Slow. However, this skin should be able to transfer from structure-to-structure while maintaining its calibration. To test the transferability of a skin from structure-to-structure, the model response was compared to pressure-curvature data of the Smooth-Sil 936 cylindrical structure because the elastic modulus was known. For this comparison, the simulation maintained the same skin as defined by the calibration collected from the various characterizations and only the elastic modulus of the cylindrical structure was changed. The result from this test is shown in green in Figure 8.12. The model response does not fit as well as it did for the Dragonskin 10 Slow cylindrical structure, but is still a reasonable estimation of the performance, which provides confidence that the skin can be calibrated on a single structure and then that same calibration can be used on other structures.

Finally, the simulation was used to approximate the elastic modulus of the EcoFlex 00-50 cylindrical structure. The model response was compared to experimental data from EcoFlex 00-50 and the elastic modulus of the cylindrical structure was tuned to match the experimental response, shown in blue in Figure 8.12. Through tuning, the elastic modulus of EcoFlex 00-50 was found to be approximately 165 kPa. These tests demonstrate the reliability of the model to more fully capture the behavior of the system than the prior models, which did not account for gravity and sensor forces as well as the interface interaction.

8.5.2 Simulation of Feedforward Control and Experimental Validation

With the simulation matching the experimental data well, the simulation was used to test feedforward control. The behavior of the feedforward control is dependent both on the elastic modulus of the cylindrical segment as well as the robotic skin. To test feedforward control, several reference traces were used: (1) a circular spiral, (2) a square spiral, and (3) an infinity sign spiral. These reference signals were

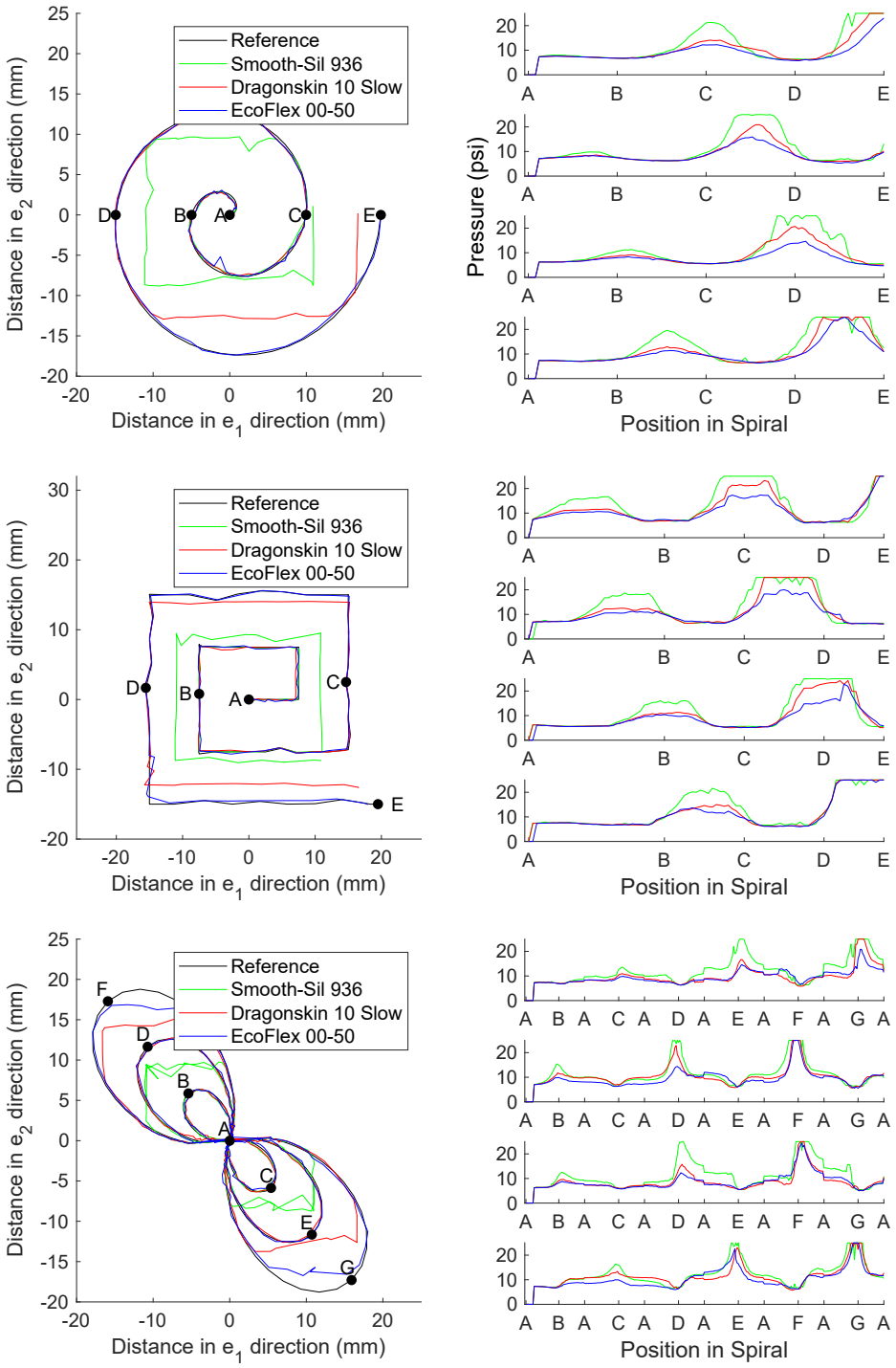

Figure 8.13. Simulated feedforward control having the cylindrical structures trace various spiral pattern. The corresponding pressures as the structures move through the spiral are provided on the right. The plots show the pressure in Actuator 1-4 from top to bottom.

designed such that the center of the top of the elastomeric cylindrical structure maps out the desired reference signal. The circular spiral follows the trace mapped out by $\kappa \in [0, 4]$ m^{-1} and $\phi \in [0, 4\pi]$. The other two reference signals were found by determining the state required to reach the desired end point position. Using the characterization of parallel skin 1 and each cylindrical structure, the simulation used the functionality that optimizes pressure to determine the pressure required in the actuators to achieve the desired position given by the reference signals. The results from these simulations are shown in Figure 8.13. Figure 8.13 shows that the simulation predicts the maximum achievable curvature for each segment. Looking at the pressure graphs in Figure 8.13, it can be seen that these points in the spiral graph correspond to moments when the pressure in actuators are maxed out and the system is unable to bend further. The pressure plots also show a quick jump to approximately 6-7 psi. This pressure jump occurs because the empirical model does not see a measurable change in force until that pressure is reached.

To validate that the predicted behavior from the simulation matched the behavior of a physical system, the spiral reference signal was tested on the three different segments using the corresponding to the circular spiral reference signal. The predicted pressures from the simulation were applied to the appropriate actuators and the top of the cylindrical structure was tracked. The results from this experiment is shown in Figure 8.14. Comparing the simulation results (Figure 8.13) to the experimental results (Figure 8.14), it can be seen that the behavior between the experimental results match well to the predicted behavior from the simulation, which further demonstrates the functionality of the model and simulation. The robotic skin model and simulation can be calibrated from experimental data and then be used to predict behavior on multiple segments. This ability to predict behavior allows the simulation to be used as a testbed for a quasi-static approximate feedforward control strategy and could be further improved by including time-dependency into the model and simulation, which would provide the ability to test various controllers and observe system behavior via

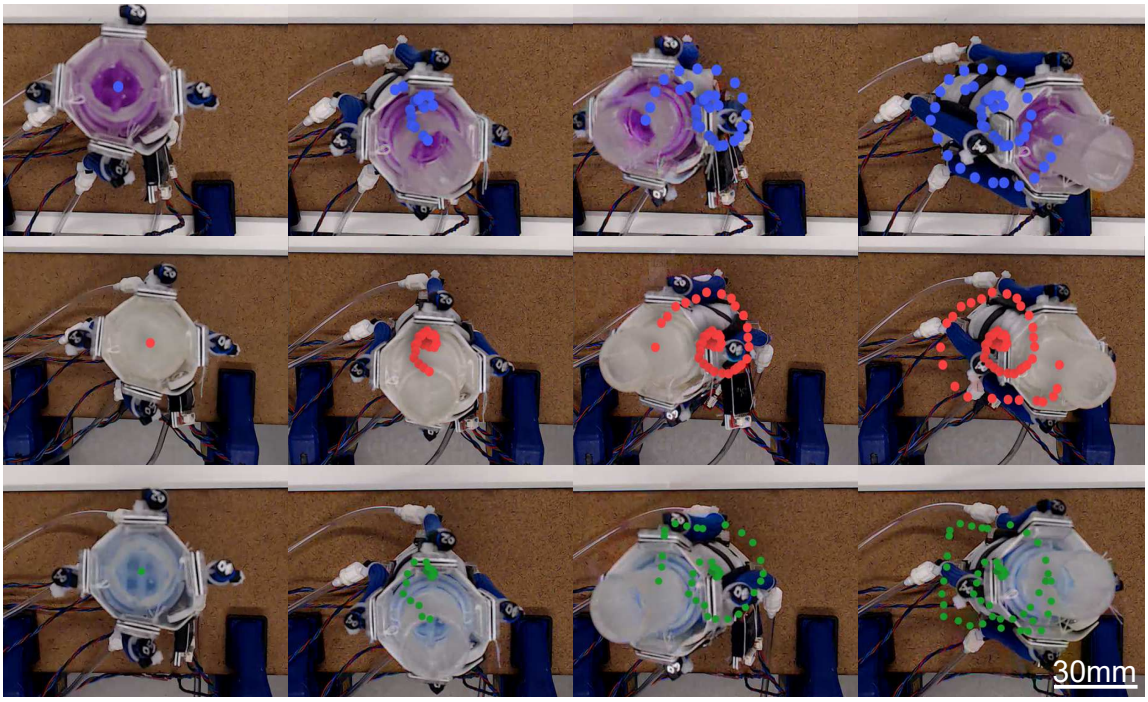

Figure 8.14. Experimental results applying the simulated feedforward pressures for the circular spiral reference signal to physical systems. The segments are (top row) EcoFlex 00-50, (middle row) Dragonskin 10 Slow, and (bottom row) Smooth-Sil 936.

simulation. Having a good testbed would allow for new designs and configurations to be tested without requiring the fabrication of a physical system.

8.5.3 Spinal Locomotion of a Legged Robot

With the above continuum model and simulation tools created and tested, it is possible to design a legged robot with spinal-driven locomotion. This more complex bending and twisting motion is easily captured by the more generalized model, thereby allowing predictable motion of actuators placed in such a manner that they spiral around the body. A legged robot was fabricated using the two twisting skins placed on EcoFlex 00-50 cylindrical structures. Compliant copper wire legs were applied on either end of the continuum robot and in between the two segments. This leg design

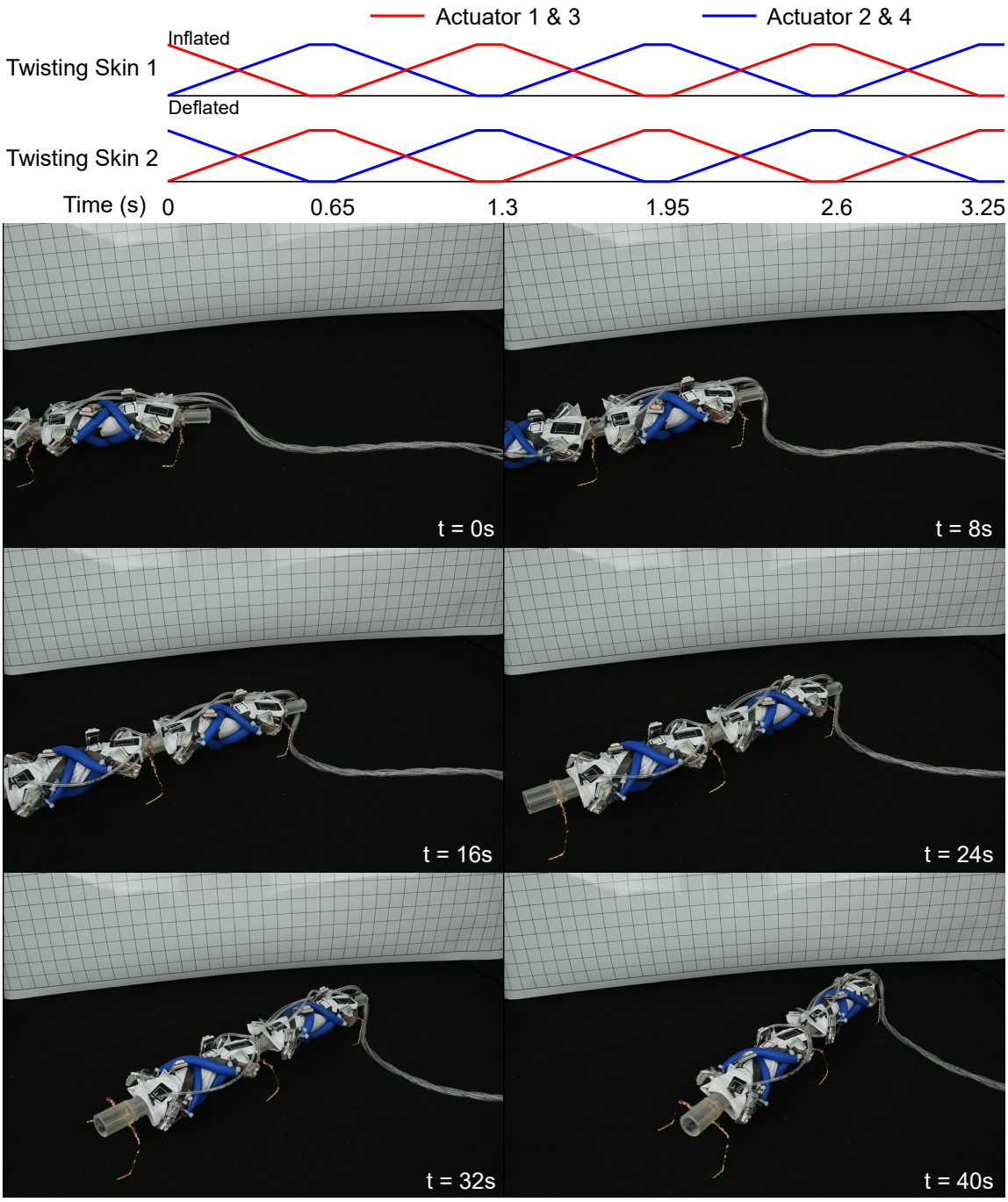

Figure 8.15. Gait of twisting walking robot and images demonstrating the walking capabilities.

was chosen to eliminate any leg-driven locomotion. The design of the robot is shown in Figure 8.15.

To achieve walking, a simple counter-twist gait was implemented on the two twisting skins. This gait is shown in Figure 8.15 and was run open-loop. The actuators were pressurized to 25 psi and were tied to a vacuum during deflation to increase the speed at which the robot could operate. With the proposed gait, the robot was able to achieve spinal-driven locomotion at 7.5 mm/s, which means each step was approximately 4.875 mm. While this robot has not been fully optimized in terms of gait or leg design, it demonstrates that spinal-driven locomotion alone can achieve decent locomotion of a soft robot with minimal required deformation of the elastomeric body itself.

8.6 Conclusion

This chapter presented an improved, generalized model and simulation for robotic skins on continuum segments that allowed for improved design of both the skins and the cylindrical structures they are wrapped around. The simulation was able to predict the behavior of fully characterized skins on various cylindrical structures, which means the work could be expanded to include a time-dependent model to use the simulation as a testbed for various control strategies.

Additionally, a legged robot was created that achieved spinal-driven locomotion through the use of twisting skins. This demonstration highlights the power of utilizing the ofen-neglected spinal section of legged robots for locomotion. By including spinal-driven locomotion in soft robots, burden of locomotion can be lessened from the legs. This means potentially lower deformations required in leg motion, which could increase the life cycles of the legs, while maintaining the same velocity of the soft robot. By incorporating more distributed deformation of soft robots through the use of more distributed actuator networks, the efficiency of soft robots can be improved.

9. SUMMARY

In order to bring soft robots from controlled laboratory environments to real-world applications, achieving closed-loop control is required. Control of soft robots has thus far focused more heavily on open-loop or feedforward control due to the complexities of embedding sensing. Sensing, however, is necessary for the robot to interact with an unknown environment without the help of a human teleoperator. Control of soft robots is also highly dependent upon the design of the systems, which involves materials, geometry, sensor and actuator placement, and desired motion. The work demonstrated in this thesis moves the field toward the goal of implementing control in continuum-type soft robots by exploring the effects of performance on control of various design choices.

9.1 Contributions

The work presented here contributes six advancements to the field of soft robotics.

1. A verification that sensors made from soft materials can be designed in such a way that their response is decoupled from complex material behaviors, such as nonlinear stress-strain curves and viscoelasticity.

   The behaviors of soft robots are complicated and having sensors that experience the time-dependent behaviors of the materials only convolutes the problem further. A study demonstrated viscoelastic behaviors of bulk elastomers as well as how those behaviors do not affect the sensor responses of liquid-metal-embedded sensors made from those same elastomers. This highlighted that decoupling of those undesirable material behaviors is possible and soft sensors should be designed in such a way that this decoupling is built into the sensing capabilities. This goal of decoupling sensor response from viscoelastic material behaviors

was also achieved in subsequent work on conductive composite capacitive sensors [43].

2. A soft robot design study considering both material choice and geometry for controllability of soft systems.

   This study looked at beams of elastomer and explored how changing the geometry and materials of the system can affect the controllability and behavior of the system. A prismatic, homogeneous beam was well controlled and experiences continuum deformation as it bends. A simple geometric change in the beam created a discrete point of bending, but changed the stability of the system for the worse. Keeping the geometric change, but changing the region of the bending to a softer material, brought back the original stability seen in the prismatic, homogeneous beam, while maintaining the discrete point of bending. This study emphasizes the important roles that both material and geometry play in terms of control of a soft system. These two design components can be used alongside appropriately placed actuators to achieve desired behaviors from a soft system.

3. A 2D cable-driven multi-segment continuum soft robot model with cables that cross sides of the robot between soft segments.

   A model and simulation was developed to explore how highly coupled cabling patterns can improve the performance of cable-driven continuum robots. This work took a Monte Carlo approach to testing all possible crossing cable patterns to find the best pattern that most closely matched the workspace performance of a traditionally cabled continuum robot. A physical robot was built to test and verify the model. This work demonstrated that highly coupled actuation methods can reduce the actuator requirements without affecting performance. The inspiration for this work is muscle patterns in animals, which are also highly coupled. It stands to reason that, while this demonstration was done on a cable-

driven continuum robot, the concept of using highly coupled actuation would transfer to other systems as well.

4. A new continuum segment model that estimates state based on measured lengths of the segment at locations parallel to the neutral axis and the model was inverted to predicted actuator commands.

   In order use sensory feedback to control soft structures, the sensory data must be put into a model to provide state estimation. A model was developed to estimate the state of a cylindrical segment given strain sensors readings from four sensors placed equidistance around the circumference of the segment. This model required that the sensors be parallel to neutral axis alongside four actuators. The actuators contracted to achieve bending in the segment while the sensors were able to measure this bending and use the model to predict the state of the system. The ability to estimate shape allowed for the demonstration of feedback control of this system. This model was inverted with a model of the actuators to achieve feedforward control of the same system. Combining the feedforward and feedback control improved the settling time and accuracy of the system's ability to track a reference signal. The ability to achieve state estimation via soft sensory input is important for tracking the true position of the system. This has implications in using the sensory feedback to tell when the robot has not achieved a desired position, which could indicate an obstacle or a failure in a component of the robot.

5. A model to estimate the material properties of soft cylindrical segments based on the observed deformation and under known actuator commands.

   A model was developed and verified to estimate the elastic modulus and stiffness of cylindrical structures. This capability was demonstrated with multiple skins and enabled the ability to initialize feedforward models by utilizing measurements provided from this model. This is important for robotic skins because they were designed to be applied on-the-fly. This work demonstrates that nec-

essary measurements can be taken by the skin as long as as the robotic skins are properly characterized.

6. A generalized continuum segment model that relaxes the requirements for sensor and actuator placement from previously derived models.

   A model and simulation was developed to explore how changes in actuator and sensor placement can affect the behavior of continuum segments. This work demonstrated a verification of the model and a demonstration of how the model can be used to predict the behavior of the system as well as provide feedforward actuator commands. Additionally, a demonstration was provided of off-angle sensors and actuators to create a walking legged robot that utilized spinal locomotion. The simulation provides a design tool in the construction of future skins as well as a tool to test control strategies before implementing on a physical system.

9.2 Future Work

The models and results presented in this paper touch on a number of important features for design and control of soft robots. However, more in-depth studies are necessary for building a stronger foundation on which future soft robots can be developed. A soft material library where various soft material properties are provided would help in the design of future soft robots. As it stands now, researchers tend to characterize the few materials they work with and then continue to use those materials when other materials may be more beneficial. This is further complicated by the changes to these properties by curing temperatures, etc. Additionally, adding additives to the bulk elastomers, such as carbon black and exfoliated graphite, can further change those properties. Developing theory to describe these changes and design tools that researchers can use to help in the material selection process can help lower the barrier to entry in working with soft robots.

While this work demonstrates sensory-enabled control, the sensors used were limited to strain sensors. This limits the type of systems that can be designed and how the sensors need to be placed within systems. Many actuators in soft robotics contract rather than extend and this is difficult to observe with a strain sensor unless the sensor is highly pre-strained. For the future of soft robotics, the continued development of new sensor technology is required to enable proprioception and navigation. Additionally, both sensors used in this work are sensitive to other inputs, such as pressure. In the work presented in this thesis, the systems were designed and operated in an environment to minimize that effect. However, in real-world applications, the sensors may unexpectedly experience an alternative input mode. To address this, redundancies in sensors or more complex sensor networks that could detect if this has happened should be considered. Sensors also have the ability to detect when the system has run into obstacles and is unable to perform a desired motion. While this should be possible, it was not demonstrated in the presented work.

For future design of models of soft robots, the integration of finite element modeling is necessary. While continuum robots can take advantage of analytical models, more complex soft robots will require more complex models and resolving the stress fields experienced by the materials requires some level of finite element modeling. Additionally, finite element modeling can be used alongside controllers. There have been promising results running a reduced-order finite element model in real-time to control soft robots [67]. Because of the complexities involved with continuum deformations, there is a limit to analytical models in terms of geometric complexity of soft robot structures. To design more complex geometries, more complex design tools must be used.

The future of soft robotics will see more development and integration of design tools in the creation of future systems. These design tools will help select materials, actuators, and sensors necessary to perform given tasks. They will be reliant upon the collection of empirical measurements to map theory to reality. These tools will simplify design and control of soft structures. Sensors and actuators would be able

to move on a model to observe changes in behavior, observability, and controllability of the system without the need to manufacture entire systems one system at a time. Faster iterations of fully integrated (structure, sensors, and actuators) systems can occur in simulation than through experimentation. Additionally, optimization methods could then be used to assist in the design of future soft robots, which can provide unique solutions that researchers may not come across through intuition. These tools could revolutionize how soft robots are designed and controlled.

REFERENCES

[1] R. F. Shepherd, F. Ilievski, W. Choi, S. A. Morin, A. A. Stokes, A. D. Mazzeo, X. Chen, M. Wang, and G. M. Whitesides, "Multigait soft robot," *Proceedings of the National Academy of Sciences*, vol. 108, no. 51, pp. 20 400–20 403, Nov. 2011.

[2] A. D. Marchese, C. D. Onal, and D. Rus, "Autonomous Soft Robotic Fish Capable of Escape Maneuvers Using Fluidic Elastomer Actuators," *Soft Robotics*, vol. 1, no. 1, pp. 75–87, Feb. 2014.

[3] Z. Chen, T. I. Um, and H. Bart-Smith, "Bio-inspired robotic manta ray powered by ionic polymermetal composite artificial muscles," *International Journal of Smart and Nano Materials*, vol. 3, no. 4, pp. 296–308, Dec. 2012.

[4] K. Oliver-Butler, J. Till, and C. Rucker, "Continuum Robot Stiffness Under External Loads and Prescribed Tendon Displacements," *IEEE Transactions on Robotics*, pp. 1–17, 2019.

[5] E. W. Hawkes, L. H. Blumenschein, J. D. Greer, and A. M. Okamura, "A soft robot that navigates its environment through growth," *Science Robotics*, vol. 2, no. 8, p. eaan3028, Jul. 2017.

[6] J. W. Booth, D. Shah, J. C. Case, E. L. White, M. C. Yuen, O. Cyr-Choiniere, and R. Kramer-Bottiglio, "OmniSkins: Robotic skins that turn inanimate objects into multifunctional robots," *Science Robotics*, vol. 3, no. 22, p. eaat1853, Sep. 2018.

[7] D. Drotman, M. Ishida, S. Jadhav, and M. T. Tolley, "Application-Driven Design of Soft, 3d Printed, Pneumatic Actuators with Bellows," *IEEE/ASME Transactions on Mechatronics*, pp. 1–1, 2018.

[8] J. Konstantinova, H. Wurdemann, and A. Shafti, *Soft and Stiffness-controllable Robotics Solutions for Minimally Invasive Surgery:*. River Publishers, Jun. 2018.

[9] M. Vespignani, J. M. Friesen, V. SunSpiral, and J. Bruce, "Design of SUPERball v2, a Compliant Tensegrity Robot for Absorbing Large Impacts," in *2018 IEEE/RSJ International Conference on Intelligent Robots and Systems (IROS)*, Oct. 2018, pp. 2865–2871.

[10] M. Wehner, R. L. Truby, D. J. Fitzgerald, B. Mosadegh, G. M. Whitesides, J. A. Lewis, and R. J. Wood, "An integrated design and fabrication strategy for entirely soft, autonomous robots," *Nature*, vol. 536, no. 7617, pp. 451–455, Aug. 2016.

[11] R. L. Truby and J. A. Lewis, "Printing soft matter in three dimensions," *Nature*, vol. 540, no. 7633, pp. 371–378, Dec. 2016.

[12] J. Diani, B. Fayolle, and P. Gilormini, "A review on the Mullins effect," *European Polymer Journal*, vol. 45, no. 3, pp. 601–612, Mar. 2009.

[13] G. M. Whitesides, "Soft Robotics," *Angewandte Chemie International Edition*, vol. 57, no. 16, pp. 4258–4273, 2018.

[14] R. W. Ogden, *Non-linear Elastic Deformations*. Courier Corporation, 1997.

[15] W. N. Findley and F. A. Davis, *Creep and Relaxation of Nonlinear Viscoelastic Materials*. Courier Corporation, Jan. 2013.

[16] N. G. McCrum, C. P. Buckley, and C. B. Bucknall, *Principles of Polymer Engineering*. Oxford University Press, Jan. 1997.

[17] J. C. Simo and T. J. R. Hughes, *Computational Inelasticity*. Springer Science & Business Media, May 2006.

[18] M. Mooney, "A Theory of Large Elastic Deformation," *Journal of Applied Physics*, vol. 11, no. 9, pp. 582–592, Sep. 1940.

[19] R. S. Rivlin, "Large elastic deformations of isotropic materials IV. further developments of the general theory," *Phil. Trans. R. Soc. Lond. A*, vol. 241, no. 835, pp. 379–397, Oct. 1948.

[20] O. H. Yeoh, "Some Forms of the Strain Energy Function for Rubber," *Rubber Chemistry and Technology*, vol. 66, no. 5, pp. 754–771, Nov. 1993.

[21] A. N. Gent, "A New Constitutive Relation for Rubber," *Rubber Chemistry and Technology*, vol. 69, no. 1, pp. 59–61, Mar. 1996.

[22] L. Mullins, "Effect of stretching on the properties of rubber," *Rubber Chemistry and Technology*, vol. 21, no. 2, pp. 281–300, 1948.

[23] T. K. Kim, J. K. Kim, and O. C. Jeong, "Measurement of nonlinear mechanical properties of PDMS elastomer," *Microelectronic Engineering*, vol. 88, no. 8, pp. 1982–1985, Aug. 2011.

[24] F. Schneider, T. Fellner, J. Wilde, and U. Wallrabe, "Mechanical properties of silicones for MEMS," *Journal of Micromechanics and Microengineering*, vol. 18, no. 6, p. 065008, Jun. 2008.

[25] S. Kim, E. Hawkes, K. Cho, M. Joldaz, J. Foleyz, and R. Wood, "Micro artificial muscle fiber using NiTi spring for soft robotics," in *IEEE/RSJ International Conference on Intelligent Robots and Systems, 2009. IROS 2009*, Oct. 2009, pp. 2228–2234.

[26] J. Till and D. C. Rucker, "Elastic Stability of Cosserat Rods and Parallel Continuum Robots," *IEEE Transactions on Robotics*, vol. 33, no. 3, pp. 718–733, Jun. 2017.

[27] S.-W. Yeom and I.-K. Oh, "A biomimetic jellyfish robot based on ionic polymer metal composite actuators," *Smart Materials and Structures*, vol. 18, no. 8, p. 085002, Aug. 2009.

[28] F. Ilievski, A. D. Mazzeo, R. F. Shepherd, X. Chen, and G. M. Whitesides, "Soft Robotics for Chemists," *Angewandte Chemie*, vol. 123, no. 8, pp. 1930–1935, Feb. 2011.

[29] P. Ohta, L. Valle, J. King, K. Low, J. Yi, C. G. Atkeson, and Y.-L. Park, "Design of a Lightweight Soft Robotic Arm Using Pneumatic Artificial Muscles and Inflatable Sleeves," *Soft Robotics*, Oct. 2017.

[30] I. M. Koo, K. Jung, J. C. Koo, J.-D. Nam, Y. K. Lee, and H. R. Choi, "Development of Soft-Actuator-Based Wearable Tactile Display," *IEEE Transactions on Robotics*, vol. 24, no. 3, pp. 549–558, Jun. 2008.

[31] C. Laschi, "Soft Robotics: from scientific challenges to technological applications," in *Micro and Nanotechnology Sensors, Systems, and Applications VIII*, vol. 9836, 2016, pp. 983 626–983 626–8.

[32] I. Mihlcz, "Fundamental characteristics and design method for nickel-titanium shape memory alloy," *Mechanical Engineering*, vol. 45, no. 1, pp. 75–86, 2001.

[33] R. J. Webster and B. A. Jones, "Design and Kinematic Modeling of Constant Curvature Continuum Robots: A Review," *The International Journal of Robotics Research*, Jun. 2010.

[34] M. Manti, T. Hassan, G. Passetti, N. dElia, M. Cianchetti, and C. Laschi, "An Under-Actuated and Adaptable Soft Robotic Gripper," in *Biomimetic and Biohybrid Systems*, ser. Lecture Notes in Computer Science. Springer, Cham, Jul. 2015, pp. 64–74.

[35] N. Lu and D.-H. Kim, "Flexible and Stretchable Electronics Paving the Way for Soft Robotics," *Soft Robotics*, vol. 1, no. P, pp. 53–62, Jul. 2013.

[36] Y. Bahramzadeh and M. Shahinpoor, "A Review of Ionic Polymeric Soft Actuators and Sensors," *Soft Robotics*, vol. 1, no. P, pp. 38–52, Jul. 2013.

[37] V. Vogel, "Soft robotics: Bionic jellyfish," *Nature Materials*, vol. 11, no. 10, pp. 841–842, Oct. 2012.

[38] M. T. Tolley, R. F. Shepherd, M. Karpelson, N. W. Bartlett, K. C. Galloway, M. Wehner, R. Nunes, G. M. Whitesides, and R. J. Wood, "An untethered jumping soft robot," in *2014 IEEE/RSJ International Conference on Intelligent Robots and Systems*, Sep. 2014, pp. 561–566.

[39] M. Loepfe, C. Schumacher, U. Lustenberger, and W. Stark, "An Untethered, Jumping Roly-Poly Soft Robot Driven by Combustion," *Soft Robotics*, vol. 2, no. 1, pp. 33–41, Mar. 2015.

[40] A. I. Nawroj, J. P. Swensen, and A. M. Dollar, "Toward Modular Active-Cell Robots (MACROs): SMA Cell Design and Modeling of Compliant, Articulated Meshes," *IEEE Transactions on Robotics*, vol. 33, no. 4, pp. 796–806, Aug. 2017.

[41] S. Seok, C. Onal, K.-J. Cho, R. Wood, D. Rus, and S. Kim, "Meshworm: A Peristaltic Soft Robot With Antagonistic Nickel Titanium Coil Actuators," *IEEE/ASME Transactions on Mechatronics*, vol. 18, no. 5, pp. 1485–1497, Oct. 2013.

[42] J. Bruce, K. Caluwaerts, A. Iscen, A. P. Sabelhaus, and V. SunSpiral, "Design and evolution of a modular tensegrity robot platform," in *2014 IEEE International Conference on Robotics and Automation (ICRA)*, May 2014, pp. 3483–3489.

[43] E. L. White, M. C. Yuen, J. C. Case, and R. K. Kramer, "Low-Cost, Facile, and Scalable Manufacturing of Capacitive Sensors for Soft Systems," *Advanced Materials Technologies*, vol. 2, no. 9, p. 1700072, 2017.

[44] M. C. S. Yuen, T. R. Lear, H. Tonoyan, M. Telleria, and R. Kramer-Bottiglio, "Toward Closed-Loop Control of Pneumatic Grippers During Pack-and-Deploy Operations," *IEEE Robotics and Automation Letters*, vol. 3, no. 3, pp. 1402–1409, Jul. 2018.

[45] R. A. Bilodeau, M. C. Yuen, J. C. Case, T. L. Buckner, and R. Kramer-Bottiglio, "Design for Control of a Soft Bidirectional Bending Actuator," in *2018 IEEE/RSJ International Conference on Intelligent Robots and Systems (IROS)*, Oct. 2018, pp. 1–8.

[46] M. Luo, E. H. Skorina, W. Tao, F. Chen, S. Ozel, Y. Sun, and C. D. Onal, "Toward Modular Soft Robotics: Proprioceptive Curvature Sensing and Sliding-Mode Control of Soft Bidirectional Bending Modules," *Soft Robotics*, Feb. 2017.

[47] B. S. Homberg, R. K. Katzschmann, M. R. Dogar, and D. Rus, "Robust proprioceptive grasping with a soft robot hand," *Autonomous Robots*, pp. 1–16, Apr. 2018.

[48] A. Koivikko, E. S. Raei, V. Sariola, M. Mosallaei, and M. Mantysalo, "Soft actuators with screen-printed curvature sensors," in *2017 IEEE SENSORS*, Oct. 2017, pp. 1–3.

[49] Y.-L. Park, B.-r. Chen, C. Majidi, R. J. Wood, R. Nagpal, and E. Goldfield, "Active modular elastomer sleeve for soft wearable assistance robots," in *Intelligent Robots and Systems (IROS), 2012 IEEE/RSJ International Conference on*, 2012, pp. 1595–1602.

[50] R. A. Bilodeau, E. L. White, and R. K. Kramer, "Monolithic fabrication of sensors and actuators in a soft robotic gripper," in *2015 IEEE/RSJ International Conference on Intelligent Robots and Systems (IROS)*, Sep. 2015, pp. 2324–2329.

[51] N. Farrow and N. Correll, "A soft pneumatic actuator that can sense grasp and touch," in *2015 IEEE/RSJ International Conference on Intelligent Robots and Systems (IROS)*, Sep. 2015, pp. 2317–2323.

[52] J. Fra, J. Czarnowski, M. Macia, J. Gwka, M. Cianchetti, and A. Menciassi, "New STIFF-FLOP module construction idea for improved actuation and sensing," in *2015 IEEE International Conference on Robotics and Automation (ICRA)*, May 2015, pp. 2901–2906.

[53] D. Rus and M. T. Tolley, "Design, fabrication and control of soft robots," *Nature*, vol. 521, no. 7553, pp. 467–475, May 2015.

[54] P. Polygerinos, N. Correll, S. A. Morin, B. Mosadegh, C. D. Onal, K. Petersen, M. Cianchetti, M. T. Tolley, and R. F. Shepherd, "Soft Robotics: Review of Fluid-Driven Intrinsically Soft Devices; Manufacturing, Sensing, Control, and Applications in Human-Robot Interaction," *Advanced Engineering Materials*, vol. 19, no. 12, p. 1700016, 2017.

[55] T. George Thuruthel, Y. Ansari, E. Falotico, and C. Laschi, "Control Strategies for Soft Robotic Manipulators: A Survey," *Soft Robotics*, Jan. 2018.

[56] C. D. Onal and D. Rus, "Autonomous undulatory serpentine locomotion utilizing body dynamics of a fluidic soft robot," *Bioinspiration & Biomimetics*, vol. 8, no. 2, p. 026003, Jun. 2013.

[57] V. Vikas, P. Grover, and B. Trimmer, "Model-free control framework for multi-limb soft robots," in *2015 IEEE/RSJ International Conference on Intelligent Robots and Systems (IROS)*, Sep. 2015, pp. 1111–1116.

[58] C. Duriez, "Control of elastic soft robots based on real-time finite element method," in *2013 IEEE International Conference on Robotics and Automation*, May 2013, pp. 3982–3987.

[59] A. Parvaresh and S. A. A. Moosavian, "Modeling and Model-free Fuzzy Control of a Continuum Robotic Arm," in *2018 6th RSI International Conference on Robotics and Mechatronics (IcRoM)*, Oct. 2018, pp. 501–506.

[60] J. Burgner-Kahrs, D. C. Rucker, and H. Choset, "Continuum Robots for Medical Applications: A Survey," *IEEE Transactions on Robotics*, vol. 31, no. 6, pp. 1261–1280, Dec. 2015.

[61] D. Camarillo, C. Milne, C. Carlson, M. Zinn, and J. Salisbury, "Mechanics Modeling of Tendon-Driven Continuum Manipulators," *IEEE Transactions on Robotics*, vol. 24, no. 6, pp. 1262–1273, Dec. 2008.

[62] R. J. Webster, J. P. Swensen, J. M. Romano, and N. J. Cowan, "Closed-Form Differential Kinematics for Concentric-Tube Continuum Robots with Application to Visual Servoing," in *Experimental Robotics*, ser. Springer Tracts in Advanced Robotics. Springer, Berlin, Heidelberg, 2009, pp. 485–494.

[63] A. D. Marchese and D. Rus, "Design, kinematics, and control of a soft spatial fluidic elastomer manipulator," *The International Journal of Robotics Research*, p. 0278364915587925, Oct. 2015.

[64] M. Cianchetti, T. Ranzani, G. Gerboni, I. D. Falco, C. Laschi, and A. Menciassi, "STIFF-FLOP surgical manipulator: Mechanical design and experimental characterization of the single module," in *2013 IEEE/RSJ International Conference on Intelligent Robots and Systems*, Nov. 2013, pp. 3576–3581.

[65] F. Renda, V. Cacucciolo, J. Dias, and L. Seneviratne, "Discrete Cosserat approach for soft robot dynamics: A new piece-wise constant strain model with torsion and shears," in *2016 IEEE/RSJ International Conference on Intelligent Robots and Systems (IROS)*, Oct. 2016, pp. 5495–5502.

[66] D. C. Rucker and R. J. W. III, "Statics and Dynamics of Continuum Robots With General Tendon Routing and External Loading," *IEEE Transactions on Robotics*, vol. 27, no. 6, pp. 1033–1044, Dec. 2011.

[67] R. K. Katzschmann, M. Thieffry, O. Goury, A. Kruszewski, T. Guerra, C. Duriez, and D. Rus, "Dynamically Closed-Loop Controlled Soft Robotic Arm using a Reduced Order Finite Element Model with State Observer," in *2019 2nd IEEE International Conference on Soft Robotics (RoboSoft)*, Apr. 2019, pp. 717–724.

[68] Y. Zhang, M. Su, Y. Guan, H. Zhu, and S. Mao, "An Integrated Framework for Modular Reconfigurable Soft Robots," in *2018 IEEE International Conference on Robotics and Biomimetics (ROBIO)*, Dec. 2018, pp. 606–611.

[69] M. C. Yuen, H. Tonoyan, E. L. White, M. Telleria, and R. K. Kramer, "Fabric sensory sleeves for soft robot state estimation," in *2017 IEEE International Conference on Robotics and Automation (ICRA)*, May 2017, pp. 5511–5518.

[70] N. Lin, P. Wu, M. Wang, J. Wei, F. Yang, S. Xu, Z. Ye, and X. Chen, "IMU-based Active Safe Control of a Variable Stiffness Soft Actuator," *IEEE Robotics and Automation Letters*, pp. 1–1, 2019.

[71] G. Fang, X. Wang, K. Wang, K. Lee, J. D. Ho, H. C. Fu, K. C. D. Fu, and K. Kwok, "Vision-based Online Learning Kinematic Control for Soft Robots using Local Gaussian Process Regression," *IEEE Robotics and Automation Letters*, pp. 1–1, 2019.

[72] M. Yuen, A. Cherian, J. Case, J. Seipel, and R. Kramer, "Conformable actuation and sensing with robotic fabric," in *2014 IEEE/RSJ International Conference on Intelligent Robots and Systems (IROS 2014)*, Sep. 2014, pp. 580–586.

[73] C. M. A. Ashruf, "Thin flexible pressure sensors," *Sensor Review*, vol. 22, no. 4, pp. 322–327, Dec. 2002.

[74] Pang Changhyun, Lee Chanseok, and Suh KahpYang, "Recent advances in flexible sensors for wearable and implantable devices," *Journal of Applied Polymer Science*, vol. 130, no. 3, pp. 1429–1441, Jun. 2013.

[75] S. Khan, L. Lorenzelli, and R. S. Dahiya, "Technologies for Printing Sensors and Electronics Over Large Flexible Substrates: A Review," *IEEE Sensors Journal*, vol. 15, no. 6, pp. 3164–3185, Jun. 2015.

[76] P. J. Codd, A. Veaceslav, A. H. Gosline, and P. E. Dupont, "Novel pressure-sensing skin for detecting impending tissue damage during neuroendoscopy: Laboratory investigation," *Journal of Neurosurgery: Pediatrics*, pp. 1–8, Nov. 2013.

[77] A. T. Asbeck, S. M. M. D. Rossi, K. G. Holt, and C. J. Walsh, "A biologically inspired soft exosuit for walking assistance," *The International Journal of Robotics Research*, p. 0278364914562476, Mar. 2015.

[78] J.-B. Chossat, Y. Tao, V. Duchaine, and Y.-L. Park, "Wearable soft artificial skin for hand motion detection with embedded microfluidic strain sensing," in *2015 IEEE International Conference on Robotics and Automation (ICRA)*, May 2015, pp. 2568–2573.

[79] K. Galloway, P. Polygerinos, C. Walsh, and R. Wood, "Mechanically programmable bend radius for fiber-reinforced soft actuators," in *2013 16th International Conference on Advanced Robotics (ICAR)*, Nov. 2013, pp. 1–6.

[80] M. Wehner, B. Quinlivan, P. M. Aubin, E. Martinez-Villalpando, M. Baumann, L. Stirling, K. Holt, R. Wood, and C. Walsh, "A lightweight soft exosuit for gait assistance," in *2013 IEEE International Conference on Robotics and Automation*, May 2013, pp. 3362–3369.

[81] D.-H. Kim, Y.-S. Kim, J. Wu, Z. Liu, J. Song, H.-S. Kim, Y. Y. Huang, K.-C. Hwang, and J. A. Rogers, "Ultrathin Silicon Circuits With Strain-Isolation Layers and Mesh Layouts for High-Performance Electronics on Fabric, Vinyl, Leather, and Paper," *Advanced Materials*, vol. 21, no. 36, pp. 3703–3707, Sep. 2009.

[82] J. C. McDonald and G. M. Whitesides, "Poly(dimethylsiloxane) as a Material for Fabricating Microfluidic Devices," *Accounts of Chemical Research*, vol. 35, no. 7, pp. 491–499, Jul. 2002.

[83] S. Zhu, J.-H. So, R. Mays, S. Desai, W. R. Barnes, B. Pourdeyhimi, and M. D. Dickey, "Ultrastretchable Fibers with Metallic Conductivity Using a Liquid Metal Alloy Core," *Advanced Functional Materials*, vol. 23, no. 18, pp. 2308–2314, May 2013.

[84] A. Bratov, J. Munoz, C. Dominguez, and J. Bartroli, "Photocurable polymers applied as encapsulating materials for ISFET production," *Sensors and Actuators B: Chemical*, vol. 25, no. 1, pp. 823–825, Apr. 1995.

[85] R. K. Kramer, C. Majidi, R. Sahai, and R. J. Wood, "Soft curvature sensors for joint angle proprioception," in *Intelligent Robots and Systems (IROS), 2011 IEEE/RSJ International Conference on*, 2011, pp. 1919–1926.

[86] J. C. Case, E. L. White, and R. K. Kramer, "Soft Material Characterization for Robotic Applications," *Soft Robotics*, vol. 2, no. 2, pp. 80–87, Jun. 2015.

[87] M. A. Eddings, M. A. Johnson, and B. K. Gale, "Determining the optimal PDMSPDMS bonding technique for microfluidic devices," *Journal of Micromechanics and Microengineering*, vol. 18, no. 6, p. 067001, Jun. 2008.

[88] D.-H. Kim, Z. Liu, Y.-S. Kim, J. Wu, J. Song, H.-S. Kim, Y. Huang, K.-c. Hwang, Y. Zhang, and J. A. Rogers, "Optimized Structural Designs for Stretchable Silicon Integrated Circuits," *Small*, vol. 5, no. 24, pp. 2841–2847, Dec. 2009.

[89] D.-Y. Khang, H. Jiang, Y. Huang, and J. A. Rogers, "A Stretchable Form of Single-Crystal Silicon for High-Performance Electronics on Rubber Substrates," *Science*, vol. 311, no. 5758, pp. 208–212, Jan. 2006.

[90] D.-H. Kim, J.-H. Ahn, W. M. Choi, H.-S. Kim, T.-H. Kim, J. Song, Y. Y. Huang, Z. Liu, C. Lu, and J. A. Rogers, "Stretchable and Foldable Silicon Integrated Circuits," *Science*, vol. 320, no. 5875, pp. 507–511, Apr. 2008.

[91] J. A. Fan, W.-H. Yeo, Y. Su, Y. Hattori, W. Lee, S.-Y. Jung, Y. Zhang, Z. Liu, H. Cheng, L. Falgout, M. Bajema, T. Coleman, D. Gregoire, R. J. Larsen, Y. Huang, and J. A. Rogers, "Fractal design concepts for stretchable electronics," *Nature Communications*, vol. 5, Feb. 2014.

[92] G. M. Whitesides, "The origins and the future of microfluidics," *Nature*, vol. 442, no. 7101, pp. 368–373, Jul. 2006.

[93] C. Majidi, R. Kramer, and R. J. Wood, "A non-differential elastomer curvature sensor for softer-than-skin electronics," *Smart Materials and Structures*, vol. 20, no. 10, p. 105017, Oct. 2011.

[94] Y.-L. Park, B.-R. Chen, and R. J. Wood, "Design and Fabrication of Soft Artificial Skin Using Embedded Microchannels and Liquid Conductors," *IEEE Sensors Journal*, vol. 12, no. 8, pp. 2711–2718, Aug. 2012.

[95] A. Anderson, Y. Menguc, R. Wood, and D. Newman, "Development of the Polipo Pressure Sensing System for Dynamic Space-Suited Motion," *IEEE Sensors Journal*, vol. 15, no. 11, pp. 6229–6237, Nov. 2015.

[96] J. W. Boley, E. L. White, G. T.-C. Chiu, and R. K. Kramer, "Direct Writing of Gallium-Indium Alloy for Stretchable Electronics," *Advanced Functional Materials*, vol. 24, no. 23, pp. 3501–3507, Jun. 2014.

[97] J.-B. Chossat, H.-S. Shin, Y.-L. Park, and V. Duchaine, "Soft Tactile Skin Using an Embedded Ionic Liquid and Tomographic Imaging," *Journal of Mechanisms and Robotics*, vol. 7, no. 2, pp. 021 008–021 008, May 2015.

[98] A. P. Gerratt, H. O. Michaud, and S. P. Lacour, "Elastomeric Electronic Skin for Prosthetic Tactile Sensation," *Advanced Functional Materials*, vol. 25, no. 15, pp. 2287–2295, Apr. 2015.

[99] F. Hammond, R. Kramer, Q. Wan, R. Howe, and R. Wood, "Soft tactile sensor arrays for micromanipulation," in *2012 IEEE/RSJ International Conference on Intelligent Robots and Systems (IROS)*, Oct. 2012, pp. 25–32.

[100] R. K. Kramer, C. Majidi, and R. J. Wood, "Wearable tactile keypad with stretchable artificial skin," in *Robotics and Automation (ICRA), 2011 IEEE International Conference on*, 2011, pp. 1103–1107.

[101] R. Matsuzaki and K. Tabayashi, "Highly Stretchable, Global, and Distributed Local Strain Sensing Line Using GaInSn Electrodes for Wearable Electronics," *Advanced Functional Materials*, vol. 25, no. 25, pp. 3806–3813, Jul. 2015.

[102] J. T. B. Overvelde, Y. Meng, P. Polygerinos, Y. Wang, Z. Wang, C. J. Walsh, R. J. Wood, and K. Bertoldi, "Mechanical and electrical numerical analysis of soft liquid-embedded deformation sensors analysis," *Extreme Mechanics Letters*, vol. 1, pp. 42–46, Dec. 2014.

[103] J. Choi, S. Kim, J. Lee, and B. Choi, "Improved Capacitive Pressure Sensors Based on Liquid Alloy and Silicone Elastomer," *IEEE Sensors Journal*, vol. 15, no. 8, pp. 4180–4181, Aug. 2015.

[104] S. Baek, D.-J. Won, J. G. Kim, and J. Kim, "Development and analysis of a capacitive touch sensor using a liquid metal droplet," *Journal of Micromechanics and Microengineering*, vol. 25, no. 9, p. 095015, Sep. 2015.

[105] R. D. Ponce Wong, J. D. Posner, and V. J. Santos, "Flexible microfluidic normal force sensor skin for tactile feedback," *Sensors and Actuators A: Physical*, vol. 179, pp. 62–69, Jun. 2012.

[106] K. Noda, E. Iwase, K. Matsumoto, and I. Shimoyama, "Stretchable liquid tactile sensor for robot-joints," in *2010 IEEE International Conference on Robotics and Automation (ICRA)*, May 2010, pp. 4212–4217.

[107] J.-B. Chossat, Y.-L. Park, R. J. Wood, and V. Duchaine, "A Soft Strain Sensor Based on Ionic and Metal Liquids," *IEEE Sensors Journal*, vol. 13, no. 9, pp. 3405–3414, Sep. 2013.

[108] C. R. Merritt, H. T. Nagle, and E. Grant, "Textile-Based Capacitive Sensors for Respiration Monitoring," *IEEE Sensors Journal*, vol. 9, no. 1, pp. 71–78, Jan. 2009.

[109] M. Stoppa and A. Chiolerio, "Wearable Electronics and Smart Textiles: A Critical Review," *Sensors*, vol. 14, no. 7, pp. 11 957–11 992, Jul. 2014.

[110] C. Mattmann, F. Clemens, and G. Trster, "Sensor for Measuring Strain in Textile," *Sensors*, vol. 8, no. 6, pp. 3719–3732, Jun. 2008.

[111] L. M. Castano and A. B. Flatau, "Smart fabric sensors and e-textile technologies: a review," *Smart Materials and Structures*, vol. 23, no. 5, p. 053001, 2014.

[112] L. Capineri, "Resistive Sensors with Smart Textiles for Wearable Technology: From Fabrication Processes to Integration with Electronics," *Procedia Engineering*, vol. 87, pp. 724–727, Jan. 2014.

[113] R. Xu, K.-I. Jang, Y. Ma, H. N. Jung, Y. Yang, M. Cho, Y. Zhang, Y. Huang, and J. A. Rogers, "Fabric-based stretchable electronics with mechanically optimized designs and prestrained composite substrates," *Extreme Mechanics Letters*, vol. 1, pp. 120–126, Dec. 2014.

[114] L. Hu, M. Pasta, F. L. Mantia, L. Cui, S. Jeong, H. D. Deshazer, J. W. Choi, S. M. Han, and Y. Cui, "Stretchable, Porous, and Conductive Energy Textiles," *Nano Letters*, vol. 10, no. 2, pp. 708–714, Feb. 2010.

[115] C. Cochrane, V. Koncar, M. Lewandowski, and C. Dufour, "Design and Development of a Flexible Strain Sensor for Textile Structures Based on a Conductive Polymer Composite," *Sensors*, vol. 7, no. 4, pp. 473–492, Apr. 2007.

[116] R. L. Crabb and F. C. Treble, "Thin Silicon Solar Cells for Large Flexible Arrays," *Nature*, vol. 213, no. 5082, pp. 1223–1224, Mar. 1967.

[117] K. A. Ray, "Flexible Solar Cell Arrays for Increased Space Power," *IEEE Transactions on Aerospace and Electronic Systems*, vol. AES-3, no. 1, pp. 107–115, Jan. 1967.

[118] K. Jain, M. Klosner, M. Zemel, and S. Raghunandan, "Flexible Electronics and Displays: High-Resolution, Roll-to-Roll, Projection Lithography and Photoablation Processing Technologies for High-Throughput Production," *Proceedings of the IEEE*, vol. 93, no. 8, pp. 1500–1510, Aug. 2005.

[119] D.-H. Kim, J. Song, W. M. Choi, H.-S. Kim, R.-H. Kim, Z. Liu, Y. Y. Huang, K.-C. Hwang, Y.-w. Zhang, and J. A. Rogers, "Materials and noncoplanar mesh designs for integrated circuits with linear elastic responses to extreme mechanical deformations," *Proceedings of the National Academy of Sciences*, vol. 105, no. 48, pp. 18 675–18 680, Dec. 2008.

[120] G. H. Gelinck, H. E. A. Huitema, E. v. Veenendaal, E. Cantatore, L. Schrijnemakers, J. B. P. H. v. d. Putten, T. C. T. Geuns, M. Beenhakkers, J. B. Giesbers, B.-H. Huisman, E. J. Meijer, E. M. Benito, F. J. Touwslager, A. W. Marsman, B. J. E. v. Rens, and D. M. d. Leeuw, "Flexible active-matrix displays and shift registers based on solution-processed organic transistors," *Nature Materials*, vol. 3, no. 2, pp. 106–110, Feb. 2004.

[121] J. A. Rogers, Z. Bao, K. Baldwin, A. Dodabalapur, B. Crone, V. R. Raju, V. Kuck, H. Katz, K. Amundson, J. Ewing, and P. Drzaic, "Paper-like electronic displays: Large-area rubber-stamped plastic sheets of electronics and microencapsulated electrophoretic inks," *Proceedings of the National Academy of Sciences*, vol. 98, no. 9, pp. 4835–4840, Apr. 2001.

[122] C. Wang and G. G. Wallace, "Flexible Electrodes and Electrolytes for Energy Storage," *Electrochimica Acta*, vol. 175, pp. 87–95, Sep. 2015.

[123] Perera Sanjaya D., Patel Bijal, Nijem Nour, Roodenko Katy, Seitz Oliver, Ferraris John P., Chabal Yves J., and Balkus Kenneth J., "Vanadium Oxide NanowireCarbon Nanotube BinderFree Flexible Electrodes for Supercapacitors," *Advanced Energy Materials*, vol. 1, no. 5, pp. 936–945, Sep. 2011.

[124] S.-I. Park, Y. Xiong, R.-H. Kim, P. Elvikis, M. Meitl, D.-H. Kim, J. Wu, J. Yoon, C.-J. Yu, Z. Liu, Y. Huang, K.-c. Hwang, P. Ferreira, X. Li, K. Choquette, and J. A. Rogers, "Printed Assemblies of Inorganic Light-Emitting Diodes for Deformable and Semitransparent Displays," *Science*, vol. 325, no. 5943, pp. 977–981, Aug. 2009.

[125] P. Salonen, M. Keskilammi, J. Rantanen, and L. Sydanheimo, "A novel Bluetooth antenna on flexible substrate for smart clothing," in *2001 IEEE International Conference on Systems, Man and Cybernetics. e-Systems and e-Man for Cybernetics in Cyberspace (Cat.No.01CH37236)*, vol. 2, 2001, pp. 789–794 vol.2.

[126] C. Cibin, P. Leuchtmann, M. Gimersky, R. Vahldieck, and S. Moscibroda, "A flexible wearable antenna," in *IEEE Antennas and Propagation Society Symposium, 2004.*, vol. 4, Jun. 2004, pp. 3589–3592 Vol.4.

[127] J. C. G. Matthews and G. Pettitt, "Development of flexible, wearable antennas," in *2009 3rd European Conference on Antennas and Propagation*, Mar. 2009, pp. 273–277.

[128] Kim DaeHyeong, Xiao Jianliang, Song Jizhou, Huang Yonggang, and Rogers John A., "Stretchable, Curvilinear Electronics Based on Inorganic Materials," *Advanced Materials*, vol. 22, no. 19, pp. 2108–2124, May 2010.

[129] D.-H. Kim, N. Lu, R. Ma, Y.-S. Kim, R.-H. Kim, S. Wang, J. Wu, S. M. Won, H. Tao, A. Islam, K. J. Yu, T.-i. Kim, R. Chowdhury, M. Ying, L. Xu, M. Li, H.-J. Chung, H. Keum, M. McCormick, P. Liu, Y.-W. Zhang, F. G. Omenetto, Y. Huang, T. Coleman, and J. A. Rogers, "Epidermal Electronics," *Science*, vol. 333, no. 6044, pp. 838–843, Aug. 2011.

[130] Baca Alfred J., Ahn Jong-Hyun, Sun Yugang, Meitl Matthew A., Menard Etienne, Kim Hoon-Sik, Choi Won Mook, Kim Dae-Hyeong, Huang Young, and

Rogers John A., "Semiconductor Wires and Ribbons fo High- Performance Flexible Electronics," *Angewandte Chemie International Edition*, vol. 47, no. 30, pp. 5524–5542, Jul. 2008.

[131] J. A. Rogers, T. Someya, and Y. Huang, "Materials and Mechanics for Stretchable Electronics," *Science*, vol. 327, no. 5973, pp. 1603–1607, Mar. 2010.

[132] Ko Heung Cho, Shin Gunchul, Wang Shuodao, Stoykovich Mark P., Lee Jeong Won, Kim DongHun, Ha Jeong Sook, Huang Yonggang, Hwang KehChih, and Rogers John A., "Curvilinear Electronics Formed Using Silicon Membrane Circuits and Elastomeric Transfer Elements," *Small*, vol. 5, no. 23, pp. 2703–2709, Dec. 2009.

[133] D.-H. Kim, N. Lu, Y. Huang, and J. A. Rogers, "Materials for stretchable electronics in bioinspired and biointegrated devices," *MRS Bulletin*, vol. 37, no. 3, pp. 226–235, Mar. 2012.

[134] P. J. Hung, K. Jeong, G. L. Liu, and L. P. Lee, "Microfabricated suspensions for electrical connections on the tunable elastomer membrane," *Applied Physics Letters*, vol. 85, no. 24, pp. 6051–6053, Dec. 2004.

[135] S. P. Lacour, J. Jones, S. Wagner, T. Li, and Z. Suo, "Stretchable Interconnects for Elastic Electronic Surfaces," *Proceedings of the IEEE*, vol. 93, no. 8, pp. 1459–1467, Aug. 2005.

[136] D.-H. Kim and J. A. Rogers, "Stretchable Electronics: Materials Strategies and Devices," *Advanced Materials*, vol. 20, no. 24, pp. 4887–4892, Dec. 2008.

[137] S. Xu, Y. Zhang, J. Cho, J. Lee, X. Huang, L. Jia, J. A. Fan, Y. Su, J. Su, H. Zhang, H. Cheng, B. Lu, C. Yu, C. Chuang, T.-i. Kim, T. Song, K. Shigeta, S. Kang, C. Dagdeviren, I. Petrov, P. V. Braun, Y. Huang, U. Paik, and J. A. Rogers, "Stretchable batteries with self-similar serpentine interconnects and integrated wireless recharging systems," *Nature Communications*, vol. 4, p. 1543, Feb. 2013.

[138] Kim Jeonghyun, Banks Anthony, Cheng Huanyu, Xie Zhaoqian, Xu Sheng, Jang KyungIn, Lee Jung Woo, Liu Zhuangjian, Gutruf Philipp, Huang Xian, Wei Pinghung, Liu Fei, Li Kan, Dalal Mitul, Ghaffari Roozbeh, Feng Xue, Huang Yonggang, Gupta Sanjay, Paik Ungyu, and Rogers John A., "Epidermal Electronics with Advanced Capabilities in NearField Communication," *Small*, vol. 11, no. 8, pp. 906–912, Feb. 2015.

[139] Hu Xiaolong, Krull Peter, de Graff Bassel, Dowling Kevin, Rogers John A., and Arora William J., "Stretchable InorganicSemiconductor Electronic Systems," *Advanced Materials*, vol. 23, no. 26, pp. 2933–2936, Jul. 2011.

[140] Gray D. S., Tien J., and Chen C. S., "High-Conductivity Elastomeric Electronics," *Advanced Materials*, vol. 16, no. 5, pp. 393–397, Feb. 2004.

[141] Y. Y. Hsu, B. Dimcic, M. Gonzalez, F. Bossuyt, J. Vanfleteren, and I. D. Wolf, "Reliability assessment of stretchable interconnects," in *2010 5th International Microsystems Packaging Assembly and Circuits Technology Conference*, Oct. 2010, pp. 1–4.

[142] F. Bossuyt, J. Guenther, T. Lher, M. Seckel, T. Sterken, and J. de Vries, "Cyclic endurance reliability of stretchable electronic substrates," *Microelectronics Reliability*, vol. 51, no. 3, pp. 628–635, Mar. 2011.

[143] S. P. Lacour, D. Chan, S. Wagner, T. Li, and Z. Suo, "Mechanisms of reversible stretchability of thin metal films on elastomeric substrates," *Applied Physics Letters*, vol. 88, no. 20, p. 204103, May 2006.

[144] N. B. Morley, J. Burris, L. C. Cadwallader, and M. D. Nornberg, "GaInSn usage in the research laboratory," *Review of Scientific Instruments*, vol. 79, no. 5, p. 056107, May 2008.

[145] M. D. Dickey, R. C. Chiechi, R. J. Larsen, E. A. Weiss, D. A. Weitz, and G. M. Whitesides, "Eutectic Gallium-Indium (EGaIn): A Liquid Metal Alloy for the Formation of Stable Structures in Microchannels at Room Temperature," *Advanced Functional Materials*, vol. 18, no. 7, pp. 1097–1104, Apr. 2008.

[146] C. Ladd, J.-H. So, J. Muth, and M. D. Dickey, "3d Printing of Free Standing Liquid Metal Microstructures," *Advanced Materials*, vol. 25, no. 36, pp. 5081–5085, Sep. 2013.

[147] Y.-L. Park, C. Majidi, R. Kramer, P. Brard, and R. J. Wood, "Hyperelastic pressure sensing with a liquid-embedded elastomer," *Journal of Micromechanics and Microengineering*, vol. 20, no. 12, p. 125029, Dec. 2010.

[148] M. D. Dickey, "Emerging Applications of Liquid Metals Featuring Surface Oxides," *ACS Applied Materials & Interfaces*, vol. 6, no. 21, pp. 18 369–18 379, Nov. 2014.

[149] A. Tabatabai, A. Fassler, C. Usiak, and C. Majidi, "Liquid-Phase GalliumIndium Alloy Electronics with Microcontact Printing," *Langmuir*, vol. 29, no. 20, pp. 6194–6200, May 2013.

[150] J. Wissman, T. Lu, and C. Majidi, "Soft-matter electronics with stencil lithography," in *2013 IEEE Sensors*, 2013, pp. 1–4.

[151] Q. Zhang, Y. Gao, and J. Liu, "Atomized spraying of liquid metal droplets on desired substrate surfaces as a generalized way for ubiquitous printed electronics," *Applied Physics A*, pp. 1–7, 2013.

[152] D. Kim, D.-W. Lee, W. Choi, and J.-B. Lee, "A Super-Lyophobic 3-D PDMS Channel as a Novel Microfluidic Platform to Manipulate Oxidized Galinstan," *Journal of Microelectromechanical Systems*, vol. 22, no. 6, pp. 1267–1275, Dec. 2013.

[153] R. K. Kramer, J. W. Boley, H. A. Stone, J. C. Weaver, and R. J. Wood, "Effect of Microtextured Surface Topography on the Wetting Behavior of Eutectic GalliumIndium Alloys," *Langmuir*, vol. 30, no. 2, pp. 533–539, Jan. 2014.

[154] G. Li, X. Wu, and D.-W. Lee, "Selectively plated stretchable liquid metal wires for transparent electronics," *Sensors and Actuators B: Chemical*, vol. 221, pp. 1114–1119, Dec. 2015.

[155] J. W. Boley, E. L. White, and R. K. Kramer, "Mechanically Sintered GalliumIndium Nanoparticles," *Advanced Materials*, vol. 27, no. 14, pp. 2355–2360, Apr. 2015.

[156] Lu Tong, Finkenauer Lauren, Wissman James, and Majidi Carmel, "Rapid Prototyping for SoftMatter Electronics," *Advanced Functional Materials*, vol. 24, no. 22, pp. 3351–3356, Jun. 2014.

[157] D. M. Vogt, Y.-L. Park, and R. J. Wood, "Design and Characterization of a Soft Multi-Axis Force Sensor Using Embedded Microfluidic Channels," *IEEE Sensors Journal*, vol. 13, no. 10, pp. 4056–4064, Oct. 2013.

[158] So JuHee, Thelen Jacob, Qusba Amit, Hayes Gerard J., Lazzi Gianluca, and Dickey Michael D., "Reversibly Deformable and Mechanically Tunable Fluidic Antennas," *Advanced Functional Materials*, vol. 19, no. 22, pp. 3632–3637, Nov. 2009.

[159] Kubo Masahiro, Li Xiaofeng, Kim Choongik, Hashimoto Michinao, Wiley Benjamin J., Ham Donhee, and Whitesides George M., "Stretchable Microfluidic Radiofrequency Antennas," *Advanced Materials*, vol. 22, no. 25, pp. 2749–2752, Apr. 2010.

[160] k. h. Zhigang Wu, "Microfluidic Stretchable Radio Frequency Devices," *Proceedings of the IEEE*, 2015.

[161] E. Palleau, S. Reece, S. C. Desai, M. E. Smith, and M. D. Dickey, "Self-Healing Stretchable Wires for Reconfigurable Circuit Wiring and 3d Microfluidics," *Advanced Materials*, vol. 25, no. 11, pp. 1589–1592, Mar. 2013.

[162] J.-H. So, H.-J. Koo, M. D. Dickey, and O. D. Velev, "Ionic Current Rectification in Soft-Matter Diodes with Liquid-Metal Electrodes," *Advanced Functional Materials*, vol. 22, no. 3, pp. 625–631, Feb. 2012.

[163] W.-Y. Tseng, J. S. Fisher, J. L. Prieto, K. Rinaldi, G. Alapati, and A. P. Lee, "A slow-adapting microfluidic-based tactile sensor," *Journal of Micromechanics and Microengineering*, vol. 19, no. 8, p. 085002, Aug. 2009.

[164] N. Wettels, V. J. Santos, R. S. Johansson, and G. E. Loeb, "Biomimetic Tactile Sensor Array," *Advanced Robotics*, vol. 22, no. 8, pp. 829–849, Jan. 2008.

[165] Y.-N. Cheung, Y. Zhu, C.-H. Cheng, C. Chao, and W. W.-F. Leung, "A novel fluidic strain sensor for large strain measurement," *Sensors and Actuators A: Physical*, vol. 147, no. 2, pp. 401–408, Oct. 2008.

[166] G. Cummins and M. P. Y. Desmulliez, "Inkjet printing of conductive materials: a review," *Circuit World*, vol. 38, no. 4, pp. 193–213, Nov. 2012.

[167] Y. Zhang, P. Zhu, G. Li, T. Zhao, X. Fu, R. Sun, F. Zhou, and C.-p. Wong, "Facile Preparation of Monodisperse, Impurity-Free, and Antioxidation Copper Nanoparticles on a Large Scale for Application in Conductive Ink," *ACS Applied Materials & Interfaces*, vol. 6, no. 1, pp. 560–567, Jan. 2014.

[168] S. Merilampi, T. Laine-Ma, and P. Ruuskanen, "The characterization of electrically conductive silver ink patterns on flexible substrates," *Microelectronics Reliability*, vol. 49, no. 7, pp. 782–790, Jul. 2009.

[169] S. Hong, J. Yeo, G. Kim, D. Kim, H. Lee, J. Kwon, H. Lee, P. Lee, and S. H. Ko, "Nonvacuum, Maskless Fabrication of a Flexible Metal Grid Transparent Conductor by Low-Temperature Selective Laser Sintering of Nanoparticle Ink," *ACS Nano*, vol. 7, no. 6, pp. 5024–5031, Jun. 2013.

[170] M. Grouchko, A. Kamyshny, C. F. Mihailescu, D. F. Anghel, and S. Magdassi, "Conductive Inks with a Built-In Mechanism That Enables Sintering at Room Temperature," *ACS Nano*, vol. 5, no. 4, pp. 3354–3359, Apr. 2011.

[171] Kamyshny Alexander, BenMoshe Matti, Aviezer Shai, and Magdassi Shlomo, "InkJet Printing of Metallic Nanoparticles and Microemulsions," *Macromolecular Rapid Communications*, vol. 26, no. 4, pp. 281–288, Feb. 2005.

[172] F. Loffredo, A. D. G. D. Mauro, G. Burrasca, V. La Ferrara, L. Quercia, E. Massera, G. Di Francia, and D. D. Sala, "Ink-jet printing technique in polymer/carbon black sensing device fabrication," *Sensors and Actuators B: Chemical*, vol. 143, no. 1, pp. 421–429, Dec. 2009.

[173] S. M. Bidoki, D. M. Lewis, M. Clark, A. Vakorov, P. A. Millner, and D. McGorman, "Ink-jet fabrication of electronic components," *Journal of Micromechanics and Microengineering*, vol. 17, no. 5, p. 967, 2007.

[174] T.-H. Kang, C. Merritt, B. Karaguzel, J. Wilson, P. Franzon, B. Pourdeyhimi, E. Grant, and T. Nagle, "Sensors on Textile Substrates for Home-Based Healthcare Monitoring," in *1st Transdisciplinary Conference on Distributed Diagnosis and Home Healthcare, 2006. D2H2.*, Apr. 2006, pp. 5–7.

[175] Y.-L. Tai and Z.-G. Yang, "Fabrication of paper-based conductive patterns for flexible electronics by direct-writing," *Journal of Materials Chemistry*, vol. 21, no. 16, pp. 5938–5943, 2011.

[176] H.-T. Wang, O. A. Nafday, J. R. Haaheim, E. Tevaarwerk, N. A. Amro, R. G. Sanedrin, C.-Y. Chang, F. Ren, and S. J. Pearton, "Toward conductive traces: Dip Pen Nanolithography of silver nanoparticle-based inks," *Applied Physics Letters*, vol. 93, no. 14, p. 143105, Oct. 2008.

[177] Russo Analisa, Ahn Bok Yeop, Adams Jacob J., Duoss Eric B., Bernhard Jennifer T., and Lewis Jennifer A., "PenonPaper Flexible Electronics," *Advanced Materials*, vol. 23, no. 30, pp. 3426–3430, Jun. 2011.

[178] L. Y. Xu, G. Y. Yang, H. Y. Jing, J. Wei, and Y. D. Han, "Aggraphene hybrid conductive ink for writing electronics," *Nanotechnology*, vol. 25, no. 5, p. 055201, 2014.

[179] S. Khan, L. Lorenzelli, and R. Dahiya, "Screen printed flexible pressure sensors skin," in *Advanced Semiconductor Manufacturing Conference (ASMC), 2014 25th Annual SEMI*, May 2014, pp. 219–224.

[180] K.-Y. Chun, Y. Oh, J. Rho, J.-H. Ahn, Y.-J. Kim, H. R. Choi, and S. Baik, "Highly conductive, printable and stretchable composite films of carbon nanotubes and silver," *Nature Nanotechnology*, vol. 5, no. 12, pp. 853–857, Dec. 2010.

[181] M. Park, J. Im, M. Shin, Y. Min, J. Park, H. Cho, S. Park, M.-B. Shim, S. Jeon, D.-Y. Chung, J. Bae, J. Park, U. Jeong, and K. Kim, "Highly stretchable electric circuits from a composite material of silver nanoparticles and elastomeric fibres," *Nature Nanotechnology*, vol. 7, no. 12, pp. 803–809, Dec. 2012.

[182] Y. J. Yang, M. Y. Cheng, W. Y. Chang, L. C. Tsao, S. A. Yang, W. P. Shih, F. Y. Chang, S. H. Chang, and K. C. Fan, "An integrated flexible temperature and tactile sensing array using PI-copper films," *Sensors and Actuators A: Physical*, vol. 143, no. 1, pp. 143–153, May 2008.

[183] R. Verdejo, M. M. Bernal, L. J. Romasanta, and M. A. Lopez-Manchado, "Graphene filled polymer nanocomposites," *J. Mater. Chem.*, vol. 21, no. 10, pp. 3301–3310, 2011.

[184] M. Chen, T. Tao, L. Zhang, W. Gao, and C. Li, "Highly conductive and stretchable polymer composites based on graphene/MWCNT network," *Chemical Communications*, vol. 49, no. 16, p. 1612, 2013.

[185] M. Knite, V. Teteris, A. Kiploka, and J. Kaupuzs, "Polyisoprene-carbon black nanocomposites as tensile strain and pressure sensor materials," *Sensors and Actuators A: Physical*, vol. 110, no. 13, pp. 142–149, Feb. 2004.

[186] D. J. Lipomi, M. Vosgueritchian, B. C.-K. Tee, S. L. Hellstrom, J. A. Lee, C. H. Fox, and Z. Bao, "Skin-like pressure and strain sensors based on transparent elastic films of carbon nanotubes," *Nature Nanotechnology*, vol. 6, no. 12, pp. 788–792, Dec. 2011.

[187] S. Jung, J. H. Kim, J. Kim, S. Choi, J. Lee, I. Park, T. Hyeon, and D.-H. Kim, "Reverse-Micelle-Induced Porous Pressure-Sensitive Rubber for Wearable HumanMachine Interfaces," *Advanced Materials*, vol. 26, no. 28, pp. 4825–4830, Jul. 2014.

[188] A. Fassler and C. Majidi, "Liquid-Phase Metal Inclusions for a Conductive Polymer Composite," *Advanced Materials*, vol. 27, no. 11, pp. 1928–1932, Mar. 2015.

[189] Lin Yiliang, Cooper Christopher, Wang Meng, Adams Jacob J., Genzer Jan, and Dickey Michael D., "Handwritten, Soft Circuit Boards and Antennas Using Liquid Metal Nanoparticles," *Small*, vol. 11, no. 48, pp. 6397–6403, Nov. 2015.

[190] S. G. Kandlikar and W. J. Grande, "Evolution of Microchannel Flow Passages: Thermohydraulic Performance and Fabrication Technology," *Heat Transfer Engineering*, vol. 24, no. 1, pp. 3–17, 2003.

[191] Y. Xia and a. G. M. Whitesides, "Soft Lithography," *Annual Review of Materials Science*, vol. 28, no. 1, pp. 153–184, 1998.

[192] L. Geppert, "Semiconductor lithography for the next millennium," *IEEE Spectrum*, vol. 33, no. 4, pp. 33–38, Apr. 1996.

[193] S. Okazaki, "Resolution limits of optical lithography," *Journal of Vacuum Science & Technology B: Microelectronics and Nanometer Structures Processing, Measurement, and Phenomena*, vol. 9, no. 6, pp. 2829–2833, Nov. 1991.

[194] E. A. Waddell, "Laser Ablation as a Fabrication Technique for Microfluidic Devices," in *Microfluidic Techniques*, ser. Methods In Molecular Biology. Humana Press, 2006, pp. 27–38.

[195] H. J. Kim, T. Maleki, P. Wei, and B. Ziaie, "A Biaxial Stretchable Interconnect With Liquid-Alloy-Covered Joints on Elastomeric Substrate," *Journal of Microelectromechanical Systems*, vol. 18, no. 1, pp. 138–146, Feb. 2009.

[196] H.-J. Kim, C. Son, and B. Ziaie, "A multiaxial stretchable interconnect using liquid-alloy-filled elastomeric microchannels," *Applied Physics Letters*, vol. 92, no. 1, p. 011904, Jan. 2008.

[197] T. Li, Z. Huang, Z. Suo, S. P. Lacour, and S. Wagner, "Stretchability of thin metal films on elastomer substrates," *Applied Physics Letters*, vol. 85, no. 16, pp. 3435–3437, Oct. 2004.

[198] Y. Arafat, I. Dutta, and R. Panat, "Super-stretchable metallic interconnects on polymer with a linear strain of up to 100%," *Applied Physics Letters*, vol. 107, no. 8, p. 081906, Aug. 2015.

[199] T. Lu, J. Wissman, Ruthika, and C. Majidi, "Soft Anisotropic Conductors as Electric Vias for Ga-Based Liquid Metal Circuits," *ACS Applied Materials & Interfaces*, vol. 7, no. 48, pp. 26 923–26 929, Dec. 2015.

[200] Y. L. Zheng, X. R. Ding, C. C. Y. Poon, B. P. L. Lo, H. Zhang, X. L. Zhou, G. Z. Yang, N. Zhao, and Y. T. Zhang, "Unobtrusive Sensing and Wearable Devices for Health Informatics," *IEEE Transactions on Biomedical Engineering*, vol. 61, no. 5, pp. 1538–1554, May 2014.

[201] H.-K. Lee, S.-I. Chang, and E. Yoon, "A Flexible Polymer Tactile Sensor: Fabrication and Modular Expandability for Large Area Deployment," *Journal of Microelectromechanical Systems*, vol. 15, no. 6, pp. 1681–1686, Dec. 2006.

[202] J. Engel, J. Chen, and C. Liu, "Development of polyimide flexible tactile sensor skin," *Journal of Micromechanics and Microengineering*, vol. 13, no. 3, p. 359, May 2003.

[203] J. K. Paik, R. K. Kramer, and R. J. Wood, "Stretchable circuits and sensors for robotic origami," in *Intelligent Robots and Systems (IROS), 2011 IEEE/RSJ International Conference on*, 2011, pp. 414–420.

[204] Y.-L. Park and R. J. Wood, "Smart pneumatic artificial muscle actuator with embedded microfluidic sensing," in *2013 IEEE Sensors*, 2013, pp. 1–4.

[205] G. Berselli, Ed., *Smart Actuation and Sensing Systems - Recent Advances and Future Challenges*. InTech, Oct. 2012.

[206] P. Polygerinos, Z. Wang, K. C. Galloway, R. J. Wood, and C. J. Walsh, "Soft robotic glove for combined assistance and at-home rehabilitation," *Robotics and Autonomous Systems*, vol. 73, pp. 135–143, Nov. 2015.

[207] A. T. Asbeck, K. Schmidt, I. Galiana, D. Wagner, and C. J. Walsh, "Multi-joint soft exosuit for gait assistance," in *2015 IEEE International Conference on Robotics and Automation (ICRA)*, May 2015, pp. 6197–6204.

[208] A. T. Asbeck, S. M. M. D. Rossi, I. Galiana, Y. Ding, and C. J. Walsh, "Stronger, Smarter, Softer: Next-Generation Wearable Robots," *IEEE Robotics Automation Magazine*, vol. 21, no. 4, pp. 22–33, Dec. 2014.

[209] Y. Meng, Y. L. Park, E. Martinez-Villalpando, P. Aubin, M. Zisook, L. Stirling, R. J. Wood, and C. J. Walsh, "Soft wearable motion sensing suit for lower limb biomechanics measurements," in *2013 IEEE International Conference on Robotics and Automation*, May 2013, pp. 5309–5316.

[210] Lu Nanshu, Lu Chi, Yang Shixuan, and Rogers John, "Highly Sensitive Skin-Mountable Strain Gauges Based Entirely on Elastomers," *Advanced Functional Materials*, vol. 22, no. 19, pp. 4044–4050, Jun. 2012.

[211] F. Gemperle, N. Ota, and D. Siewiorek, "Design of a wearable tactile display," in *Proceedings Fifth International Symposium on Wearable Computers*, 2001, pp. 5–12.

[212] G. Saccomandi and R. W. Ogden, Eds., *Mechanics and Thermomechanics of Rubberlike Solids*, ser. CISM International Centre for Mechanical Sciences. Wien: Springer-Verlag, 2004.

[213] R. W. Ogden, G. Saccomandi, and I. Sgura, "Fitting hyperelastic models to experimental data," *Computational Mechanics*, vol. 34, no. 6, pp. 484–502, Nov. 2004.

[214] R. W. Ogden and R. W. Ogden, "Nonlinear elasticity with application to material modelling," 2003.

[215] A. Dorfmann and R. W. Ogden, "A pseudo-elastic model for loading, partial unloading and reloading of particle-reinforced rubber," *International Journal of Solids and Structures*, vol. 40, no. 11, pp. 2699–2714, Jun. 2003.

[216] G. A. Holzapfel and R. W. Ogden, *Mechanics of Biological Tissue*. Springer Science & Business Media, Jun. 2006, google-Books-ID: TL0dGo0FINwC.

[217] H.-K. Lee, S.-I. Chang, and E. Yoon, "Dual-Mode Capacitive Proximity Sensor for Robot Application: Implementation of Tactile and Proximity Sensing Capability on a Single Polymer Platform Using Shared Electrodes," *IEEE Sensors Journal*, vol. 9, no. 12, pp. 1748–1755, Dec. 2009.

[218] E. Meng, X. Zhang, and W. Benard, "Additive Processes for Polymeric Materials," in *MEMS Materials and Processes Handbook*, ser. MEMS Reference Shelf. Springer, Boston, MA, 2011, pp. 193–271.

[219] C. Laschi and M. Cianchetti, "Soft Robotics: New Perspectives for Robot Bodyware and Control," *Frontiers in bioengineering and biotechnology*, vol. 2, Jan. 2014.

[220] A. Mozeika, E. Steltz, and H. M. Jaeger, "The first steps of a robot based on jamming skin enabled locomotion," in *2009 IEEE/RSJ International Conference on Intelligent Robots and Systems*, Oct. 2009, pp. 408–409.

[221] E. Steltz, A. Mozeika, N. Rodenberg, E. Brown, and H. Jaeger, "JSEL: Jamming Skin Enabled Locomotion," in *IEEE/RSJ International Conference on Intelligent Robots and Systems, 2009. IROS 2009*, Oct. 2009, pp. 5672–5677.

[222] F. Renda, M. Cianchetti, M. Giorelli, A. Arienti, and C. Laschi, "A 3d steady-state model of a tendon-driven continuum soft manipulator inspired by the octopus arm," *Bioinspiration & Biomimetics*, vol. 7, no. 2, p. 025006, 2012.

[223] M. Luo, Y. Pan, E. H. Skorina, W. Tao, F. Chen, S. Ozel, and C. D. Onal, "Slithering towards autonomy: a self-contained soft robotic snake platform with integrated curvature sensing," *Bioinspiration & Biomimetics*, vol. 10, no. 5, p. 055001, 2015.

[224] C. D. Onal, R. J. Wood, and D. Rus, "An Origami-Inspired Approach to Worm Robots," *IEEE/ASME Transactions on Mechatronics*, vol. 18, no. 2, pp. 430–438, Apr. 2013.

[225] N. G. Cheng, M. B. Lobovsky, S. J. Keating, A. M. Setapen, K. I. Gero, A. E. Hosoi, and K. D. Iagnemma, "Design and Analysis of a Robust, Low-cost, Highly Articulated manipulator enabled by jamming of granular media," in *2012 IEEE International Conference on Robotics and Automation*, May 2012, pp. 4328–4333.

[226] S. M. Felton, M. T. Tolley, C. D. Onal, D. Rus, and R. J. Wood, "Robot self-assembly by folding: A printed inchworm robot," in *2013 IEEE International Conference on Robotics and Automation*, May 2013, pp. 277–282.

[227] S. M. Felton, M. T. Tolley, B. Shin, C. D. Onal, E. D. Demaine, D. Rus, and R. J. Wood, "Self-folding with shape memory composites," *Soft Matter*, vol. 9, no. 32, pp. 7688–7694, Jul. 2013.

[228] C. Yu, Z. Duan, P. Yuan, Y. Li, Y. Su, X. Zhang, Y. Pan, L. L. Dai, R. G. Nuzzo, Y. Huang, H. Jiang, and J. A. Rogers, "Electronically Programmable, Reversible Shape Change in Two- and Three-Dimensional Hydrogel Structures," *Advanced Materials*, vol. 25, no. 11, pp. 1541–1546, 2013.

[229] N. W. Bartlett, M. T. Tolley, J. T. B. Overvelde, J. C. Weaver, B. Mosadegh, K. Bertoldi, G. M. Whitesides, and R. J. Wood, "A 3d-printed, functionally graded soft robot powered by combustion," *Science*, vol. 349, no. 6244, pp. 161–165, Jul. 2015.

[230] L. Zheng, S. Yoshida, Y. Morimoto, H. Onoe, and S. Takeuchi, "Pneumatic balloon actuator with tunable bending points," in *2015 28th IEEE International Conference on Micro Electro Mechanical Systems (MEMS)*, Jan. 2015, pp. 18–21.

[231] C. Liu, "Recent Developments in Polymer MEMS," *Advanced Materials*, vol. 19, no. 22, pp. 3783–3790, 2007.

[232] H. L. Filiatrault, R. S. Carmichael, R. A. Boutette, and T. B. Carmichael, "A Self-Assembled, Low-Cost, Microstructured Layer for Extremely Stretchable Gold Films," *ACS Applied Materials & Interfaces*, vol. 7, no. 37, pp. 20 745–20 752, Sep. 2015.

[233] S. Ozel, N. A. Keskin, D. Khea, and C. D. Onal, "A precise embedded curvature sensor module for soft-bodied robots," *Sensors and Actuators A: Physical*, vol. 236, pp. 349–356, Dec. 2015.

[234] R. C. Chiechi, E. A. Weiss, M. D. Dickey, and G. M. Whitesides, "Eutectic GalliumIndium (EGaIn): A Moldable Liquid Metal for Electrical Characterization of Self-Assembled Monolayers," *Angewandte Chemie International Edition*, vol. 47, no. 1, pp. 142–144, 2008.

[235] C. M. Jackson, H. M. Wagner, and R. J. Wasilewski, "55-Nitinol - The Alloy with a Memory: It's Physical Metallurgy Properties, and Applications. NASA SP-5110," *NASA Special Publication*, vol. 5110, 1972.

[236] C. Liang and C. A. Rogers, "Design of Shape Memory Alloy Actuators," *Journal of Mechanical Design*, vol. 114, no. 2, pp. 223–230, Jun. 1992.

[237] K. Otsuka and X. Ren, "Recent developments in the research of shape memory alloys," *Intermetallics*, vol. 7, no. 5, pp. 511–528, May 1999.

[238] M. Singaperumal, M. Sreekumar, T. Nagarajan, R. Molfino, and M. Zoppi, "Critical review of current trends in shape memory alloy actuators for intelligent robots," *Industrial Robot: the international journal of robotics research and application*, vol. 34, no. 4, pp. 285–294, Jun. 2007.

[239] Y. Bellouard, "Shape memory alloys for microsystems: A review from a material research perspective," *Materials Science and Engineering: A*, vol. 481-482, pp. 582–589, May 2008.

[240] P. Kumar and D. Lagoudas, "Introduction to Shape Memory Alloys," in *Shape Memory Alloys: Modeling and Engineering Applications*. Boston, MA: Springer US, 2008, pp. 1–51.

[241] D. Tarnita, D. N. Tarnita, N. Bzdoaca, I. Mndrila, and M. Vasilescu, "Properties and medical applications of shape memory alloys," *Romanian Journal of Morphology and Embyology*, vol. 50, no. 1, pp. 15–21, 2009.

[242] L. Sun, W. M. Huang, Z. Ding, Y. Zhao, C. C. Wang, H. Purnawali, and C. Tang, "Stimulus-responsive shape memory materials: A review," *Materials & Design*, vol. 33, pp. 577–640, Jan. 2012.

[243] S. Barbarino, E. I. S. Flores, R. M. Ajaj, I. Dayyani, and M. I. Friswell, "A review on shape memory alloys with applications to morphing aircraft," *Smart Materials and Structures*, vol. 23, no. 6, p. 063001, Apr. 2014.

[244] R. A. A. de Aguiar, W. C. de Castro Leo Neto, M. A. Savi, and P. M. Calas Lopes Pacheco, "Shape Memory Alloy Helical Springs Performance: Modeling and Experimental Analysis," 2013.

[245] K. Ikuta, M. Tsukamoto, and S. Hirose, "Shape memory alloy servo actuator system with electric resistance feedback and application for active endoscope," in *1988 IEEE International Conference on Robotics and Automation Proceedings*, Apr. 1988, pp. 427–430 vol.1.

[246] K. Ikuta, "Micro/miniature shape memory alloy actuator," in *, IEEE International Conference on Robotics and Automation Proceedings*, May 1990, pp. 2156–2161 vol.3.

[247] K. Ikuta, M. Tsukamoto, and S. Hirose, "Mathematical model and experimental verification of shape memory alloy for designing micro actuator," in *IEEE Micro Electro Mechanical Systems, 1991, MEMS '91, Proceedings. An Investigation of Micro Structures, Sensors, Actuators, Machines and Robots*, Jan. 1991, pp. 103–108.

[248] D. Grant and V. Hayward, "Variable structure control of shape memory alloy actuators," *IEEE Control Systems Magazine*, vol. 17, no. 3, pp. 80–88, Jun. 1997.

[249] S. Majima, K. Kodama, and T. Hasegawa, "Modeling of shape memory alloy actuator and tracking control system with the model," *IEEE Transactions on Control Systems Technology*, vol. 9, no. 1, pp. 54–59, Jan. 2001.

[250] F. Gao, H. Deng, and Y. Zhang, "Hybrid actuator combining shape memory alloy with DC motor for prosthetic fingers," *Sensors and Actuators A: Physical*, vol. 223, pp. 40–48, Mar. 2015.

[251] J. Koh and K. Cho, "Omegabot : Biomimetic inchworm robot using SMA coil actuator and smart composite microstructures (SCM)," in *2009 IEEE International Conference on Robotics and Biomimetics (ROBIO)*, Dec. 2009, pp. 1154–1159.

[252] H. Godaba, J. Li, Y. Wang, and J. Zhu, "A Soft Jellyfish Robot Driven by a Dielectric Elastomer Actuator," *IEEE Robotics and Automation Letters*, vol. 1, no. 2, pp. 624–631, Jul. 2016.

[253] W.-S. Chu, K.-T. Lee, S.-H. Song, M.-W. Han, J.-Y. Lee, H.-S. Kim, M.-S. Kim, Y.-J. Park, K.-J. Cho, and S.-H. Ahn, "Review of biomimetic underwater robots using smart actuators," *International Journal of Precision Engineering and Manufacturing*, vol. 13, no. 7, pp. 1281–1292, Jul. 2012.

[254] S. Mao, E. Dong, S. Zhang, M. Xu, and J. Yang, "A new soft bionic starfish robot with multi-gaits," in *2013 IEEE/ASME International Conference on Advanced Intelligent Mechatronics (AIM)*, Jul. 2013, pp. 1312–1317.

[255] D. Trivedi, C. D. Rahn, W. M. Kier, and I. D. Walker, "Soft robotics: Biological inspiration, state of the art, and future research," *Applied Bionics and Biomechanics*, vol. 5, no. 3, pp. 99–117, Dec. 2008.

[256] I. D. Walker, "Continuous Backbone Continuum Robot Manipulators," *ISRN Robotics*, vol. 2013, pp. 1–19, 2013.

[257] T. Kawamura, T. Tandai, and H. Takanobu, "Mechanism and control of tongue robot," in *2005 IEEE/RSJ International Conference on Intelligent Robots and Systems*, Aug. 2005, pp. 1041–1046.

[258] H. Takanobu, T. Tandai, and H. Miura, "Multi-DOF flexible robot base on tongue," in *2004 IEEE International Conference on Robotics and Automation, 2004. Proceedings. ICRA '04*, vol. 3, Apr. 2004, pp. 2673–2678 Vol.3.

[259] M. Sfakiotakis, A. Kazakidi, N. Pateromichelakis, and D. Tsakiris, "Octopus-inspired eight-arm robotic swimming by sculling movements," in *2013 IEEE International Conference on Robotics and Automation (ICRA)*, May 2013, pp. 5155–5161.

[260] C. Laschi, M. Cianchetti, B. Mazzolai, L. Margheri, M. Follador, and P. Dario, "Soft Robot Arm Inspired by the Octopus," *Advanced Robotics*, vol. 26, no. 7, pp. 709–727, Jan. 2012.

[261] S. Kim, C. Laschi, and B. Trimmer, "Soft robotics: a bioinspired evolution in robotics," *Trends in Biotechnology*, vol. 31, no. 5, pp. 287–294, May 2013.

[262] S. Gracovetsky, "An hypothesis for the role of the spine in human locomotion: A challenge to current thinking," *Journal of Biomedical Engineering*, vol. 7, no. 3, pp. 205–216, Jul. 1985.

[263] S. A. Wainwright, *Axis and Circumference, The Cylindrical Shape of Plants and Animals*, reprint 2014 ed. Boston: Harvard University Press, 2014.

[264] Q. Zhao, H. Sumioka, K. Nakajima, X. Yu, and R. Pfeifer, "Spine as an engine: effect of spine morphology on spine-driven quadruped locomotion," *Advanced Robotics*, vol. 28, no. 6, pp. 367–378, Mar. 2014.

[265] U. ulha and U. Saranli, "Quadrupedal bounding with an actuated spinal joint," in *2011 IEEE International Conference on Robotics and Automation (ICRA)*, May 2011, pp. 1392–1397.

[266] Q. Zhao, K. Nakajima, H. Sumioka, X. Yu, and R. Pfeifer, "Embodiment enables the spinal engine in quadruped robot locomotion," in *2012 IEEE/RSJ International Conference on Intelligent Robots and Systems*, Oct. 2012, pp. 2449–2456.

[267] J. Reinecke, B. Deutschmann, and D. Fehrenbach, "A structurally flexible humanoid spine based on a tendon-driven elastic continuum," in *2016 IEEE International Conference on Robotics and Automation (ICRA)*, May 2016, pp. 4714–4721.

[268] K. P. Deashapriya, P. A. G. Sampath, W. M. S. B. Wijekoon, N. D. Jayaweera, and A. L. Kulasekera, "Biomimetic flexible robot arm design and kinematic analysis of a novel flexible robot arm," in *2016 Moratuwa Engineering Research Conference (MERCon)*, Apr. 2016, pp. 385–390.

[269] Y. Wei, Y. Chen, Y. Yang, and Y. Li, "A soft robotic spine with tunable stiffness based on integrated ball joint and particle jamming," *Mechatronics*, vol. 33, pp. 84–92, 2016.

[270] T. Kato, I. Okumura, H. Kose, K. Takagi, and N. Hata, "Extended kinematic mapping of tendon-driven continuum robot for neuroendoscopy," in *2014 IEEE/RSJ International Conference on Intelligent Robots and Systems*, Sep. 2014, pp. 1997–2002.

[271] J. S. Mehling, M. A. Diftler, M. Chu, and M. Valvo, "A Minimally Invasive Tendril Robot for In-Space Inspection," in *The First IEEE/RAS-EMBS International Conference on Biomedical Robotics and Biomechatronics, 2006. BioRob 2006.*, Feb. 2006, pp. 690–695.

[272] M. M. Tonapi, I. S. Godage, A. M. Vijaykumar, and I. D. Walker, "Spatial kinematic modeling of a long and thin continuum robotic cable," in *2015 IEEE International Conference on Robotics and Automation (ICRA)*, May 2015, pp. 3755–3761.

[273] D. Palmer, S. Cobos-Guzman, and D. Axinte, "Real-time method for tip following navigation of continuum snake arm robots," *Robotics and Autonomous Systems*, vol. 62, no. 10, pp. 1478–1485, Oct. 2014.

[274] J. Starke, E. Amanov, M. T. Chikhaoui, and J. Burgner-Kahrs, "On the merits of helical tendon routing in continuum robots," in *2017 IEEE/RSJ International Conference on Intelligent Robots and Systems (IROS)*, Sep. 2017, pp. 6470–6476.

[275] D. B. Camarillo, C. R. Carlson, and J. K. Salisbury, "Configuration Tracking for Continuum Manipulators With Coupled Tendon Drive," *IEEE Transactions on Robotics*, vol. 25, no. 4, pp. 798–808, Aug. 2009.

[276] G. Lewis and F. Monasa, "Large deflections of cantilever beams of non-linear materials of the Ludwick type subjected to an end moment," *International Journal of Non-Linear Mechanics*, vol. 17, no. 1, pp. 1–6, 1982.

[277] D. Drotman, S. Jadhav, M. Karimi, P. deZonia, and M. T. Tolley, "3d printed soft actuators for a legged robot capable of navigating unstructured terrain," in *2017 IEEE International Conference on Robotics and Automation (ICRA)*, May 2017, pp. 5532–5538.

[278] K. C. Galloway, K. P. Becker, B. Phillips, J. Kirby, S. Licht, D. Tchernov, R. J. Wood, and D. F. Gruber, "Soft Robotic Grippers for Biological Sampling on Deep Reefs," *Soft Robotics*, vol. 3, no. 1, pp. 23–33, Jan. 2016.

[279] A. D. Marchese, K. Komorowski, C. D. Onal, and D. Rus, "Design and control of a soft and continuously deformable 2d robotic manipulation system," in *2014 IEEE International Conference on Robotics and Automation (ICRA)*, May 2014, pp. 2189–2196.

[280] A. A. Stokes, R. F. Shepherd, S. A. Morin, F. Ilievski, and G. M. Whitesides, "A Hybrid Combining Hard and Soft Robots," *Soft Robotics*, vol. 1, no. P, pp. 70–74, Jul. 2013.

[281] M. Calisti, A. Arienti, F. Renda, G. Levy, B. Hochner, B. Mazzolai, P. Dario, and C. Laschi, "Design and development of a soft robot with crawling and grasping capabilities," in *2012 IEEE International Conference on Robotics and Automation*, May 2012, pp. 4950–4955.

[282] M. Calisti, M. Giorelli, G. Levy, B. Mazzolai, B. Hochner, C. Laschi, and P. Dario, "An octopus-bioinspired solution to movement and manipulation for soft robots," *Bioinspiration & Biomimetics*, vol. 6, no. 3, p. 036002, Sep. 2011.

[283] S. W. Kwok, S. A. Morin, B. Mosadegh, J.-H. So, R. F. Shepherd, R. V. Martinez, B. Smith, F. C. Simeone, A. A. Stokes, and G. M. Whitesides, "Magnetic Assembly of Soft Robots with Hard Components," *Advanced Functional Materials*, vol. 24, no. 15, pp. 2180–2187, Apr. 2014.

[284] S. A. Morin, Y. Shevchenko, J. Lessing, S. W. Kwok, R. F. Shepherd, A. A. Stokes, and G. M. Whitesides, "Using Click-e-Bricks to Make 3d Elastomeric Structures," *Advanced Materials*, vol. 26, no. 34, pp. 5991–5999, Sep. 2014.

[285] M. C. Yuen, R. A. Bilodeau, and R. K. Kramer, "Active Variable Stiffness Fibers for Multifunctional Robotic Fabrics," *IEEE Robotics and Automation Letters*, vol. 1, no. 2, pp. 708–715, Jul. 2016.

[286] A. Mehringer, A. Kandhari, H. Chiel, R. Quinn, and K. Daltorio, "An Integrated Compliant Fabric Skin Softens, Lightens, and Simplifies a Mesh Robot," in *Biomimetic and Biohybrid Systems*, ser. Lecture Notes in Computer Science. Springer, Cham, Jul. 2017, pp. 315–327.

[287] M. W. Hannan and I. D. Walker, "Kinematics and the Implementation of an Elephant's Trunk Manipulator and Other Continuum Style Robots," *Journal of Robotic Systems*, vol. 20, no. 2, pp. 45–63, Feb. 2003.

[288] J. C. Case, E. L. White, V. SunSpiral, and R. Kramer-Bottiglio, "Reducing Actuator Requirements in Continuum Robots Through Optimized Cable Routing," *Soft Robotics*, Oct. 2017.

[289] J. W. Booth, J. C. Case, E. L. White, D. S. Shah, and R. Kramer-Bottiglio, "An addressable pneumatic regulator for distributed control of soft robots," in *2018 IEEE International Conference on Soft Robotics (RoboSoft)*, Apr. 2018, pp. 25–30.

[290] F. Daerden and D. Lefeber, "Pneumatic Artificial Muscles: actuators for robotics and automation," *European Journal of Mechanical and Environmental Engineering*, vol. 47, no. 1, pp. 11–21, 2002.

[291] J. C. Case, J. Booth, D. S. Shah, M. C. Yuen, and R. Kramer-Bottiglio, "State and stiffness estimation using robotic fabrics," in *2018 IEEE International Conference on Soft Robotics (RoboSoft)*, Apr. 2018, pp. 522–527.

[292] J. Case, M. Yuen, M. Mohammed, and R. Kramer, "Sensor Skins: An Overview," in *Stretchable Bioelectronics for Medical Devices and Systems*, ser. Microsystems and Nanosystems, J. A. Rogers, R. Ghaffari, and D.-H. Kim, Eds. Springer International Publishing, 2016, pp. 173–191.

[293] E. L. White, J. C. Case, and R. Kramer-Bottiglio, "A Soft Parallel Kinematic Mechanism," *Soft Robotics*, vol. 5, no. 1, pp. 36–53, Feb. 2018.

[294] S. Ozel, E. H. Skorina, M. Luo, W. Tao, F. Chen, Y. Pan, and C. D. Onal, "A composite soft bending actuation module with integrated curvature sensing," in *2016 IEEE International Conference on Robotics and Automation (ICRA)*, May 2016, pp. 4963–4968.

[295] D. C. Rucker and R. J. Webster, "Mechanics of Continuum Robots with External Loading and General Tendon Routing," in *Experimental Robotics*, ser. Springer Tracts in Advanced Robotics. Springer, Berlin, Heidelberg, 2014, pp. 645–654.

[296] F. Renda, M. Giorelli, M. Calisti, M. Cianchetti, and C. Laschi, "Dynamic Model of a Multibending Soft Robot Arm Driven by Cables," *IEEE Transactions on Robotics*, vol. 30, no. 5, pp. 1109–1122, Oct. 2014.

[297] E. Tatlicioglu, I. Walker, and D. Dawson, "New dynamic models for planar extensible continuum robot manipulators," in *IEEE/RSJ International Conference on Intelligent Robots and Systems, 2007. IROS 2007*, Oct. 2007, pp. 1485–1490.

[298] F. Renda, F. Giorgio-Serchi, F. Boyer, C. Laschi, J. Dias, and L. Seneviratne, "A unified multi-soft-body dynamic model for underwater soft robots," *The International Journal of Robotics Research*, vol. 37, no. 6, pp. 648–666, May 2018.

[299] J. Barreiros, K. W. O'Brien, S. Hong, M. F. Xiao, H. Yang, and R. F. Shepherd, "Configurable Tendon Routing in a 3d-printed Soft Actuator for Improved Locomotion in a Multi-Legged Robot," in *2019 2nd IEEE International Conference on Soft Robotics (RoboSoft)*, Apr. 2019, pp. 94–101.

[300] A. J. Ijspeert, A. Crespi, D. Ryczko, and J.-M. Cabelguen, "From Swimming to Walking with a Salamander Robot Driven by a Spinal Cord Model," *Science*, vol. 315, no. 5817, pp. 1416–1420, Mar. 2007.

[301] J. K. Hopkins, B. W. Spranklin, and S. K. Gupta, "A survey of snake-inspired robot designs," *Bioinspiration & Biomimetics*, vol. 4, no. 2, p. 021001, Jun. 2009.

[302] A. P. Sabelhaus, L. J. van Vuuren, A. Joshi, E. Zhu, H. J. Garnier, K. A. Sover, J. Navarro, A. K. Agogino, and A. M. Agogino, "Design, Simulation, and Testing of a Flexible Actuated Spine for Quadruped Robots," Apr. 2018.

[303] A. Seibel and L. Schiller, "Systematic engineering design helps creating new soft machines," *Robotics and Biomimetics*, vol. 5, no. 1, p. 5, Oct. 2018.

[304] J. C. Case, M. C. Yuen, J. Jacobs, and R. Kramer-Bottiglio, "Robotic Skins That Learn to Control Passive Structures," *IEEE Robotics and Automation Letters*, vol. 4, no. 3, pp. 2485–2492, Jul. 2019.

[305] C.-P. Chou and B. Hannaford, "Measurement and modeling of McKibben pneumatic artificial muscles," *IEEE Transactions on Robotics and Automation*, vol. 12, no. 1, pp. 90–102, Feb. 1996.

[306] B. Tondu and P. Lopez, "Modeling and control of McKibben artificial muscle robot actuators," *IEEE Control Systems*, vol. 20, no. 2, pp. 15–38, Apr. 2000.

[307] S. Davis, N. Tsagarakis, J. Canderle, and D. G. Caldwell, "Enhanced Modelling and Performance in Braided Pneumatic Muscle Actuators , Enhanced Modelling and Performance in Braided Pneumatic Muscle Actuators," *The International Journal of Robotics Research*, vol. 22, no. 3-4, pp. 213–227, Mar. 2003.

[308] N. Tsagarakis and D. G. Caldwell, "Improved modelling and assessment of pneumatic muscle actuators," in *Proceedings 2000 ICRA. Millennium Conference. IEEE International Conference on Robotics and Automation. Symposia Proceedings (Cat. No.00CH37065)*, vol. 4, 2000, pp. 3641–3646 vol.4.

[309] R. W. Colbrunn, G. M. Nelson, and R. D. Quinn, "Modeling of braided pneumatic actuators for robotic control," in *Proceedings 2001 IEEE/RSJ International Conference on Intelligent Robots and Systems. Expanding the Societal Role of Robotics in the the Next Millennium (Cat. No.01CH37180)*, vol. 4, Oct. 2001, pp. 1964–1970 vol.4.

[310] S. P. Timoshenko and J. M. Gere, *Theory of elastic stability.* McGraw-Hill, New York, 1961.

[311] C. Wang, C. Wang, and J. Reddy, *Exact Solutions for Buckling of Structural Members.* CRC Press, Jul. 2004.

[312] G. R. Cowper, "The Shear Coefficient in Timoshenkos Beam Theory," *Journal of Applied Mechanics*, vol. 33, no. 2, pp. 335–340, Jun. 1966.

[313] M. T. Tolley, R. F. Shepherd, B. Mosadegh, K. C. Galloway, M. Wehner, M. Karpelson, R. J. Wood, and G. M. Whitesides, "A Resilient, Untethered Soft Robot," *Soft Robotics*, vol. 1, no. 3, pp. 213–223, Aug. 2014.

[314] C. D. Onal, X. Chen, G. M. Whitesides, and D. Rus, "Soft Mobile Robots with On-Board Chemical Pressure Generation," in *Robotics Research*, ser. Springer Tracts in Advanced Robotics. Springer, Cham, 2017, pp. 525–540.

[315] R. F. Shepherd, A. A. Stokes, J. Freake, J. Barber, P. W. Snyder, A. D. Mazzeo, L. Cademartiri, S. A. Morin, and G. M. Whitesides, "Using Explosions to Power a Soft Robot," *Angewandte Chemie International Edition*, vol. 52, no. 10, pp. 2892–2896, Mar. 2013.

[316] N. Napp, B. Araki, M. T. Tolley, R. Nagpal, and R. J. Wood, "Simple passive valves for addressable pneumatic actuation," in *2014 IEEE International Conference on Robotics and Automation (ICRA)*, May 2014, pp. 1440–1445.

[317] "Custom circuit board," https://github.com/the-faboratory/PressureServoCircuitBoard.

[318] "Fluidic control board," https://softroboticstoolkit.com/book/control-board, accessed: 2017-12-07.

[319] "Valve terminal cpv14-vi," https://www.festo.com/net/ro_ro/SupportPortal/default.aspx?q=cpv14-vi+atex&tab=3, accessed: 2017-12-07.

[320] "Itv series catalog," http://www.smcpneumatics.com/pdfs/ITV.pdf, accessed: 2018-1-19.

[321] M. A. Robertson, H. Sadeghi, J. M. Florez, and J. Paik, "Soft Pneumatic Actuator Fascicles for High Force and Reliability," *Soft Robotics*, vol. 4, no. 1, pp. 23–32, Oct. 2016.

[322] "X-valve - miniature pneumatic solenoid valve," http://ph.parker.com/us/12051/en/x-valve-miniature-pneumatic-solenoid-valve, accessed: 2017-12-07.

[323] "Ten-x - miniature pneumatic solenoid valve," http://ph.parker.com/us/12051/en/ten-x-miniature-pneumatic-solenoid-valve, accessed: 2017-12-07.

A. SUPPLEMENTARY MATERIAL FOR SENSOR ENABLED CLOSED-LOOP CONTROL OF SOFT BEAMS

A.1 Fabrication

A.1.1 Elastomer Beam Fabrication

The fabrication process for the elastomer beams differs slightly between the three beams. All of the start with pouring Smooth-Sil 935 (Shore hardness: 35A; Smooth-On) into a 3D printed mold, shown in Figure 4.4a. For the prismatic beam, this was a 168mm x 15mm x 10mm mold; for the non-prismatic and non-homogeneous beams, this was a 80mm x 15mm x 10mm mold. The elastomer was initially two liquid parts, which were combined 1:10 by weight. We pre-mixed by hand first and then mixed and degassed the pre-polymer in a THINKY ARE 310 orbital mixer. The molds were over-filled and the excess was removed by scraping the flat side of a plastic knife over the molds. The molds were left to cure overnight at room temperature, after which the elastomer was removed, shown in Figure 4.4b. In the case of the prismatic beam, this was the final fabrication step; for the other beams, the pieces of elastomer became the bones of the elastomer structure. To complete the non-prismatic and non-homogeneous beams, two elastomer bones were taken and placed into a 3D printed joint mold, shown in Figure 4.4c. We then poured elastomer into the joint mold and allowed it to cure overnight at room temperature, shown in Figure 4.4d. For the non-prismatic beam, our elastomer was Smooth-Sil 935; for the non-homogeneous, Dragon Skin 10 Slow (Shore hardness: 10A; Smooth-On). Dragon Skin 10 Slow was made the same way as the Smooth-Sil 935 with the exception of being combined 1:1 by weight. After it was finished curing, we removed our elastomer beams, shown in Figure 4.4e.

A.1.2 Sensor Fabrication

The strain sensors used to measure joint angle were fabricated from two sheets of elastomer sandwiching microchannels filled with liquid metal. The sensor fabrication sequence is shown in Figure 4.5a-e. We began by casting a bottom elastomer film layer using a rod-coating technique and Dragon Skin 10 Slow, as shown in Figure 4.5a. We poured the liquid elastomer onto a PET substrate and spread it using a 12" x 1/2"-13 Acme threaded rod. The resulting film, once cured, was approximately 300µm thick. Onto this layer, we applied polymer-infused fabric reinforcement tabs, as shown in Figure 4.5b. Once cured, we inverted this film so that the fabric tabs were facing down, and used a VLS 2.30 laser patterning system (Universal Laser Systems) to create microchannels in the exposed face of the film and to roughly pattern the outline, as shown in Figure 4.5c. We then used sonication and a sequence of acetone, isopropanol, ethanol, and distilled water to remove the soot left over from the laser patterning sequence. Once clean, we prepared another film of Dragon Skin 10 Slow elastomer using the same procedure as the base layer. Instead of allowing the new layer to fully cure, we placed the bottom halves of the sensors, microchannel side down, while the former was still partially uncured, as shown in Figure 4.5d. This "tacky bond" provided an optimal combination of adhesion between layers and low probability of uncured elastomer filling the channels. We allowed the complete sensor bodies to cure overnight to promote adhesion between layers. Once cured, we used the VLS 2.30 laser system to finalize the outer shape of the sensors, as shown in Figure 4.5e. We remove the soot from this process using acetone. At this point, the sensor bodies were complete. To functionalize them, we injected a room temperature liquid alloy of gallium and indium (EGaIn, Sigma-Aldrich). We did this by inserting a 28ga needle into one of the fill ports visible at the left of the microchannel structure shown in Figure 4.5f. We manually injected the liquid metal using a 3ml syringe. After removing the excess liquid metal from the outside of the sensor, we inserted four 34ga wires into the smaller ports shown in the left part of the microchannel

network in Fig. 4.5f. We finished the device by applying drops of liquid Sylgard 184 (Dow Corning) to seal the microchannels and hold the wires in position. We have found Sylgard 184 to be effective for sealing channels since it is significantly less viscous than Dragon Skin 10 Slow, and therefore less likely to leave air bubbles by the channel ports. Finished devices had a resistance of $1\Omega \sim 2\Omega$.

A.1.3 Actuator Fabrication

The SMA actuators used in this structure were fabricated from NiTiNOL wire (Dynalloy) with a diameter of 0.25mm. This was programmed into counterspun coils, meaning that half the coil was wound clockwise while the other half was wound counterclockwise, with an inner diameter of 3.2mm; a 6.4mm spacer separates the two halves of the coil. The counterspinning is intended to counteract the force generated through torsion, since the torques from the two halves of the actuator counteract at the midpoint. The wire was heated to 390°C in a Lindberg Blue M 1100 Box Furnace for 10min and quenched in water. This processes was repeated for 10 cycles. An SMA coil is attached on either side of the soft structure to create an antagonistic actuator pair. The SMA placement was inspired by the muscles in an elbow joint and also easily allows for additional bones and joints without the SMA wires intersecting each other.

A.2 Supplemental Experimental Data

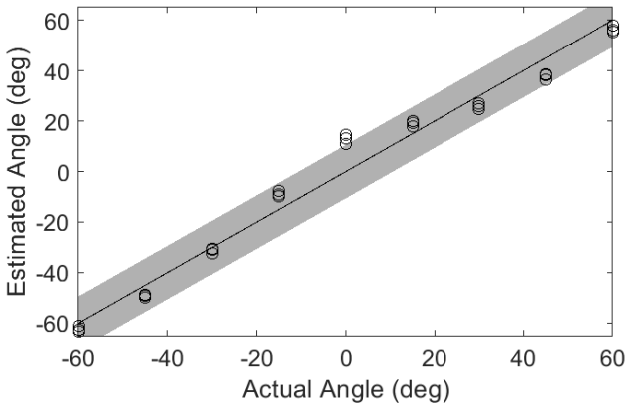

Figure A.1. Sensor calibration results for the prismatic beam showing how the actual angle compares to the estimated angle. The shaded region represents the 95% confidence interval.

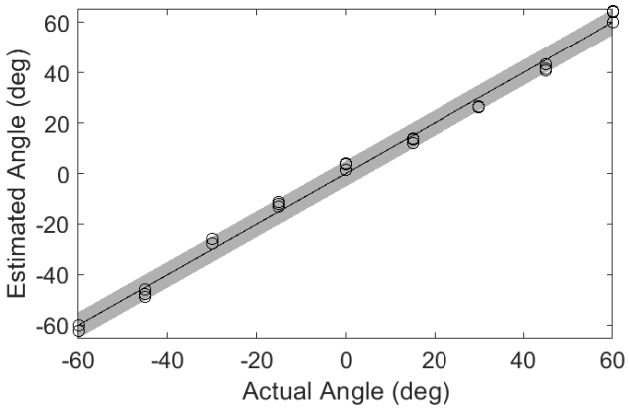

Figure A.2. Sensor calibration results for the non-prismatic beam showing how the actual angle compares to the estimated angle. The shaded region represents the 95% confidence interval.

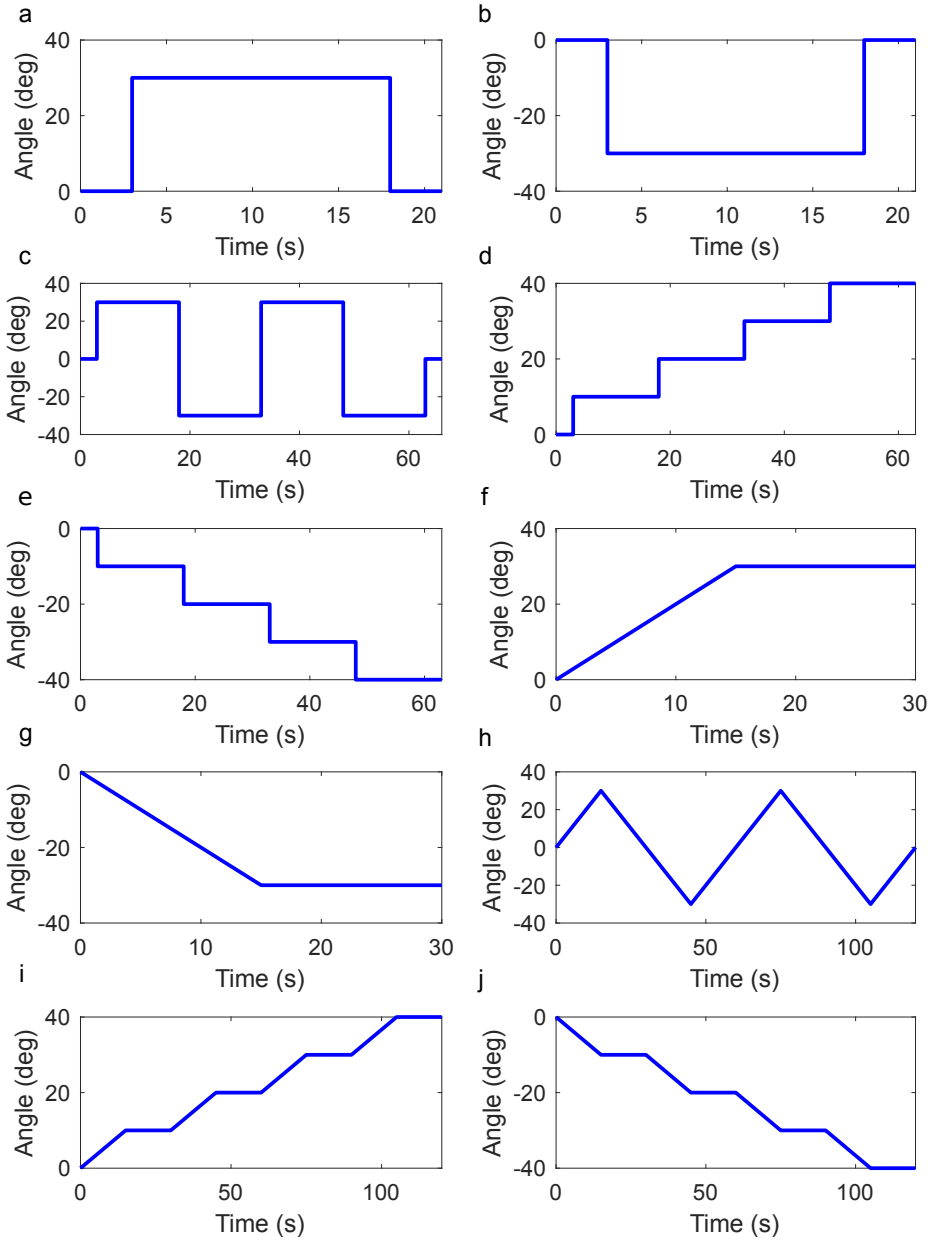

Figure A.3. Reference signals used for testing controllers. Reference signals were sent to the controllers in alphabetical order with a ten second period in between each signal where power to both SMA coils was turned off.

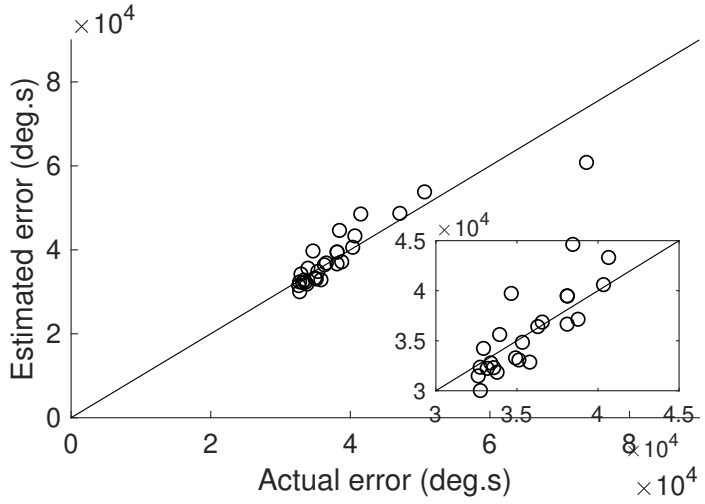

Figure A.4. Optimization of PID controller for prismatic beam. Blue dots represent represent test controllers. The line represents the one-to-one mapping of actual sum of errors against the theoretical sum of errors.

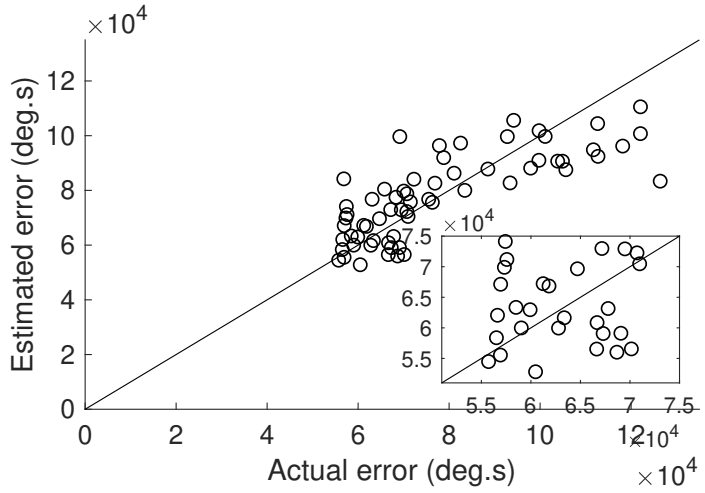

Figure A.5. Optimization of PID controller for non-prismatic beam. Blue dots represent represent test controllers. The line represents the one-to-one mapping of actual sum of errors against the theoretical sum of errors.

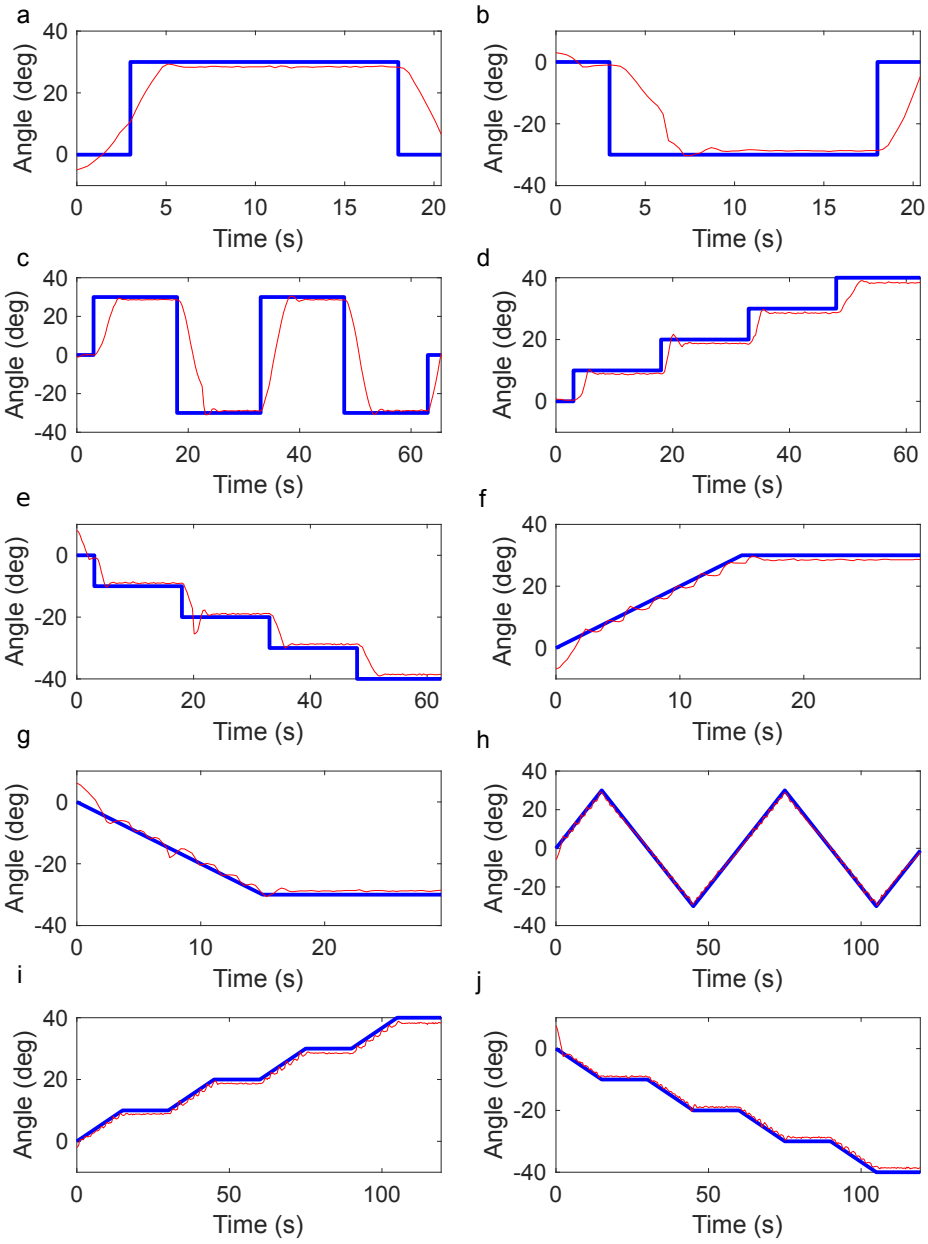

Figure A.6. Results for optimal controller for the prismatic elastomer beam ($k_p = 20$, $k_i = 0.4$, $k_d = 0.1$). Reference signals were sent to the controllers in alphabetical order with a ten second period in between each signal where power to both SMA coils was turned off. Blue represents the reference signal and red represents the controller response.

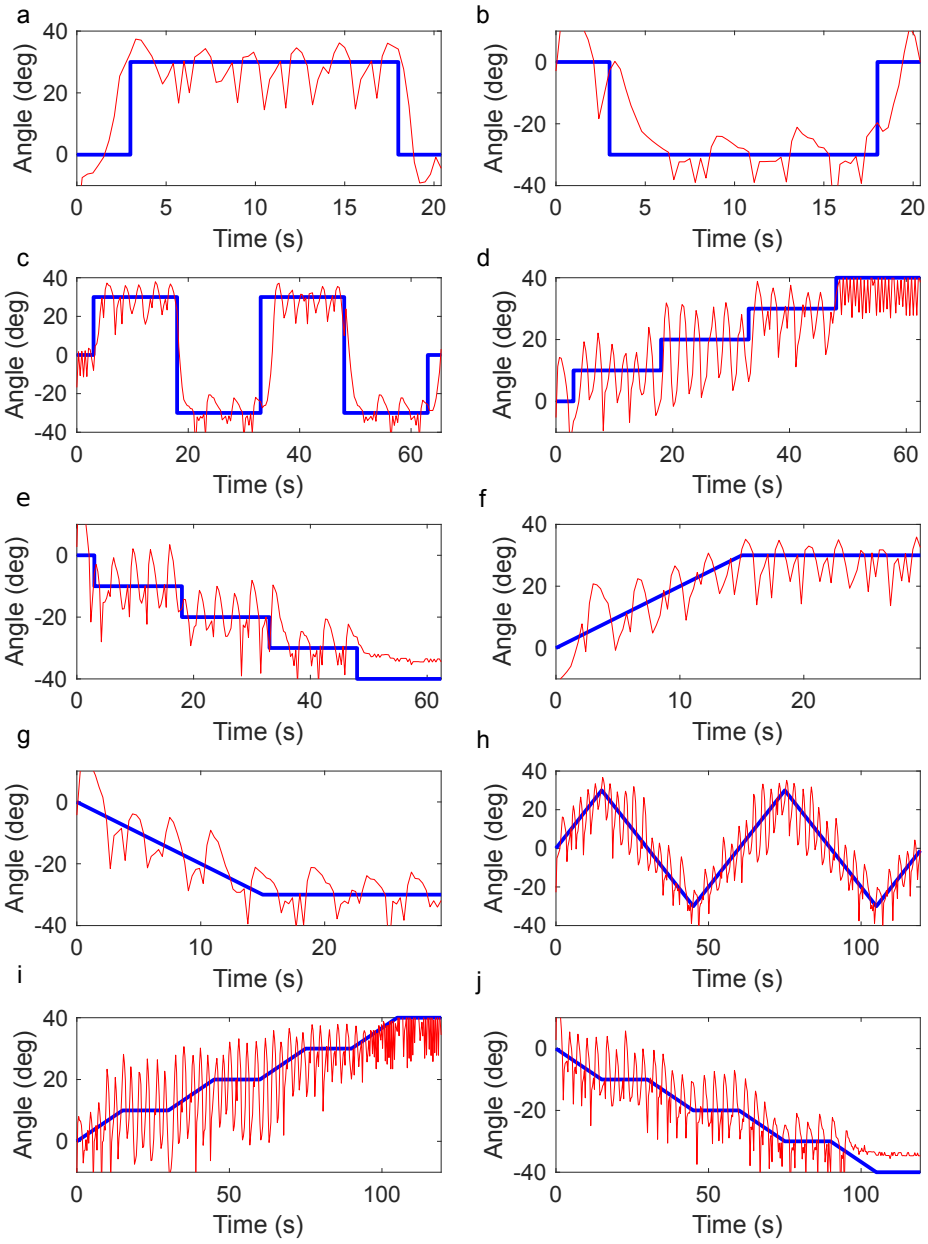

Figure A.7. Results for optimal controller for the non-prismatic elastomer beam ($k_p = 15$, $k_i = 0.4$, $k_d = 0.1$). Reference signals were sent to the controllers in alphabetical order with a ten second period in between each signal where power to both SMA coils was turned off. Blue represents the reference signal and red represents the controller response.

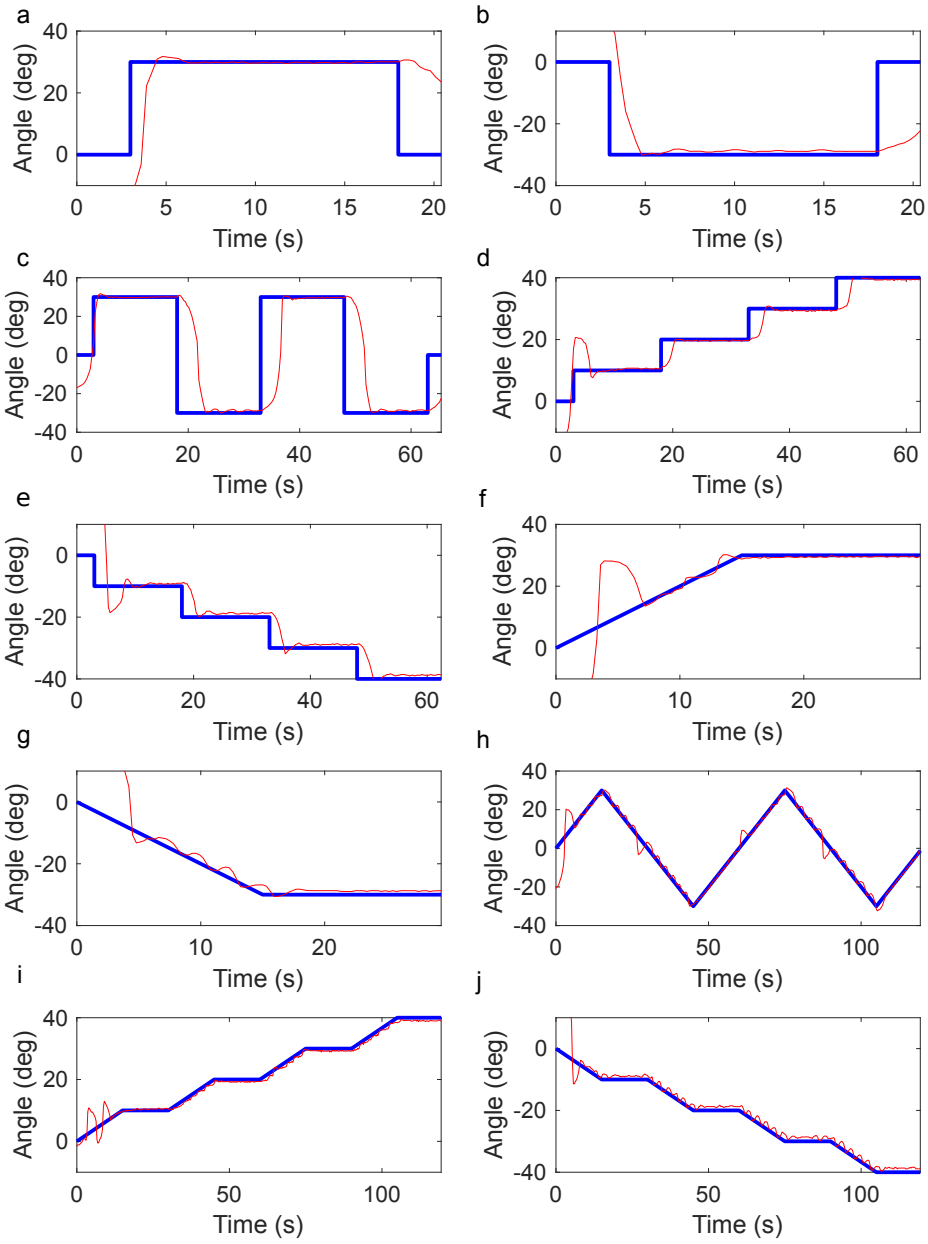

Figure A.8. Results for optimal controller for the non-homogeneous elastomer beam ($k_p = 20$, $k_i = 0.1$, $k_d = 0.8$). Reference signals were sent to the controllers in alphabetical order with a ten second period in between each signal where power to both SMA coils was turned off. Blue represents the reference signal and red represents the controller response.

B. SUPPLEMENTARY MATERIAL FOR REDUCING ACTUATOR REQUIREMENTS IN CONTINUUM ROBOTS THROUGH OPTIMIZED CABLE ROUTING

B.1 Model Derivation

Start with free end of the model, on the jth segment.

Sum of forces:

$$\sum \mathbf{F} = 0$$

$$\mathbf{F}_{R,j} + \sum_{i=0}^{n-1} {}^{j}\mathbf{R}^{e}{}_{e'} \mathbf{F}_{T_i,j} = 0$$

$$\mathbf{F}_{R,j} = -\sum_{i=0}^{n-1} {}^{j}\mathbf{R}^{e}{}_{e'} \mathbf{F}_{T_i,j}$$

$$\mathbf{F}_{R,j} = \sum_{i=0}^{n-1} T_i \begin{Bmatrix} -\sin\frac{\theta_j}{2} \\ \cos\frac{\theta_j}{2} \end{Bmatrix}$$

where $\mathbf{F}_{R,j}$ is the reaction force of the jth segment, ${}^{j}\mathbf{R}^{e}{}_{e'}$ is the rotation matrix for the jth segment,$\mathbf{F}_{T_i,j}$ is the force vector for the ith cable in the e' frame, θ_j is the angle for the jth segment, and n is the number of cables.

Sum of moments:

$$\sum M = 0$$

$$M_{R,j} + \sum_{i=0}^{n-1} \mathbf{r}_{T_i,j} \times {}^{j}\mathbf{R}^{e}{}_{e'} \mathbf{F}_{T_i,j} = 0$$

$$M_{R,j} = -\sum_{i=0}^{n-1} \mathbf{r}_{T_i,j} \times {}^{j}\mathbf{R}^{e}{}_{e'} \mathbf{F}_{T_i,j}$$

$$M_{R,j} = -\sum_{i=0}^{n-1} T_i d_i \cos\frac{\theta_j}{2}$$

where $M_{R,j}$ is the reaction moment of the jth segment, $\mathbf{r}_{T_i,j}$ is the moment arm from the origin of the e frame to the end of the ith cable.

When we move to the $(j-1)$th segment, we consider the reaction forces from the previous (jth) segment, the cables from the previous (jth) segment, and the cables from the current ($(j-1)$th) segment.

Sum of forces:

$$\sum \mathbf{F} = 0$$

$$\mathbf{F}_{R,j-1} + \sum_{i=0}^{n-1} {}^{j-1}\mathbf{R}_{e'}^{e}\mathbf{F}_{T_i,j-1} - \sum_{i=0}^{n-1} {}^{j-1}\mathbf{R}_{e'}^{e}\,{}^{j}\mathbf{R}_{e'}^{e}\mathbf{F}_{T_i,j} - {}^{j-1}\mathbf{R}_{e'}^{e}\mathbf{F}_{R,j} = 0$$

$$\mathbf{F}_{R,j-1} = -\sum_{i=0}^{n-1} {}^{j-1}\mathbf{R}_{e'}^{e}\mathbf{F}_{T_i,j-1}$$

$$\mathbf{F}_{R,j-1} = \sum_{i=0}^{n-1} T_i \begin{Bmatrix} -\sin\frac{\theta_{j-1}}{2} \\ \cos\frac{\theta_{j-1}}{2} \end{Bmatrix}$$

Sum of moments:

$$\sum M = 0$$

$$M_{R,j-1} + \sum_{i=0}^{n-1} \mathbf{r}_{T_i,j-1} \times {}^{j-1}\mathbf{R}_{e'}^{e}\mathbf{F}_{T_i,j-1} - M_{R,j} - \mathbf{r}_{j-1} \times {}^{j-1}\mathbf{R}_{e'}^{e}\mathbf{F}_{R,j} -$$
$$\sum_{i=0}^{n-1} \mathbf{r}_{T_i,j-1} \times {}^{j-1}\mathbf{R}_{e'}^{e}\,{}^{j}\mathbf{R}_{e'}^{e}\mathbf{F}_{T_i,j} = 0$$

$$M_{R,j-1} = -\sum_{i=0}^{n-1} \mathbf{r}_{T_i,j-1} \times {}^{j-1}\mathbf{R}_{e'}^{e}\mathbf{F}_{T_i,j-1} + M_{R,j} + \mathbf{r}_{j-1} \times {}^{j-1}\mathbf{R}_{e'}^{e}\mathbf{F}_{R,j} +$$
$$\sum_{i=0}^{n-1} \mathbf{r}_{T_i,j-1} \times {}^{j-1}\mathbf{R}_{e'}^{e}\,{}^{j}\mathbf{R}_{e'}^{e}\mathbf{F}_{T_i,j}$$

Note that:

$$\mathbf{r}_{j-1} = \begin{Bmatrix} \frac{1}{\kappa_{j-1}}\cos\theta_{j-1} - \frac{1}{\kappa_{j-1}} \\ \frac{1}{\kappa_{j-1}}\sin\theta_{j-1} \end{Bmatrix} \qquad \mathbf{r}_{T_i,j-1} = \begin{Bmatrix} \left(\frac{1}{\kappa_{j-1}} + d_i\right)\cos\theta_{j-1} - \frac{1}{\kappa_{j-1}} \\ \left(\frac{1}{\kappa_{j-1}} + d_i\right)\sin\theta_{j-1} \end{Bmatrix}$$

Using this, we find:

$$\sum_{i=0}^{n-1} \mathbf{r}_{T_i,j-1} \times {}^{j-1}\mathbf{R}_{e'}^{e}\mathbf{F}_{T_i,j-1} = \sum_{i=0}^{n-1} T_i d_i \cos\frac{\theta_{j-1}}{2}$$

$$\mathbf{r}_{j-1} \times {}^{j-1}\mathbf{R}^{e}{}_{e'}\mathbf{F}_{R,j} = \sum_{i=0}^{n-1} \frac{T_i}{\kappa_{j-1}} \left(\cos\left(\theta_{j-1} + \frac{\theta_j}{2}\right) - \cos\frac{\theta_j}{2} \right)$$

$$\sum_{i=0}^{n-1} \mathbf{r}_{T_i,j-1} \times {}^{j-1}\mathbf{R}^{e}{}_{e'}{}^{j}\mathbf{R}^{e}{}_{e'}\mathbf{F}_{T_i,j} = -\sum_{i=0}^{n-1} \frac{T_i}{\kappa_{j-1}} \left(\cos\left(\theta_{j-1} + \frac{\theta_j}{2}\right) - \cos\frac{\theta_j}{2} \right) + \sum_{i=0}^{n-1} T_i d_i \cos\frac{\theta_j}{2}$$

Thus, we find our moment to be:

$$M_{R,j-1} = -\sum_{i=0}^{n-1} T_i d_i \cos\frac{\theta_{j-1}}{2}$$

Thus, we can see the equations for both force and moment hold regardless of segment.

B.2 Experimental Validation

B.3 Tension Comparisons between Crossing and Traditional Cable Configurations

Tension comparisons were done using the experimental validation spine positions since this provided a large sample for comparisons. The following table shows the maximum tension for the spine positions using both traditional and crossing cable configurations.

Table B.1. : Maximum tension for a given spine position.
Bolded values are the higher value.

Spine position	Maximum tension (traditional)	Maximum tension (crossing)
Figure 12(b)	**0.813N**	0.714N
Figure 12(c)	0.565N	**0.674N**
Figure 12(d)	**0.826N**	0.636N
Figure S1(a)	**1.195N**	0.680N
Figure S1(b)	0.563N	**0.880N**
Figure S1(c)	**1.775N**	0.721N
Figure S1(d)	**0.716N**	0.648N
Figure S1(e)	0.449N	**0.727N**
Figure S1(f)	**1.675N**	0.606N
Figure S1(g)	**1.146N**	0.734N
Figure S1(h)	**1.305N**	0.737N
Figure S1(i)	**1.288N**	0.597N
Figure S1(j)	**1.480N**	0.791N
Figure S1(k)	**1.615N**	0.750N
Figure S1(l)	0.733N	**0.750N**
Figure S1(m)	0.394N	**0.812N**

continued on next page

Table B.1. : *continued.*

Spine position	Maximum tension (traditional)	Maximum tension (crossing)
Figure S1(n)	0.670N	**0.831N**
Figure S1(o)	0.493N	**0.844N**
Figure S1(p)	**0.811N**	0.671N
Figure S1(q)	**1.030N**	0.511N
Figure S1(r)	0.714N	**0.719N**
Figure S1(s)	**0.742N**	0.586N
Figure S1(t)	**1.109N**	0.822N
Figure S1(u)	**1.149N**	0.702N
Figure S1(v)	**1.244N**	0.588N
Figure S1(w)	**1.213N**	0.717N
Figure S1(x)	**0.715N**	0.607N
Figure S1(y)	0.381N	**0.726N**
Figure S1(z)	**0.693N**	0.586N
Figure S1(A)	0.713N	**0.937N**
Figure S1(B)	**1.337N**	0.770N
Figure S1(C)	0.503N	**0.854N**
Figure S1(D)	0.566N	**0.582N**
Figure S1(E)	**2.002N**	0.723N
Figure S1(F)	**1.290N**	0.838N

B.4 Dimensions of Physical System

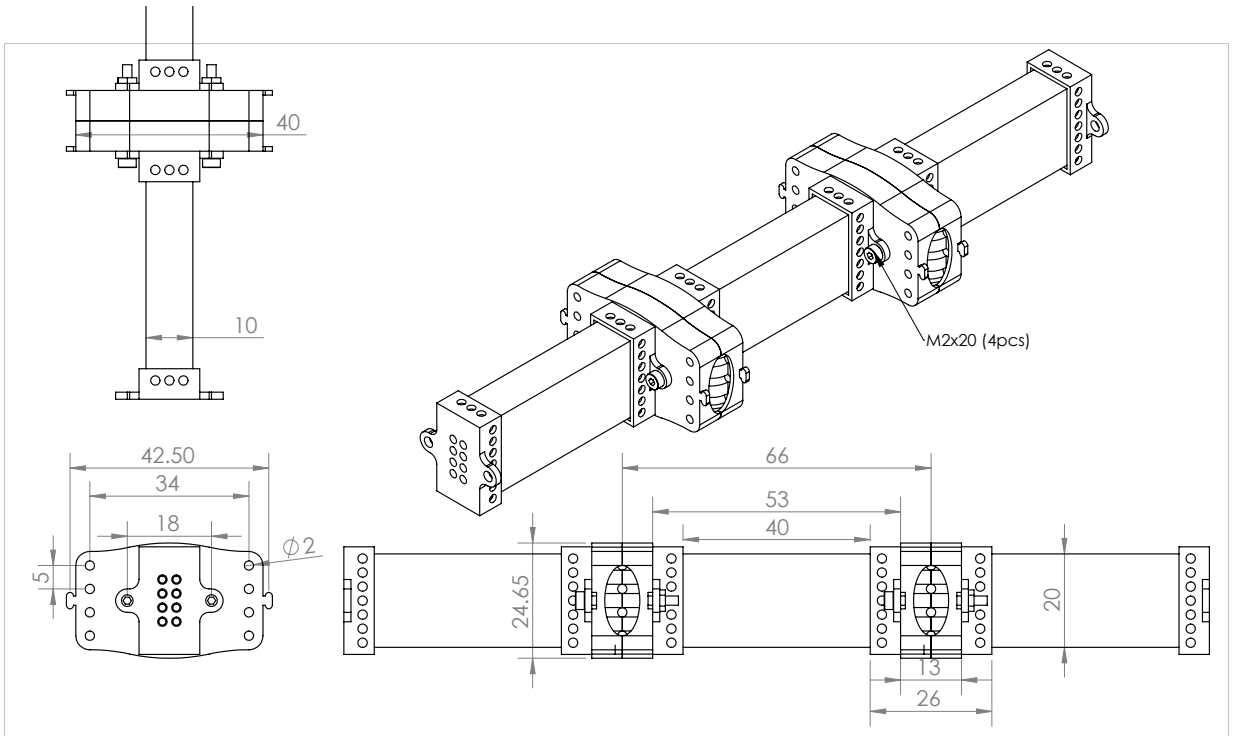

		UNLESS OTHERWISE SPECIFIED:		NAME	DATE
		DIMENSIONS ARE IN MM TOLERANCES: 0.1mm FRACTIONAL ± ANGULAR: MACH ± BEND ± TWO PLACE DECIMAL ± THREE PLACE DECIMAL ±	DRAWN	ELW	1/31/2016
			CHECKED		
			ENG APPR.		
			MFG APPR.		
		INTERPRET GEOMETRIC TOLERANCING PER:	Q.A.		
		MATERIAL	COMMENTS:		
NEXT ASSY	USED ON	FINISH			
APPLICATION		DO NOT SCALE DRAWING			

TITLE: Single Elastomer Segment

SIZE	DWG. NO.	REV
A	10x20_robot_segment	

SCALE: 1:1 | WEIGHT: | SHEET 1 OF 1

5 4 3 2 1

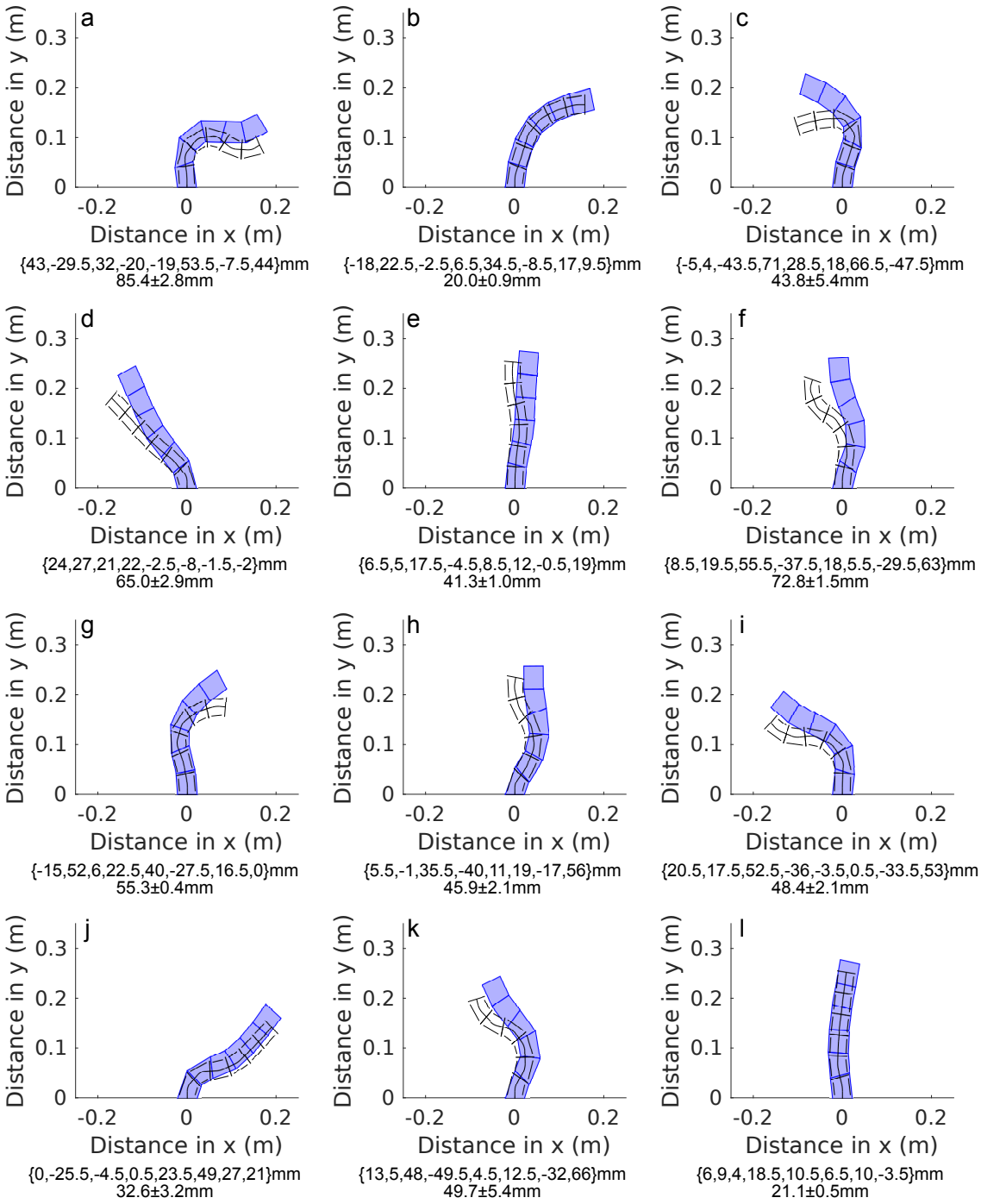

Figure B.1. Experimental tests for model validation. The recreation of the spine is shaded blue while the model prediction is shown as a black outline. Changes in lengths are listed in the first row and end point error is listed in the second row below the figures.

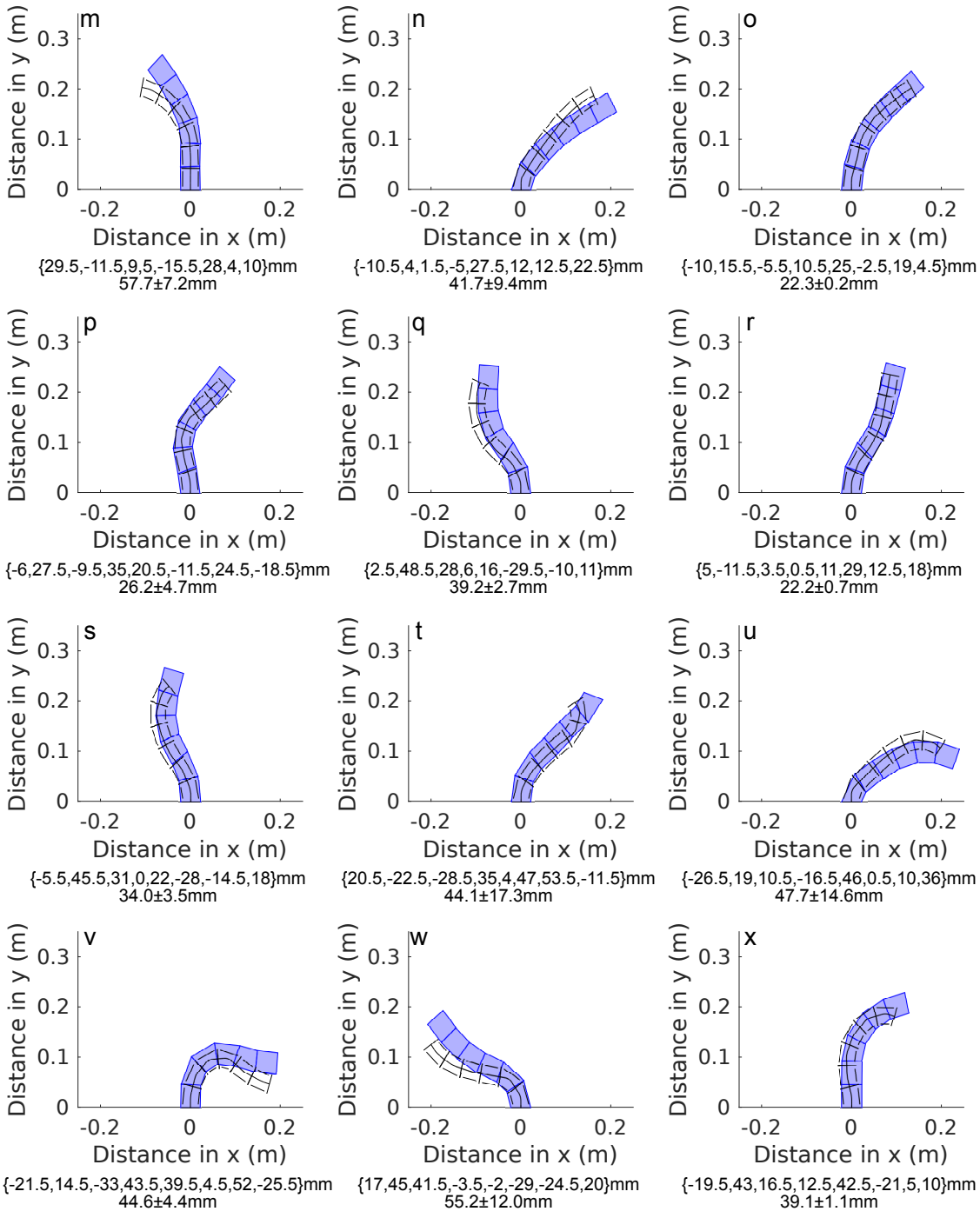

Figure B.1. *continued.*

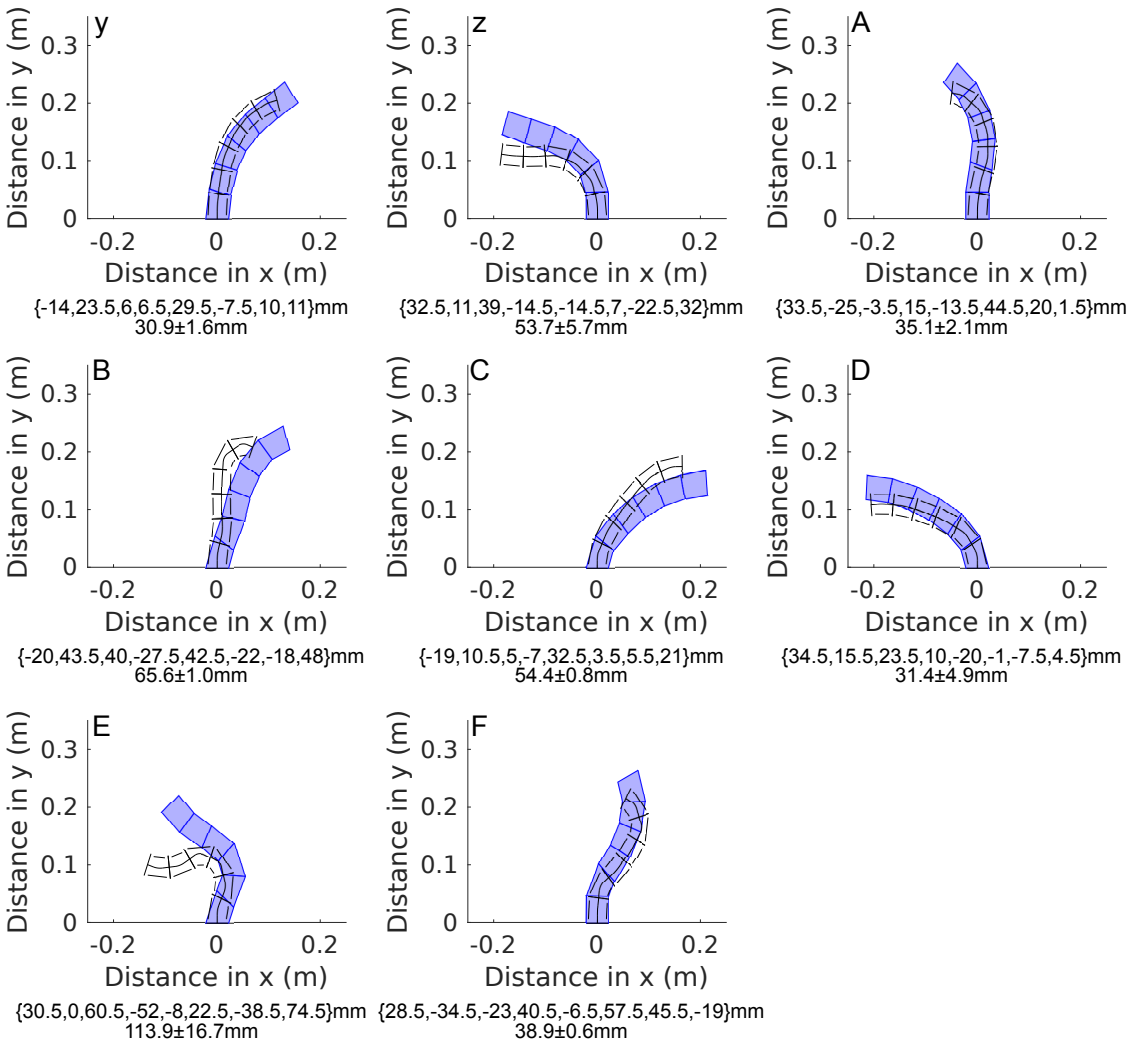

Figure B.1. *continued.*

C. SUPPLEMENTARY MATERIAL FOR A GENERALIZED MODEL OF ROBOTIC SKINS FOR DESIGN AND CONTROL

C.1 Comparison of actuator models

A comparison between the Chou-Hannaford model and our empirically-derived polynomial model is given in Figure C.1. For this, we used a McKibben actuator with $l_{act.} = 120$ mm, $\theta_{k,0} = \pi/6$, $D_k = 6.35$ mm. The constants for the polynomial fit were found to be $c_0 = 200.$ N, $c_1 = -5.35\text{E}{-4}$ N/Pa, $c_2 = -4.41\text{E}3$ N/m, $c_3 = 6.70\text{E}{-3}$ N/Pa·m, and $c_4 = 2.38\text{E}4$ N/m^2.

The Chou-Hannaford model tends to overestimate the force output of the actuator, which can get worse as the length decreases. However, it does not require empirical data to derive, which means we can easily change parameters without needing to fabricate a new actuator and collect experimental data. For this reason, we believe the

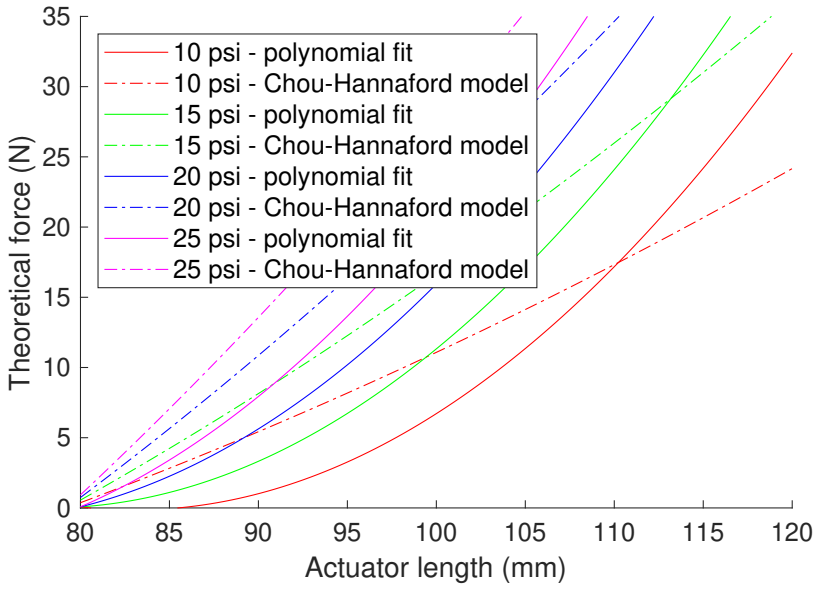

Figure C.1. Comparison showing the different behavior of the two actuator models.

Chou-Hannaford model is useful during the design phase since it can approximate the behavior. However, when controlling a physical system, it is better to characterize the system and use that characterization in the system model rather than the approximate model achieved with the Chou-Hannaford model.

To further emphasize the difference between the two, feedforward control was simulated with a skin on a Dragonskin 10 Slow cylindrical structure where the actuators were changed between the theoretical and empirical models. It can be seen in Figure C.2 that the theoretical model completes the desired path and requires significantly less pressure than the empirically derived model. The difference between the pressures make the theoretical model impractical to use when controlling a physical system. This is why it is beneficial for design, but not for control.

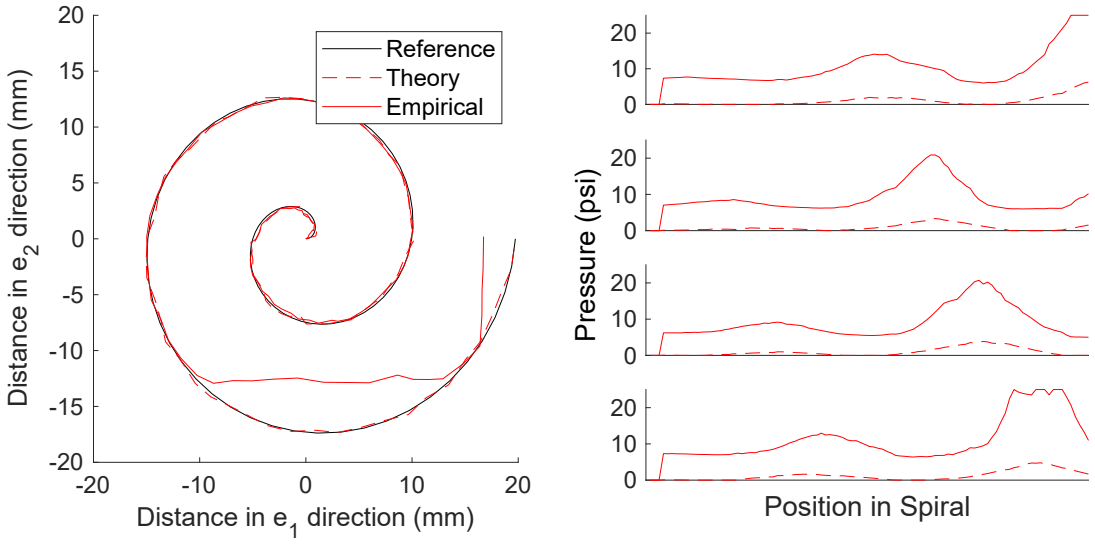

Figure C.2. Simulated feedforward control of Dragonskin 10 Slow cylindrical structure tracing a spiral pattern. This compares the behavior of the theoretical model to the empirically derived model of the actuators. The corresponding pressures as the structures move through the spiral are provided on the right. The plots show the pressure in Actuator 1-4 from top to bottom.

C.2 Plastic deformation of sensors

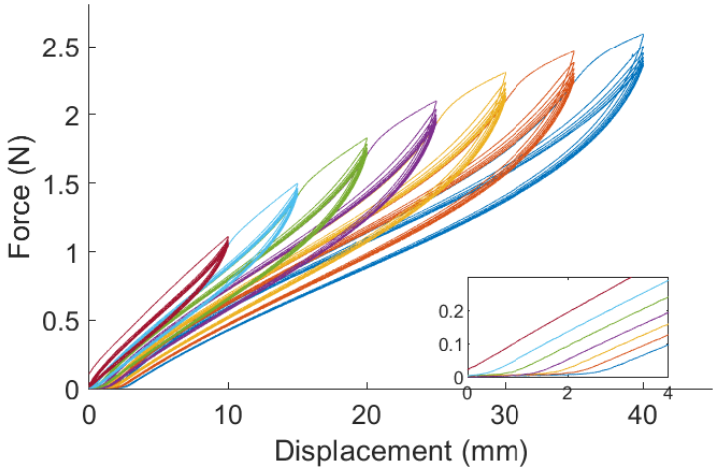

Figure C.3. Raw data for determining how the plastic deformation develops as the sensor is strained. Each of the seven strains is given in a different color. The inset shows a close-up of the plastic deformation plateau for the third cycle at each strain. For the inset, only the part of the curve where the length is decreasing is shown for easier interpretation of the data.

C.3 Fabrication and Characterization

C.3.1 Design

To design the system, a simulation running the described model was used. For the first step of this analysis, the radius and length of the cylindrical segment was varied to determine how this affected the maximum curvature and buckling force of the system. The system was assumed to be a skin with no additional stiffness contribution (i.e., the stiffness comes from only the elastomer cylindrical structure) and a single actuator that ran parallel to the neutral axis of the system. The gravitational effects were turned off for this analysis. The elastic modulus of Dragonskin 10 Slow was used (E = 265 kPa). The range of radii tested were from r = 10 mm to 35 mm in steps of 2.5 mm. The range of lengths tested were from $l_{cyl.}$ = 50 mm to 150 mm in steps of 10 mm. The length of the actuator was 20 mm longer than the length tested. The results from this test is shown in Figure C.4a. The selected radius (15 mm) and length (100 mm) is highlighted as a red dot.

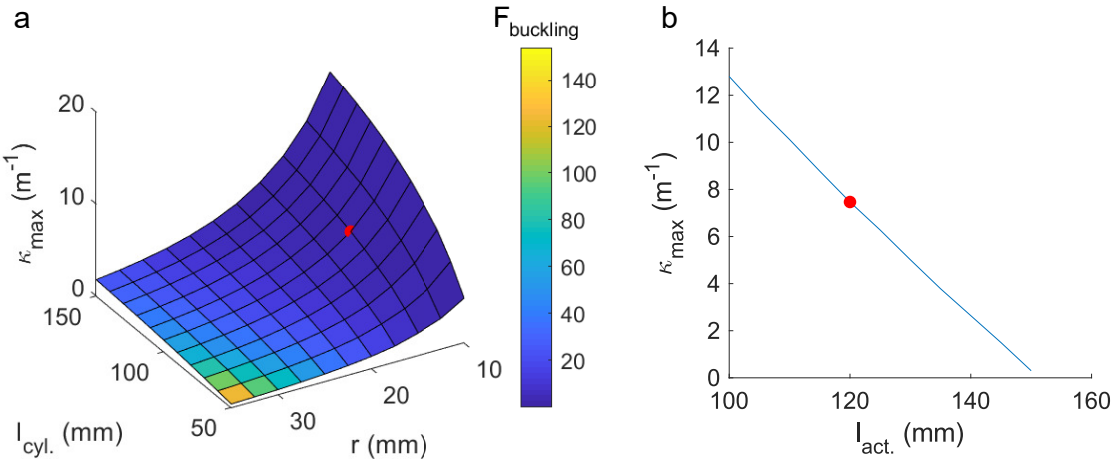

Figure C.4. (a) Simulation results varying radius and length of the cylindrical structure. (b) Simulation results showing how length of the actuator affects the maximum curvature achieved by the system.

For a second analysis, a cylindrical structure of the selected dimensions was used and the length of the actuator was allowed to change between 100 mm and 150 mm at steps of 5 mm to determine how this affected the maximum curvature of the system. This analysis is shown in Figure C.4b. While the curvature increases as length of the actuator decreases, a slightly longer actuator was selected, shown by the red dot, so that the braid of various actuators did not unintentionally pose as strain limiters on the skin.

C.3.2 Substrate

The substrate used in this study is a white spandex. The spandex was cut to approximately 125 mm by 158 mm using a Universal Laser System (VLS 2.30). To determine the behavior of the spandex, the material was placed in a materials testing machine and pulled 15 mm at a rate of 100 mm/min for seven cycles both length-wise and width-wise. To determine the spring constants from Equation (8.3b-c), the last five cycles were averaged together and a polynomial with an x-intercept at zero was fit to the data. These spring constants are reported in Table C.1 for each skin.

Table C.1. Spring constants to describe the anisotropic behavior of the spandex substrate for the robotic skins.

	Parallel		Twisting	
Skin 1	k_1	210 N/m	k_1	190 N/m
	k_3	130 N/m	k_3	170 N/m
Skin 2	k_1	220 N/m	k_1	220 N/m
	k_3	150 N/m	k_3	160 N/m

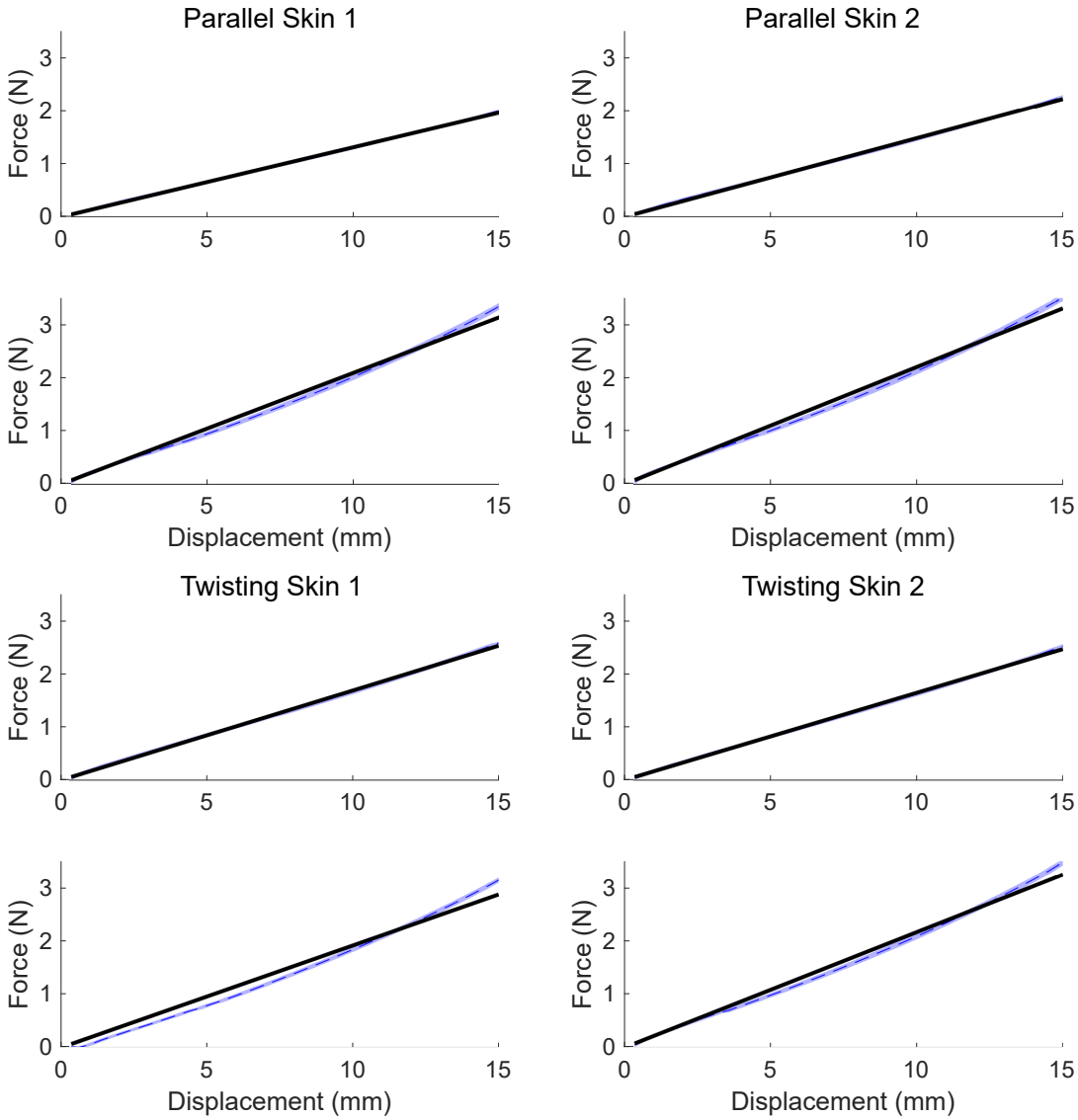

Figure C.5. Substrate characterization of each skin. The top graph shows the results when the skin was stretched length-wise and the bottom graph shows the results when the skin was stretched width-wise. The dashed blue line shows the average response from the last five cycles. The shaded region shows the 95% confidence interval. The black line shows the polynomial fit to the average experimental data.

C.3.3 Actuators

Similar to previous work [6,291,304], the robotic skins in this chapter utilize McKibben actuators [290, 305]. These actuators are made from latex balloons and 1/4" diameter braid mesh (9284K2, McMaster-Carr). This diameter mesh was selected to minimize the profile of the robotic skin at the cost of force generation. Either ends of the McKibben are zip-tied to an 1/8" end plug (5463K75, McMaster-Carr) and a 1/8" to 1/4" reducer (5463K47, McMaster-Carr), which is used to connect the actuator to the pneumatic network that powers the skins. Two actuator lengths were fabricated: 120 mm long for the parallel skins and 140 mm long for the twisting skins. The actuators are slightly oversized for the skins, which are designed for a 100 mm long cylindrical structure to prevent the braids of the McKibbens from acting as a strain limiter and affecting the deformation of the system. The actuators were tested individually in a materials testing machine (3345 Instron). For the 120 mm long actuators, each actuator was inflated to a given pressure and cycled 12 times between 120 mm and 80 mm at a rate of 500 mm/min. For the 140 mm long actuators, each actuator was inflated to a given pressure and cycled 12 times between 140 mm and 90 mm at a rate of 500 mm/min. The actuators were tested at four different pressure values: 10, 15, 20, 25 psi. To process the data, the first two cycles were discarded and the other ten cycles were averaged together. All this data is then compiled for each actuator and the empirical data was fit to Equation (8.6).

Twelve actuators of each the 120 mm length and the 140 mm length were characterized. From these, the best eight were selected to be incorporated into the skins. Here, we provide the plots showing the experimental data as well as the polynomial fit for each of the selected actuators. Additionally, Tables C.3 provides the polynomial fit constants.

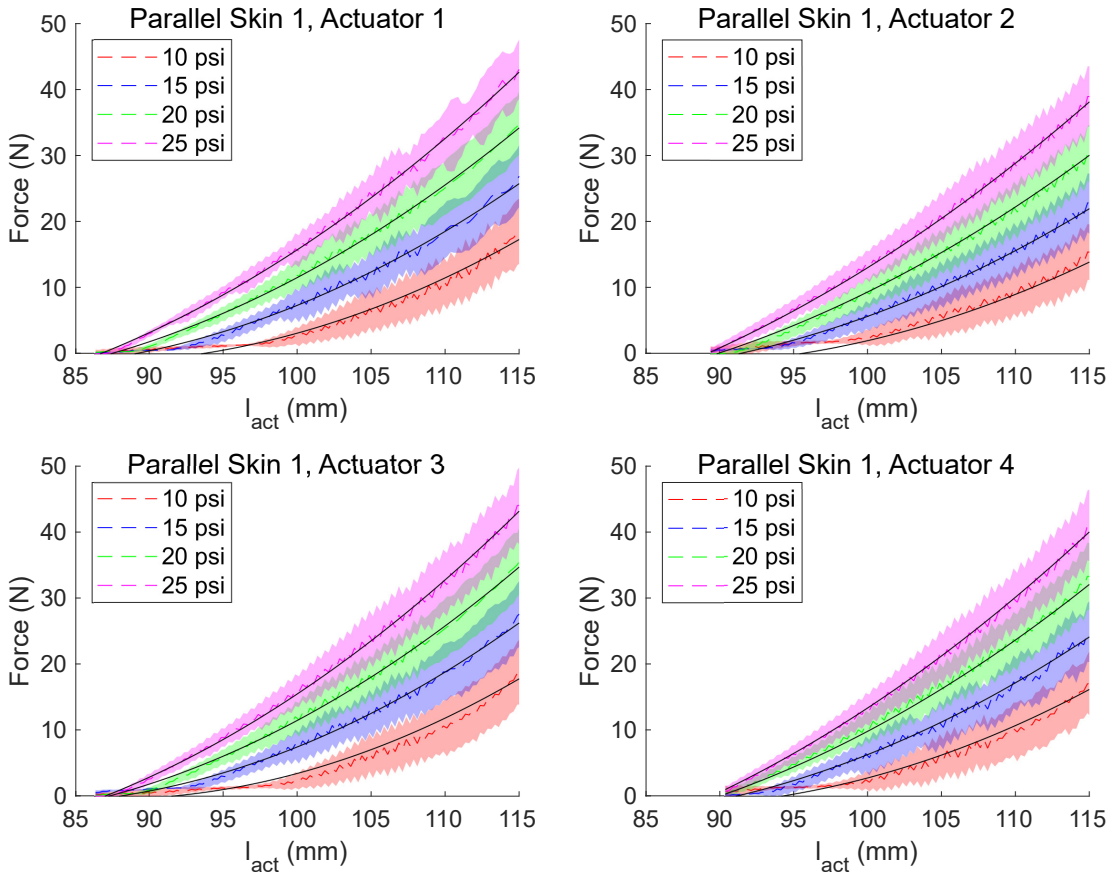

Figure C.6. Experimental results and polynomial fits for the 120 mm long actuators used on Parallel Skin 1. The average experimental data is shown as colored, dashed lines with corresponding 95% confidence intervals, shown as the shaded regions. The theoretical polynomial fit is shown as black lines.

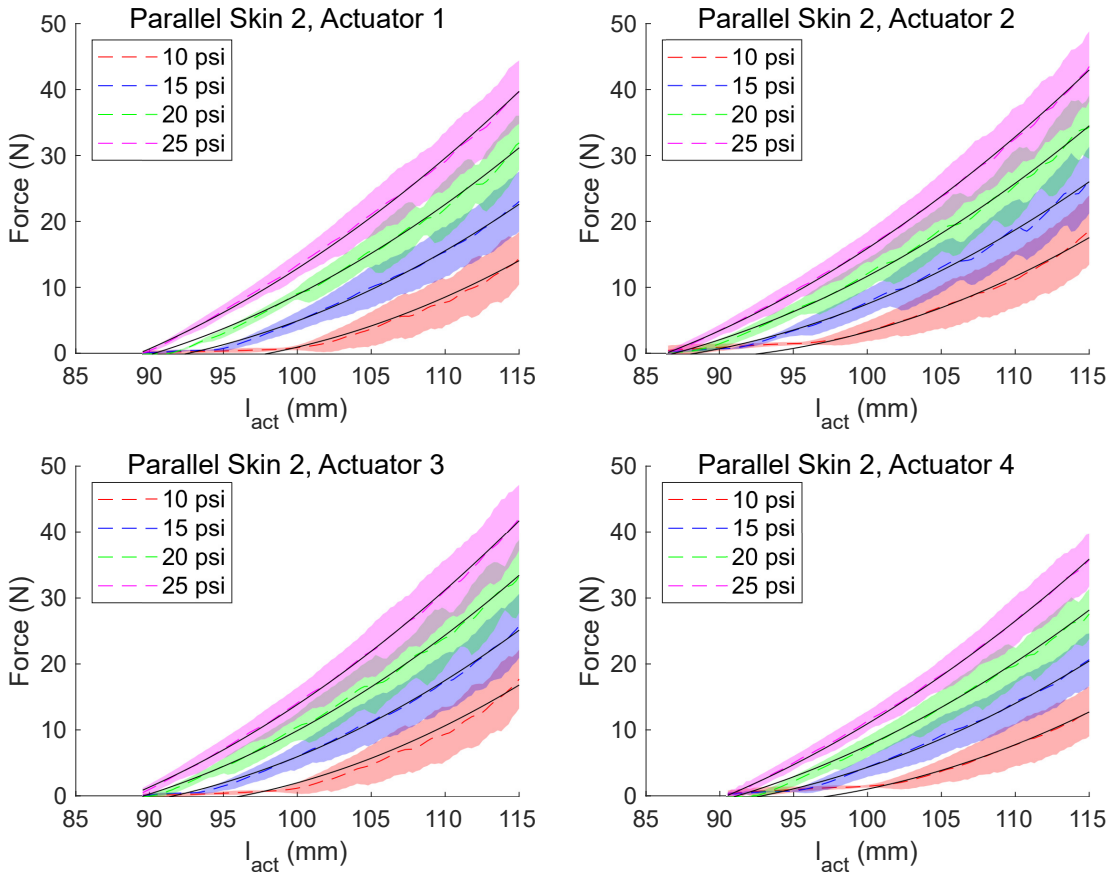

Figure C.7. Experimental results and polynomial fits for the 120 mm long actuators used on Parallel Skin 2. The average experimental data is shown as colored, dashed lines with corresponding 95% confidence intervals, shown as the shaded regions. The theoretical polynomial fit is shown as black lines.

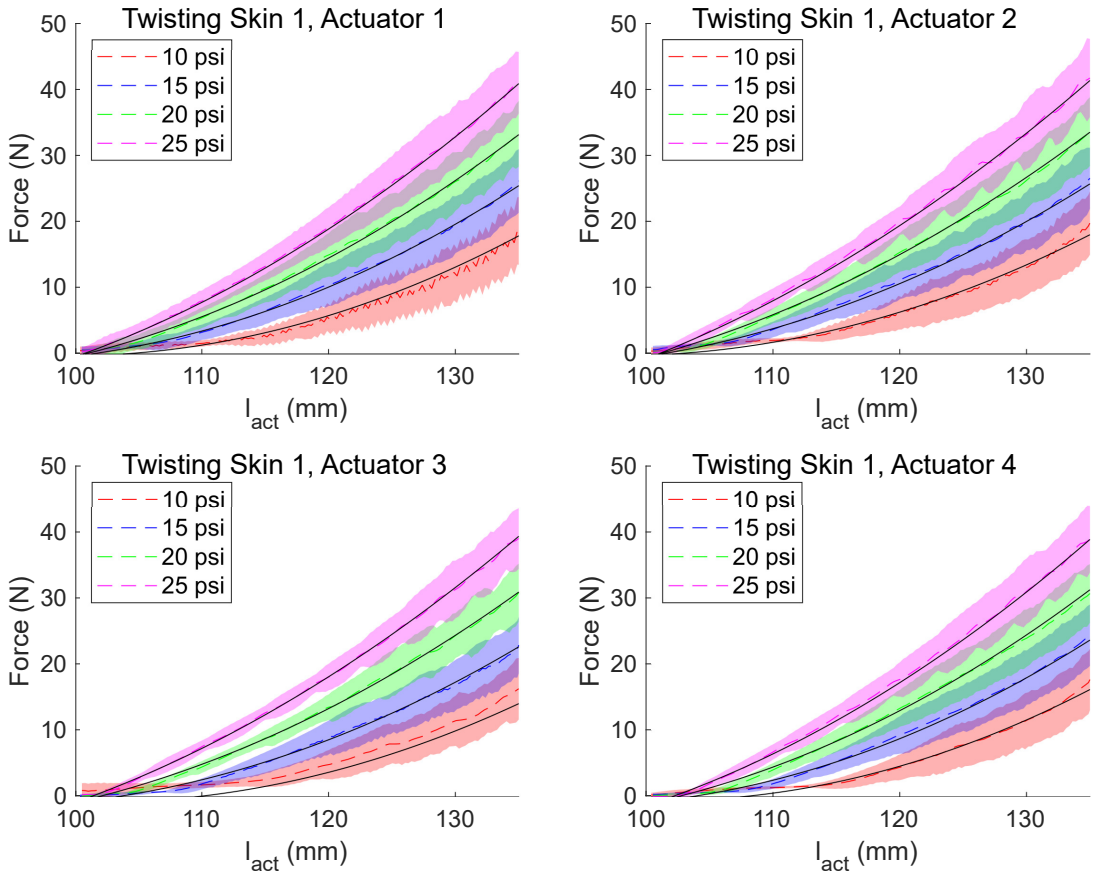

Figure C.8. Experimental results and polynomial fits for the 120 mm long actuators used on Twisting Skin 1. The average experimental data is shown as colored, dashed lines with corresponding 95% confidence intervals, shown as the shaded regions. The theoretical polynomial fit is shown as black lines.

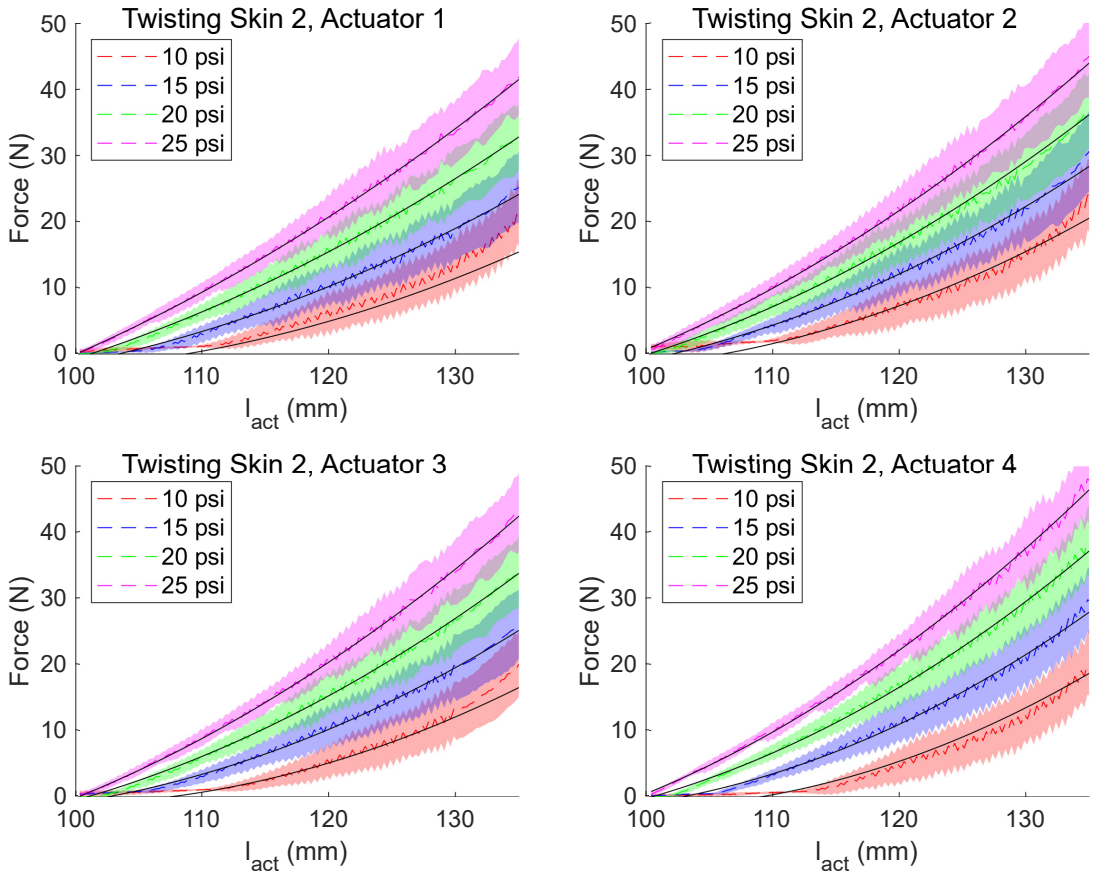

Figure C.9. Experimental results and polynomial fits for the 120 mm long actuators used on Twisting Skin 2. The average experimental data is shown as colored, dashed lines with corresponding 95% confidence intervals, shown as the shaded regions. The theoretical polynomial fit is shown as black lines.

Table C.2. Theoretical polynomial constants for each corresponding 120 mm long actuator.

Skin	Actuator	c_0 (N)	c_1 (N/Pa)	c_2 (N/m)	c_3 (N/Pa·m)	c_4 (N/m^2)
Parallel 1	1	204	-6.97E-4	-4.25E3	8.19E-3	2.15E4
Parallel 1	2	185	-7.44E-4	-3.74E3	8.51E-3	1.84E4
Parallel 1	3	228	-7.42E-4	-4.66E3	8.59E-3	2.33E4
Parallel 1	4	196	-7.51E-4	-4.01E3	8.53E-3	2.00E4
Parallel 2	1	231	-7.69E-4	-4.67E3	8.84E-3	2.29E4
Parallel 2	2	212	-7.01E-4	-4.39E3	8.23E-3	2.22E4
Parallel 2	3	232	-7.26E-4	-4.80E3	8.40E-3	2.42E4
Parallel 2	4	217	-7.56E-4	-4.32E3	8.51E-3	2.10E4

Table C.3. Theoretical polynomial constants for each corresponding 140 mm long actuator.

Skin	Actuator	c_0 (N)	c_1 (N/Pa)	c_2 (N/m)	c_3 (N/Pa·m)	c_4 (N/m^2)
Twisting 1	1	185	-6.44E-4	-3.28E3	6.44E-3	1.43E4
Twisting 1	2	169	-6.66E-4	-2.99E3	6.62E-3	1.30E4
Twisting 1	3	184	-6.97E-4	-3.17E3	6.97E-3	1.33E4
Twisting 1	4	194	-6.57E-4	-3.40E3	6.50E-3	1.46E4
Twisting 2	1	126	-6.44E-4	-2.29E3	6.64E-3	9.94E3
Twisting 2	2	141	-5.60E-4	-2.69E3	5.82E-3	1.24E4
Twisting 2	3	166	-6.77E-4	-2.95E3	6.87E-3	1.27E4
Twisting 2	4	192	-6.83E-4	-3.47E3	7.04E-3	1.52E4

C.3.4 Sensors

Similar to previous work [6, 291, 304], the robotic skins in this chapter utilize capacitive sensors made from exfoliated graphite composite [43]. The fabrication of the sensor material is described in [43] and the fabrication of the sensor is described in [304]. Two sensor lengths were fabricated: 90 mm long sensors that run from the base of the cylindrical structure to the top and 60 mm long sensors that run around the circumference of the cylindrical segment. In previous work, the sensors were characterized after they were placed on the skin; however, this is not necessary. In this work, the sensors are characterized prior to being attached to the skins. Each 90 mm sensor was placed in a material testing machine (Instron 3345) and pulled between 100 mm and 125 mm in steps of 2.5 mm. Each 60 mm sensor was pulled between 62.5 mm and 87.5 mm in steps of 2.5 mm. Three sensor readings were collected for each sensor at each step. This process was repeated 5 times for a total of 15 data points at each step. From the data, a linear fit was found for each sensor to relate the sensor response to the length of the sensor.

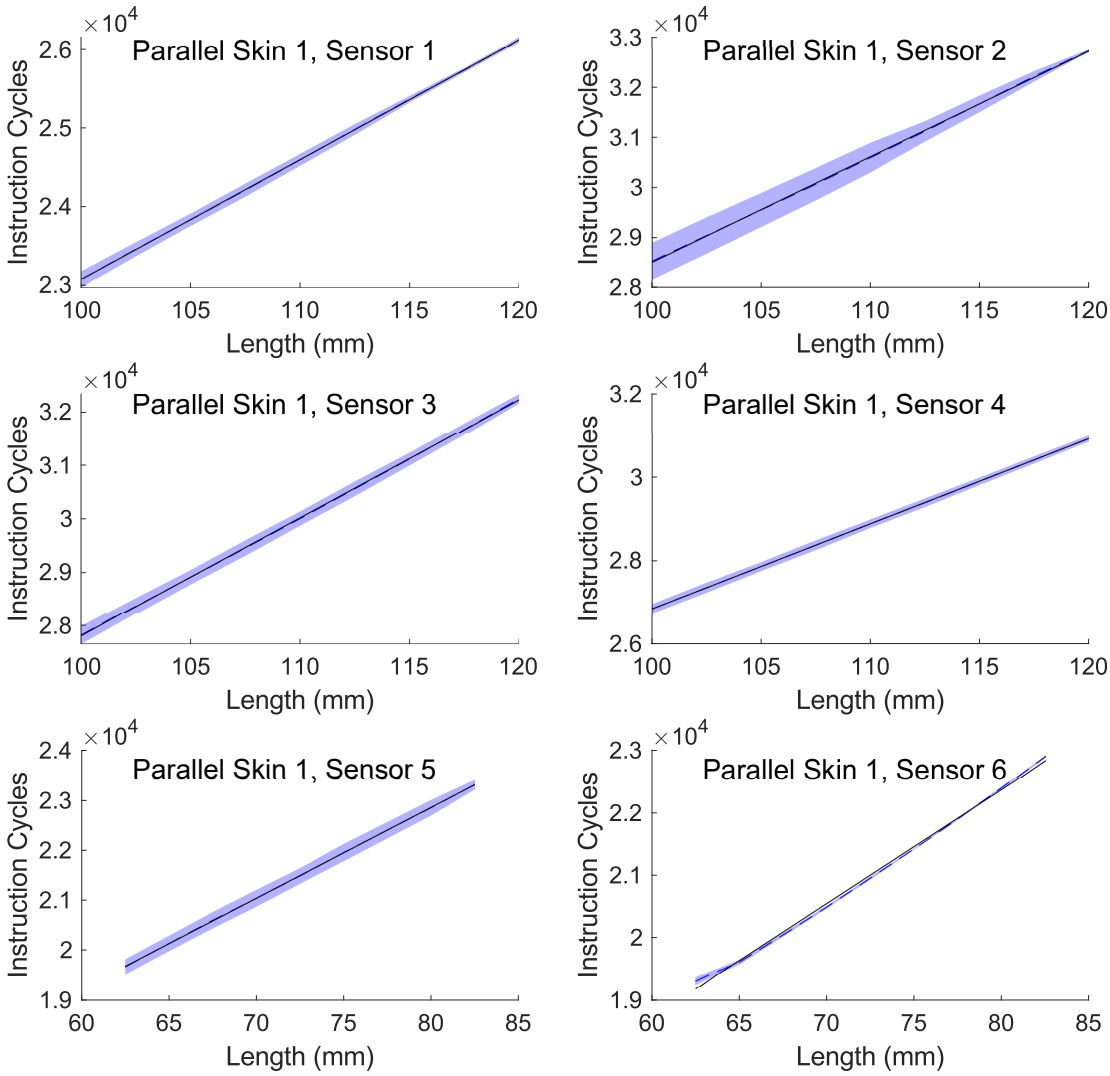

Figure C.10. Experimental results and linear fits for sensors used on Parallel Skin 1. The average experimental data is shown as a blue dashed line with the corresponding 95% confidence interval shown as the shaded region. The linear fit is shown as a black line.

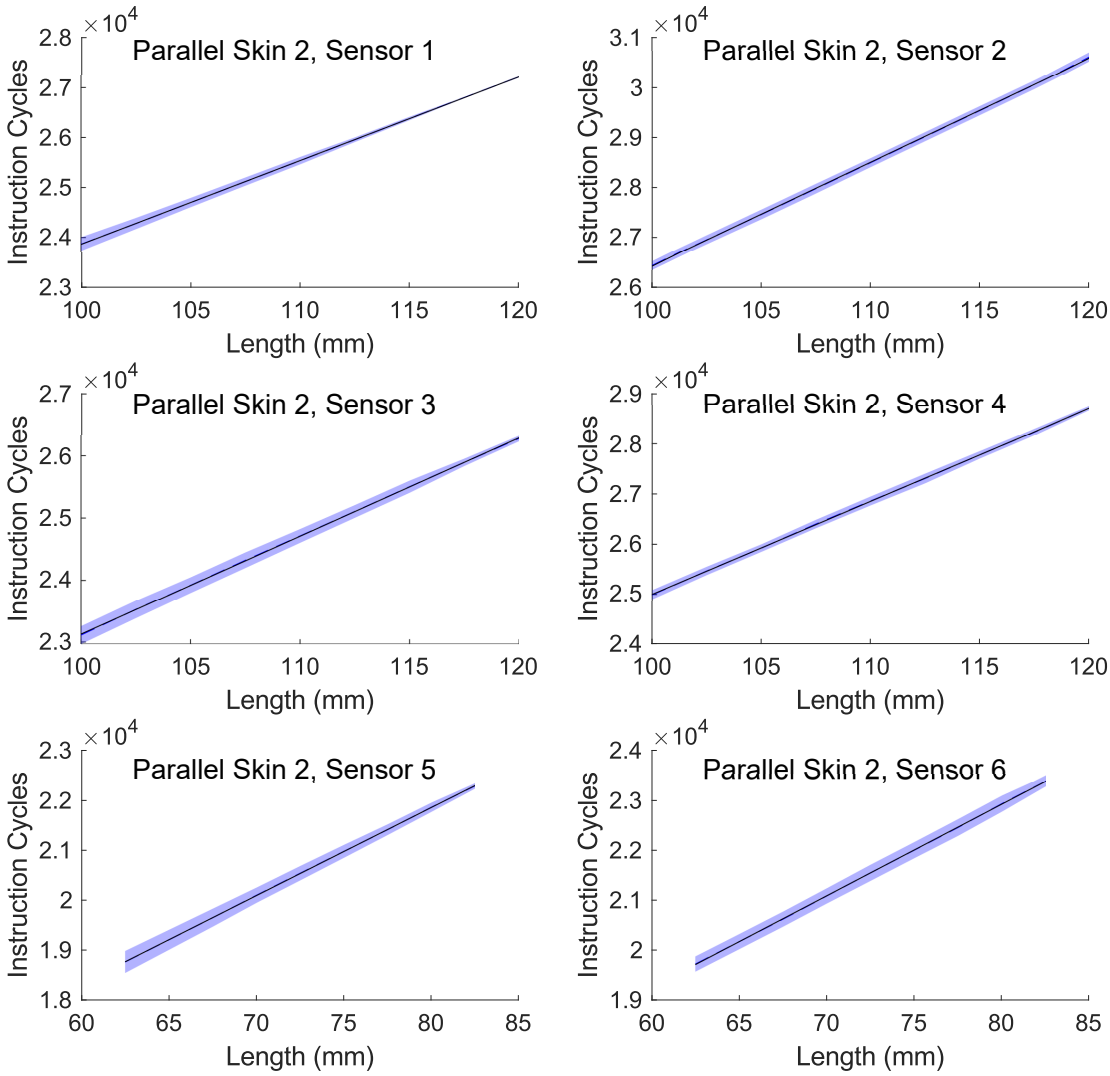

Figure C.11. Experimental results and linear fits for sensors used on Parallel Skin 2. The average experimental data is shown as a blue dashed line with the corresponding 95% confidence interval shown as the shaded region. The linear fit is shown as a black line.

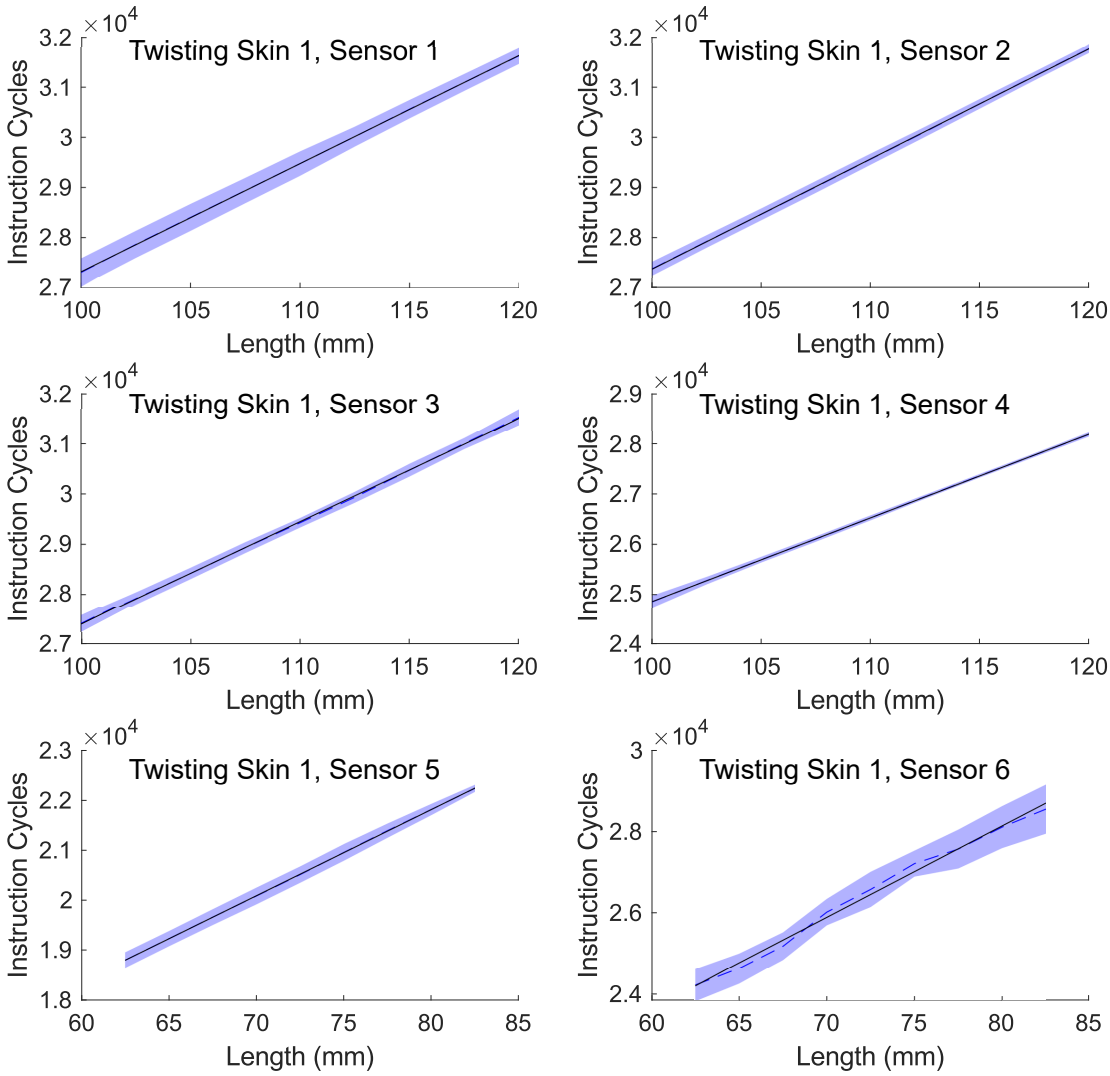

Figure C.12. Experimental results and linear fits for sensors used on Twisting Skin 1. The average experimental data is shown as a blue dashed line with the corresponding 95% confidence interval shown as the shaded region. The linear fit is shown as a black line.

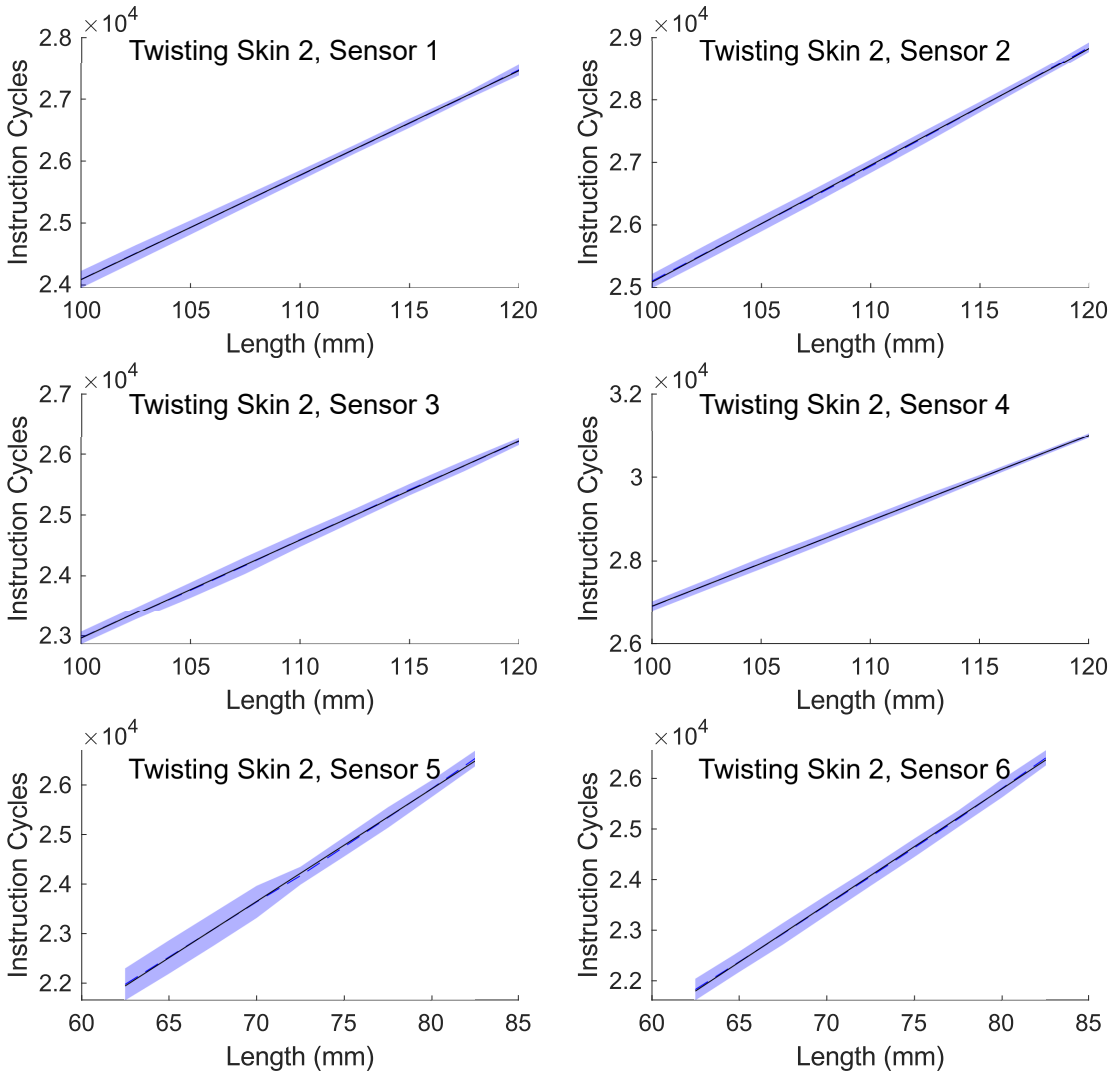

Figure C.13. Experimental results and linear fits for sensors used on Twisting Skin 2. The average experimental data is shown as a blue dashed line with the corresponding 95% confidence interval shown as the shaded region. The linear fit is shown as a black line.

Table C.4. Theoretical linear constants for sensors on the parallel skins.

Skin	Actuator	a_0 (IC/mm)	a_1 (IC)
Parallel 1	1	152	7830
Parallel 1	2	211	7390
Parallel 1	3	221	5700
Parallel 1	4	204	6450
Parallel 1	5	182	8290
Parallel 1	6	183	7760
Parallel 2	1	168	7090
Parallel 2	2	208	5660
Parallel 2	3	158	7320
Parallel 2	4	185	7320
Parallel 2	5	176	7770
Parallel 2	6	183	8280

Table C.5. Theoretical linear constants for sensors on the twisting skins.

Skin	Actuator	a_0 (IC/mm)	a_1 (IC)
Twisting 1	1	216	5710
Twisting 1	2	220	5360
Twisting 1	3	206	6840
Twisting 1	4	167	8200
Twisting 1	5	172	8030
Twisting 1	6	225	10200
Twisting 2	1	169	7220
Twisting 2	2	187	6420
Twisting 2	3	163	6670
Twisting 2	4	204	6560
Twisting 2	5	227	7760
Twisting 2	6	228	7550

C.4 Characterization of Sensor Individually and on the Skin

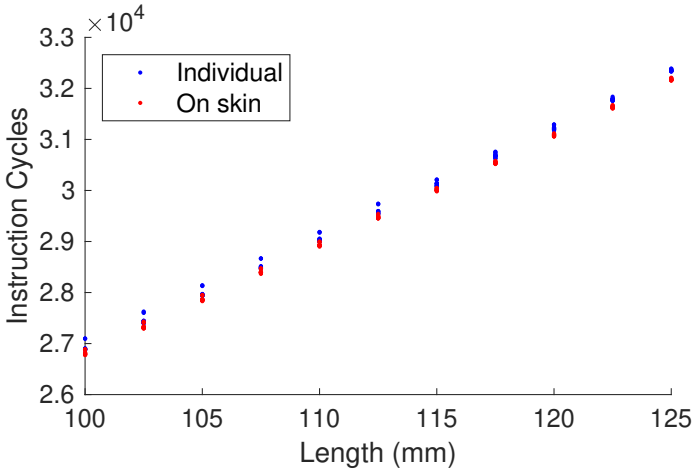

Figure C.14. Raw data of sensor reading when it was measured individually and on the skin.

D. AN ADDRESSABLE PNEUMATIC REGULATOR FOR DISTRIBUTED CONTROL OF SOFT ROBOTS

D.1 Abstract

In this paper, we describe a digitally-controlled, miniature, multi-mode pressure regulator for integration directly into centimeter-scale soft robots. This regulator integrates best-of-class commercially-available pneumatic valves and pressure sensors to achieve a small and lightweight servo-controlled pressure regulator. We demonstrate that the regulator is able to track both step and ramp commands and quantify the error in the resulting pressure. In order to facilitate integration of many such regulators into a single soft robot, we have implemented an addressable digital communication system, based on the industry-standard I2C bus. This allows us to connect up to 127 regulators on a single 4-line bus, significantly reducing the mass and complexity of the required wiring.

D.2 Introduction

Soft robots use low-modulus and multi-functional materials to create highly deformable robotic systems. The resulting systems possess many novel properties, such as light weight, robust structures, and the ability to operate in unstructured environments. The majority of research in the field to-date has focused on these novel

structures, while comparatively little attention has been paid to the support elements which enable these capabilities. In the case of pneumatically-powered soft robots, pressure regulators are required to control the inflation of the actuators. The majority of current pneumatic robots use off-board pressure supplies and regulators and require a tether between the robot and the hardware. This strategy allows for the use of commercially-available pressure regulators, but limits the range and utility of the resulting robots.

An important goal for pneumatic soft robots is to have generalizable strategies for easily creating untethered robots. In this paper, we present a miniature pneumatic regulator capable of continuous pressure control, small enough to fit on centimeter-scale soft robots (Figure D.1). The regulators can operate in two modes: a servo-controlled mode for distributed closed-loop operation and an manual mode to enable off-board control. In servo-controlled mode, the regulator can be commanded to achieve a specific pressure. In manual mode, the regulator can be commanded to execute specific states, including fill, release, and hold, allowing the valves within the regulator to be activated from off-board. Each regulator is commanded over an addressable digital bus, enabling groups of regulators to achieve distributed control on a robotic body. This work advances the state of the art in soft robotics by simplifying valve control and distributed control in soft robots.

D.3 Background

Several groups have worked towards the goal of untethering pneumatically actuated soft robots. Tetherless robots have been created using several strategies. One strategy is to make the robot so large and correspondingly powerful, that it can lift its own power supply [313]. While this strategy is successful for meter-sized robots, the size and weight constraints of commercially available pneumatic components make it infeasible for smaller scales. Another strategy has the robot drag its power supply behind it on wheels [56, 223] or have an additional rigid robot carry the soft robot's

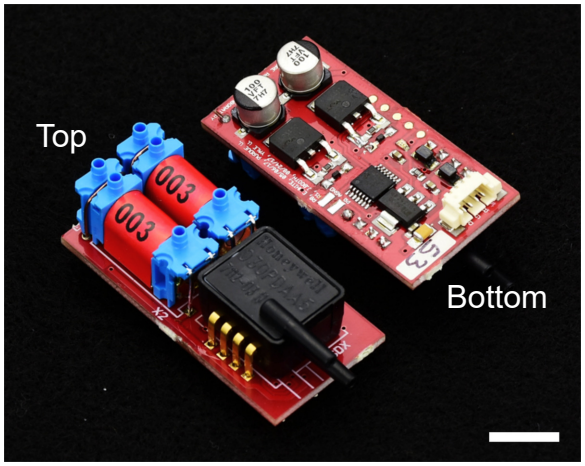

Figure D.1. The addressable pneumatic regulator. The regulator is able to imitate the function of a proportional valve, despite its compact size. By using the I2C protocol, the regulator is able to achieve distributed actuation while staying in a size small enough for centimeter-scale soft robots. The regulator measures 22 x 50 x 20 mm. The scale bar represents 1 cm.

power supply [280]. This strategy is good for testing robots, but may limit their use for in-field applications, such as search and rescue. An additional approach is to use chemical pressure generation, often through the decomposition of a monopropellant such as hydrogen peroxide [10, 38, 229, 314, 315] rather than to use an electrical air pump. This approach is easily scaled to centimeter-sized robots or smaller and is more weight efficient than a traditional pneumatic system. A final, partial step, is to locate the control valves on the robot. Some research groups have incorporated miniature valves into their design [314], whereas others have created custom soft valves that are built into the robot body [10, 314, 315]. All these approaches are still nascent and have to be custom-designed for each new robot.

One problem with embedded valves, to date, is that they are limited to on-off functionality only. In addition, the embedded soft valves are driven by pressure gradients and current examples are passive and unable to be controlled by a central processor. While fluidic control has been demonstrated for a logic circuit [10] and as an addressable array of valves [316], each requires a highly customized system that

is not generalizable. Further, fluidic control generally requires bulky and elaborate vascular systems for basic functions. It is unlikely that fluidic control will be a significant strategy for controlling pneumatic soft robots in the near-term. An additional problem with the current state-of-the-art is that large numbers of solenoid valves require complex wiring. Finally, all the examples of embedded valves discussed above use 2-way or 1-way valves. However, in many circumstances, it is desirable to hold a specific pressure in the actuator, which is why proportional valves are often used in off-board setups. Our approach to address these shortcomings is a miniaturized board capable of distributed control for variable pressure regulation.

D.4 Materials

The pneumatic regulator board is composed of a pressure sensor (Honeywell, ASDXRRX030PDAA5), two miniature 2-way valves (Parker X-valve, 912-000001-003), and a custom circuit board (see github link [317]).

with an embedded microcontroller (Microchip, PIC16F1825T-I/ST). Firmware for the PIC and for an Arduino can also be found in [317]. The above pressure sensor and 2-way valves are limited to 207 kPa (30 psi). The resolution of the pressure sensor is 2% of the total range, which in the case shown in this paper is ±8.3 kPa (1.2 psi). While the pressure sensors and 2-way valves demonstrated in this paper are limited to 207 kPa, we can achieve pressures up to 690 kPa (100 psi) by swapping the pressure sensor and valves with 100 psi versions (Honeywell ASDXRRX100PGAA5 and Parker 912-000001-021, respectively). The board uses I2C protocol to communicate with an external microcontroller (*e.g.*, Arduino, RaspberryPi). This architecture allows up to 127 regulators to connect to a single microprocessor. By using I2C protocol, only four lines are needed (power, ground, clock, and data), resulting in a simplified wiring harness for large numbers of regulators. The valves and pressure sensor are mounted on one side of the board, and the remaining circuit is mounted on the other side. The complete regulator assembly, including tubing, weighs 18 g. The regulator assembly

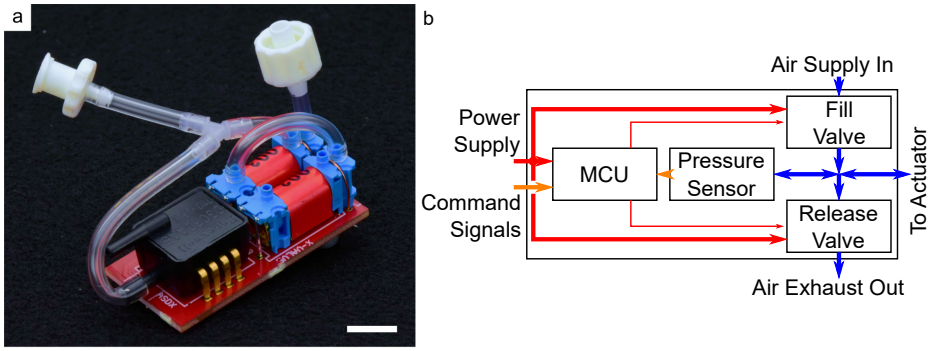

Figure D.2. (a) Photo and diagram showing how airflow occurs through the valves on the pressure regulator. The scale bar represents 1 cm. Alternate airflow configurations are possible with minimal changes to the firmware. (b) Schematic showing the functionality of the regulator.

is 22.2 mm x 49.5 mm x 20.0 mm without tubing. With tubing, it is about 22.2 mm x 56 mm x 30 mm, though this could be improved for a specific application.

The regulator is capable of replicating the function of a 3-way valve, which is not commercially available at the size of our modules. It does so by opening the first valve, which connects the supply in-line pressure to an actuator; closing both valves to hold the air in the actuator; and opening the second valve to release the air from the actuator to the atmosphere. A diagram of the port configuration is found in Figure D.2. The regulator can operate in two modes: manual and servo-controlled. In manual mode, the servo receives state commands (release, hold, or inflate) over the I2C communication lines and executes those states. Without the hold state, the system would need to alternate between fill and release to maintain a given pressure. The hold state reduces chatter and energy consumption and, thus, increases the lifetime of the regulator. Manual mode allows an external controller to actuate regulators, and may be used for open-loop control, or with an off-board logic controller that can be nested inside a feedforward or sensor-based control loop. In servo-controlled mode, an external microcontroller sends a desired pressure to the regulator over the I2C communication line. The regulator then uses the on-board

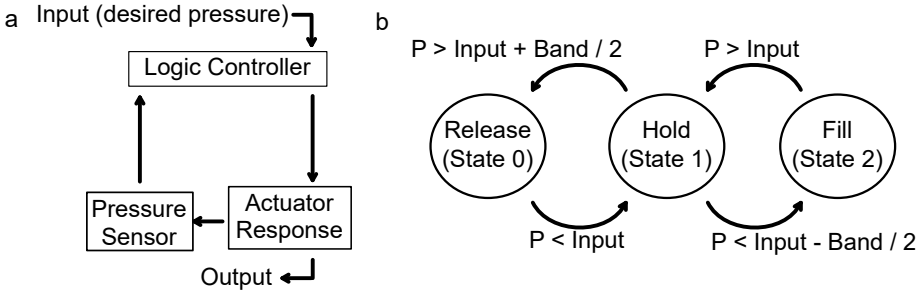

Figure D.3. (a) The control loop used by the on-board microprocessor when in servo-controlled mode. (b) The state machine used for the logic controller. When filling or releasing, the system stops and holds the pressure when the input pressure is crossed. However, it resumes filling or releasing if the pressure reading falls outside the band around the input pressure.

sensor and logic controller to achieve the desired pressure. We implemented a simple bang-bang controller with a minimum deadband of 1 bit, which corresponds to 2 kPa. The sample frequency is constrained by the time it takes to operate each control loop, and is 17.8 kHz. Figure D.3 shows the logic controller and state machine used by the on-board microprocessor. The following sections highlight the performance of the regulator in servo-controlled mode, since this allows for distributed control of multiple actuators.

D.5 Results & Discussion

In order to highlight the utility of our pressure regulators, we first compare various parameters of our system to other existing pneumatic systems that have been reported. Additionally, we characterized the regulators looking at both system response and power consumption. We also show the system performance in terms of step and ramp inputs as well as response to disturbances. For our experiments, we used an in-line pressure of approximately 190 kPa and had a band of 2 bits on our servo-controlled pressure regulator, which corresponds to 4 kPa. Our characterization and system performance tests were done with a McKibben actuator that was 1 cm in

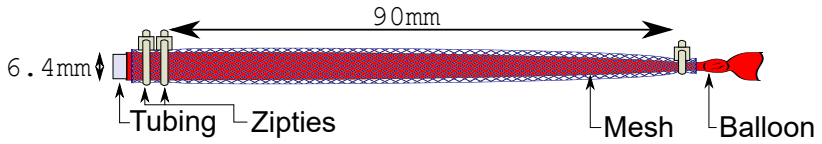

Figure D.4. Drawing of McKibben actuator with dimensions labeled.

diameter and 9 cm in active length when at rest, as seen in Figure D.4. Finally, we demonstrate these regulators on a five-actuator multi-gait soft robot [1].

D.5.1 Comparison

While many researchers do not report their pressure regulators, we compare our regulators to the fluidic control board reported on the Soft Robotics Toolkit website and the few reported hardware components we could find in the literature. This comparison is shown in Table D.1. Our pressure regulator is much smaller and lighter and performs the same number of functions or more than other reported systems.

D.5.2 System Characterization

System Response

We characterized the system response of the pneumatic regulator servo by measuring settling time, percent overshoot, and steady state error of the system using a McKibben actuator. Ten trials were collected at pressures ranging from 5 to 25 psi at 5 psi intervals (or 34, 69, 103, 138, 172 kPa). Each trial lasted 30 s. The settling time was defined to be how long it takes the system to reach and stay within 5% of the set point. The percent overshoot is found as the maximum value before the settling time. The steady state error is the set point minus the average pressure. This error was calculated using the average of the data after the system is considered settled via the calculated settling time. The results of the first second of these trials are shown

Table D.1. A comparison with other common pneumatic valve control systems used in soft robotics research. This comparison is not comprehensive since few research groups publish details on their off-board hardware. The Parker X-Valve is the same as on our regulator, but we include it in the comparison since it could be used independently. The Soft Robotics Toolkit (SRT) board includes more functions than our regulator provides, such as pressure generation, physical switches and an Arduino. We omit these elements when calculating the volume for this board.

Valve and Controller	Range	# Actuators	Package Volume	Flow Rate	Volume Specific Flow Rate	Weight	Control
Faboratory Regulator	0-207 kPa	1	22 cc/actuator	6.4 Lpm	290 s^{-1}	18g	Logic
Soft Robotics Toolkit [318]	0-700 kPa	4	770 cc/actuator	174 Lpm	226 s^{-1}	–	PWM
COTS Festo CPV 14-VI 18210 [319]	0-1000 kPa	6	236 cc/actuator	800 Lpm	3390 s^{-1}	1530g	PLC
COTS SMC ITV1031-21F1N-Q [320, 321]	0-500 kPa	1	244 cc/actuator	200 Lpm	818 s^{-1}	350 g	PLC
Valve Only							
COTS Parker X-Valve (207 kPa) [322]	0-207 kPa	1	2.2cc/actuator	6 Lpm	2730s^{-1}	4.5g	N/A
COTS Parker Ten-X (207 kPa) [313, 323]	0-207 kPa	1	9.6cc/actuator	12 Lpm	1250s^{-1}	12g	N/A

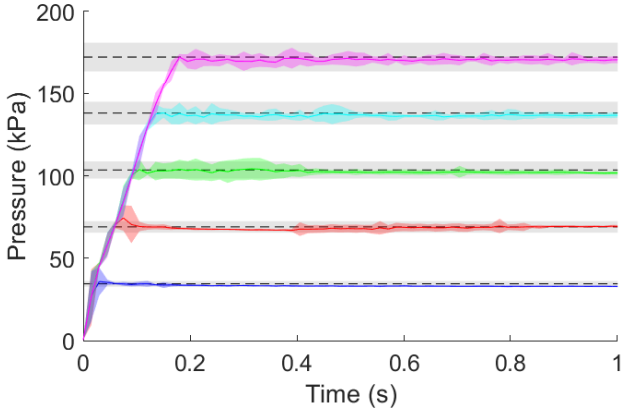

Figure D.5. System response for various pressures. The desired pressure is shown as black dashed lines with a 5% band shown in a gray cloud around the dashed line. The averaged response for 34 kPa is shown as blue; 69 kPa is shown as red; 103 kPa is shown as green; 138 kPa is shown as cyan; and 172 kPa is shown as magenta. The colored clouds around the averages represent 95% confidence intervals for 10 trials.

in Figure D.5 and the settling times, percent overshoots, and steady state errors are presented in Table D.2.

Table D.2. Characterization for 9 cm McKibben actuator at given desired pressures. Ten trials are used to calculate means and standard deviations.

Pressure (kPa)	**Settling Time (s)**	**% Overshoot (%)**	**Steady State Error (kPa)**
34	0.08 ± 0.04	10 ± 6	-0.0 ± 0.4
69	0.09 ± 0.01	12 ± 4	-1.0 ± 0.2
103	0.27 ± 0.12	6 ± 4	-1.2 ± 0.1
138	0.21 ± 0.14	3 ± 2	-1.5 ± 0.1
172	0.17 ± 0.00	0	-1.8 ± 0.1

The settling times for the McKibben actuator are all under 0.3 s. The settling times for the low pressures (34 and 69 kPa) were below 0.1 s. The settling time for the highest pressure (172 kPa) did not overshoot the desired pressure and, thus, the settling time is based on how long it takes to inflate to the desired pressure (0.17 s), which was very consistent, as can be seen in Figure D.5. This may be due to the fact that the pressure is close to the in-line pressure, which was chosen due to component limitations on the regulator. In contrast, the settling times for the 103 and 138 kPa trials were longer due to the system oscillating before coming to rest. We suspect that while filling at these intermediate pressures, the momentum of the air entering the actuator creates a shock-wave and resulting spike in pressure that is not sufficiently damped by the elasticity of the air or the actuator, similar to water hammer. An important consideration is that the settling time for actuators is limited by the pressure, flow-rate, and inflated volume of the actuator, which means that larger actuators will take a longer time to reach a desired pressure.

Looking at percent overshoot, we see that the lower pressures have larger overshoots than the higher pressures. We suspect this is due to the larger difference in the desired and in-line pressure for lower pressures. The steady state error shows that for all the pressures that we tested, we get errors within the range of the accuracy of the pressure sensor itself ($\pm$8.3 kPa). Therefore, the limitation in our regulators is due to the accuracy of the sensor rather than our controller.

Power Consumption

The power consumption of the pressure regulator depends on which state is active and is composed of two independent components: air and electrical power. The air power consumed by a robot depends on the application, but can be easily estimated if the flow rate is known. As a result, we do not report power consumption due to air, but as an aid to future researchers we report the maximum flow rate that our regulator can achieve. In our experiments with the complete regulator assembly at

Table D.3. Power characteristics for the pressure regulator, by state. Power expenditure due to air is not shown since it is dependent on the application and can be estimated with the flow rate.

State	Volts	Amps	Power
Hold	12V	0.022A	0.264W
Fill	12V	0.105A	1.26W
Release	12V	0.105A	1.26W

room temperature, we measured a flow rate of 6.4 Lpm for 138 kPa over 10 trials using a 30 cm length of 3.2 mm (1/8") inner diameter (ID) tubing, but measured a flow rate of 4.7 Lpm when we used 90 cm length of 1.6 mm (1/16") ID tubing.

The electrical power consumed by the module is dependent on which state it is in. The regulator has three states: fill, hold, and release the air. The hold state consumes less power than the fill and release states. The fill and release states actuate a solenoid valve (X-Valve 912-000001-021, by Parker) which consumes 1 W when activated. The control board consumes 0.022 A, resulting in a power draw of 0.264 W. When in the hold state, the board consumes 0.264 W. When in the fill or release states, the regulator consumes 1.26 W. These results are summarized in Table D.3.

D.5.3 System Performance

To demonstrate the capabilities of the regulator to follow commanded pressures, we tested the regulator using both step and ramp inputs. First, the regulator was commanded to hold each pressure (0, 34, 69, 103, 138, and 172 kPa) for 5 s stepping both up and down. Then the regulator was commanded to ramp up from 0 kPa to 172 kPa and back down over the course of 45 s. This procedure was done for 10 trials using our McKibben actuator. The results are shown in Figure D.6. This shows the capabilities of the regulator to not only hold a specific pressure, but to track desired pressure over time.

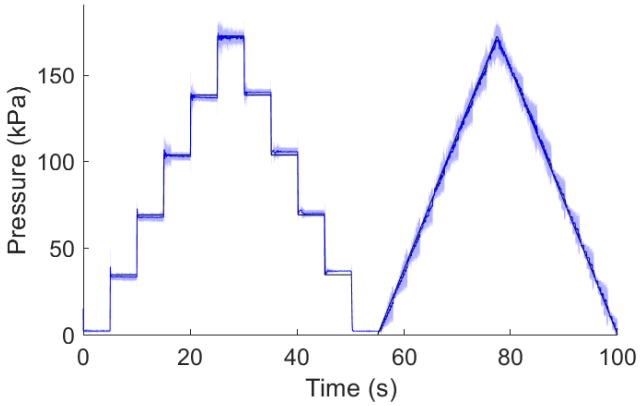

Figure D.6. Step and ramp responses of pressure regulator. The black line shows the desired pressure while the blue line shows the achieved pressure. The colored cloud around the average represent 95% confidence intervals for ten trials.

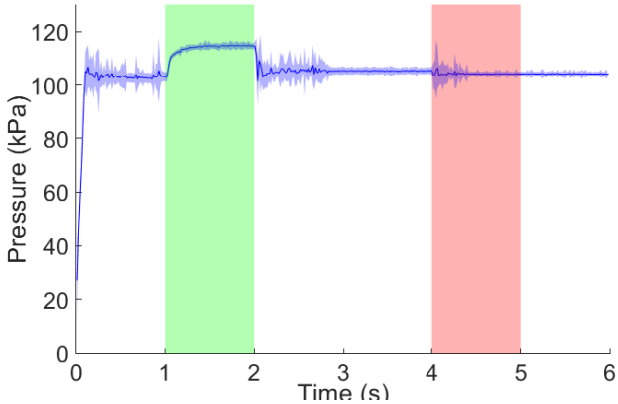

Figure D.7. Disturbance response of actuator (shown as the blue line) when exposed to approximately 190 kPa pressure for 1 s (green) and atmospheric pressure for 1 s (red). The blue clouds represent the 95% confidence intervals for 10 trials.

Because the logic controller is on-board, we are able to take advantage of the distributed control. The regulators are able to locally respond to disturbances, such as those caused by external conditions. To demonstrate this feature, we took our McKibben actuator and briefly exposed it to both 190 kPa and atmospheric pressure.

In order to do this, we used two regulators that connected to the same actuator. One regulator was run in servo-controlled mode to maintain an actuator pressure of 103 kPa while the other regulator was run in manual mode to introduce the changes in pressure for 1 s intervals. Figure D.7 shows the regulator's response to these disturbances for 10 trials. When the pressure increase was imposed on the actuator, the servo-controlled regulator was not able to fully compensate and we observed a pressure increase on the order of 10 kPa. This was because the airflow into the actuator from the manual regulator was higher than the airflow out from the servo-controlled regulator. The inflow rate and outflow rate are different in all pneumatic valves, so this behavior is expected. Further, the pressure plateaus, suggesting that the increased pressure and therefore increased inflow rate comes into equilibrium with the outflow rate. When we used the manual regulator to vent the actuator, we observed an immediate disturbance that quickly settled back to 103 kPa. The servo-controlled regulator fully compensated for the leaking. The results of this experiment demonstrate that the regulators are able to compensate for minor leaks in actuators and other disturbances.

D.5.4 Robot Application

In order to demonstrate the regulators on a soft robot, we have utilized the multi-gait soft robot design from Shepherd *et al.* [1]. We chose this robot because it has multiple actuators and is well-known. Previously, this robot (approximately 14 cm in length) required five pneumatic tethers going to off-board control of its four legs and central body. A larger scale version of this robot (approximately 65 cm in length) has been previously made untethered by having the robot itself carry its power supply [313]. In contrast, the robot we employ here is approximately 20 cm in length and requires only a single pneumatic tether and a set of four wires for communication with the regulators. To position our pressure regulators on-board the quadruped soft robot, we strapped the regulators onto its back, as seen in Figure D.8. While this regulator

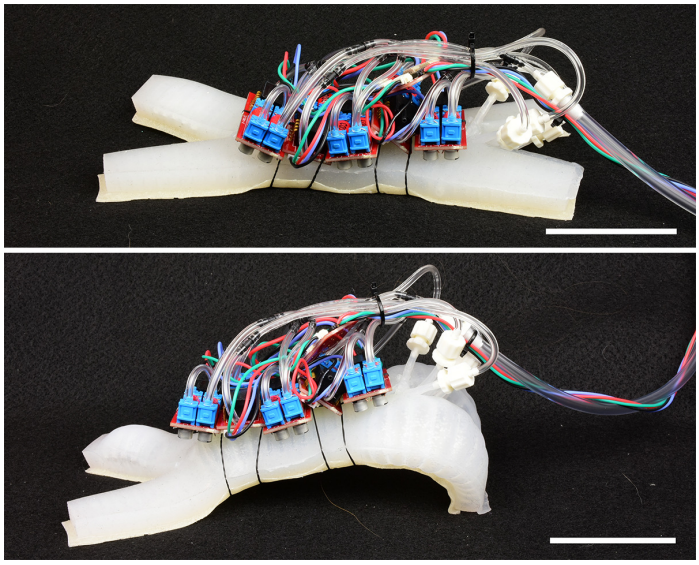

Figure D.8. Images of a soft locomotion robot with five regulators on board. Note that the tether consists of only one supply line and four wires. The scale bars represent 5 cm.

placement is non-ideal since it limits the inflation of the central actuator, we are still able to show that regulators control the inflation of the limbs (Figure D.8). Future robots that use these regulators should consider the placement of the components and accommodate for them during the design of the robot.

One important case where our regulator design may be especially useful is in robot implementations where there is significant variability between actuators. For example, in the case of the multi-gait soft robot, each leg actuates to a slightly different position in response to the same input pressure. This problem is due to inherent imperfections in the manufacturing or material defects and is common in soft actuators. Using our regulators and a calibration, the variations between actuators could be corrected using only a single pressure supply to the robot. Furthermore, on-board pressure regulators would allow actuators with vastly different pressure requirements to use the same pressure supply.

D.6 Conclusion

In this paper, we have demonstrated the functionality of pressure regulators that can be used for soft robots. These regulators are designed to be compact enough to be put on-board centimeter-scale soft robots while also giving full control of pressure and allowing for addressability of individual actuators. We revealed basic characteristics of the pressure regulator and demonstrated its ability to follow a desired pressure over time, as well as its ability to respond to disturbances in pressure. Finally, we showed briefly how these regulators can be placed on a soft robot to reduce the number of pneumatic tethers in the system. One impact of this work is that the regulators can be used to account for the variations that typically arise in the manufacture of soft actuators. Additionally, because these regulators can be controlled remotely using I2C communication, they can be scaled to large arrays while maintaining a single pneumatic tether and a single bus of four wires coming from the robot. While not fully untethering a robot, this regulator brings us one step closer to untethered centimeter-scale soft robots by generalizing pressure control in a way that can be easily adapted to on-board pressure generation methods.

E. DESIGNING ROBUST ELECTRICAL INTERFACES FOR SOFT LIQUID METAL SENSORS

Many soft elastomeric sensors use copper wires to connect to their active element, such as liquid metal. One of the disadvantages of this is that the wires can pull out fairly easily and if this occurs, the entire device is lost in most cases. This requires either the sensors to be handled with care or the development of more robust sensor interfaces.

Researchers have been exploring ways to create contact liquid metal circuits without the use of copper wires. Chossat, *et al.*, made a soft interface of conductive nanoparticles-doped elastomer to connect between liquid metal and saline solution channels [107]. Later, this same concept was accomplished with the use of conductive thread between liquid metal and ionic liquid channels [78]. Theoretically, these methods could be applied at the outward interface of the sensors as well. Lu, *et al.*, created a soft interface to seal liquid metal electronics since that is more stretchable than a rigid interface [199]. The proposed methods to create these soft interfaces is rather involved (with the exception of the conductive thread) and in the end winds up being connected to rigid electrical components anyway, such as alligator clips, ICs, and pins.

Lu, *et al.*, makes a compelling argument for soft sensors by pointing out that straining the sensors around the wires causes tearing and often leaking, which renders the sensors unusable. Rather than developing soft sensor interfaces, many researchers look for methods to reduce strain around the sensors using methods such as implanting flex circuits [85,209] or using stiff fabric [86]. The disadvantage of the fabric technique is that the wires can still pull out fairly easily by user handling. To address the failure due to wires pulling out, we tried both copper disks and copper polyimide strips. The copper polyimide strips were tested both untreated and with a coating of solder.

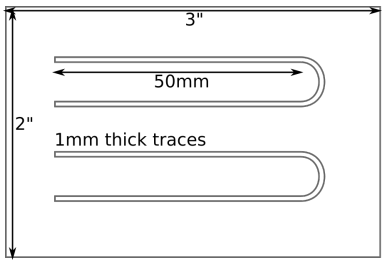

Figure E.1. Sensor design. Mask made from paper was used to create the traces used in sensors.

For the following three techniques (copper disks, copper polyimide film, and copper polyimide film treated with solder), we looked at sensor fabrication using Sylgard 184 and eGaIn. The PDMS was coated onto 2" by 3" glass slides using a Specialty Coating Systems Spincoat G3-8 spin coater. The slides were spun for 60s at 200RPM with 10s acceleration and deceleration. The PDMS was cured in an incubator at 60°C.

Since the intention of this work was to test the effectiveness of the interface, we use a simplified sensor design with a single turn. This was done to ensure that the input and output of the sensors were on the same side. We found that traditional methods of syringe filling were ineffective since the new interface techniques interfered in the channel fabrication process by either allowing channels to be filled with elastomer or by created large air bubbles around the interface. Instead, we used a print mask technique using a paper mask [150], which creates freestanding traces of eGaIn. The mask we used is shown in Figure E.1. Similarly, we could have used 3D printing techniques to lay out traces [96, 146].

Copper disks: The first method we tried was replacing wires with copper disks. These disks were made by punching disks out of 0.002" copper film. Four disks were placed manually over the eGaIn traces; two in each side. More PDMS was poured over the top of the the traces and cured in the incubator. When we started working with the copper disks, we noticed that they were likely to cause and propogate tears in the material due to being a high stress concentrator. To alleviate this problem,

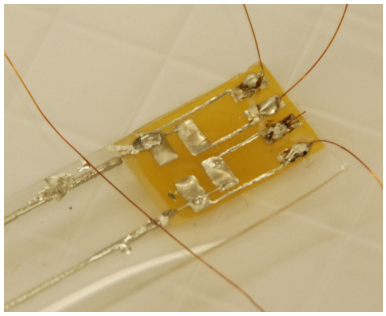

Figure E.2. Robust sensor interface made from soldered copper polyimide film.

we used fabric reinforcement to limit stress that can occur around the disks. Finally, small holes were cut out on top of the copper disks such that they were less than the diameter of the disks. Copper wire was then soldered onto the copper disks to complete the sensor. The sensors were cut out with an X-acto knife.

Copper polyimide film: The next method replaced wires with copper polyimide films (Pyralux). The films were made by creating a kapton mask on top of the film and etching the unwanted copper with hydrogen peroxide and hydrochloric acid solution (Note: if it is not working add more hydrogen peroxide). This film was tacky bonded to our PDMS films while they were curing. Traces were made over the films and the PDMS when curing was completed. The eGaIn did not stick to the surface of the polyimide and copper well during the lithography, so the traces connecting to the polyimide film were added manually with a syringe. PDMS was then coated over this and cured in the incubator. An X-acto knife was used to scrap PDMS off the copper electrodes and copper wires were soldered to them.

Copper polyimide film with solder coating: This method is very similar to the copper polyimide film method with the exception that after curing, the copper was coated with a solder film. This was done since eGaIn will bond better to solder than it will to copper. This interface can be seen in Figure E.2.

We had connectivity issues with both the copper disks and the copper polyimide films when the sensors were strained. We suspect that the copper disks were squeezing the eGaIn into the channels and losing connection which made them unreliable. We

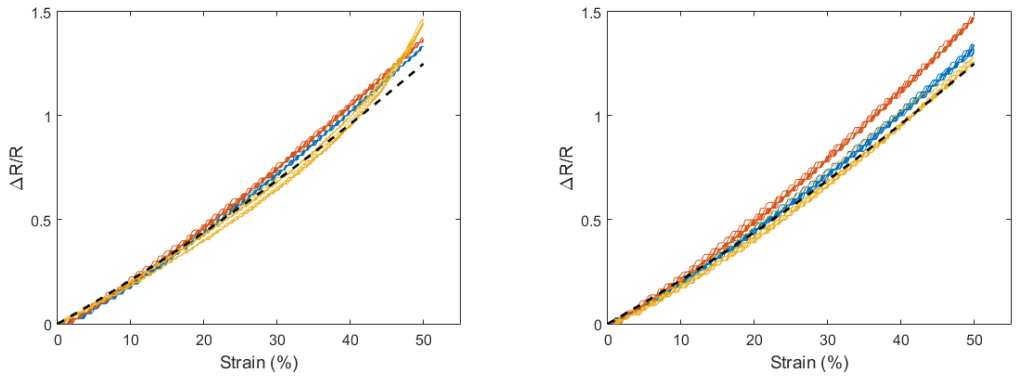

(a) (b)

Figure E.3. Strain response cyclical tests for (a) wire samples and (b) soldered polyimide samples. There are three samples in each. The theoretical fit is shown by the black dashed line [86].

also suspect that the copper polyimide film was doing the same. The copper polyimide film that had been soldered coated, however, performed well in comparison. There was no lose of conductivity.

A comparison of the sensor performance of the soldered copper polyimide film sensors and traditional wire sensors are shown in Figure E.3. The sensors were strained to 50% at a rate of 20mm/min for 5 cycles in an 3345 Instron material testing machine. It can be seen that the functionality of the soldered polyimide devices are comparable to the traditional wiring method.

Once we had functional sensors, we ran tests using the Instron to test the force required to mechanical pull the copper wire out. This was done by pulling a single wire from the devices and tracking the force at failure. The wires were pulled at 20mm/min. The soldered polyimide device required a breaking force 4 times that of the traditional wiring method. It should be noted that the failure of the copper polyimide device did not occur at the solder joint, but rather on the wire itself. Specifically, the part that had been mechanically weakened by steel wool that was used to rub off the coating on the wire. This is promising since even stronger interfaces can be created by using either thicker wire or wire that is not similarly weakened.

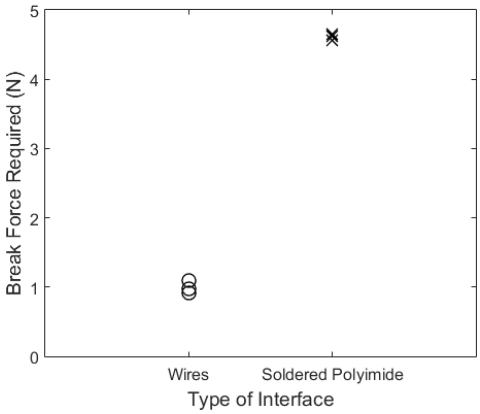

Figure E.4. Results from ripping wires from devices.

However, this is strong enough that handling should not result in potential device failure.

However, despite this promising result, there was too much variability in performance of liquid-metal-embedded sensors for them to be reliable in soft systems. Therefore, our lab shifted focus from liquid-metal-embedded sensors to conductive polymer composite sensors for use in soft systems. We selected exfoliated graphite as our conductive material since it does not significantly change the material properties of the base elastomer. Our initial work on this elastomer tests both a resistive and 3-layer capacitive sensor made from this composite as well as fully describes how the composite itself is made [43]. This work showed that while the resistive sensor was subject to material degradation, the capacitive sensor was not. Thus, we have been using capacitive sensors in our soft systems. While the 3-layer capacitive sensor device works, it is subject to environmental noise. To reduce this noise, we have moved from 3-layer to 5-layer capacitive sensors, which isolate the active element by having the two outer layers grounded [6]. There is still some noise in these 5-layer devices, but it has been significantly reduced.

F. 3D CABLE-DRIVEN SOFT CONTINUUM ROBOT MODEL

F.1 Robot Kinematics

Previous cable-driven continuum manipulators have cables that run parallel to the body of the manipulator causing bending and compression. Their deformation can be expressed using the following described with the state vector $\mathbf{q} = \{\kappa, \phi, \lambda\}^T = \{\kappa_x, \kappa_y, \lambda\}^T$ where $\kappa = \sqrt{\kappa_x^2 + \kappa_y^2}$ and $\phi = \tan^{-1}(\kappa_y/\kappa_x)$ [287]. Here, κ is the curvature, ϕ is the angular offset of the curve, κ_x describes the curvature with respect to the x-axis, κ_y describes the curvature with respect to the y-axis, and λ denotes the stretch.

To define the kinematics for this system, we have utilized homogeneous transformations. This approach is a familiar approach to robotics and is able to easily describe the deformation of the entire structure.

The deformation for a single elastomer segment of a traditionally cabled system can be described as [33]:

$$ {}^{i-1}T_i = \begin{bmatrix} c_\phi^2 v_\theta + 1 & s_\phi c_\phi v_\theta & -c_\phi s_\theta & \frac{1}{\kappa} c_\phi v_\theta \\ s_\phi c_\phi v_\theta & c_\phi^2 v_\theta + c_\theta & -s_\phi s_\theta & \frac{1}{\kappa} s_\phi v_\theta \\ c_\phi s_\theta & s_\phi s_\theta & c_\theta & \frac{1}{\kappa} s_\theta \\ 0 & 0 & 0 & 1 \end{bmatrix} \tag{F.1} $$

where $c_x = \cos(x)$, $s_x = \sin(x)$, $v_x = c_x - 1$, $\theta = \kappa s$ is the angle of curvature, $s = \lambda l_e$ is the length of the curve, and l_e is the initial length of the elastomer segment.

In contrast, our system employs spiraling cables that impart twist as well as bending and compression. The state vector for this case can be described as $\mathbf{q} = \{\kappa, \phi, \lambda, \alpha\}^T = \{\kappa_x, \kappa_y, \lambda, \alpha\}^T$, where α is the angle of twist. To capture this behavior, we assume that the system compresses and bends according to the matrix given in Equation (F.1) and then twists with respect to the original z-axis. While this does

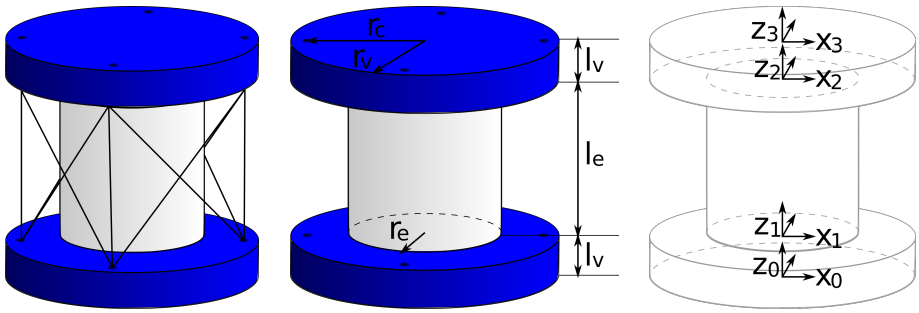

(a) (b) (c)

Figure F.1. Single segment with (a) both parallel cables and spiraling cables, (b) lengths labeled, and (c) axes drawn on the segment.

not capture the exact behavior of the system, we are only looking for a model that gets close enough to the physical system to be used in a feedforward control system. The error in the model can then be handled by sensory feedback control. To capture this additional twist, we have:

$$ {}^{1}T_{2} = \begin{bmatrix} c_{\alpha+\phi}c_{\phi}v_{\theta} + c_{\alpha} & -s_{\alpha-\phi}c_{\phi}v_{\theta} - s_{\alpha}c_{\theta} & -c_{\alpha+\phi}s_{\theta} & \frac{1}{\kappa}c_{\alpha+\phi}v_{\theta} \\ s_{\alpha+\phi}c_{\phi}v_{\theta} + s_{\alpha} & c_{\alpha-\phi}c_{\phi}v_{\theta} + c_{\alpha}c_{\theta} & -s_{\alpha+\phi}s_{\theta} & \frac{1}{\kappa}s_{\alpha+\phi}v_{\theta} \\ c_{\phi}s_{\theta} & s_{\phi}s_{\theta} & c_{\theta} & \frac{1}{\kappa}s_{\theta} \\ 0 & 0 & 0 & 1 \end{bmatrix} \tag{F.2} $$

where $c_{x+y} = \cos(x+y)$ and $s_{x+y} = \sin(x+y)$. Note that the numbers in ${}^{2}T_{3}$ refer to the coordinate frames in Figure F.1(c). However, this just captures the deformation of the elastomer segment rather than the segment as a whole. On either side of the elastomer are rigid vertebrae that help guide the cables. The transformations for these are given by:

$$ {}^{0}T_{1} = {}^{2}T_{3} = \begin{bmatrix} 1 & 0 & 0 & 0 \\ 0 & 1 & 0 & 0 \\ 0 & 0 & 1 & l_{v} \\ 0 & 0 & 0 & 1 \end{bmatrix} \tag{F.3} $$

where l_v is the length of half a vertebra, l_d is the length of the rigid stabilizer. To get the total deformation of the segment, we must put all of these transforms together:

$$
\begin{aligned}
{}^0T_3 &= {}^0T_1\,{}^1T_2\,{}^2T_3 \\
&= \begin{bmatrix}
c_{\alpha+\phi}c_\phi v_\theta + c_\alpha & -s_{\alpha-\phi}c_\phi v_\theta - s_\alpha c_\theta & -c_{\alpha+\phi}s_\theta & \frac{1}{\kappa}c_{\alpha+\phi}v_\theta - c_{\alpha+\phi}s_\theta l_v \\
s_{\alpha+\phi}c_\phi v_\theta + s_\alpha & c_{\alpha-\phi}c_\phi v_\theta + c_\alpha c_\theta & -s_{\alpha+\phi}s_\theta & \frac{1}{\kappa}s_{\alpha+\phi}v_\theta - s_{\alpha+\phi}s_\theta l_v \\
c_\phi s_\theta & s_\phi s_\theta & c_\theta & \frac{1}{\kappa}s_\theta + (1+c_\theta)l_v \\
0 & 0 & 0 & 1
\end{bmatrix}
\end{aligned}
\tag{F.4}
$$

These five transformations describe the state for a single segment in the system. If we let ${}^0T_3 = {}^0A_1$, the ${}^{i-1}T_i$ describes the transformations in a given segment, while ${}^{i-1}A_i$ describes the whole transformation for a single segment. Thus, if we want to know the transformation of multiple segments, we simply combine them:

$$
{}^0A_4 = {}^0A_1\,{}^1A_2\,{}^2A_3\,{}^3A_4 \tag{F.5}
$$

where it is important to note that each ${}^{i-1}A_i$ has a $\mathbf{q}_{i-1} = \{\kappa_{x,i-1}, \kappa_{y,i-1}, \epsilon_{a,i-1}, \alpha_{i-1}\}^T$ defining the ${}^2T_3$ deformation given in Equation (F.2) for each segment.

F.2 Robot Kinetics

For this manipulator, we are exploring the effects of adding spiraling cables. We will be specifically considering a four-segment manipulator, as shown in Figure F.2, which shows the various cables that will be used and labels both the segments and cables for reference.

For this manipulator, we make several assumptions that are generally used in continuum manipulators: (1) linear material properties; (2) constant curvature of segments; (3) friction is negligible; (4) cables do not contact the body of the spine; and (5) external loads are negligible.

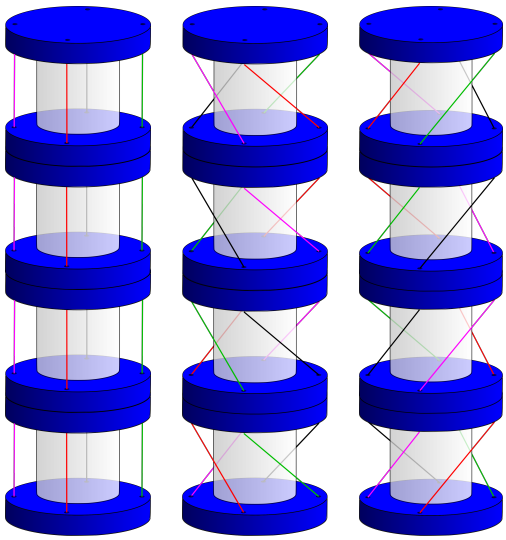

(a) (b) (c)

Figure F.2. Four-segment manipulator with (a) segments labeled, (b) parallel cables labeled, (c) counter-clockwise cables labeled, and (d) clockwise cables labeled. The segment $s0$ is rigidly fixed.

F.2.1 Single Segment

We start our kinetic derivations with a single segment, which we will build upon for a multi-segment spine. Since this system is intended to hang upside-down, our system is affected by the cable tension as well as the weight of the system itself. To describe the deformation of the sensor, we need to know both the start and end points of the cables. These points are described in Figure F.3.

For a single segment, we have $\mathbf{q} = \{\kappa_x, \kappa_y, \epsilon_a, \alpha\}^T$ which can be described via

$$\kappa_x = -\frac{1}{K_b} M_y \tag{F.6a}$$

$$\kappa_y = -\frac{1}{K_b} M_x \tag{F.6b}$$

$$\epsilon_a = \frac{1}{K_a} \sum F_{z,i} \tag{F.6c}$$

$$\alpha = -\frac{s}{K_t} M_z \tag{F.6d}$$

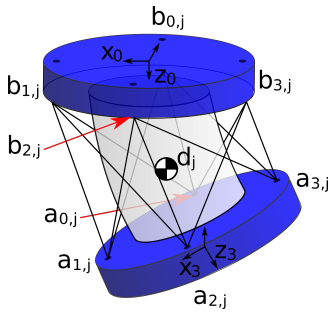

Figure F.3. Cable start and end points labeled for a single segment that is hung upside-down. $\mathbf{a}_{c,j}$ refers to the end points and $\mathbf{b}_{h,j}$ refers to the start points of the cables on the jth segment; note that the values of c and h depend on the cable pattern. $\mathbf{d}_j$ refers to the midpoint of the jth segment.

where $K_b = EI$ is bending stiffness, $K_a = EA$ is axial stiffness, $K_t = GJ$ is torsional stiffness, E is Young's modulus, I is the second moment of inertia of the segment, A is the cross-sectional area of the segment, G is the modulus of rigidity, J is the is the second moment of area, M_n is the moment about the n-axis, and $F_{z,i}$ is the force along the z-axis for the ith cable. The modulus of rigidity can be described as $G = E/(2(1+\nu))$, where ν is Poisson's ratio.

In order to determine the state of our segment, we need to know how the cables and weight are creating forces on the segments. We will start by focusing on the cable forces. Each cable has a tension, T_i for the ith cable, that influences the segment deformation. This tension creates a force that is applied along the length of the cable. Therefore, for a single cable, we can describe the force of a single cable as

$$T_i \mathbf{v}_i = T_i \frac{\mathbf{b}_{h,j} - \mathbf{a}_{c,j}}{||\mathbf{b}_{h,j} - \mathbf{a}_{c,j}||} \tag{F.7}$$

where $\mathbf{F}_i$ describes the force for the ith cable, $\mathbf{a}_{c,j}$ describes end point and $\mathbf{b}_{h,j}$ of the ith cable in the $x0$-$y0$-$z0$ coordinate frame for the jth segment. The moment arm ($\mathbf{r}_{i,j}$ for the ith cable on the jth segment), which spans from the center of the $x0$-$y0$-$z0$ coordinate frame for the jth segment to the end points of the cables, is given as $\mathbf{r}_i = \mathbf{a}_{c,j}$.

The weight of a segment is described as

$$\begin{Bmatrix} \mathbf{W}_j \\ 0 \end{Bmatrix} = ({}^0A_j)^{-1} \begin{Bmatrix} 0 \\ 0 \\ m_j g \\ 0 \end{Bmatrix} = \mathbf{w}_j m_j g \tag{F.8}$$

where m_{sj} is the mass of the jth segment, g is the gravitational constant, and $\mathbf{w}_j$ is the third column of the $({}^0A_j)^{-1}$ matrix for the jth segment. Note that we use the A transformations here because weight is in the $z0$ direction of the 0th segment. The weight is in the positive $z0$ direction because the spine will be hanging upside-down, and thus pointing in that direction. The moment arm for the weight, which spans from the center of the $x0$-$y0$-$z0$ coordinate frame for the jth segment to the center of the mass of the segment, is given by $\mathbf{d}_j$.

Considering the spine in Figure F.2, we will allow the 0th segment to be fixed while the nth segment is free. If we are looking at a single segment, this means that we only consider the nth segment. We are assuming loads are applied slowly and thus analyze the quasi-static response of the system. Looking at the sum of forces and moments, we find

$$\mathbf{F}_n = -m_n g \mathbf{w}_n - \sum_{i=0}^{k-1} T_i \mathbf{v}_{i,n} \tag{F.9a}$$

$$\mathbf{M}_n = -m_n g (\mathbf{d}_n \times \mathbf{w}_n) - \sum_{i=0}^{k-1} T_i (\mathbf{r}_{i,n} \times \mathbf{v}_{i,n}) \tag{F.9b}$$

where $\mathbf{F}_n$ is the reaction forces and $\mathbf{M}_n$ is the reaction moments of the nth segment, and k is the number of cables. Using these reaction forces together with Equation (F.6), we have defined the kinetics for a single segment.

F.2.2 Multiple Segments

Adding multiple segments requires an expanded form of the model. This can be done easily by transferring the reaction forces and moments along the length of the

spine. For an arbitrary $j-1$th segment where $j \in [1, n]$, we find the reaction forces and moments to be

$$\mathbf{F}_{j-1} = -m_{j-1}g\mathbf{w}_{j-1} - \sum_{i=0}^{k-1} T_i \mathbf{v}_{i,j-1} + \mathbf{F}_{j,adj} + \sum_{i=0}^{k-1} T_i \mathbf{v}_{i,j,adj} \tag{F.10a}$$

$$\begin{aligned}\mathbf{M}_{j-1} = &-m_{j-1}g(\mathbf{d}_{j-1} \times \mathbf{w}_{j-1}) - \sum_{i=0}^{k-1} T_i(\mathbf{r}_{i,j-1} \times \mathbf{v}_{i,j-1}) + \mathbf{M}_{j,adj} + (\mathbf{l}_{j-1} \times \mathbf{F}_{j,adj}) \\ &+ \sum_{i=0}^{k-1} T_i(\mathbf{r}_{i,j-1} \times \mathbf{v}_{i,j,adj})\end{aligned} \tag{F.10b}$$

where $\mathbf{l}_{j-1}$ is the vector that goes from the center of the $x0$-$y0$-$z0$ coordinate frame to the center of the $x5$-$y5$-$z5$ coordinate frame for the $(j-1)$th segment. We have adjusted values for some variables that are defined as follows

$$\begin{Bmatrix} \mathbf{F}_{j,adj} \\ 0 \end{Bmatrix} = {}^{j-1}A_j \begin{Bmatrix} \mathbf{F}_j \\ 0 \end{Bmatrix} \tag{F.11a}$$

$$\begin{Bmatrix} \mathbf{M}_{j,adj} \\ 0 \end{Bmatrix} = {}^{j-1}A_j \begin{Bmatrix} \mathbf{M}_j \\ 0 \end{Bmatrix} \tag{F.11b}$$

$$\begin{Bmatrix} \mathbf{v}_{i,j,adj} \\ 0 \end{Bmatrix} = {}^{j-1}A_j \begin{Bmatrix} \mathbf{v}_{i,j} \\ 0 \end{Bmatrix} \tag{F.11c}$$

Equations (F.9-F.11) define the spine kinetics for a spine with $(n+1)$ segments.

VITA

Education

Purdue University, West Lafayette, IN 08/2013 - 08/2019

Ph.D. Candidate in **Mechanical Engineering**

Advisors: Rebecca Kramer-Bottiglio and James Gibert

Dissertation Title: "Designing Soft Continuum Robots for Sensor-Enabled Control"

M.S. in **Mechanical Engineering**

Northern Illinois University, DeKalb, IL 08/2009 - 05/2013

B.S. in **Mechanical Engineering**

Graduated with University Honors, Minor in Applied Mathematics

Journal Publications

J. Case, M. Yuen, J. Jacobs, and R. Kramer-Bottiglio. "Robotic Skins that Learn to Control Passive Structures." *IEEE Robotics and Automation Letters* 4.3 (2019): 2485-2492.

J. Booth, D. Shah, **J. Case**, E. White, M. Yuen, O. Cyr-Choiniere, and R. Kramer-Bottiglio. "OmniSkins: Robotic skins that turn inanimate objects into multi-functional robots." *Science Robotics* 3.22 (2018).

E. White, **J. Case**, and R. Kramer-Bottiglio. "A Soft Parallel Kinematic Mechanism." *Soft Robotics* 5.1 (2018): 36-53.

J. Case, E. White, V. SunSpiral, and R. Kramer-Bottiglio. "Reducing Actuator Requirements in Continuum Robots through Optimized Cable Routing." *Soft Robotics* 5.1 (2018): 109-118.

E. White, M. Yuen, **J. Case**, and R. Kramer. "Low-cost, Facile, and Scalable Manufacturing of Capacitive Sensors for Soft Systems." *Advanced Materials Technologies* 2.9 (2017).

E. White, **J. Case**, and R. Kramer. "Multi-mode strain and curvature sensors for soft robotic applications." *Sensors and Actuators A: Physical* 253 (2017): 188-197.

J. Case, E. White, and R. Kramer. "Sensor enabled closed-loop bending control of soft beams." *Smart Materials and Structures* 25.4 (2016).

E. White, **J. Case**, and R. Kramer. "Multi-element strain gauge modules for soft sensory skins." *IEEE Sensors Journal* 16.8 (2016): 2607-2616.

J. Case, E. White, and R. Kramer. "Soft Material Characterization for Robotic Applications." *Soft Robotics* 2.2 (2015): 80-87.

Book Chapters

J. Case, M. Yuen, M. Mohammed, R. Kramer. "Sensor Skins: An Overview." *Stretchable Bioelectronics for Medical Devices and Systems* (2016): 173-191.

Conference Proceedings

R. Bilodeau, M. Yuen, **J. Case**, T. Buckner, and R. Kramer-Bottiglio. "Design for Control of a Soft Bidirectional Bending Actuator," in *Intelligent Robots and Systems (IROS 2018), 2018 IEEE/RSJ International Conference on*, pp. 1-8, IEEE, 2018.

J. Booth*, **J. Case***, E. White, D. Shah, and R. Kramer-Bottiglio. "An Addressable Pneumatic Regulator for Distributed Control of Soft Robots," in *2018 IEEE International Conference on Soft Robotics (RoboSoft)*, pp. 25-30. IEEE, 2018. * indicates co-first authorship.

J. Case, J. Booth, D. Shah, M. Yuen, and R. Kramer-Bottiglio. "State and Stiffness Estimation using Robotic Fabrics," in *2018 IEEE International Conference on Soft Robotics (RoboSoft)*, pp. 522-527. IEEE, 2018.

E. White, **J. Case**, and R. Kramer. "Reconfigurable Logic Devices Connected with Laser-Sintered Liquid Metal Nanoparticles," in *IEEE Sensors 2017*, IEEE, 2017.

M. Yuen, A. Cherian, **J. Case**, J. Seipel, and R. Kramer. "Conformable Actuation and Sensing with Robotic Fabric," in *Intelligent Robots and Systems (IROS 2014), 2014 IEEE/RSJ International Conference on*, pp. 580-586. IEEE, 2014.

T. Chenal, **J. Case**, J. Paik, and R. Kramer. "Variable Stiffness Fabrics with Embedded Shape Memory Materials for Wearable Applications," in *Intelligent Robots and Systems (IROS 2014), 2014 IEEE/RSJ International Conference on*, pp. 2827-2831. IEEE, 2014.

Manuscripts in preparation

O. Cyr-Choiniere, J. Booth, **J. Case**, D. Shah, M. Yuen, N. Pham, and R. Kramer-Bottiglio. "Surface actuation and sensing of a tensegrity structure using robotic skins," In Preparation.

J. Case, G. Branin, V. SunSpiral, J. Gibert, R. Kramer-Bottiglio. "A Generalized Model of Robotic Skins for Design and Control of Continuum Robots," In Preparation.

Oral Presentations

"Robotic Skins that Learn to Control Passive Structures," presented at the *2019 IEEE International Conference on Soft Robotics (RoboSoft)*, Seoul, Korea, April 2019.

"State and Stiffness Estimation using Robotic Fabrics," presented at the *2018 IEEE International Conference on Soft Robotics (RoboSoft)*, Livorno, Italy, April 2018.

"Soft Spines: Controlling Spine-Like Soft Robots," presented at National Institute of Standards and Technology, by invitation, Gaithersburg, MD, November 2017.

"Reconfigurable Logic Devices Connected with Laser-Sintered Liquid Metal Nanoparticles," presented at the *IEEE Sensors 2017*, Glasgow, Scotland, October 2017.

"The Importance of Design in Soft Robotic Control," presented at the *Society of Engineering Science Conf.*, College Park, MD, October 2016.

"The Impacts of Material Properties on Soft Robotic Control," presented at the *ASME International Mechanical Engineering Congress and Exposition*, Houston, TX, November 2015.

"Materials for Soft Robotics," presented at the *Society of Engineering Science Conf.*, West Lafayette, IN, October 2014.

Poster Presentations

"Alternative Actuation Methods for Continuum Robots," poster presented at *Women in Robotics* workshop at the *Robotics: Science and Systems Conf.*, Pittsburgh, PA, June 2018.

"Control of an Active Sensor Skin for Extreme Terrain Mobility," poster presented at NASA Space Technology Day-On-The-Hill, by invitation, Washington, DC, November 2017.

"Fluid dynamics at transition regions of enhanced heat transfer channels," poster presented at the *Bulletin of the American Physical Society Division of Fluid Dynamics Conf.*, San Diego, CA, November 2012.

Awards

NIST NRC Postdoctoral Research Associateship Program

NASA Space Technology Research Fellowship 2015-2019

NSF Graduate Research Fellowship Declined

Purdue Doctoral Fellowship 2013-2015